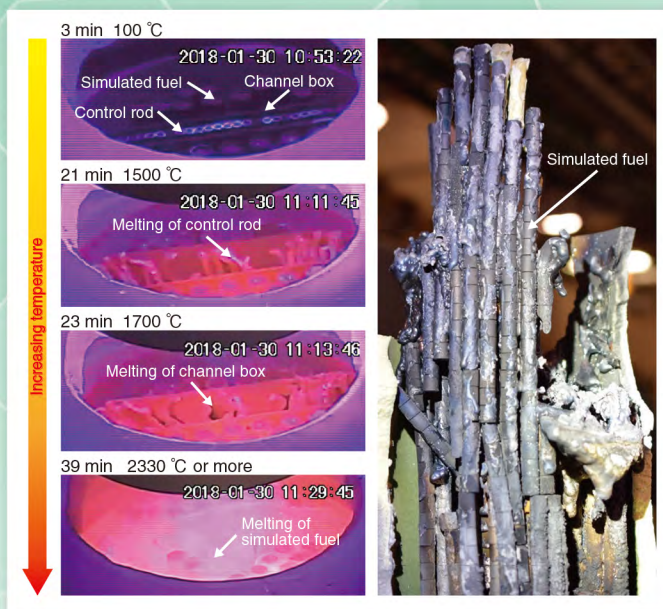
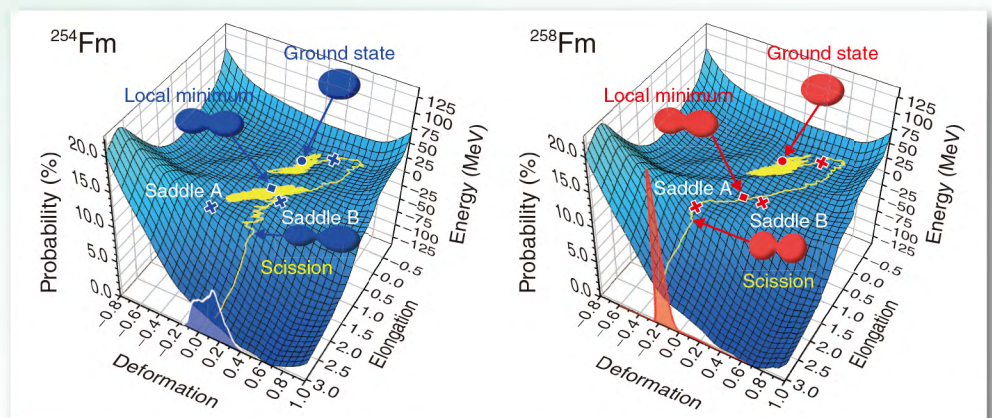


JAEA R&D Review

2019-20



Core-material melting and relocation (CMMR) test (Topic 1-1)



Shape evolution and fission for two fermium isotopes, ^{254}Fm and ^{258}Fm (Topic 3-1)



Message from the President

児玉 敏雄

President Toshio KODAMA

We sincerely thank you for your understanding and continuous support regarding the research and development (R&D) activities of the Japan Atomic Energy Agency (JAEA).

JAEA's mission as the only comprehensive nuclear R&D institution in Japan is to contribute to the welfare and prosperity of human society through nuclear science and technology. Therefore, we undertake R&D in active cooperation and collaboration with industries and universities. Our studies have included cases such as the accident at the Fukushima Daiichi Nuclear Power Station (NPS) operated by the Tokyo Electric Power Company Holdings, Inc.; research on nuclear safety improvement; R&D toward the establishment of nuclear fuel recycling technologies, including fast reactors and reprocessing; and the development of technology for the treatment and disposal of radioactive waste. Furthermore, to support these activities and create new technologies, nuclear science and engineering research has also been implemented, together with the development in human resources.

Regarding the efforts to respond to the accident at the Fukushima Daiichi NPS, we have conducted and will continue to further research into the decommissioning and environmental recovery based on the medium- to long-term roadmap for decommissioning and the “Basic Guidelines for the Reconstruction and Revitalization of Fukushima”. Additionally, we are preparing to resume the operation of research reactors, such as the JRR-3, and strive to provide world-leading fundamental research and research on the improvement of safety. Based on the strategic roadmap developed by the government last December, we have conducted research on various types of reactor technologies, including the development of fast reactors and advanced reactors.

Additionally, based on the “Back-end Roadmap” and “Medium/Long-Term Management Plan of JAEA Facilities”, we have and will continue to safely and steadily advance decommissioning and back-end measures for, among others, the Monju, Fugen, and Tokai Reprocessing Plant.

This work aims to introduce representative topics of the latest our R&D achievements.

We are pleased to provide further understanding into JAEA's accomplishments through this publication, and we appreciate your continued encouragement and cooperation for our R&D activities.

About This Publication and the JAEA Organizational Outline.....	8
-----------------------------------------------------------------	---

1 *Research and Development on the Post-Accident Environmental Restoration and Decommissioning of Fukushima Daiichi NPS*

Providing Advanced Scientific Knowledge by Concentrating Expertise.....	11
-------------------------------------------------------------------------	----

1. Estimate the State of the RPV and PCV after a Severe Accident	12
– Upgrading of the Comprehensive Identification of Conditions Inside Reactor –	
2. Numerical Evaluation of Fuel Debris Hardness.....	13
– First-Principle Calculation of the Mechanical Properties of Fuel Debris –	
3. Degradation Mechanism of a BWR Control Blade.....	14
– Understanding the Behavior of Boron Compounds during a Severe Accident –	
4. Uncertainty Estimation in the Criticality of Nuclear Systems Containing Fuel Debris	15
– Development of a Criticality Calculation Method for Randomly Distributed Materials –	
5. Measuring Alpha-Particle Emitters Flying in Nuclear Facility Buildings	16
– A Highly Reliable Alpha Dust Monitor Using a GPS Scintillator Plate –	
6. Determination of the Optimum Shape of Hydrogen Recombination Catalysts	17
– Hydrogen Elimination Effect Experimentally Verified for Full-Size Equipment –	
7. Estimating Radioactive Waste Inventory.....	18
– Sorption Behavior of Actinides on Zeolite –	
8. Towards Routine Analysis of Difficult-to-Measure Radionuclides.....	19
– Preparation of Analysis Manuals for ⁹³ Zr, ⁹³ Mo, ¹⁰⁷ Pd, and ¹²⁶ Sn Waste –	
9. Assessing the Safety of Reusing Contaminated Rubble	20
– Restricted Reuse in the TEPCO's Fukushima Daiichi NPS Site –	
10. Development of Robot Simulator for Decommissioning Task Training.....	21
– Multi-Copter Simulator and Virtual Operator Proficiency Training System –	
11. Observed Decrease of Radiocesium in River Water.....	22
– Result of Three-Year-Long Observation –	
12. Radiocesium Behavior from Forest to Stream Water and River	23
– Understanding How Dissolved Radiocesium is Discharged from Upstream –	
13. Clarifying the Distribution of Sediment-Associated Radiocesium at the Bottom of a Pond without Sediment Sampling ---	24
– Visualizing the Vertical Distribution of Sediment-Associated Radiocesium –	
14. Exploring the Migration of Radionuclides to the Deep Ocean.....	25
– Elucidation of Subduction from the Vertical Distribution of Concentration –	
15. Quickly and Accurately Measuring Environmental Radiation Levels.....	26
– Advanced Conversion Method for Airborne Radiation Monitoring –	
16. Evaluating the Effective Dose Based on a Detailed Radiation Map.....	27
– Providing Protection from Radiation in the Specified Reconstruction and Revitalization Base –	
17. Modeling the Distribution of Air Dose Rates in Habited Areas of Fukushima Prefecture	28
– Developing the 3D Air Dose Rate Evaluation System –	

2 Nuclear Safety Research

Implementing Continuous Improvements in Safety	29
1. Uncertainty Reduction in Source Term Evaluation	30
– Dependence of Decontamination Factor on Aerosol Particle Number Concentration in Pool Scrubbing –	
2. Toward a More Reliable Safety Evaluation for Loss-of-Coolant Accidents	31
– Uncertainty Quantification of Fracture Limit of Fuel Cladding Tube –	
3. Safety Evaluation Considering Uncertainties of Accident Progression	32
– Development of Simulation-Based Risk Assessment Methodologies –	
4. Evaluating of Sheltering Effectiveness against Internal Exposure at a Nuclear Accident	33
– Factors Affecting Sheltering Effectiveness and Influence of Environmental Factors on Indoor/Outdoor Ratio –	
5. Detailed Investigation of the Fracture Toughness of a Reactor Pressure Vessel	34
– Fracture Toughness Evaluation of Heat-Affected Zone under Overlay Cladding Using Miniature Specimen –	
6. More Rational Inspection of the Piping System	35
– Evaluating the Ratio of Welds to be Inspected Based on a Risk Informed In-Service Inspection –	

3 Advanced Scientific Research

Advanced Science Pioneers the Future	36
1. Unveiling the Unique Fission Process of Fermium Nuclides	37
– Clues towards Understanding the Existing Limit of Super-Heavy Elements –	
2. How Removal of Strontium from Seawater ?	38
– Use of Coprecipitation Method by Barite Controlled Chemical Composition –	
3. Observation of a New Double Lambda Hypernucleus during a J-PARC Experiment	39
– As a Microscopic Image, the Second Case Where the Nuclide is Identified –	
4. Superconductivity Driven by Ferromagnetic Fluctuations in the Uranium Compound UGe ₂	40
– Correlation between Superconductivity and Ferromagnetic Fluctuations Studied by Magnetic Measurements at High Pressure –	

4 Nuclear Science and Engineering Research

Fundamental Technologies for Nuclear Energy Innovation	41
1. Contribution by Nuclear Physics to Transmutation Study	42
– Accurate Prediction of Deuteron Transmutation –	
2. Microscopic Corrosion Behavior in High-Temperature, High-Pressure Environments	43
– In-Situ Measurement of Electrical Conductivity of Solution in Stainless Steel Crevices –	
3. Origin of Am/Cm Selectivity Elucidated by Chemical Bonding	44
– Focusing on the Covalent Interaction between Metal Ions and Separation Ligands –	
4. Accurate Detection of Particles in Accelerators, Space, and Medicine	45
– Understanding the Mechanism that Determines the Scintillation Light Yields –	
5. Evaluation of Exposure Doses Considering Variations in Physiques of Japanese	46
– Completion of Adult Japanese Human Model Series –	

6. Estimation of Fission Product in a Light Water Reactor under a Severe Accident-----	47
– Development of Fission Product Chemistry Database ECUME –	
7. Improving the Prediction Accuracy of Spallation Product Yields-----	48
– Improving a Stochastic Model of Nuclear Fission Induced by a High-Energy Particle –	

5 *Applied Neutron and Synchrotron-Radiation Research and Development*

Contributions to Developments in Science, Technology, and Academic Research

Using Neutron and Synchrotron Radiation ----- 49

1. Long-Term, Stable Production of a High-Intensity and High-Quality Beam-----	50
– Development of an RF-Driven Negative Hydrogen Ion Source –	
2. Linking Spin-Fluctuations to Electron Correlations-----	51
– A Combined Neutron and ARPES Study –	
3. Two-Dimensional Neutron Measurement with High Sensitivity and High Precision-----	52
– Development of a Bump Cathode Neutron Detection Element –	
4. Measuring the Neutron Brightness Distribution from Liquid Hydrogen Moderators-----	53
– Measuring and Validating the Neutron Brightness Distribution from Liquid Hydrogen Moderators at a High-Intensity Spallation Neutron Source –	
5. Capturing of a Unique Spin Texture of a 4f Electron-----	54
– Discovery of a Magnetic Skyrmion Lattice in the 4f Electron Magnet EuPtSi –	
6. Towards Higher-Performance Steels-----	55
– Elucidating the Microstructural Formation Mechanism via Electron and Neutron Beams –	
7. Successful Observation of the Melting and Solidification Phenomena of Metal with a Time Resolution of One Millisecond----	56
– Contributing to the Advancement of Laser Welding Technology –	
8. Compound Developed to Recognize Slight Size Differences of Rare-Earth Elements-----	57
– Towards Efficient Recycling of Lanthanides –	

6 *HTGR Hydrogen and Heat Application Research*

Research and Development on HTGR, Hydrogen Production, and Heat Application Technologies----- 58

1. Proposal of Innovative Nuclear Fuel Cycle Based on High Temperature Gas-Cooled Reactor-----	59
– Reduction of Cooling Time of Potential Toxicity of Radioactive Waste –	
2. Towards Implementation of Improved HTGRs-----	60
– Conceptual Design of an Experimental HTGR for Steam Supply Based on an HTTR –	
3. Improving the Fuel Safety of High Temperature Gas-Cooled Reactors during Severe Oxidation Accident----	61
– Fabrication of Oxidation-Resistant Fuel Elements for Oxygen Ingress Accidents –	
4. Toward Load-Following, Demand-Dependent Operation of an HTGR-----	62
– Confirming the Thermal Load Fluctuation Absorption Characteristics of an HTTR –	
5. Improving Hydrogen Production Efficiency Using Innovative Technologies-----	63
– High-Efficiency Process Design of the Thermochemical IS Process –	
6. Reliability Improvements of Corrosion-Resistant Equipment for Hydrogen Production by the IS Process-----	64
– Refined Quality Management of Glass-Lined Steel Material –	
7. Membrane Makes IS Process Chemical Reaction Efficiently-----	65
– Use of an Ion-Exchange Membrane to Reduce Water Permeation by Cross-Linking –	

7 *Research and Development of Fast Reactors*

Endeavors in Research and Development of Fast Reactor Cycle for Nuclear Innovation	66
1. Examining the Behavior of Core Elements during a Strong Earthquake	67
– Development of 3-Dimensional Reactor Core Group Vibration Analytical Model –	
2. Clarifying the Discharge Behavior of Molten Core Materials	68
– Simulated Experiments Using a Shallow Water Pool for Molten Core Discharge –	
3. Uncertainty Analyses of MA Sample Irradiation Test Data	69
– For Better Utilization of the Rare Data –	
4. Development of a Long Life Fast Reactor Control Rod	70
– Irradiation Behavior of a Sodium-Bonded Absorber Pin –	
5. Advancing Microwave Heating Denitration Technology	71
– Development of Particle Control Technology to Improve Powder Characteristics –	

8 *Research and Development on Fuel Reprocessing, Decommissioning, and Radioactive Waste Management*

Toward Decommissioning of Nuclear Facilities and Radioactive Waste Management	72
1. Simplification of the Analysis of Uranyl Ions in Radioactive Wastes	74
– Development of an Analytical Method with Capillary Electrophoresis Using Novel Fluorescent Reagents –	
2. Reducing the Generation of Uranium Waste	75
– Decontaminating Metal Using Acidic Electrolytic Water –	
3. Ensuring the Stability of Trench-Type Radioactive Waste Disposal Facilities	76
– Examination of Waste Acceptance Criteria of Sand Filling to Reduce Voids in Waste Packages –	
4. Improvement of Matching Method for Seepage Flow Analysis	77
– Application of Inversion for Seepage Flow Analysis in Multi-Layered Earthen Cover –	
5. Evaluating the Uncertainty of the Redox Potential in Groundwater	78
– An Application Example Based on Monitoring Data of Water Quality in the Horonobe Area –	
6. Estimating the Hydraulic Conductivity around a Gallery before Excavation	79
– An Estimation Method Applying the Mean Stress Index –	
7. Dating Calcium Carbonate Using a Micro-Scale Analytical Method	80
– A Method for Tracing Prior Underground Water Environments –	
8. Chemical Analysis and Identification of Many Mineral Grains	81
– New Technique to Elucidate the Mountain Uplifting Process –	
9. Unified Management of Repository Design Information	82
– Development of a Design Support System for Geological Disposal Projects –	
10. Realistic Modeling of Tracer Migration in Rock Fracture	83
– Effects of Fine-Scale Surface Alterations on the Tracer Retention in Fractured Crystalline Rock –	
11. Stabilization of Low-Level Radioactive Waste Solutions	84
– Cement Solidification of Low-Level Radioactive Waste Solutions Containing Carbonates –	
12. Investigation of Fuel-Cladding Materials for the Reprocessing of Spent Nuclear Fuel	85
– Evaluation of the Nitric Acid Resistance of New Materials Preventing Severe-Accident Progression –	
13. Predicting the Flow and Mixing Behavior in an Extractor	86
– Simulating Fluidity, Dispersion, and Mass Transfer in a Centrifugal Contactor –	

9 Computational Science and E-Systems Research

Computational Science for Nuclear Research and Development	87
1. Acceleration of Plume Dispersion Model	88
– Reduced-Communication Algorithm for GPU-Based Supercomputers –	
2. Matrix Solvers for Multiphase CFD Simulations with One Hundred Billion Grids	89
– Communication Avoiding Multigrid Methods –	
3. Prediction of Laser Irradiation Condition in Laser Processing	90
– Provision of Laser Irradiation Condition for Melting and Solidification Processing Using Computational Science Code SPLICE –	
4. Modeling the Effects of Hydrogen on Metallic Materials	91
– Spontaneous Separation of Aluminum Grain Boundaries by Hydrogen –	
5. AI-Assisted Acceleration of Quantum Simulations	92
– Analysis of Strongly Correlated Electron Systems with Sparse Modeling –	

10 Development of Science & Technology for Nuclear Nonproliferation

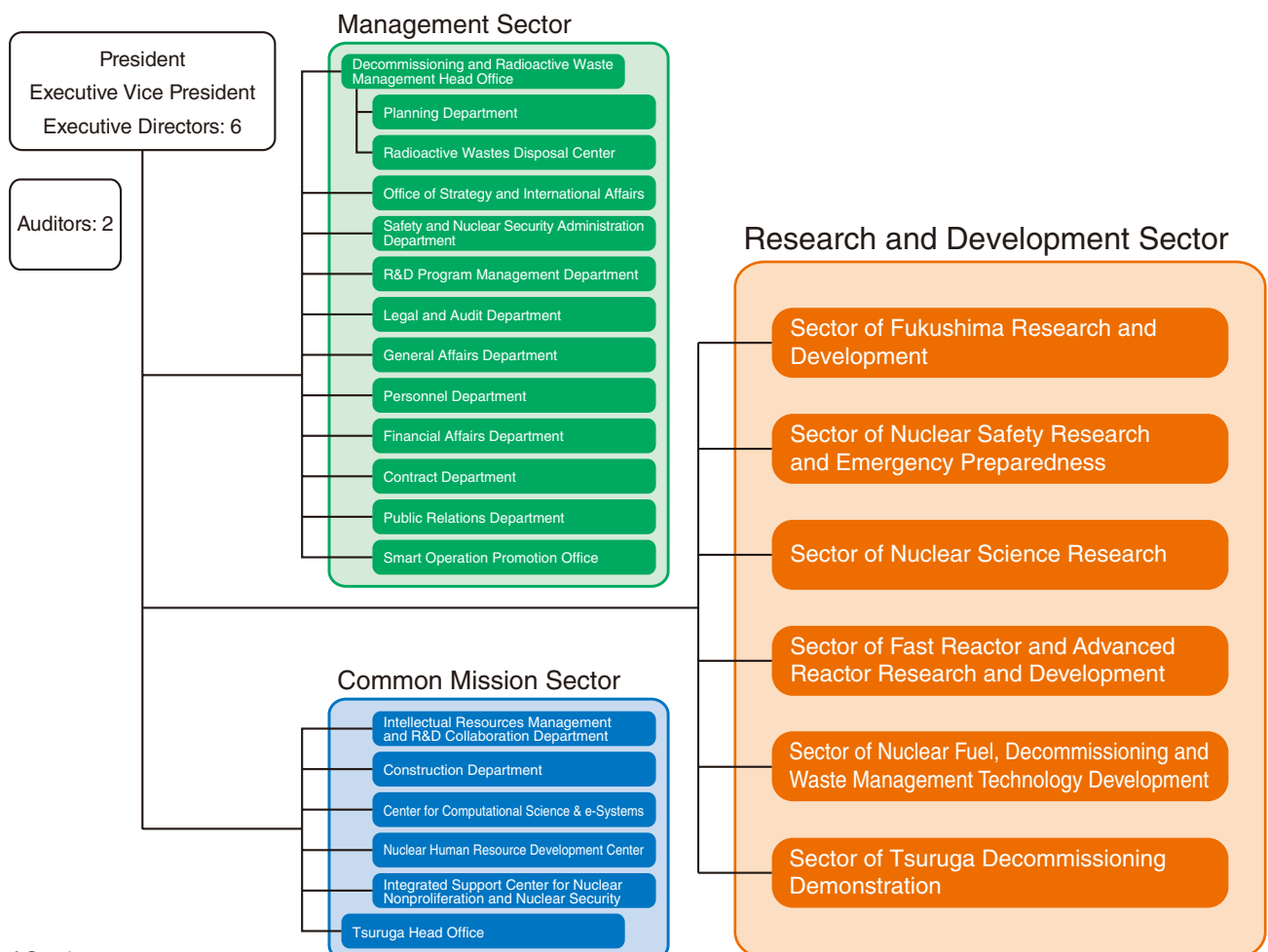
Development of Technology and Human-Capacity Building in the Nuclear-Nonproliferation and Nuclear-Security Fields to Support the Peaceful Use of Nuclear Energy	93
1. Nondestructive Assay of Nuclear Materials Using γ -rays	94
– Development of Simulation Code for γ -ray Elastic Scattering –	
Research Field Index	95

About This Publication and the JAEA Organizational Outline

This publication introduces the latest research and development (R&D) endeavors of JAEA in each field, with each chapter presenting the activities from one sector. The various R&D sectors discussed perform their activities through one or more R&D centers or institutes consisting of one or more sites. These centers and institutes are located throughout Japan, as shown on the map below. The following brief introduction outlines the research undertaken by each sector.

1. **The Sector of Fukushima Research and Development** is promoting R&D towards the decommissioning and the environmental restoration corresponding to the accident of the Fukushima Daiichi Nuclear Power Station (1F) of Tokyo Electric Power Company Holdings, Inc. (TEPCO). The Sector is also promoting the development of R&D infrastructure that is essential to the 1F decommissioning efforts.
2. **The Nuclear Safety Research Center in the Sector of Nuclear Safety Research and Emergency Preparedness** performs research into safety measures that support the national nuclear safety bodies that regulate nuclear power plants, nuclear fuel cycle facilities, and radioactive waste-disposal facilities. This work is conducted at the Nuclear Science Research Institute.
3. **The Advanced Science Research Center in the Sector of Nuclear Science Research** explores novel disciplines in advanced atomic energy sciences to develop theories and investigate novel phenomena, materials, and technologies. In particular, seven research themes have been organized under three divisions: advanced actinides science, advanced nuclear materials science, and advanced theoretical physics.
4. **The Nuclear Science and Engineering Center in the Sector of Nuclear Science Research** carries out fundamental research on various key technologies for the use of nuclear energy at the Nuclear Science Research Institute.
5. **The Materials Sciences Research Center in the Sector of Nuclear Science Research** is engaged in research using neutrons at the Nuclear Science Research Institute and the Japan Proton Accelerator Research Complex (J-PARC). Research using synchrotron radiation is performed at the Harima SR Radioisotope Laboratory.
6. **The Reactor Systems Design Department and the HTGR Research and Development Center in the Sector of Fast Reactor and Advanced Reactor Research and Development** further the development of High Temperature Gas-cooled Reactor (HTGR) technology, technology for hydrogen production through high-temperature water splitting, and technology for helium gas turbines at the Oarai Research and Development Institute.

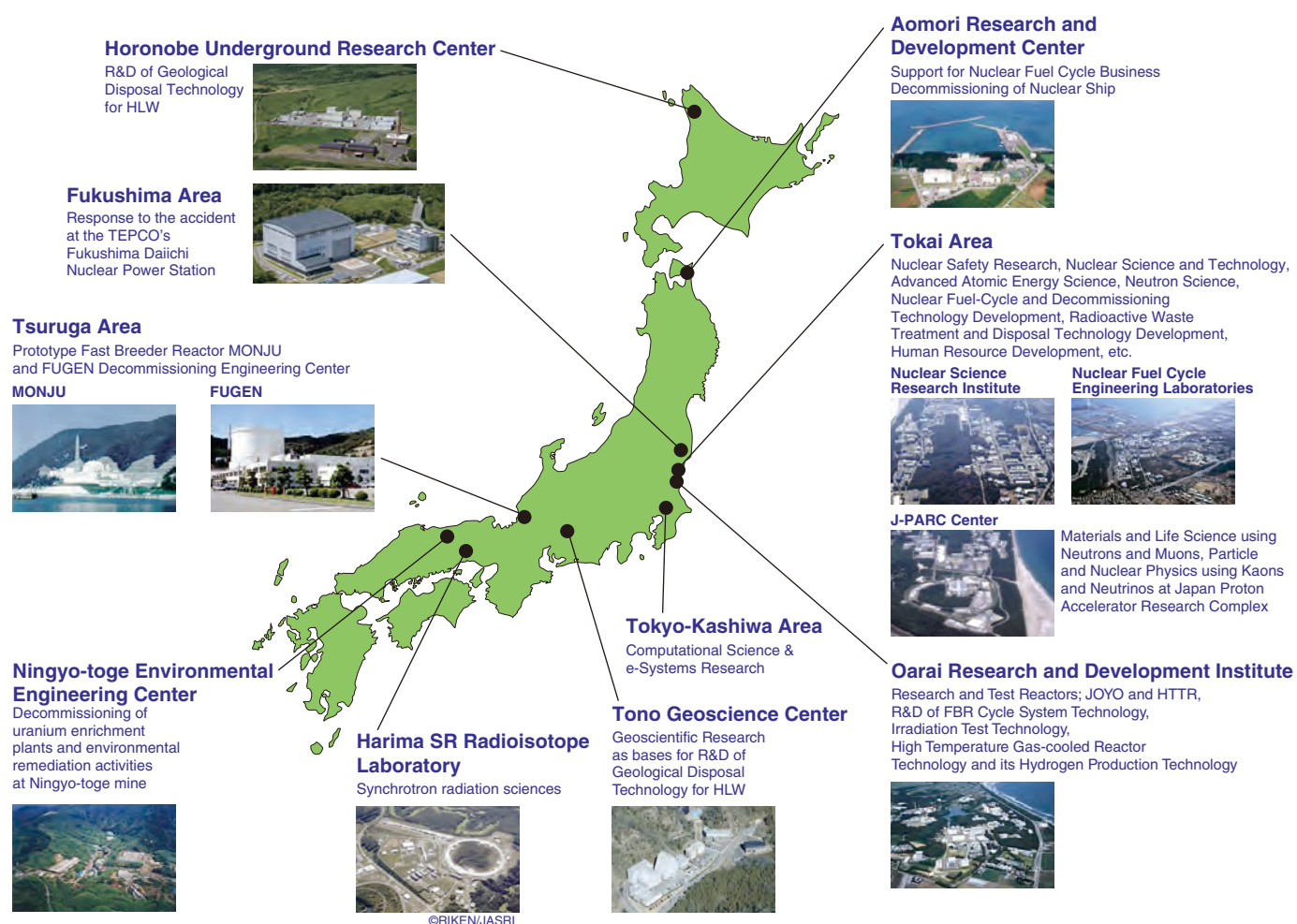
Japan Atomic Energy Agency -Organizational Outline-



As of October, 2019

7. **The Reactor Systems Design Department, Fuel Cycle Design Department, Fast Reactor Cycle System Research and Development Center, and Tsuruga Comprehensive Research and Development Center in the Sector of Fast Reactor and Advanced Reactor Research and Development** are working toward the establishment of fast reactor (FR) cycles to address long-term energy security and global environmental issues. This includes enhancing the safety of the FR system at the Oarai Research and Development Institute, compiling the results on the Prototype Fast Breeder Reactor Monju (MONJU), attaining inspection and repair technologies for the FR system at the Tsuruga Comprehensive Research and Development Center, and manufacturing plutonium fuel and reprocessing spent FR fuel at the Nuclear Fuel Cycle Engineering Laboratories in cooperation with the Sector of Nuclear Fuel, Decommissioning and Waste Management Technology Development.
8. **The Sector of Nuclear Fuel, Decommissioning and Waste Management Technology Development** is developing technologies for the safe and rational decommissioning of nuclear power facilities as well as measures for processing and disposing of radioactive waste. Multidisciplinary R&D aimed at improving the reliability of the geological disposal of high-level radioactive waste in Japan is also performed. A particular focus is the establishment of techniques for investigating the deep geological environment at the Tono Geoscience Center and the Horonobe Underground Research Center. The focus at the Nuclear Fuel Cycle Engineering Laboratories is on improving the technologies for geological disposal facility design and safety assessment, and on developing nuclear fuel cycle technology for light water reactors (LWRs).
9. **The Center for Computational Science & e-Systems** aims to advance simulation technologies and fundamental technologies in computational science, as well as the operation and maintenance of computer systems and networks. These activities are mainly conducted at the Nuclear Science Research Institute and the Kashiwa Office.
10. **The Integrated Support Center for Nuclear Nonproliferation and Nuclear Security (ISCN)** plays an active role in technology development to support the activities of international organizations such as the International Atomic Energy Agency, and other countries to strengthen nuclear nonproliferation and nuclear security, activities to ensure transparency in nuclear material management and peaceful uses, and policy research. Moreover, the ISCN continues to support the human resources development activities of Asian countries. These efforts are carried out mainly at the Head Office and the Nuclear Science Research Institute.

R&D Institutes/Centers of JAEA



Providing Advanced Scientific Knowledge by Concentrating Expertise

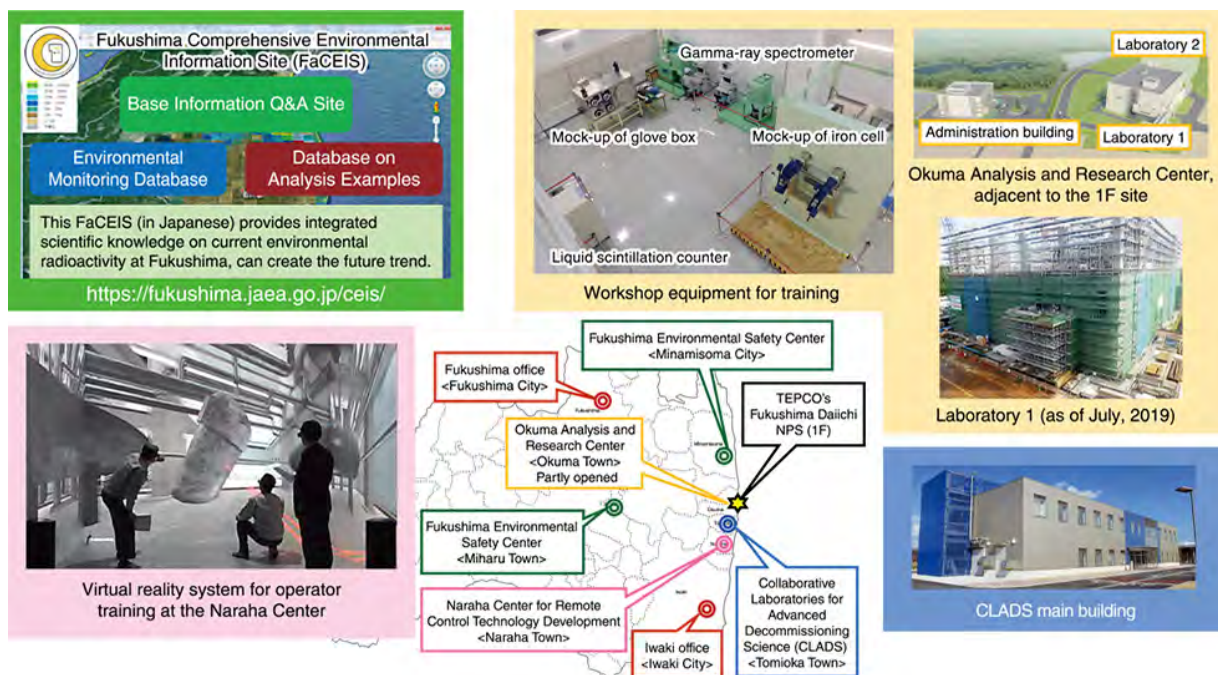


Fig.1-1 Sector of Fukushima research and development: fields and activities

As a comprehensive R&D institute in the field of nuclear energy, JAEA has been supporting the post-accident environmental restoration and decommissioning of the TEPCO's Fukushima Daiichi NPS (1F) (Fig.1-1).

The Collaborative Laboratories for Advanced Decommissioning Science (CLADS) is a research hub for R&D on decommissioning. JAEA has been studying to clarify the debris distribution inside reactors toward a retrieval of nuclear fuel debris (Topic 1-1). In order to understand the debris characteristics, JAEA has evaluated their mechanical characteristics by computer simulation (Topic 1-2) and investigated experimentally the behavior of boron that causes the debris to harden (Topic 1-3).

To ensure radiation protection during debris retrieval, JAEA has been developing the nuclear criticality evaluation method for debris (Topic 1-4) as well as an alpha-ray monitor that is available inside 1F buildings where temperature and humidity have not been controlled yet (Topic 1-5). JAEA also is studying the storage, treatment, disposal and reuse of liquid or solid types of radioactive wastes generated from decommissioning work (Topics 1-6–1-9). Additionally, a dedicated lab in collaboration with universities and industries was established in FY2019 to develop human resources and concentrate expertise toward future 1F decommissioning (Fig.1-1, bottom right).

The Naraha Center for Remote Control Technology Development was also established as a facility for the development and demonstration of remote control devices contributing to 1F decommissioning work. Here, virtual reality systems prepared for operator training (Fig.1-1, bottom left) and robot simulators for decommissioning work (Topic 1-10) are under development. The facilities are available for external researchers. For example, the International Research Institute for Nuclear Decommissioning (IRID) has performed a development of technology for Water Circulation Systems in Primary Containment Vessel (Full-scale Test) using this center.

The Okuma Analysis and Research Center is designed to analyze and characterize radioactive wastes and nuclear fuel debris for the development of long-term waste management. Laboratory 1, which will deal with low-to-medium-level radioactive waste

including rubble and secondary waste, is under construction. Laboratory 2, in the design phase, will deal with high-level radioactive material such as fuel debris. To ensure analysis work in the future, JAEA is training for analyzing work at workshop in Administration Building and so on (Fig.1-1, top right).

These centers will contribute to the decommissioning of 1F and are regarded as decommissioning-related facilities that will play a part in the Fukushima Innovation Coast Framework.

The Fukushima Environmental Safety Center has performed R&D for the environmental restoration. For the long-term assessment of transport of radioactive cesium in the environment, its discharge of radioactive cesium in the dissolved form from the overland to rivers was investigated through long-term concentration monitoring in river water (Topic 1-11) and computer simulations (Topic 1-12). The center has developed a technique to evaluate the vertical distribution of radioactive cesium in pond subsoil based on the gamma-ray spectra (Topic 1-13). JAEA discovered a phenomenon in which radionuclides drastically sink to the deep ocean due to the serpentine current (Topic 1-14). JAEA has promoted the technological development of environmental radiation monitoring and mapping to establish rapid evaluation methods for the distribution of radionuclides. JAEA has succeeded in the definition of radiation exposure dose evaluation for residence at the zone designated for reconstruction and recovery by developing the inverse analysis method for airborne radiation monitoring (Topic 1-15). JAEA has also showed the effective dose estimation at the zone designated for reconstruction and recovery using new approaches for the evaluation of the effective dose (Topic 1-16), and developed an evaluation system to create detailed 3D models of residential areas to improve the precision of calculations of air dose rate distributions (Topic 1-17).

The R&D results are published on an information website (Fig.1-1, top left), contributing to building residents' sense of security and studying the measures for municipalities.

Furthermore, JAEA is contributing to Fukushima's revitalization through R&D activities with development of human resources by building networks with regional industries, research institutes, and educational institutes.

1-1 Estimate the State of the RPV and PCV after a Severe Accident

— Upgrading of the Comprehensive Identification of Conditions Inside Reactor —

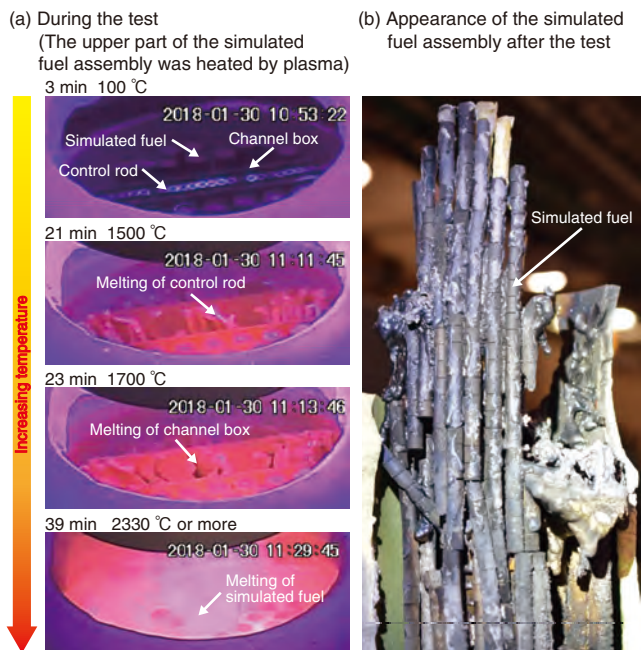


Fig.1-2 Core-material melting and relocation (CMMR) test
The simulated fuel assembly at the top was heated by plasma. A ZrO_2 pellet was used, rather than UO_2 . (a) A downward flow was observed in order of materials with lower melting points. (b) The simulated fuel retained the column shape until its melting temperature.

The decommissioning of the TEPCO's Fukushima Daiichi NPS (1F) has been underway since its severe accident (SA) in March 2011. Estimating and comprehending the state of the remaining fuel debris and fission products inside the nuclear reactor is essential for this process. However, understanding the state the reactor pressure vessel (RPV) and primary containment vessel (PCV) is extremely difficult after an accident, as direct observation of the reactor interior is difficult due to the high radiation environment. Additionally, as Unit 1–Unit 3 at 1F lost their cooling functions during the tsunami, as well as their direct-current electric power supply, measurements cannot easily be collected from the onboard meters. Thus, information measured during the accident progression is in short supply. To make up for this lack of accident information, SA models based on knowledge of the Three Mile Island (TMI-2) accident and some experimental work can be applied. However, core degradation in a boiling water reactor (BWR) like the 1F has not been comprehensively studied. Since the TMI-2 accident, many researchers have focused on the initial core melting process and aspects related to the rupture of the pressure vessel in a pressurized water reactor (PWR). The differing structure between a BWR and a PWR may result in different core damage, melting, and slumping in the 1F accident.

In the “Upgrading of the comprehensive identification of conditions inside reactor” project, core-material melting and relocation (CMMR) tests were conducted to understand the collapsing, melting and relocation of core materials during 1F accident (Fig.1-2). A fuel assembly simulating the core of a BWR

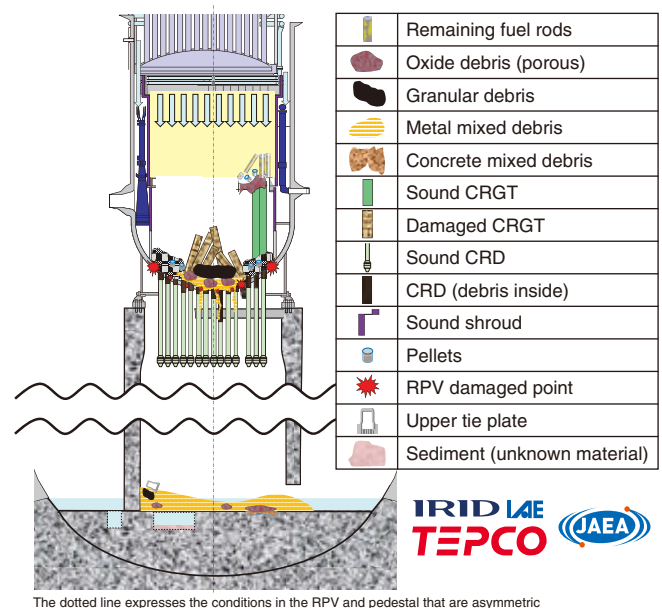


Fig.1-3 Estimated debris distribution and the RPV and PCV conditions in Unit 2

The state of residual fuel in the lower plenum were estimated via the results presented in Fig.1-2.

using ZrO_2 pellets rather than fuel pellets was heated by high-temperature plasma. The simulated fuel assembly at the top was heated above the oxide melting temperature, not yet achieved in prior tests simulating the BWR system, reproducing the axial temperature gradient at the initial stage of core material melting and relocation in the 1F accident. The results indicated that the macroscopic gas permeability of the heated core remained intact until the ceramic fuel melting point. Furthermore, as hot fuel remained in columns, effective fuel relocation, i.e., the removal of hottest fuel from the middle of the core to heat the support structure, was shown to be unlikely. These results will assist in the development of better BWR-specific SA progression models. The 1F plant data collected from CMMR testing, SA analysis, and the 1F internal investigation was then further analyzed to estimate post-accident reactor conditions. The resulting estimation of debris distribution in the Unit 2 RPV/PCV is shown in Fig.1-3.

Future work will involve analyzing the data from 1F internal investigations to further understand reactor conditions and upgrade estimated diagrams of debris distribution in the RPV and PCV. These estimations will contribute to the development of effective policies for removing fuel debris from the 1F site.

This work was the result of the subsidy for Project of Decommissioning and contaminated Water Management, “Upgrading for Identifying Comprehensive Conditions inside the Reactor”, supported by the Agency of Natural Resources and Energy (ANRE), the Ministry of Economy, Trade and Industry (METI), Japan.

Reference

Yamashita, T. et al., The CMMR Program: BWR Core Degradation in the CMMR-4 Test, Proceedings of the 9th European Review Meeting on Severe Accident Research (ERMSAR 2019), Prague, Czech Republic, 2019, 012, 13p.

1-2 Numerical Evaluation of Fuel Debris Hardness

—First-Principle Calculation of the Mechanical Properties of Fuel Debris—

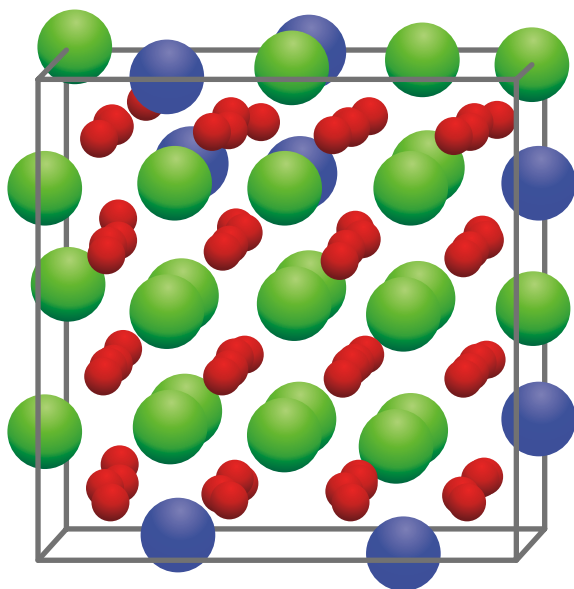


Fig.1-4 Crystalline structure of uranium-zirconium oxide
This structure, constructed by 24 uranium atoms (●), 8 zirconium atoms (●), and 64 oxygen atoms (●), represents one of the crystalline structures used in the calculations.

Proper removal of fuel debris formed from melting fuel is necessary to the safe decommissioning of the TEPCO's Fukushima Daiichi NPS (1F). To remove debris safely, its mechanical properties should be understood, including the hardness, elastic modulus, and fracture toughness. As these have not yet been studied in detail, property estimation using simulated debris is essential. Furthermore, since the detailed components of the debris are not yet completely understood, a vast array of simulated debris must be created and analyzed, thus requiring extensive time and costs. Estimating the mechanical properties of debris with numerical models could therefore greatly reduce costs and help debris removal efforts.

As such, an atomic nuclear model was developed to simulate the mechanical properties of uranium-zirconium oxide (Fig.1-4), the main component of the fuel debris. A first-principles calculation method was adopted, as this reliable method does not require any empirical parameters. The calculated Young's

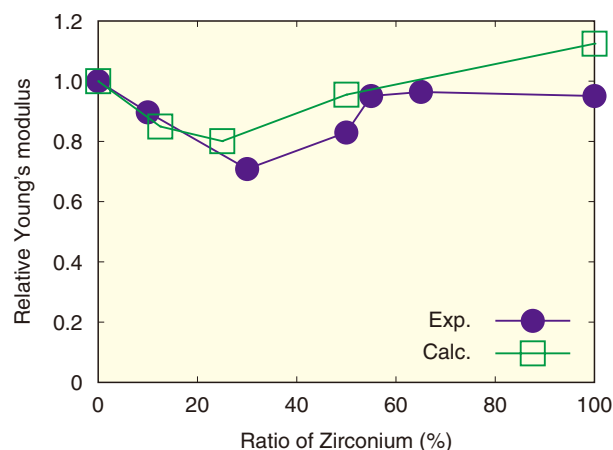


Fig.1-5 Relative Young's modulus of uranium-zirconium oxide
Here, the horizontal axis corresponds to the ratio of zirconium atoms to the sum of uranium and zirconium atoms, and the vertical axis shows the relative Young's modulus of uranium-zirconium dioxide to that of uranium dioxide. The closed circles and open squares represent experimental and calculated results, respectively.

modulus, one of elastic moduli, for uranium-zirconium oxides, is shown in Fig.1-5. Prior experimental work has indicated that Young's modulus decreases as the zirconium ratio increases until 25% and increases above 25%. The calculated Young's modulus showed a similar behavior. Analyzing the simulation results, we found that the distortion of the oxygen atom configuration became the greatest at 25%, and reduced the Young's modulus. Thus, this demonstrated another benefit of numerical models: not only can the physical properties be evaluated, but their causes can be elucidated.

This work focused on evaluating the mechanical properties of fuel debris by atomic numerical simulations. However, more information regarding the properties of fuel debris properties is still required. The developed numerical method can support future experimental analysis of fuel debris properties, this contributing to decommissioning activities at 1F.

Reference

Itakura, M., Nakamura, H. et al., First-Principles Calculation of Mechanical Properties of Simulated Debris $Zr_xU_{1-x}O_2$, Journal of Nuclear Science and Technology, vol.56, issues 9–10, 2019, p.915–921.

1-3 Degradation Mechanism of a BWR Control Blade

— Understanding the Behavior of Boron Compounds during a Severe Accident —

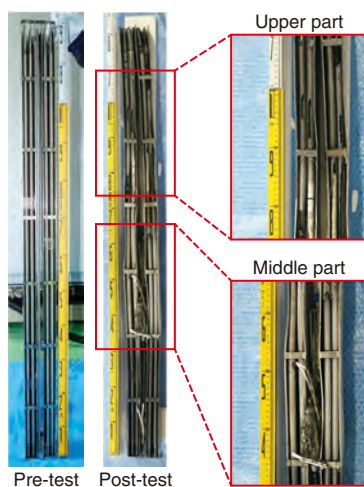


Fig.1-6 Sample used to simulate a part of a typical Japanese BWR fuel assembly

After testing, a part of the control blade remained at the top part of the sample. The blockage at the middle was composed of solidified candling sample droplets.

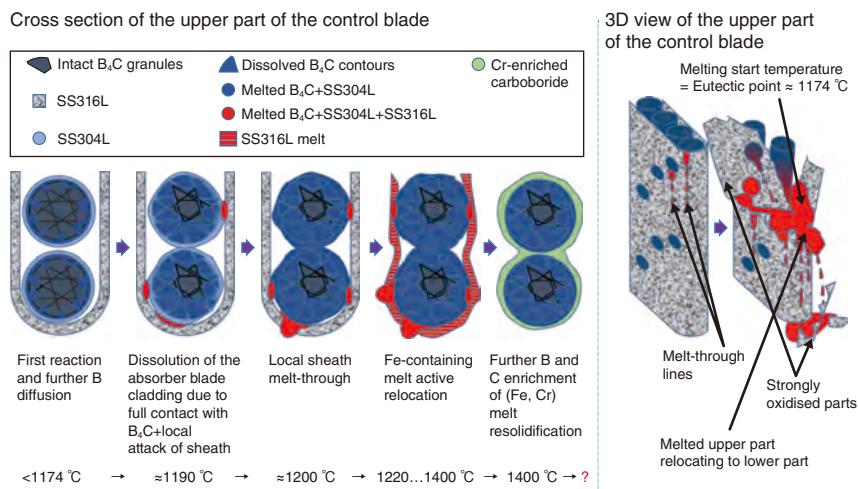


Fig.1-7 Schematic of the control blade degradation mechanism at an early phase of the nuclear accident under steam-starved conditions

During an accident conditions B and C can diffuse into the wall of the control rod tube and locally change its internal structure, causes the formation of melt. As the melt becomes further enriched with B and C, it can become Fe-enriched carboboride between the granules of B_4C , and Cr-enriched carboboride layer surrounding the granules.

Since the accident at the TEPCO's Fukushima Daiichi NPS (1F), the researchers have aimed to uncover new features of the influence of boron carbide (B_4C) on the 1F accident progression. Although boron is necessary in BWR reactors, the presence of B_4C has led to low-temperature eutectics with Fe, formation of very hard phases with Zr and Cr, and the evaporation in hot steam as B-aerosols.

To support 1F decommissioning by understanding the final redistribution of B and C, a mock-up assembly in the Large-scale Equipment for Investigation of Severe Accidents in Nuclear reactors (LEISAN) facility was designed to recreate the accident conditions of Unit 2 at 1F. The results indicated that the control blade did not melt completely and contained intact B_4C -granules even at 1500 °C, as shown in Fig.1-6.

Nevertheless, a significant portion of the stainless steel (SS) liquefied (with help of B_4C) relocated to lower elevations, and solidified. As a result, the gap between the control blade and channel box was blocked at the test sample elevations where the temperature was roughly 1174 °C–1250 °C.

A schematic representation of the control blade degradation mechanism at an early phase of nuclear accident up to 1500 °C under steam-starved conditions is represented in the Fig.1-7. An analysis of the survived residuals indicated that contact between B_4C and SS resulted in the formation of Cr-rich carboborides,

which surrounded the B_4C granules and significantly decreased further B transport outside of the control rod and, thus suppressing the formation of B-aerosols.

The upper residuals were found to be oversaturated with B and C and thus very hard, but fragile. The blockage, containing mostly melts with lower concentrations of dissolved B and C, was hard and robust, thus representing an additional difficulty for 1F decommissioning.

Thus, B and C create the first wave of melt during the early stage of an accident. This solid melt creates robust blockages, representing significant difficulties for decommissioning. The part of the control blade that survived the first melt contained trapped B_4C protected by the Cr-rich layer with carboborides. Due to encapsulation of B_4C by high-melting point compounds under Unit 2 accident conditions, direct contact with environment was limited, thus formation of B-aerosols was probably shifted to late phase of the accident, where melting of high-temperature materials can be possible.

This work was part of the project “Advanced Multi-Scale Modelling and Experimental Tests on Fuel Degradation in Severe Accident Conditions”, supported by the Agency of Natural Resources and Energy (ANRE), the Ministry of Economy, Trade and Industry (METI), Japan.

Reference

Pshenichnikov, A. et al., Features of a Control Blade Degradation Observed *In Situ* during Severe Accidents in Boiling Water Reactors, Journal of Nuclear Science and Technology, vol.56, issue 5, 2019, p.440–453.

1-4 Uncertainty Estimation in the Criticality of Nuclear Systems Containing Fuel Debris

— Development of a Criticality Calculation Method for Randomly Distributed Materials —

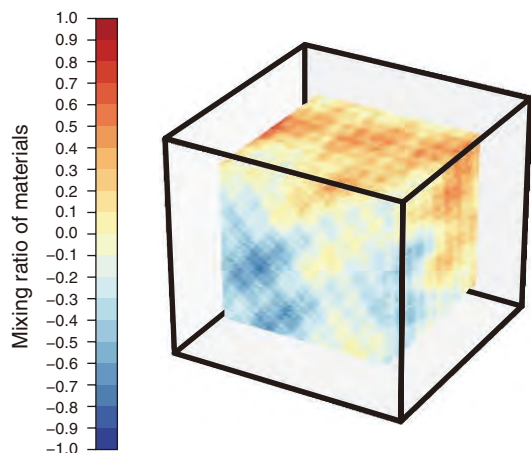


Fig.1-8 Nuclear system containing hypothetical fuel debris

An inner cube with a side of 100 cm of fuel debris is surrounded with concrete 20 cm in thickness. Fuel debris is modeled with a mixture of 2 materials such as nuclear fuel and concrete. The brown region shows one material of 100%, and the blue region shows the other material of 100%.

During the accident at the TEPCO's Fukushima Daiichi NPS, fuel debris may have formed from melted nuclear fuels and structural materials such as iron and concrete. Estimating the criticality of nuclear systems containing fuel debris, important to prevent a criticality accident, can be done using computational models for the decommissioning project including defueling. In conventional models, the calculated geometry has been divided into regions small enough to be treated as uniform. However, applying these models to fuel debris systems is difficult, as the isotopic composition varies continuously in space. In addition, conventional analysis required an input of the composition over all regions, which is unknown in fuel debris systems.

As such, a new computational model was developed in which the isotopic composition varies continuously using the Weierstrass function. Users can generate a replica, as shown in Fig.1-8, by inputting the average value and dispersion of the composition and the parameters describing the randomness. Fuel debris is represented as a mixture of two materials, e.g., nuclear fuel and concrete, of which their ratio varies continuously in space. Since a replica is generated stochastically, each replica has a different isotopic composition distribution. Users can calculate the uncertainty due to the unknown distribution of the isotopic composition by calculating criticalities for multiple systems and performing statistical processing.

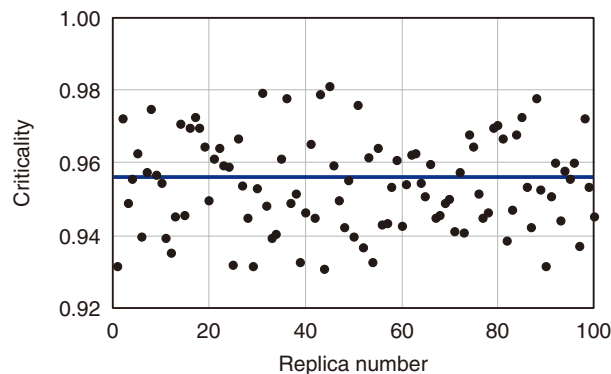


Fig.1-9 Fluctuation of criticality for a nuclear system containing hypothetical fuel debris

Fuel debris was assumed to be a mixture of nuclear fuel and concrete (mixing ratio of 1:7) and include an average of 20% stainless steel. Criticality was calculated on the assumption that the content of stainless steel varied randomly and continuously in space between 0% and 40%. The blue line shows the criticality ($=0.9562$) for the nuclear system where the isotopic composition was assumed to be uniform.

The resulting fluctuation of the criticality of a nuclear system containing hypothetical fuel debris is shown in Fig.1-9. A hundred replicas were generated and the criticality was calculated for each replica. The fuel debris was assumed to be a mixture of nuclear fuel and concrete (mixing ratio of 1:7) and included an average of 20% stainless steel. The content rate of stainless steel was assumed to vary randomly and continuously in space between 0% and 40%. In Fig.1-8, the brown region (scale of 1.0) shows the mixture at 0% stainless steel, whereas the blue region (scale of -1.0) shows the mixture with 40% stainless steel. The criticality of a nuclear system with uniform isotopic composition is shown as the blue line in Fig.1-9. One replicated case had a criticality of 0.98. This figure illustrates the importance of not only calculating the criticality for the uniform distribution but also estimating the dispersion due to the non-uniform distribution of stainless steel.

Future work will aim to develop a new model superposed with voxel geometry and the apply the model to a mixture of more than 3 materials to calculate the criticality for the various configuration of complex fuel debris systems. Future work will also involve the development of a Monte Carlo solver to implement and use the developed models easily.

This study was partly sponsored by the Secretariat of the Nuclear Regulation Authority (NRA), Japan.

References

- Ueki, T., Monte Carlo Criticality Analysis under Material Distribution Uncertainty, *Journal of Nuclear Science and Technology*, vol.54, issue 3, 2017, p.267–279.
- Nagaya, Y. et al., SOLOMON: a Monte Carlo Solver for Criticality Safety Analysis, *Proceedings of 11th International Conference on Nuclear Criticality Safety (ICNC 2019)*, Paris, France, 2019, 9p.

1-5 Measuring Alpha-Particle Emitters Flying in Nuclear Facility Buildings — A Highly Reliable Alpha Dust Monitor Using a GPS Scintillator Plate —

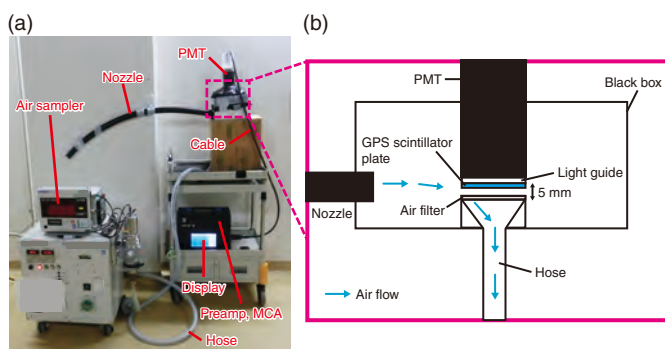


Fig.1-10 Developed (a) alpha dust monitor (b) and sample holder
The alpha-particle detector was positioned in the sampling holder facing downward, and the detection end was placed in a light-tight box. A nozzle and an air sampler were also connected to the same light-tight box.

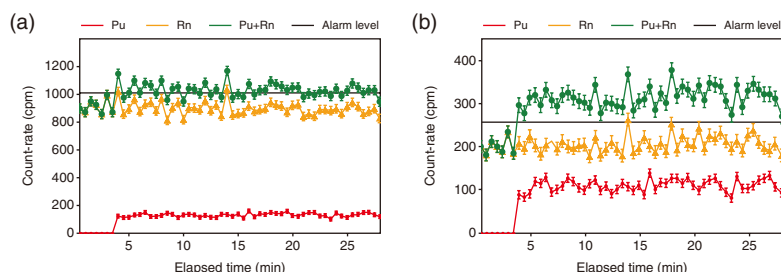


Fig.1-12 Time variation of counts with 30 s intervals
(a) without and (b) with an energy window

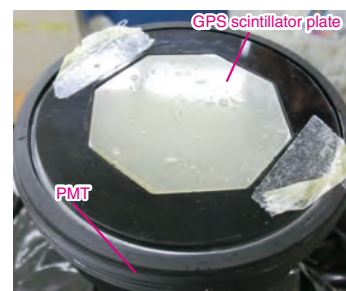


Fig.1-11 Simulation of the humidity condition
Water was dropped directly onto the GPS plate.

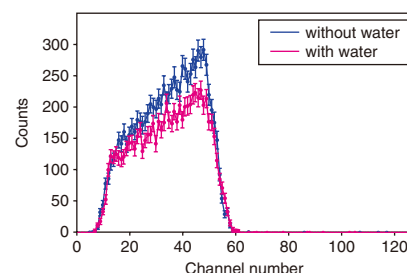


Fig.1-13 Alpha energy spectra with and without dropping water

The ratio of the total counts with/without water was 0.84. The peak number of channels without and with water were 47.1 and 47.3 channels, respectively.

A dust monitor with a silicon surface barrier detector (SSBD) was introduced at a nuclear fuel facility to detect the airborne concentration of ^{238}Pu and ^{239}Pu released by past accidents. The SSBD energy resolution can distinguish ^{238}Pu and ^{239}Pu from naturally occurring radionuclides, such as radon (Rn) progenies (e.g., ^{218}Po with a 6.0 MeV alpha particle and ^{214}Po with a 7.7 MeV alpha particle). However, the SSBD frequently produces false alarms, especially in rooms with high humidity. Under false alarms, workers must evacuate, thus interrupting operations in the room. Thus, a more reliable dust monitor that has a high energy resolution but is more resilient against external noise is required.

Therefore, an alpha-particle spectrometer based on a cerium-doped $\text{Gd}_2\text{Si}_2\text{O}_7$ (GPS) scintillator plate and a photomultiplier tube (PMT) was developed, as shown in Fig.1-10. The GPS scintillator plate is hexagonal and 50 mm in diameter with a scintillator layer of approximately 40 μm . The bottom face of the GPS scintillator plate was optically coupled to a PMT (R6233, Hamamatsu Photonics K.K., Hamamatsu, Japan) with a diameter of 3 mm in using an optical grease. The output signal from the PMT is amplified by a preamplifier (5625, Clear pulse CO., LTD., Tokyo, Japan) and transferred to a multi-channel analyzer (MCA; A2731, Clear pulse CO., LTD., Tokyo, Japan). The energy spectrum is then displayed in real-time. The alpha-particle detector was positioned facing downward and the detection end was placed in a black box, which was connected to a nozzle and an air sampler. When the air sampler operates, the

nozzle sucks up the air around the monitor, and any radioactive dust in the air is captured by the filter. The distance between the GPS scintillator plate and the filter was approximately 5 mm to allow for air passage. The ^{241}Am alpha source, Rn progeny collected on the air filter, and a PuO_2 particle were measured by our developed dust monitor. Water was dropped directly onto the surface of the GPS plate using a dropper to simulate high-humidity conditions (Fig.1-11).

The resulting energy resolution for 5.5-MeV alpha particles was $11.9\% \pm 0.2\%$ of the FWHM. A 92% efficiency was achieved, as was a uniform sensitivity. To eliminate Rn progeny counts, an energy window was set with the upper (ULD) and lower (LLD) channels of the Pu sample spectrum. By applying the energy window, the count-rate of the Rn progeny decreased by 77% (Fig.1-12). The resulting alpha spectra with and without dropping water are shown in Fig.1-13 for a measurement time of 5 min. The GPS scintillator plate could be used to measure the alpha spectrum even though the GPS scintillator got wet. The ratio of the total counts with/without water was 0.84. The peak number of channels without and with water were similar: 47.1 and 47.3 channels, respectively.

Overall, the developed dust monitor can be used to conduct alpha-particle spectroscopy despite the presence of water on the surface of the GPS scintillator plate. An alpha dust monitor using a GPS scintillator plate is therefore ideal for detecting alpha-particle emitters in places lacking temperature and humidity controls.

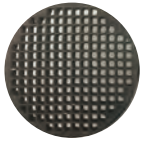
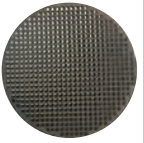

Reference

Morishita, Y. et al., Development of an Alpha Dust Monitor Using a GPS Scintillator Plate, Radiation Measurements, vol.122, 2019, p.115–120.

1-6 Determination of the Optimum Shape of Hydrogen Recombination Catalysts — Hydrogen Elimination Effect Experimentally Verified for Full-Size Equipment —

Table 1-1 Catalyst specifications

Several catalysts were prepared to identify the effect of cell density on the catalytic reaction.

Appearance			
Cell density (Cell number/mm ²)	0.047	0.16	1.4
Cell pitch (mm)	4.6	2.5	0.85
Wall thickness (mm)	0.66	0.43	0.064
Cell length (mm)	3.9	2.1	0.79

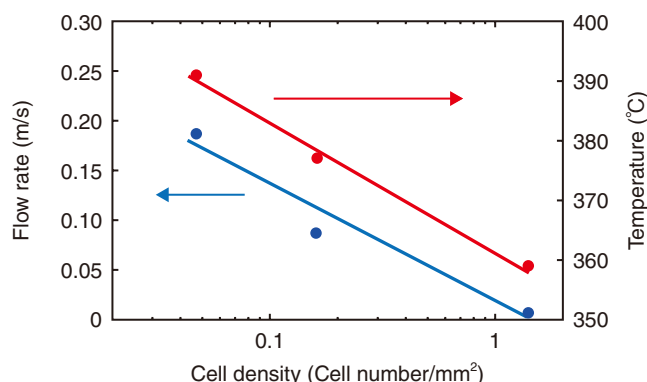


Fig.1-14 Effect of cell density on the catalytic reaction

The flow rate and gas temperature were observed when using several catalysts. The flow rate increased as the cell density decreased.

Nuclear fuel waste storage containers generate hydrogen gases due to the radiolysis of water molecules. Hydrogen elimination systems using hydrogen recombination catalysts, which do not rely upon an external electric power, have attracted much attention. The catalysts make a non-explosive reaction between atmospheric oxygen and the generated hydrogen, thus reducing the hydrogen concentration without the use of external electric power.

In this work, hydrogen recombination catalysts were developed based on an automotive catalyst and evaluated for their hydrogen elimination capabilities using full-scale equipment. The equipment used for performing the hydrogen recombination experiments was located at the Forschungszentrum Jülich in Germany and has a sealed cylindrical shape with an inner diameter of 1400 mm and a height of 3700 mm. After the catalyst was loaded, hydrogen was injected, and the variation in gas temperature, flow rate and hydrogen concentration were observed at several points in the inner space to analyze the hydrogen elimination effect of the catalysts used.

Specifications of the hydrogen recombination catalysts used are detailed in Table 1-1. Precious metal nanoparticles were sprayed on the wall of a monolithic ceramic substrate having many cells. To optimize the catalyst's shape, several catalysts with different cell densities were prepared. The catalysts were placed in a chimney-shaped tube and installed in the center of the test

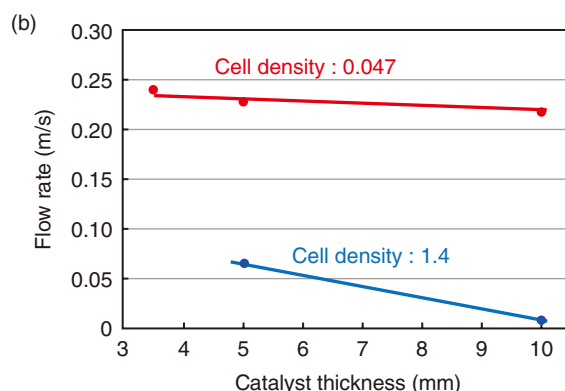
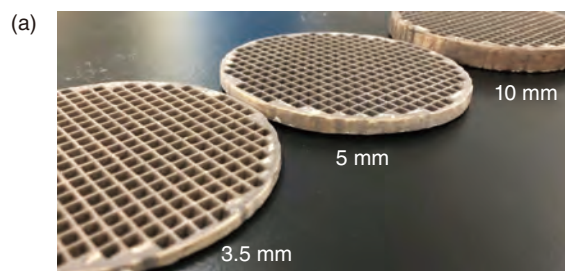


Fig.1-15 Effect of catalyst thickness

(a) Flow rate was observed for the several catalysts.
(b) The flow rate did not decrease even when using the thicker catalyst on a sample with the cell density of 0.047.

equipment. The reaction began after hydrogen injection. Because the reaction between hydrogen and oxygen is exothermic, gas convection proceeds upward through the chimney-shaped tube, reducing the hydrogen concentration in the entire space. The catalytic performance was determined by examining the flow rate, as illustrated in Fig.1-14. As the cell density decreased, the flow rate increased, i.e., the catalytic performance improved as the cell density of the catalysts decreased. Several samples with varying catalyst thickness were prepared (Fig.1-15(a)); their resulting catalytic performance is shown in Fig.1-15(b). The flow rate did not significantly decrease when the catalyst had a cell density of 0.047, even when the catalyst thickness was increased. Because the reaction itself increased as the thickness increased, these results indicate that a catalyst with a cell density of 0.047 can be effective for large amounts of hydrogen.

In collaborations with synchrotron radiation experiments and numerical simulations, studies aimed at developing more effective hydrogen recombination catalysts and at ensuring safety in waste storage have been promoted.

This work was part of the result conducted “R&D on technology for reducing concentration of flammable gases generated in long-term waste storage containers”, and supported by the Ministry of Education, Culture, Sports, Science and Technology (MEXT), Japan.

Reference

Ono, H., Matsumura, D. et al., Research on Hydrogen Safety Technology Utilizing the Automotive Catalyst, E-Journal of Advanced Maintenance, vol.11, no.1, 2019, p.40–45.

1-7 Estimating Radioactive Waste Inventory

— Sorption Behavior of Actinides on Zeolite —

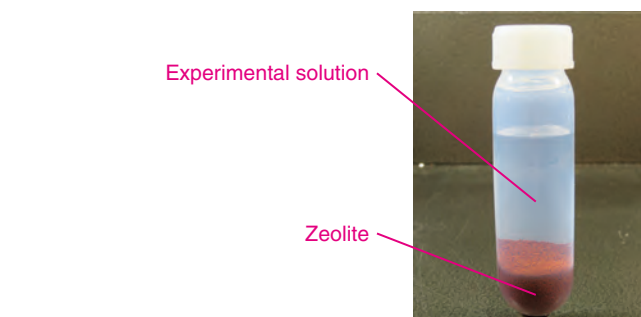


Fig.1-16 A test tube used in the sorption experiment of U and Np

U or Np is added to the experimental solution containing zeolite. The sorption behavior of U and Np is observed by the change of U and Np concentration in solution with time.

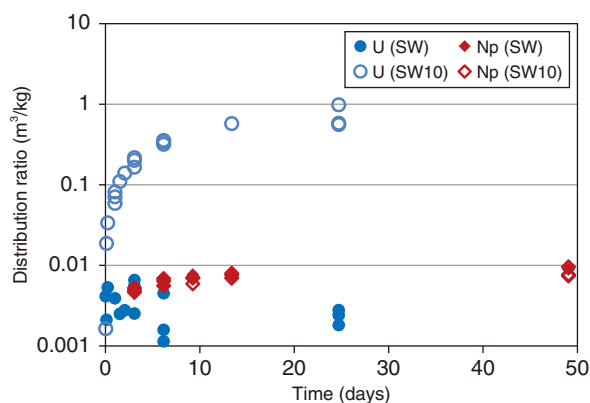


Fig.1-17 Change in distribution ratio of U and Np with time

The distribution ratio of U in simulated seawater diluted ten times by deionized water (SW10) was higher than that of Np and U in simulated seawater (SW).

At the TEPCO's Fukushima Daiichi NPS, contaminated water has been processed by water treatment apparatuses to remove radionuclides. Spent zeolite, used as an absorbing material in these apparatuses, is disposed of as radioactive waste. An estimation of the kinds and amount of the radionuclides present in this spent zeolite is necessary for selecting a suitable disposal concept and safety assessment. However, estimation of the inventory via sampling of zeolite from spent zeolite vessels is difficult because of the high dose rate and vessel structure. Therefore, sorption experiments of U and Np on zeolite (IONSIV™ IE-96, UOP), which is used in the water treatment apparatus SARRY, were conducted to develop an inventory estimation method based on the sorption behavior of radionuclides on zeolite (Fig.1-16).

The resulting distribution ratios using simulated seawater (SW) and simulated seawater diluted ten times by deionized water (SW10) are shown in Fig.1-17. Here, the distribution ratio was calculated by dividing the amount of U or Np sorption on zeolite (i.e., solid phase concentration) by the concentration of U or Np in the solution. A high distribution ratio indicates that a large amount of U or Np was sorbed onto the zeolite. The results indicated that a low distribution ratio of U was obtained in SW, whereas the distribution ratio was significantly increased in SW10. Alternatively, the distribution ratio of Np was low and independent of seawater concentration.

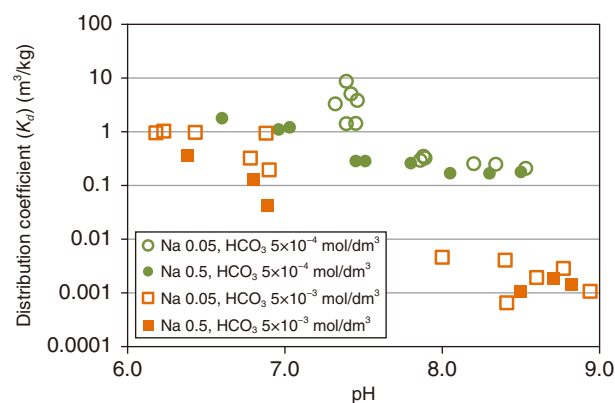


Fig.1-18 Dependency of uranium distribution coefficient on pH

The distribution coefficient of U decreased due to the increase in carbonate concentration when the pH was higher than 8. The distribution coefficient was independent of Na⁺ concentration.

To clarify the dominant factor causing the variation of the distribution ratio of U between SW and SW10, an experiment was carried out as functions of carbonate and Na⁺ concentration in the experimental solution. The resulting distribution coefficient (K_d) is shown in Fig.1-18 as a function of the pH, where K_d is defined as the distribution ratio at sorption equilibrium. In the pH range from 8 to 9, the K_d of U was low at a higher carbonate concentration, whereas the K_d was independent of Na⁺ concentration. This indicates that the difference in K_d of U between SW and SW10 is due to the difference of carbonate concentration in the solution. The decreasing K_d with increasing carbonate concentration may be caused by the increase in the concentration of uranium-carbonate complexes, which have a low sorption ability on zeolite. The K_d of Np was found to be independent of Na⁺ and carbonate concentration. This was consistent with the trend of the distribution ratio of Np observed in the experiment using SW and SW10.

Thus, the carbonate concentration may be a dominant factor in controlling the inventory of radionuclides in spent zeolite.

This work was part of the result conducted “Development of technology for treatment and disposal of accident waste”, and supported by the Agency of Natural Resources and Energy (ANRE), the Ministry of Economy, Trade and Industry (METI), Japan.

Reference

Ishidera, T. et al., Sorption Behavior of U and Np on Zeolite, Progress in Nuclear Science and Technology, vol.5, 2018, p.221–224.

1-8 Towards Routine Analysis of Difficult-to-Measure Radionuclides

— Preparation of Analysis Manuals for ^{93}Zr , ^{93}Mo , ^{107}Pd , and ^{126}Sn Waste —

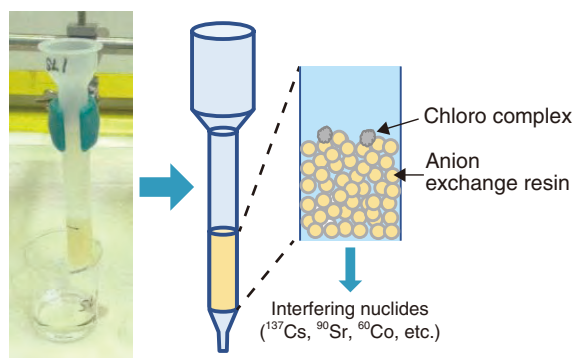


Fig.1-19 Separation of interfering nuclides using an anion exchange resin

^{126}Sn was adsorbed on an anion-exchange resin using hydrochloric acid to separate it from interfering nuclides that do not form complexes with chloride ions.

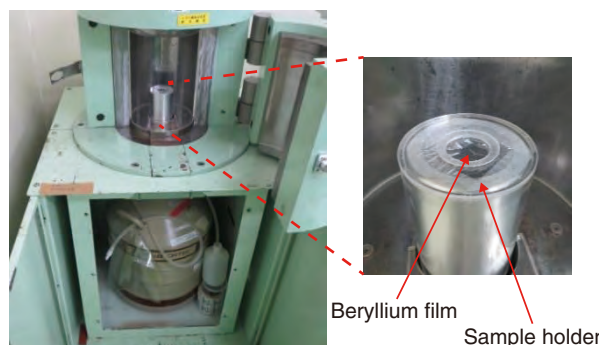


Fig.1-20 Planar high purity germanium low-energy photon spectrometer (Ge-LEPS)

The spectrometer window is made from a thin beryllium film, allowing low-energy photons (e.g., γ -rays in the case of Sn) to be measured with high efficiency.

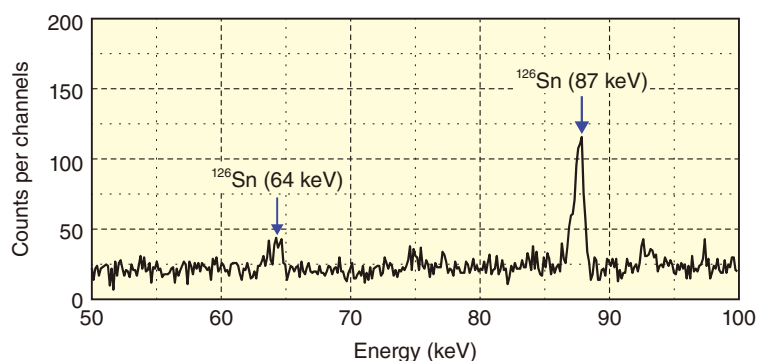


Fig.1-21 ^{126}Sn measurement spectrum using Ge-LEPS

Two γ -rays were emitted as a result of ^{126}Sn decay, shown here as peaks at 64 and 87 keV.

The establishment of waste disposal policies including future waste such as rubble is urgent for proper decommissioning of the TEPCO's Fukushima Daiichi NPS (1F). As such, radioactivity data must be collected, and new analytical methods must be established for nuclides which the analytical methods have not been determined. Analytical methods simple enough to apply during routine analysis for four such nuclides were thus developed: zirconium-93 (^{93}Zr), molybdenum-93 (^{93}Mo), palladium-107 (^{107}Pd), and tin-126 (^{126}Sn).

Among these, the analytical method for ^{126}Sn is discussed here as an example. A hydrogen peroxide pretreatment was first used to ensure the presence of only tetravalent Sn, as Sn coexists as divalent and tetravalent ions. In a hydrochloric acid solution, Sn forms a chloro complex (i.e., a complex with a chloride ion), becoming an anion that can then be adsorbed on an anion-exchange resin (Fig.1-19) and separated from interfering nuclides that do not become anions, such as cesium-137 (^{137}Cs) and strontium-90 (^{90}Sr), which emit beta rays and raise the background by bremsstrahlung.

The gamma rays were then measured using a planar high-purity germanium low-energy photon spectrometer (Ge-LEPS)

(Figs.1-20 and 1-21).

^{93}Zr and ^{93}Mo were adsorbed to a solid-phase extraction agent (TEVA resin) using a weak concentration of hydrofluoric acid, eluted with a high concentration of hydrofluoric acid and hydrochloric acid, and then quantified by mass spectrometry or radiation measurement. ^{107}Pd was adsorbed to an anion exchange resin using a hydrochloric acid, eluted with ammonia water to efficiently separate from interfering nuclides, and then quantified by mass spectrometry.

The accuracy of the developed analytical method was confirmed using contaminated water collected from 1F. Furthermore, a worker-friendly analysis manual incorporating a check sheet was developed for routine analysis of radionuclides, which is expected to assist the accelerated establishment of disposal policies involving the collecting and accumulating a large amount of radioactivity data when radiochemical analysis is started at the Okuma Analysis and Research Center.

This work was supported by the Subsidy Project of Decommissioning and Contaminated Water Management by the Agency for Natural Resources (ANRE), the Ministry of Economy, Trade and Industry (METI), Japan.

Reference

Aono, R. et al., Development of ^{93}Zr , ^{93}Mo , ^{107}Pd and ^{126}Sn Analytical Methods for Radioactive Waste from Fukushima Daiichi Nuclear Power Station, JAEA-Technology 2017-025, 2017, 32p. (in Japanese).

1-9 Assessing the Safety of Reusing Contaminated Rubble

— Restricted Reuse in the TEPCO's Fukushima Daiichi NPS Site —

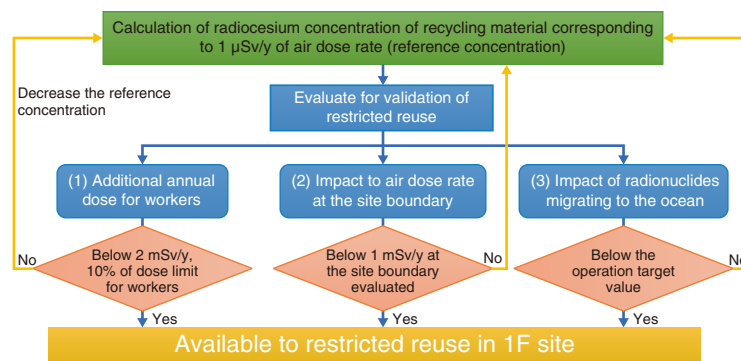


Fig.1-22 Safety assessment of reuse methodology

When reusing contaminated rubble, it is important to prevent increasing the dose rate. A validation methodology was constructed considering the current radiation management in 1F site.

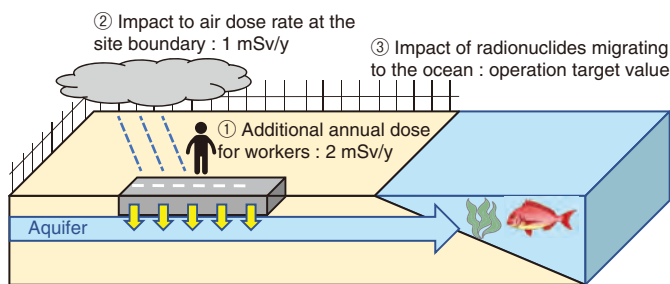


Fig.1-23 Conceptual diagram for the evaluation of reference radiocesium concentration in restricted reuse as road material

① The dose to workers should not exceed 10% of the dose limit, ② the increased annual dose by restricted reuse evaluated at the 1F site boundary should not exceed 1 mSv/y, ③ the radionuclide concentration of groundwater migrating from the recycled material should not exceed the operation target value, were confirmed.

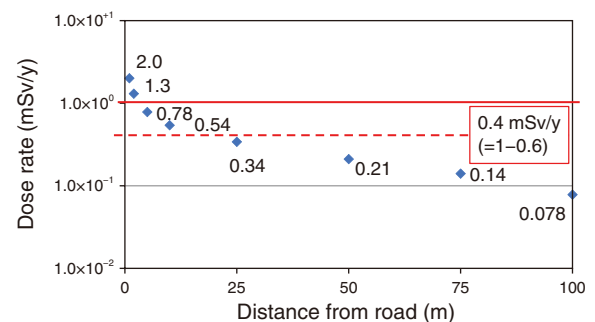


Fig.1-24 Dose rate corresponding to the distance from the site boundary to the road made of recycled material
Considering the margin decided by maximum dose rate (0.6 mSv/y) at the site boundary, the distance necessary for to be under 1 mSv/y on the site boundary was evaluate.

A large amount of contaminated rubble from the accident and subsequent activities toward the decommissioning is stored at the TEPCO's Fukushima Daiichi NPS (1F) site. Of the rubble stored outdoors with a surface dosage rate of under 0.1 mSv/h, rubble with a dose rate of less than 5 μSv/h will be recycled and applied in a restricted reuse within the 1F site. Currently, the 1F site is controlled as the existing exposure situation, where had shifted from an emergency exposure situation, and exposure doses of all persons in the 1F site are controlled. There is no precedent for establishing reference values such as dose and/or concentration for reuse of contaminated rubble under the existing exposure situation.

Therefore, a basic approach to estimate the reference radiocesium concentration for a restricted reuse of contaminated rubbles within the 1F site was designed; the used safety assessment of this approach is shown in Fig.1-22. Material was reused when the radiocesium concentration did not significantly increase the air dose rate in the 1F site to reduce any additional exposure dose to workers. The increased dose rate by restricted reuse was capped at 1 μSv/h, which is the minimum dose rate at the 1F site measured by ionization chamber detectors. In addition, in order to validate the reference concentration, we confirm the reuse does not affect the current radiation management in 1F site by three items described below, ① the dose to workers should

not exceed 10% of the dose limit, ② the increased annual dose by restricted reuse evaluated at the 1F site boundary should not exceed 1 mSv/y, ③ the radionuclide concentration of groundwater migrating from the recycled material should not exceed the operation target value (1 Bq/L for ^{134}Cs and ^{137}Cs , 5 Bq/L for all β)(Fig.1-23). When the annual dose at the 1F site boundary and radionuclides concentration in groundwater cannot clear the current radiation management, the distance from the position of reuse to the boundary not to exceed the value of the current radiation management can also be evaluated. Target nuclides in these validations include radiocesium, ^{90}Sr , which is contained in the rubble with 1% concentration against radiocesium, and ^{14}C , which was contained above the clearance level.

The reference concentration was thus calculated and verified. Road material and building bases were considered for recyclability in 1F. It is shown that the additional dose for worker not exceed 10% of dose limit by reusing for both purposes with reference concentrations. And, we evaluated the distance from the position of reuse to the boundary not to exceed the value of the current radiation management by reusing. (Fig.1-24).

This study was partly sponsored by the Secretariat of the Nuclear Regulation Authority (NRA), Japan.

References

- Shimada, T., Miwa, K. et al., Study on Restricted Use of Contaminated Rubble on Fukushima Daiichi NPS Site (1) Estimation of Reference Radiocesium Concentration for Recycling Materials, Progress in Nuclear Science and Technology, vol.6, 2019, p.203–207.
- Miwa, K. et al., Study on Restricted Use of Contaminated Rubble on Fukushima Daiichi NPS Site (2) Validation of Reference Radiocesium Concentration for Recycling Materials, Progress in Nuclear Science and Technology, vol.6, 2019, p.166–170.

1-10 Development of Robot Simulator for Decommissioning Task Training — Multi-Copter Simulator and Virtual Operator Proficiency Training System —

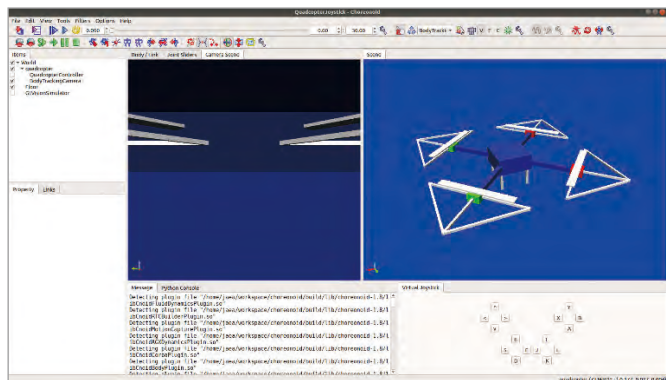


Fig.1-25 Example screen of a multi-copter simulation

A mounted camera view and bird's eye view are on the center and right, respectively.



Fig.1-26 Virtual operator proficiency training

An example training using a virtual reality system

Due to the high radiation doses present since the accident at the TEPCO's Fukushima Daiichi NPS (1F), radiation and physical survey tasks have been executed with remotely operated robots. However, maneuvering these remotely operated robots and executing the tasks safely are difficult due to unexpected environmental conditions in the reactor building. As such, specialized robots must be developed and operators must be trained. A robot simulator to support the design of remotely operated robots and operator proficiency training is thus under development.

Recently, a multi-copter was used to perform a radiation survey in the reactor building. Maneuvering a multi-copter in this indoor environment is difficult, as its behavior is affected by the local fluid dynamic interactions with nearby structures. An operator proficiency training for maneuvering the multi-copter is also required to cope with such situation. A simulator used to calculate the physical behavior of a multi-copter and a 3D real-size projection system for multi-copter operation training is thus under development.

The simulator determines the behavior of the flying multi-copter by calculating the effect of buoyancy and fluid resistance on the body of the multi-copter, as well as the Coanda and ground effects. The Coanda effect is a phenomenon in which a fluid jet is attracted to the surface of a nearby object such as a wall or ceiling,

whereas the ground effect is a phenomenon in which lift increases near the ground. These effects are important because they make maneuvering the multi-copter difficult. We implemented these effects by introducing a simple calculation model.

A full-scale simulated world projection system in real-time was also designed to provide a realistic training experience to an operator. This system was implemented utilizing the commercial application EasyVR to project the simulated world to a cave-type virtual reality screen and the GL-DLL commercial application Fusion to transfer the simulator's OpenGL (Open Graphics Library) rendering signals to EasyVR. An example view of a multi-copter simulation is shown in Fig.1-25, and an example virtual operator proficiency training is shown in Fig.1-26. Using the simulator and projection system allowed the behavior of a multi-copter in an indoor environment to be calculated in real-time, and projecting the results in 3D allowed for better operator proficiency training.

Future work will focus on extending the operator proficiency training to other required functions in contribution to the decommissioning of 1F.

The presented development is a part of the result of "Development of a Robot Simulator for Mockup Plants", supported by Fukushima Prefecture. This research was commissioned by FSK Co., Ltd. in 2017.

Reference

Suzuki, K. et al., Development of a Multi-Copter Simulator and a Projection System for Virtual Operation Experience, Proceedings of 2019 IEEE/SICE International Symposium on System Integration (SII 2019), Paris, France, 2019, 6p., in USB Flash Drive.

1-11 Observed Decrease of Radiocesium in River Water

— Result of Three-Year-Long Observation —

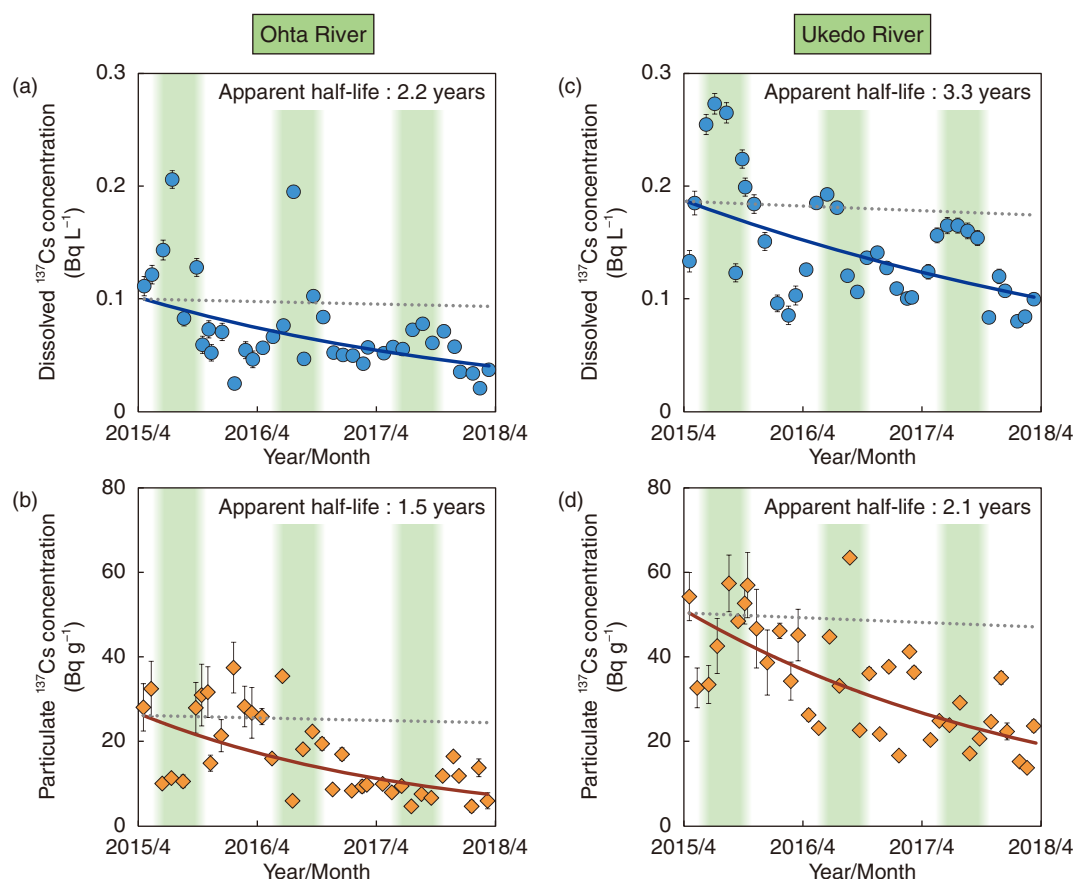


Fig.1-27 Dissolved and particulate ^{137}Cs concentrations in river water

Temporal variations in the concentrations of (a) dissolved ^{137}Cs and (b) particulate ^{137}Cs in the Ohta River, and (c) dissolved ^{137}Cs and (d) particulate ^{137}Cs in the Ukedo River. The ^{137}Cs concentrations (solid lines) declined more rapidly than physical decay (dotted lines). Green areas correspond to summertime. The error bars represent the combined uncertainty of measurements.

Radiocesium (RCs) resulting from the accident at the TEPCO's Fukushima Daiichi NPS is transported by river system. A survey of river water by the Ministry of the Environment has suggested that RCs has not been detected (detection limit: 1 Bq L^{-1}). However, the detected RCs concentration in some freshwater fish has been higher than the Japanese limit of 100 Bq kg^{-1} for general foodstuffs. To understand the mechanism of RCs uptake by freshwater fish and understand when fishing can be resumed, the RCs concentration and variation in river water must be understood. Therefore, the ^{137}Cs concentration in river water was observed from four to seven years after the accident, revealing a declining trend.

Water samples from the Ohta and Ukedo rivers in the eastern Fukushima Prefecture were thus collected monthly and filtered through $0.45\text{-}\mu\text{m}$ -pore size membrane filters from April 2015 to March 2018. The ^{137}Cs concentrations were determined by γ -spectrometry using Ge-detectors coupled with multi-channel analyzers for particulate fractions on the membrane filters and dissolved fractions that passed through the filters. The dissolved fraction was concentrated to lower the detection limit of ^{137}Cs .

As a result, the dissolved and particulate ^{137}Cs concentrations in river water were observed to be in decline (Fig.1-27). The apparent half-lives of dissolved and particulate ^{137}Cs concentrations estimated by an exponential decay model were 2.2 and 1.5 years, respectively, for the Ohta River (Figs.1-27(a) and (b)) and 3.3 and 2.1 years for the Ukedo River, respectively (Figs.1-27(c) and (d)). These observed decrease rates were 10 times faster than physical decay (half-life: 30.1 years). This suggests that the amount of RCs discharged from the land is decreasing with time.

Furthermore, the dissolved ^{137}Cs concentration increased in the summer (Figs.1-27(a) and (c)). Because RCs contained in litter and soil organic matter elutes by decomposition, the dissolved ^{137}Cs concentration might increase in the summer when decomposition is active. However, the increase of ^{137}Cs concentration in summer has decreased, indicating that the RCs discharged from land is decreasing with time.

The results of this study promote the understanding of the medium- and long-term impacts for RCs concentration in river water and freshwater fish.

Reference

Nakanishi, T. et al., Trend of ^{137}Cs Concentration in River Water in the Medium Term and Future Following the Fukushima Nuclear Accident, *Chemosphere*, vol.215, 2019, p.272–279.

1-12 Radiocesium Behavior from Forest to Stream Water and River

— Understanding How Dissolved Radiocesium is Discharged from Upstream —

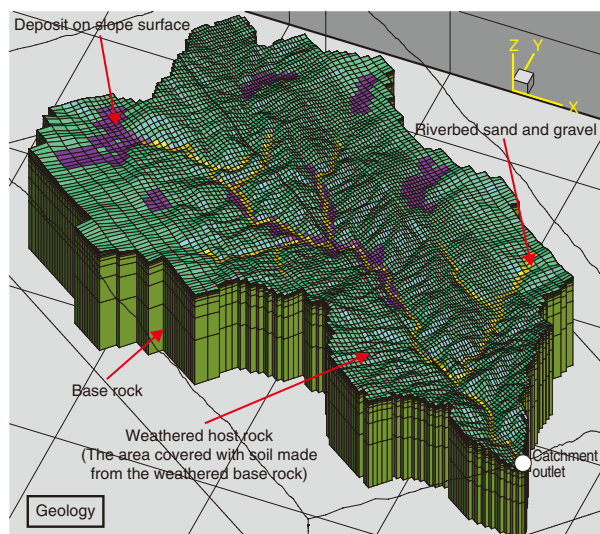


Fig.1-28 3-D-structure of the studied area

Watershed hydrological modeling (GETFLOWS) simultaneously simulates the surface and subsurface water using a 3D model based on the hydrogeological data and a 2D model based on digital elevation data. The radiocesium behavior in the environment was predicted by calculating sediment and radiocesium transport based on the obtained water velocity of the studied area.

Approximately 70% of the radiocesium (hereafter ^{137}Cs) fallout to terrestrial area from the TEPCO's Fukushima Daiichi NPS accident occurred in forest areas where decontamination work has not yet been done. Studying the behavior of ^{137}Cs from the forest to stream and river waters is thus required to understand how the ^{137}Cs concentration in agricultural products and freshwater ecosystems have changed. This includes understanding the discharge of ^{137}Cs adsorbed by soil particles (i.e., particulate ^{137}Cs) but also bio-available ^{137}Cs in water (i.e., dissolved ^{137}Cs). Therefore, water, sediment, and ^{137}Cs transport were simulated using a watershed model of the 99% forest area (in Minamisoma city and Namie town, Fig.1-28), upstream of the Ohta River catchment, in GETFLOWS. The simulated results were then compared with observed dissolved ^{137}Cs upstream discharge behavior.

The reproducibility of models related to water and sediment discharge at the discharge point were first confirmed, as shown in Fig.1-28. The partitioning of the ^{137}Cs inventory between the particulate and aqueous phases occurred instantaneously and was modeled with the distribution coefficients (K_d). In the first simulation (case 1), the K_d was based on the partitioning between the dissolved and particulate ^{137}Cs measured from river water samples taken at simulation area. In the second simulation (case 2), the K_d dataset was more realistic in its modeling ^{137}Cs

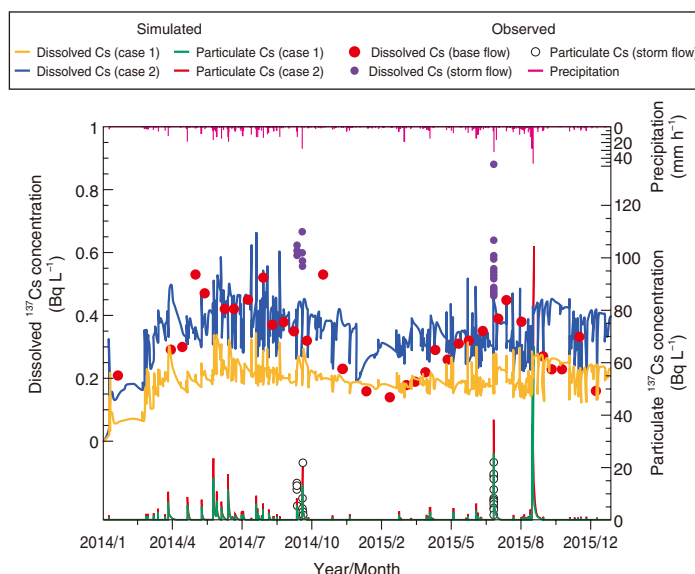


Fig.1-29 Simulated dissolved and particulate ^{137}Cs concentration in river water

Six particle sizes, including clay, silt, fine sand, sand, coarse sand, and gravel, were modeled using GETFLOWS. The distribution coefficients (K_d) for the four fine fractions of particle sizes (case 1) were set at 200000 L/kg and, the K_d value (case 2) were set at 200000 L/kg for clay and silt and 50000 L/kg for fine sand and sand.

absorption to the particulates, as absorption occurs more readily to the finer than coarser grades.

The simulated dissolved and particulate ^{137}Cs in the river water from January 2014 to December 2015 at the discharge point is shown in Fig.1-29. The case 1 simulation results (—) underestimated the observed dissolved ^{137}Cs concentration under base flow conditions (0.14–0.53 Bq L⁻¹, mean: 0.32 Bq L⁻¹); however, the case 2 simulation results (—) matched the observations more closely (mean: 0.36 Bq L⁻¹). Thus, this model was determined to accurately reproduce the mean dissolved ^{137}Cs concentration under base flow conditions.

However, neither the seasonal variability in the base flow of the dissolved ^{137}Cs concentration (●), nor the peaks in concentration that occurred during storms (○), could be reproduced with the simulation parameters used. As well as the results of field monitoring in river, these discrepancies may have been caused an additional input of ^{137}Cs to rivers by the leaching of organic matter in forest litter, i.e., its process is considered to be other mechanism except for the equilibrium between dissolved and particulate ^{137}Cs .

Future work will aim to verify and improve this simulation method by further field monitoring and experimental work to reveal the mechanisms of the dissolved ^{137}Cs leaching process from forest litter to stream and river waters.

Reference

Sakuma, K. et al., Applicability of K_d for Modelling Dissolved ^{137}Cs Concentrations in Fukushima River Water: Case Study of the Upstream Ota River, Journal of Environmental Radioactivity, vols.184–185, 2018, p.53–62.

1-13 Clarifying the Distribution of Sediment-Associated Radiocesium at the Bottom of a Pond without Sediment Sampling — Visualizing the Vertical Distribution of Sediment-Associated Radiocesium —

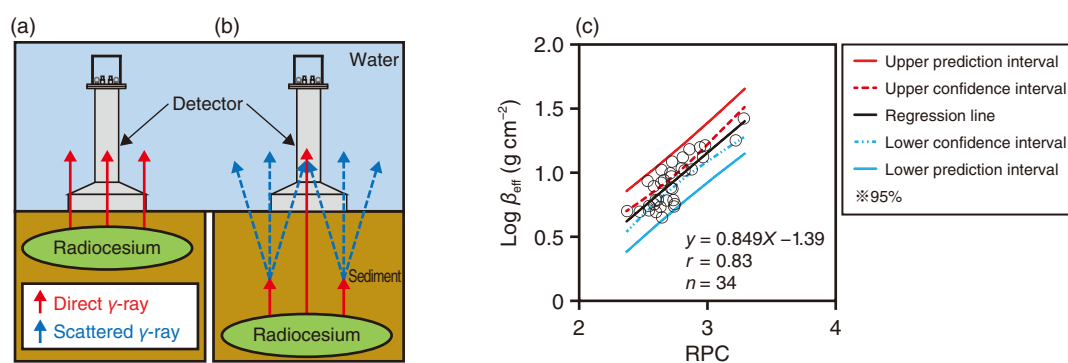


Fig.1-30 Measuring the gamma-ray spectra of surface sediment

(a) The contribution ratio of direct gamma rays emitted from radiocesium was high when radiocesium was emitted from the surface-layer sediment. (b) The contribution ratio of scattered gamma rays was high when radiocesium was emitted from deeper-layer sediment because the emitted gamma rays were shielded by soil particles. (c) Relationship between RPC obtained by in-situ measurement and β_{eff} obtained by sediment sampling.

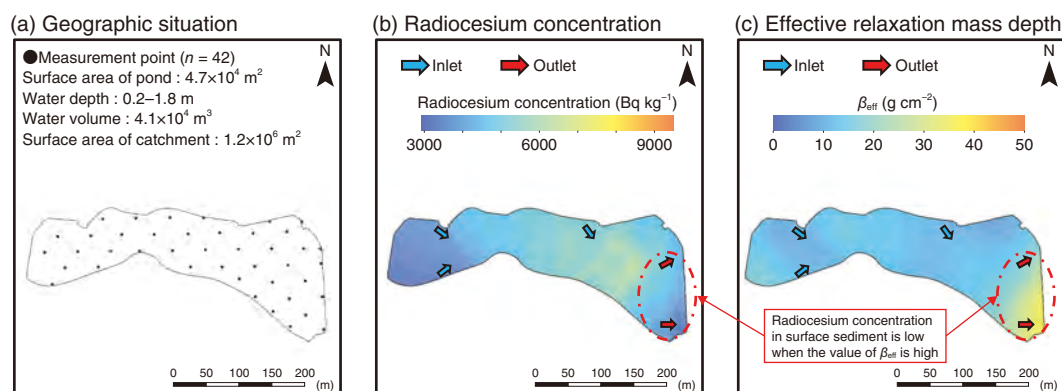


Fig.1-31 Applying the model to a real pond

(a) Measured gamma-ray spectra at the pond bottom, used to estimate the (b) radiocesium concentration of the surface sediment and (c) vertical distribution of radiocesium.

Knowing the distribution of sediment-associated radiocesium at the bottom of a pond is necessary for understanding how to decontaminate, dredge, and restart agricultural activities. The vertical distribution of radiocesium must be understood to dredge the sediment effectively. However, obtain these data is difficult and time-consuming. A radiation measurement method using a waterproof detector has thus been developed to investigate the distribution of sediment-associated radiocesium at the bottom of a pond rapidly and easily. However, this method only allows for the measurement of the radiocesium concentration in surface sediment. Therefore, a method to estimate the vertical distribution of sediment-associated radiocesium was developed to focus on the characteristics of the gamma-ray spectrum (scattered and direct) obtained from the surface sediment at a pond bottom (Fig.1-30).

It is estimated that the contribution ratio of direct and scattered gamma-ray is varied with the depth from which radiocesium is emitted. To confirm this, 253 data points regarding the characteristics of the gamma-ray spectrum and vertical distribution of radiocesium in 64 pounds of sediment samples in the Fukushima Prefecture were collected. A waterproof NaI(Tl) scintillation detector (A-Sub: Hitachi, Ltd.) was dropped into the pond and then used to measure the gamma-ray spectrum for

2 min. The sums of counting rate in scattered peak (150–250 keV) and that in photo peak (550–850 keV) based on the obtained gamma-ray spectra were calculated, respectively. The ratio of sum of counting rate in scattered peak to that in photo peak (RPC) was calculated. Core sediment samples (5–40 cm) were also sampled using a sediment sampling tube. The samples were divided into 5 cm intervals. The parameter regarding the vertical distribution of radiocesium (effective relaxation mass depth (β_{eff} g cm⁻²)) was calculated based on the measuring result of samples using Ge semiconductor detector.

Positive correlations between RPC and β_{eff} were observed (Fig.1-30(c)), indicating that the vertical distribution of sediment-associated radiocesium can be estimated via this detector by focusing on the characteristics of gamma-ray spectrum. Forty-two gamma-ray spectra were measured to cover the entire pond (Fig.1-31(a)), allowing a map of the radiocesium concentration in the surface sediment (Fig.1-31(b)) and β_{eff} (Fig.1-31(c)). As a result, the three-dimensional distribution of sediment-associated radiocesium can be more easily determined using this in-situ measurement than conventional methods. These results will further dredging and restarting the agricultural activities of ponds in the evacuation zone.

Reference

Ochi, K. et al., Development of an Analytical Method for Estimating Three-Dimensional Distribution of Sediment-Associated Radiocesium at a Reservoir Bottom, Analytical Chemistry, vol.90, no.18, 2018, p.10795–10802.

1-14 Exploring the Migration of Radionuclides to the Deep Ocean

— Elucidation of Subduction from the Vertical Distribution of Concentration —

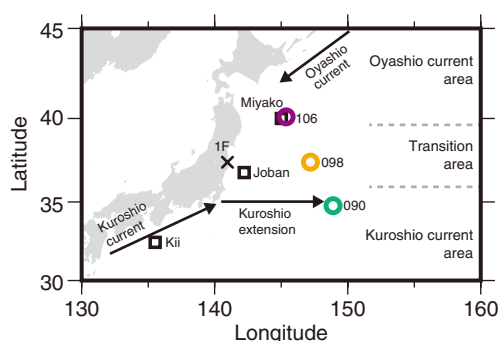


Fig.1-32 Seawater sampling locations

○, ○, and □ indicate seawater sampling locations after and before the accident, respectively.

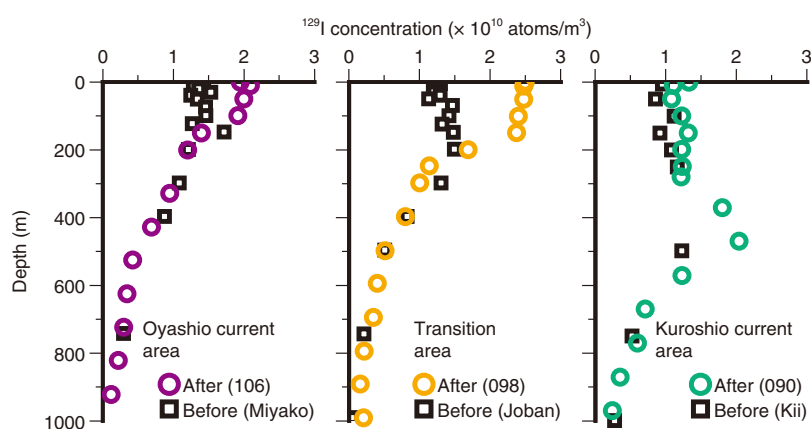


Fig.1-33 Vertical distribution of ^{129}I in each oceanic area before and after the accident

Accident-derived ^{129}I was present at the surface layer of the Oyashio current and the transition area and was subducted at a depth of around 400 m in the Kuroshio current area.

The accident at the TEPCO's Fukushima Daiichi NPS (1F) released radionuclides into the ocean. Many researches were carried out to understand the migration of radionuclides in the ocean. However, as many of these researchers have focused on the migration of radionuclides within surface layer, this work aimed to study the migration of radionuclides to deep layer.

As many deep-seawater samples were required to do so, a radionuclides detectable from a small sample volume was desired. Therefore, the vertical distribution of iodine-129 (^{129}I) was studied, as ^{129}I is detectable from 1 L of seawater using accelerator mass spectrometry; radiocesium (1 Bq/m³) detection requires 20 L of seawater. In the western North Pacific Ocean, the Oyashio and Kuroshio currents move from north and south, respectively, and provide the transitional seawater between two currents. To clarify the depth profile in the western North Pacific, seawater samples were collected from surface to a depth of 1000 m within the Oyashio current, Kuroshio current and transition areas (Fig.1-32).

The resulting depth profiles of ^{129}I are shown in Fig.1-33,

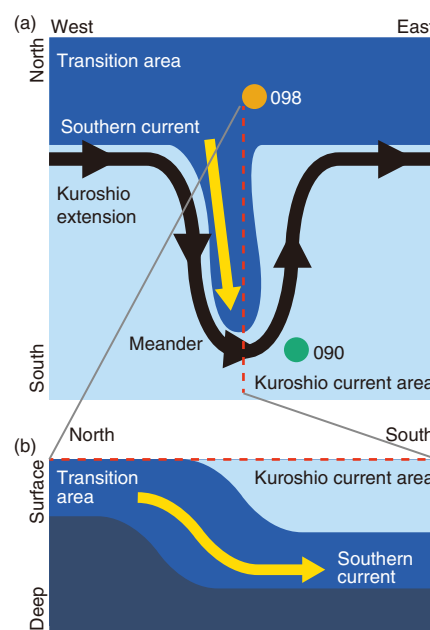


Fig.1-34 A conceptual diagram of the reproduced seawater current

(a) Studying the horizontal current showed that seawater in the transition area flowed south (→) induced by the meander of the Kuroshio Extension current (↘). (b) Studying the vertical current indicated that the southern current (→) was subducted under the seawater of the Kuroshio current area.

including data regarding the depth profiles of ^{129}I before the accident. Comparing between the vertical distribution before and after the accident demonstrates a clear increase in concentration caused by the 1F accident occurred from the surface to 150 m and 200 m depth at the Oyashio current and transition areas, respectively, and in the subsurface layer around a depth of 400 m at the Kuroshio current area. To elucidate the subduction to the subsurface layer, the seawater flow was analyzed using a data set that reproduced the flow velocity. As a result, the Kuroshio Extension current which was left from offshore of Chiba was meandering, and a southern current from transition area occurred by the influence of the meander and the southern current was subducted under the seawater of the Kuroshio current area, as the seawater density of the southern current was higher than that of the Kuroshio current area (Fig.1-34).

These results led to the discovery of new oceanographic findings that the radionuclides released by the 1F accident subducted rapidly due to the influence of the meander of the Kuroshio Extension.

Reference

Suzuki, T. et al., Vertical Distribution of ^{129}I Released from the Fukushima Daiichi Nuclear Power Plant in the Kuroshio and Oyashio Current Areas, Marine Chemistry, vol.204, 2018, p.163–171.

1-15 Quickly and Accurately Measuring Environmental Radiation Levels

— Advanced Conversion Method for Airborne Radiation Monitoring —

Conventional method :
Calculate the value directly below the measurement point

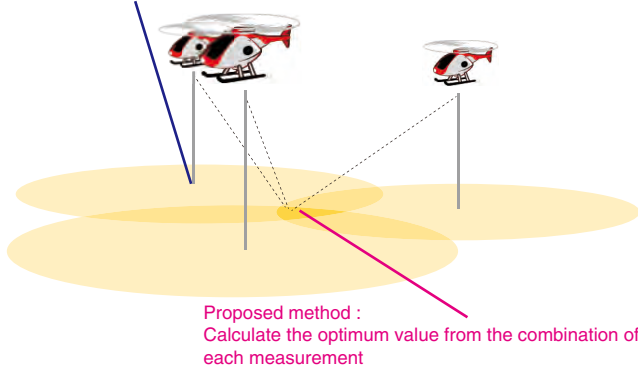


Fig.1-35 Conventional and proposed radiation measurement method

The conventional method calculates ground radiation values directly below the measurement point (i.e., point-to-point). The proposed method calculates ground radiation using multiple measured and terrain data (i.e., multi-point-to-point).

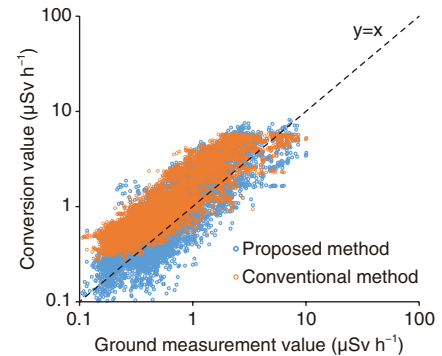
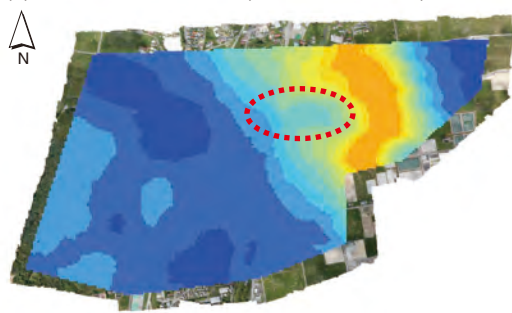


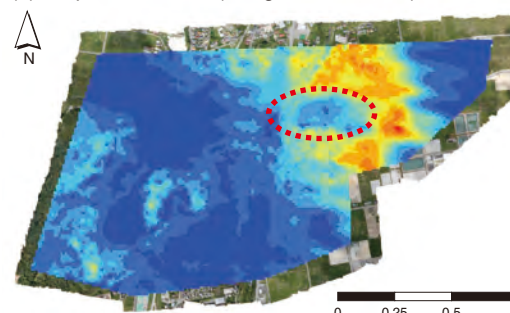
Fig.1-36 Comparison between conversion value measurement from the sky and ground measurement value

The actual and calculated dose rate 1 m above the ground using the conventional and proposed methods are shown.

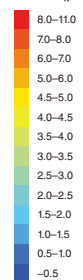
(a) Conventional method (flat surface model)



(b) Proposed method (using terrain effects)



Air dose rate ($\mu\text{Sv h}^{-1}$)



0 0.25 0.5 1 (km)

Fig.1-37 Contour maps of the calculated air dose rate

Obtained via the (a) conventional and (b) proposed methods. Both convert to 1 m above ground air dose rate.

Since the accident at the TEPCO's Fukushima Daiichi NPS (1F), manned and unmanned helicopters have been used to monitor the radiation levels around the 1F, which are then converted to indicate the dose rate at 1 m above the ground. The conventional conversion method assumes a flat topography and uniform distribution of the radiation, and uses an attenuation factor of radiation by air at the distance between the measurement point and the ground. Therefore, conversion result of actual place, which differs from this assumption, does not match with real ground measurement data. This is especially true in areas of uneven geographical features, shielding by a tree or building, and patchy radiation distribution. An analysis method using the inverse analysis method was thus developed to consider the effects of geographical features and forest shielding in the calculation of dose rate.

The maximum likelihood-expectation maximization (ML-EM) method, used to visualize internal organs in the medical radiation field, was applied. In this method, the optimal distribution of ground values is calculated from many radiation values measured

from the sky (Fig.1-35). An attenuation factor between the radiation source and the detector is calculated by taking into account the thickness of air, trees, and soil based on actual photogrammetry data.

The resulting radiation levels obtained with an unmanned helicopter using the conventional and proposed method are shown in Fig.1-36. Conversion using the proposed inverse analysis method obtained more accurate values than did the conventional method, thus improving the accuracy of conversion from the sky to the ground. Contour maps of the air dose rate obtained by the (a) conventional and (b) inverse analysis method are shown in Fig.1-37, where the red circled area shows a decontaminated area. In the conventional method, the decontaminated area was not clearly visible due to the influence of surrounding radiation, whereas the proposed method more clearly shows the decontamination.

Future work will aim to optimize the parameters of the proposed method and develop an algorithm allowing it to be applied on measurements from both the sky and ground.

Reference

Sasaki, M. et al., Development of Analysis Method for Airborne Radiation Monitoring Using the Inverse Problem Solutions, Progress in Nuclear Science and Technology, vol.6, 2019, p.63-67.

1-16 Evaluating the Effective Dose Based on a Detailed Radiation Map

— Providing Protection from Radiation in the Specified Reconstruction and Revitalization Base —

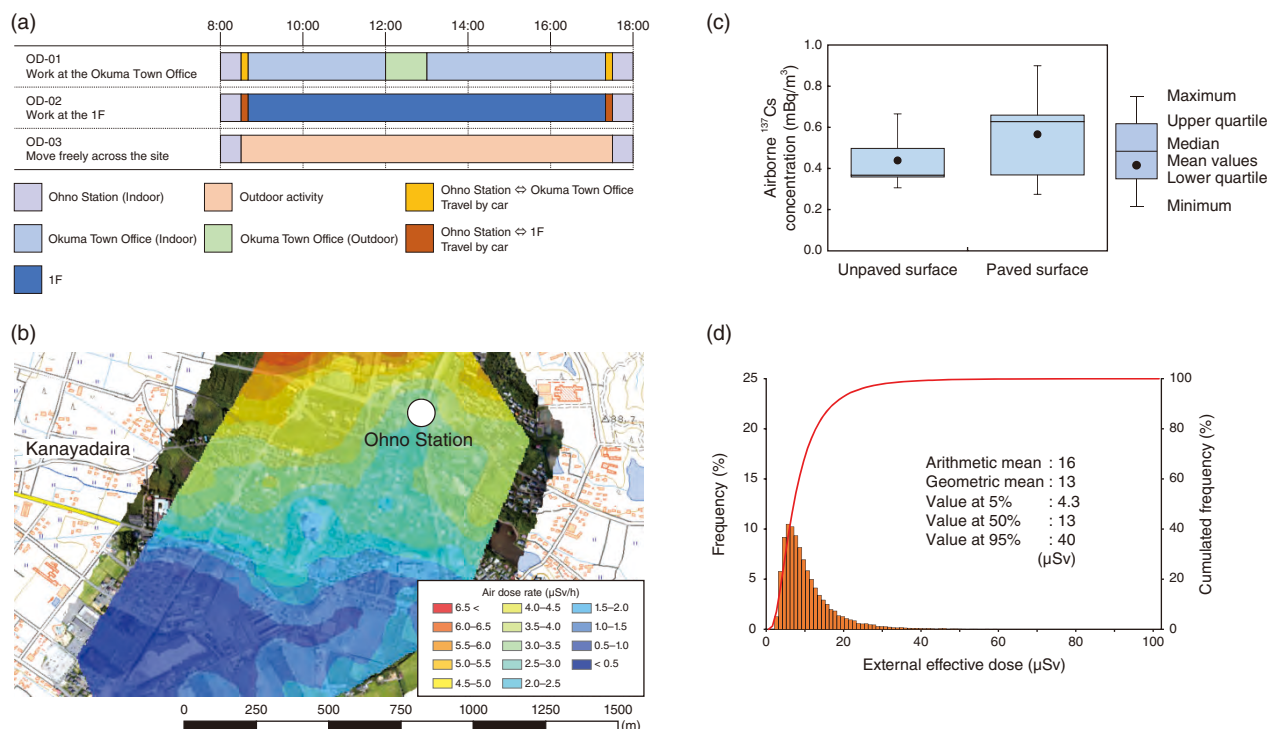


Fig.1-38 Estimating the effective dose based on detailed radiation monitoring

- (a) Typical activity patterns assumed in the specified reconstruction and revitalization base in Okuma
 (b) Distribution map of the air dose rate 1 m above the ground around Ohno Station in Okuma as measured by an autonomous unmanned helicopter
 (c) Atmospheric concentration of ^{137}Cs in Okuma collected by dust sampler
 (d) Estimation of the external effective dose about typical activity pattern at OD-03

The government decided to lift evacuation of part of the high-contamination area affected by the TEPCO's Fukushima Daiichi NPS (1F) accident, where it was anticipated that residents would not be able to return for a long time based on air dose rate. This area, known as the specified reconstruction and revitalization base is located in Okuma, Futaba, and Tomioka around the 1F, where decontamination work and infrastructure improvement have begun and are estimated to be completed in 2023. In these areas: (1) an airborne survey of air dose rate was conducted using an unmanned helicopter, (2) airborne radiocesium was evaluated by collecting air dust and (3) the external/internal effective doses for typical activity patterns were estimated.

First, three types of representative life patterns were developed for each town by interviewing local government officials (Fig.1-38(a)). The exposure dose was estimated following two approaches:

- a deterministic approach, using measuring air dose rate (Fig.1-38(b)) and airborne ^{137}Cs concentration (Fig.1-38(c)) gained from the specified reconstruction and revitalization base, and

- a probabilistic approach using Monte Carlo calculations considering the distribution of the measured air dose from the base.

The resulting frequency distribution of the number of subjects with evaluated external effective dose ranges about life pattern of OD-03 by Monte Carlo calculations is shown in Fig.1-38(d). The arithmetic mean and value at 95% dose were estimated at approximately 16 and 40 μSv per event (8 h of activity time), respectively. The internal effective dose due to inhalation accounted for less than 1% of the external effective dose.

The exposure dose is expected to be lower in 2023 than determined here by implementing air dose reduction measures such as decontamination work in the specified reconstruction and revitalization base. Future work will aim to continue to optimize the radiation monitoring and exposure assessment, and to conduct realistic evaluations of external/internal dose based on detailed radiation mapping to lift evacuation orders of the specified reconstruction and revitalization base.

Reference

Funaki, H. et al., Applied Research for the Establishment of Radiation Monitoring and Evaluation of Exposure Dose of Residence at the Zone Designated for Reconstruction and Recovery, JAEA-Research 2018-016, 2019, 48p. (in Japanese).

1-17 Modeling the Distribution of Air Dose Rates in Habited Areas of Fukushima Prefecture — Developing the 3D Air Dose Rate Evaluation System —

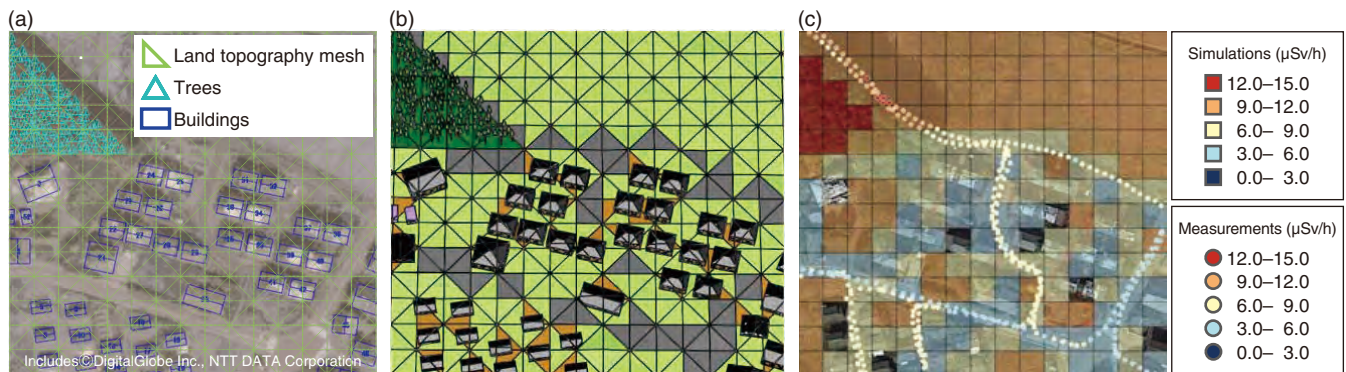


Fig.1-39 Process of modeling air dose rates with 3D-ADRES

(a) Selected areas in Fukushima Prefecture are modeled in 3D-ADRES using remote sensing data and satellite imagery. (b) Created models are converted into a format suitable for PHITS. (c) The air dose rate distribution is calculated by simulating the gamma rays emitted by radioactive cesium (^{134}Cs and ^{137}Cs). The colored squares represent modeled air dose rates, whereas the small colored circles represent air dose rates measured in a person-borne survey. Map imagery © DigiGlobe Inc., NTT Data, Google & Zenrin 2018.

To minimize the external radiation exposure of residents returning to areas where evacuation orders are being lifted after the accident at TEPCO's Fukushima Daiichi NPS (1F) eight years ago, the distribution of air dose rates in inhabited areas must be understood.

Predicting the distribution of air dose rates requires detailed calculations that reflect the differences between the amounts of radioactive cesium (^{134}Cs and ^{137}Cs) on roads and uncovered surfaces, and the effects of shielding by buildings, trees, and land topography. Previous researchers have made simplifying assumptions, such as assuming completely flat land or ignoring the shielding effect of buildings and trees. To this end, JAEA's Center for Computational Science & e-Systems has worked in collaboration with the Fukushima Environmental Safety Center to develop the 3D-ADRES (3D Air Dose Rate Evaluation System) calculation system. This system was designed to create detailed 3D models of residential areas in Fukushima Prefecture to improve the precision of calculations of air dose rate distributions.

In 3D-ADRES, models are created for a target area by first displaying a satellite image or aerial photograph of the location (Fig.1-39(a)). Digital Elevation Model (DEM) geospatial data are used to create a 3D model of the land surface topography by using a triangular mesh (Fig.1-39(a)). Buildings and trees are added on top of the land topography model with heights determined by the Digital Surface Model (DSM) data, thus creating a realistic model of the target area (Fig.1-39(b)). The model is then converted into a format suitable for the PHITS

code developed by JAEA (Fig.1-39(b)). PHITS uses the Monte Carlo method to simulate the paths taken by gamma rays emitted by radioactive cesium. It models the scattering and changes of direction of gamma rays due to interactions in air, as well as absorption by buildings and trees. In this way, it becomes possible to reproduce the complicated air dose rate distribution around buildings and houses (Fig.1-39(c)). Undertaking radiation transport simulations with PHITS allows for air dose rate distributions for the past, present, and future to be calculated.

3D-ADRES and PHITS were used to calculate the air dose rate distribution in an area near the 1F and to examine the effects of buildings, trees, and asphalt on this distribution. The results indicated that wind and rain easily washes radioactive cesium off of buildings and asphalt roads, thus causing air dose rates approximately 60% lower than expected. This effect was greater than the dose rate reduction that occurs due to the shielding of gamma rays by buildings and trees.

Future work will involve using 3D-ADRES and PHITS to evaluate air dose rates inside rooms in houses and buildings where residents tend to spend long periods of time. The developed model will contribute to minimizing residents' external radiation exposures and predicting the reduction in air dose rates in residential areas over time. Furthermore, modern technologies such as 3D laser scanners and GPS-equipped cameras will be implemented to improve the detail of the models whilst developing automation techniques to streamline model creation.

Reference

Kim, M., Malins, A. et al., Simulation Study of the Effects of Buildings, Trees and Paved Surfaces on Ambient Dose Equivalent Rates Outdoors at Three Suburban Sites near Fukushima Dai-ichi, *Journal of Environmental Radioactivity*, vol.210, 2019, p.105803-1–105803-10.

Implementing Continuous Improvements in Safety

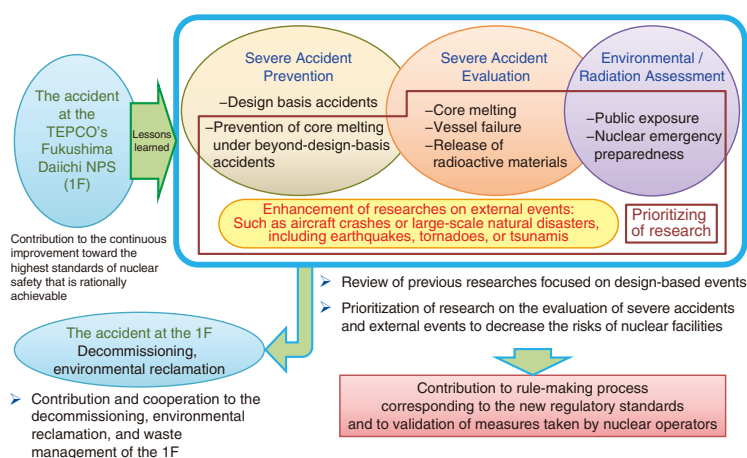


Fig.2-1 Research directions within the Sector of Nuclear Safety and Emergency Preparedness

In accordance with the lessons learned from the accident at 1F, studies on severe accident prevention efforts and nuclear emergency preparedness activities such as environmental-impact assessments and safety assessments for design basis events have been heavily promoted.

The Sector of Nuclear Safety and Emergency Preparedness performs advanced safety research to provide a technical basis for nuclear regulatory authorities in terms of nuclear safety as well as offer a long-term viewpoint through calculations, experiments, and measurement techniques. This research contributes to the development of safety criteria and supports the creation of safety regulations with continuous improvement aimed at the highest level of safety.

Our previous research regarding design basis events prior to the accident at the TEPCO's Fukushima Daiichi NPS (1F) was carefully reviewed in accordance with the lessons learned from the disaster, as shown in Fig.2-1. To reduce the risks of operating nuclear facilities, research on the prevention and mitigation during the progression of severe accidents (SAs), on preparation for and in response to emergency situations, on the consequences of radiation and the management of radioactive waste, and on nuclear criticality safety assessment of fuel debris related to the 1F accident has been expanded.

This work aims to clarify thermal-hydraulic phenomena during SAs and develop effective mitigation measures. This has involved performing experiments with a large-scale containment vessel test facility, CIGMA (Containment Integral Measurement Apparatus), as shown in Fig.2-2. These experiments focused on the gas-phase behaviors at high temperatures and the thermal-hydraulic behaviors of mixed gas, including hydrogen, which may cause containment vessel damage. By employing knowledge obtained from the benchmark exercise on the 1F accident conducted by the OECD/NEA international cooperative project, this work also aims to improve the accuracy of analyses with the computer codes for SA and improve SA evaluation methods. By using the nuclear safety research reactor (NSRR) shown in

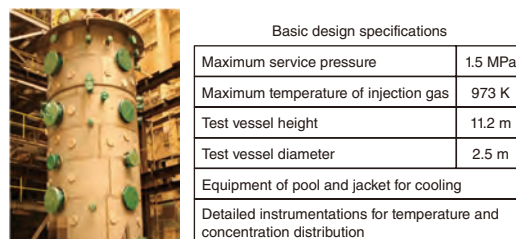


Fig.2-2 Outline of the large-scale containment vessel test facility (CIGMA)

The CIGMA facility was designed to simulate the behaviors of steam and hydrogen gas as well as have several accident mitigation measures.



Fig.2-3 Nuclear safety research reactor (NSRR)

The experiment which simulates a rapid power increase during a reactivity-initiated accident can be safely performed.

Fig.2-3, experiments have been performed to investigate, among other things, the fuel failure limit and the effect of fuel failure on the nuclear reactor during reactivity-initiated accidents, which is one of the design basis accidents for the safety evaluation of nuclear reactor.

To investigate emergency preparedness, the effectiveness of radiation protection countermeasures of shelters has been evaluated. Moreover, the radiation distribution rate around 1F following the accident was investigated using manned and unmanned helicopter, car-borne, and walking surveys; techniques aimed at integrating monitoring data have also been investigated. Nuclear power plants across the country are now monitored according to the basic disaster-management plan.

In addition, a study on ultra-trace analysis of nuclear materials for nuclear safeguards has been conducted using a clean room facility.

This chapter presents the results of recent research in the following sections: Uncertainty Reduction in Source Term Evaluation (Topic 2-1), Towards a More Reliable Safety Evaluation for Loss-of-coolant Accidents (Topic 2-2), Safety Evaluation Considering Uncertainties of Accident Progression (Topic 2-3), Evaluation of Sheltering Effectiveness for Internal Exposure at a Nuclear Accident (Topic 2-4), Detailed Investigation of Fracture Toughness of Reactor Pressure Vessel (Topic 2-5), and More Rational Inspection of Piping Systems (Topic 2-6).

Moreover, two topics related to the estimation of uncertainty in criticality of nuclear systems containing fuel debris (Topic 1-4) and the safety assessment for reuse of contaminated rubble (Topic 1-9) are described in Chapter 1.

2-1 Uncertainty Reduction in Source Term Evaluation

— Dependence of Decontamination Factor on Aerosol Particle Number Concentration in Pool Scrubbing —

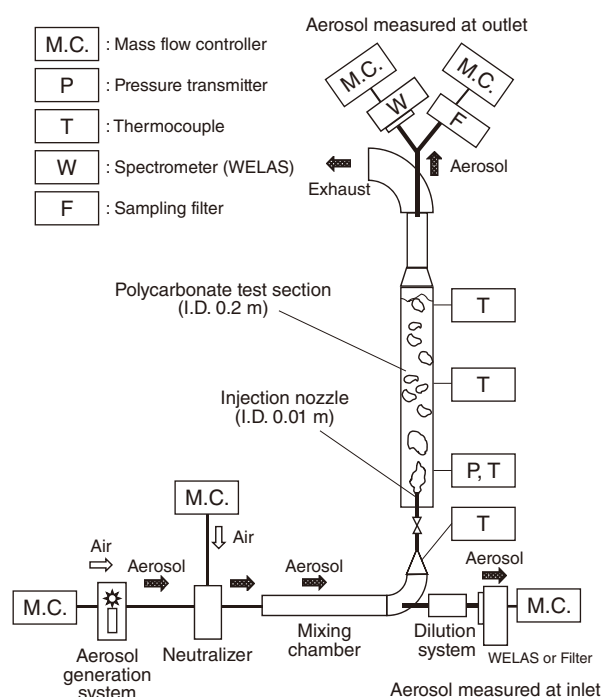


Fig.2-4 Schematic of experimental apparatus (PONTUS)

A cylindrical test section with an inner diameter of 0.2 m is filled with room-temperature water. Aerosol at the same temperature is injected from the bottom of the test section. The DF is evaluated based on the mass ratio (or number ratio) of aerosol particles measured at the inlet and outlet of the test section.

Pool scrubbing can effectively reduce fission product release to the environment during a severe accident of a nuclear reactor. Since scrubbing has a relatively high decontamination factor (DF) and a large impact on the evaluation of source term (defined by generation and release rate of contaminant in the event of an accident), it has been widely studied as an important nuclear safety issue. JAEA is currently conducting experimental research to reveal the interaction mechanism between an aerosol and two-phase flow in the pool. This work has aimed to reduce the uncertainty of measuring aerosol and improve the reliability, both of which have been regarded as important issues in previous studies.

The results indicated that the DF increased significantly with decreasing particle number density in the condition of the particle concentration without significant collision and/or agglomeration. As this phenomenon has hardly been investigated in the past, even though it may clarify the physical mechanism of pool scrubbing, the characteristics were studied in detail.

A schematic of the designed experimental apparatus (named PONTUS) is shown in Fig.2-4. By using air as a carrier gas, monodispersed SiO_2 (particle size diameter of $0.5 \mu\text{m}$) as an aerosol, and fixed thermal-hydraulic parameters such as injection flowrate and/or pool water depth, the DFs for each water depth were measured by changing only the particle number concentration as a test parameter. At a water depth of 2.4 m, aerosol spectrometers and filter sampling which have

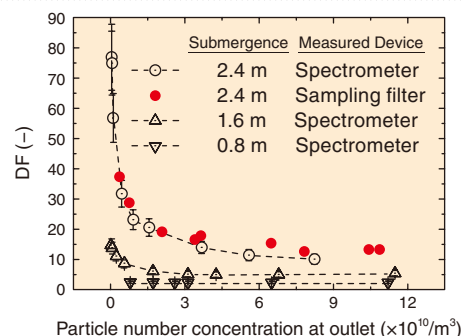


Fig.2-5 Relationship between DF and particle concentration for each water submergence

Highly reliable experimental results were obtained using two methods with different measurement principles. The DF dependency on particle number concentration becomes remarkable with an increase of water submergence.

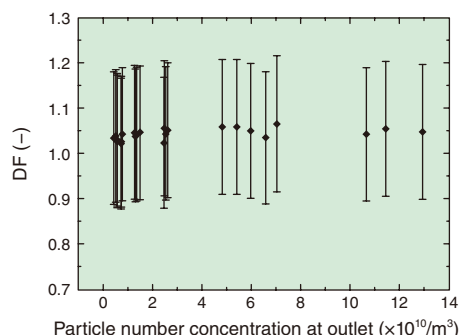


Fig.2-6 Relationship between DF and particle concentration in an empty test section

In an empty test section not filled with water, the DF maintained a nearly constant value regardless of the particle number concentration near the ideal 1. The appropriateness of the facility design can be confirmed from this result.

different measurement principles were both used to ensure measurement reliability; the results are shown in Fig.2-5. The DF results were consistent across both measurement types, indicating the data reliability and the dependence of DF on particle number concentration. The DF increased remarkably with decreasing particle number concentration. To ensure the generality of the acquired data which is not facility dependent, the DF was also measured in an empty test section without pool water in the same test section. As shown in Fig.2-6, the DF in the empty test section indicated a constant value regardless of the particle concentration, and the value is close to the ideal 1, showing the appropriateness of facility design. The resulting DF under water submergence of 0.8 m and 1.6 m is also shown in Fig.2-5. Thus, the dependence of DF on the concentration becomes more significant as the deeper water submergence. Therefore, it is considered that the dependency on particle number concentration plays a more dominant role in the bubble rising region downstream from the injection than in the gas injection region.

Overall, the effect of particle number concentration on the DF increased under high water depth and low particle number concentration. Based on these findings, future work will aim to improve the pool scrubbing model related to this phenomenon.

This study was conducted as part of the contract research sponsored by the Secretariat of the Nuclear Regulation Authority (NRA), Japan.

Reference

Sun, H. et al., Experimental Investigation of Decontamination Factor Dependence on Aerosol Concentration in Pool Scrubbing, Science and Technology of Nuclear Installations, vol.2019, 1743982, 2019, 15p.

2-2 Toward a More Reliable Safety Evaluation for Loss-of-Coolant Accidents — Uncertainty Quantification of Fracture Limit of Fuel Cladding Tube —

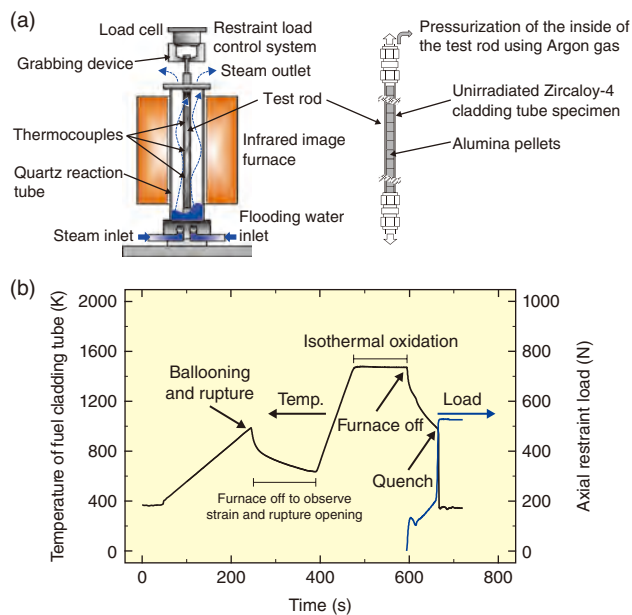


Fig.2-7 Overview of LOCA-simulated integral thermal shock test
(a) A test rod was placed in a quartz reaction tube and heated under steam flow using an infrared image furnace. (b) The test rod was heated and quenched as indicated to simulate the behavior of a fuel cladding tube postulated during LOCAs. During quenching, an axial restraint load was applied to the test rod for several minutes to simulate a restraint load caused by the components of a fuel assembly and see whether the test rod can withstand against fracture.

Loss-of-coolant accidents (LOCAs) caused by breaks in the primary piping or the like are postulated in the safety design of nuclear power plants. When the core cooling is insufficient during a LOCA, the fuel rods heat up, allowing the fuel cladding tubes to be oxidized in steam. If the fuel cladding tube is significantly embrittled due to the oxidation, it may fracture when quenched from the coolant injection from the emergency core cooling system, resulting in the loss of a reactor core's coolable geometry during the LOCA. Maintenance of the reactor core's coolable geometry during the LOCA is commonly evaluated based on the fracture limit of fuel cladding tubes. In previous studies, the fracture limit was evaluated deterministically based on experimental results obtained under conservative conditions. Therefore, the fracture limit uncertainty derived from experiments and evaluations has not been quantitatively evaluated.

Here, the uncertainty of fuel cladding tube's fracture limit was evaluated and quantified using Bayesian statistics. To do so, LOCA-simulated integral thermal shock tests were first performed using unirradiated Zircaloy-4 cladding tube specimens (Fig.2-7). The obtained results concerning the fracture and non-fracture of the specimens were converted into a binary format, using fracture = 1 and non-fracture = 0. A generalized linear model was then applied to the binary data under an assumption of a Bernoulli distribution. Finally, a fuel fracture probability estimation model was developed as

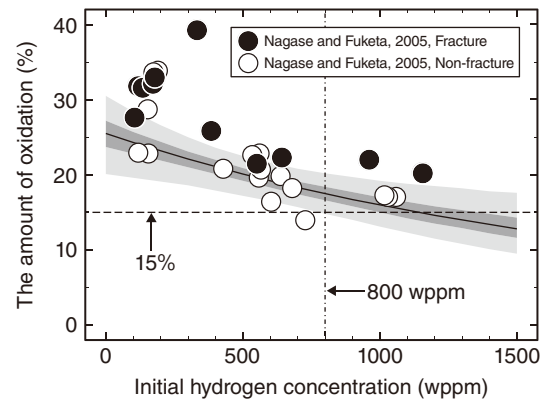


Fig.2-8 Fracture limit uncertainty of unirradiated Zircaloy-4 cladding tube

Fracture probability of the unirradiated Zircaloy-4 cladding tube was estimated using the results of the LOCA-simulated integral thermal shock tests (fracture: ●, non-fracture: ○). The lines and shaded regions show the median, 50% Bayesian prediction interval, and 95% Bayesian prediction interval.

a function of the amount of oxidation of the specimens after the test (i.e., the ratio of metal layer thickness reduced due to oxidation to initial metal layer thickness in the specimen) and the pre-test hydrogen concentration in the specimen (denoted as "initial hydrogen concentration"). Regression coefficients of this model were estimated using Bayesian inference and the fracture limit uncertainty of the unirradiated Zircaloy-4 cladding tube was quantified using probability; the results are shown in Fig.2-8.

When evaluating the fracture limit considering uncertainty based on probability theory, the probability of a fracture at that point and the extent to which the obtained samples represent the true population must both be considered. Here, the fracture limit was defined as the limit representing a 5% fracture probability with 95% confidence based on the accuracy of the fuel fracture probability estimation model and practices in safety assessments of nuclear facilities in Japan and overseas. The fracture limit defined in this way revealed to be higher than 15% in the amount of oxidation for initial hydrogen concentrations of up to 800 wppm even considering the uncertainty.

This result enables the quantitative evaluation of the safety margin of the fracture limit of the fuel cladding tube, which is important to maintain the coolable geometry of the reactor core during the LOCA.

References

- Narukawa, T. et al., Experimental and Statistical Study on Fracture Boundary of Non-Irradiated Zircaloy-4 Cladding Tube under LOCA Conditions, *Journal of Nuclear Materials*, vol.499, 2018, p.528–538.
- Narukawa, T. et al., Uncertainty Quantification of Fracture Boundary of Pre-Hydrided Zircaloy-4 Cladding Tube under LOCA Conditions, *Nuclear Engineering and Design*, vol.331, 2018, p.147–152.

2-3 Safety Evaluation Considering Uncertainties of Accident Progression — Development of Simulation-Based Risk Assessment Methodologies —

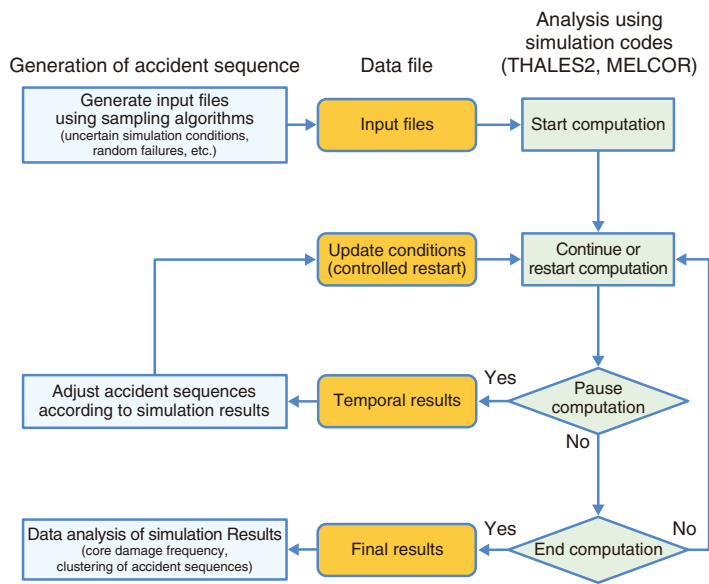


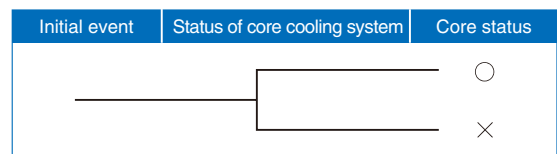
Fig.2-9 Framework of the dynamic probabilistic risk assessment tool RAPID

RAPID is used for generating and analyzing accident sequences based on probability distributions of uncertainties and occurrence timing of component failures. Accident sequences can be adjusted in RAPID based on potential correlation with temporal simulation results, for example, a change in the pressure in the reactor coolant system. Risk information is then obtained in RAPID from the simulation results.

Risk assessment of large facilities, e.g. a nuclear power plant, generally uses event trees, which are used to analyze accident scenarios represented by a combination of statuses of safety-related measures (i.e., success or failure), and fault trees, which are used to logically analyze causes of a system's failure and to evaluate its probability. Conventional risk assessment is mainly based on pre-defined accident scenarios and simplified models that cannot integrate the recovery of failed components, degraded operational performance, or changing working statuses of components into the plant dynamics, and cannot treat the responses of components according to the plant status change. To better model the time-dependent correlation between accident progression and plant system responses, a risk assessment with plant interactive dynamics tool (RAPID) is under development to support dynamic probabilistic risk assessment (PRA) with the aid of numerical simulations.

The current proposed version of RAPID, shown in Fig.2-9, can (1) perturb variables in input files of simulation codes via random sampling; (2) iteratively execute simulation codes; (3) process and plot the simulated results; and (4) perform advanced data analysis, such as construct a statistical surrogate

(a) Static event tree (without consideration of time and recovery measures)



(b) Analysis using dynamic event tree method (with consideration of time and recovery measures)

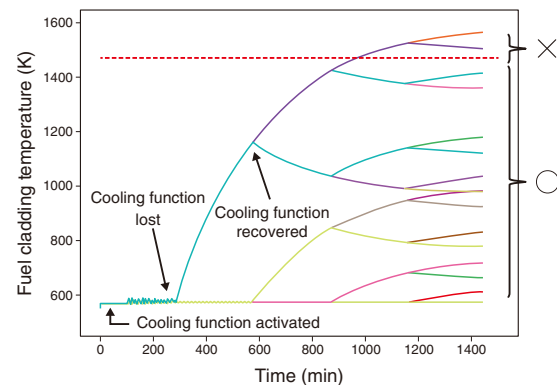


Fig.2-10 Simulation results using the DDET method

The correlation between elements of a conventional event tree and accident progression cannot be treated (a). The correlation regarding time can be treated using the DDET method; furthermore, with various accident sequences being sampled, the corresponding final reactor status can be simulated (b).

model. Furthermore, RAPID can adjust the accident simulation sequence to consider correlation between the component operational status and the plant thermal-hydraulics status, which is referred from the temporary output of the thermal-hydraulic simulation. As an example of codes coupling using RAPID, risk scenarios can be assessed regarding the thermal-hydraulics-dependent degradation of safety-related components such as coolant injection pumps.

During operation, RAPID samples accident sequences by pre-defining the branching time in the accident progression for efficiency and performs simulations for the sampled sequences using the discrete dynamic event tree (DDET) method. This methodology enables the modelling of time-dependent correlations, as shown in Fig.2-10. The simulation-based dynamic PRA methods allows a more random accident sequence sampling, and performing a greater number of simulations enhances the completeness of scenario identification. This developed tool is expected to be useful for rational decision-making in nuclear regulation.

This study was partly supported by the Secretariat of the Nuclear Regulation Authority (NRA), Japan.

Reference

Zheng, X. et al., Severe Accident Scenario Uncertainty Analysis Using the Dynamic Event Tree Method, Proceedings of 14th International Conference on Probabilistic Safety Assessment and Management (PSAM-14), Los Angeles, USA., 2018, 10p., in USB Flash Drive.

2-4 Evaluating of Sheltering Effectiveness against Internal Exposure at a Nuclear Accident

— Factors Affecting Sheltering Effectiveness and Influence of Environmental Factors on Indoor/Outdoor Ratio —

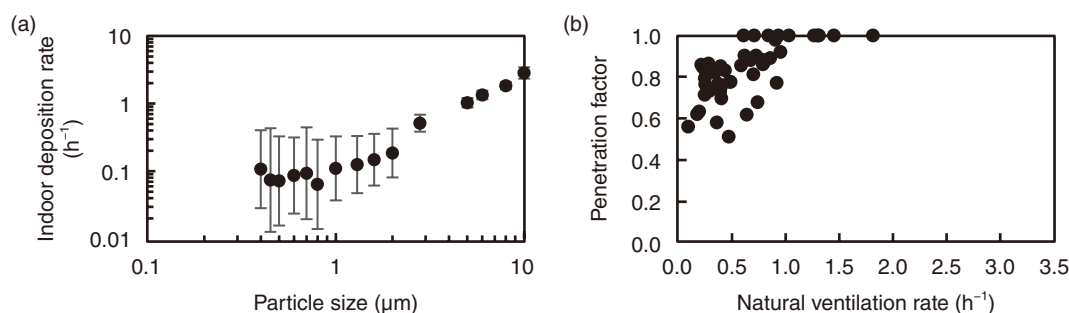


Fig.2-11 Experimental results on indoor deposition rate and penetration factor

(a) Comparison of the indoor deposition rates of varying particle sizes. Error bars indicate standard deviation.

(b) Comparison of the penetration factors for particles 0.5 μm in diameter under varying natural ventilation rates.

Used parameter values

Building year	Natural ventilation rate λ_e	Penetration factor P
Pre-1980	0.06–3.5 h ⁻¹	0.55–1
1980–1992	0.05–1.0 h ⁻¹	0.5–1
Post-1992	0.05–0.5 h ⁻¹	0.5–0.75

Indoor deposition rate λ_d : 0.1 h⁻¹

Fig.2-12 Range of relevant parameters

The range of the natural ventilation rate and penetration factor corresponds to environmental factors such as wind speed and building covering ratio.

Sheltering, which is a countermeasure aimed to protect the public from exposure at a nuclear accident, is implemented until an evacuation is taken and is preferable in certain places where evacuation and re-location are not the best option for protection.

The sheltering effectiveness against internal exposure can be expressed by a ratio of the indoor-to-outdoor radioactivity concentrations (I/O ratio). The indoor concentration is controlled by the indoor/outdoor air exchange and the indoor behavior. These phenomena are expressed by the natural ventilation rate, indoor deposition rate, and penetration factor, which is the ratio of an outdoor object that penetrates indoors. These relevant parameters have been investigated in western countries to evaluate the sheltering effectiveness. However, they cannot be applied to Japanese houses, as they depend on dwelling characteristics, such as the airtightness of houses, and environmental factors, such as wind speed. Therefore, the sheltering effectiveness of Japanese houses must also be investigated.

The relevant parameters were thus investigated via literature surveys and real house experiments. Additionally, the influence of environmental factors on the I/O ratio was investigated. The natural ventilation rate was determined using indoor and outdoor CO₂ measurements, and the penetration factor and indoor deposition rate were determined with indoor and outdoor aerosol measurements (Fig.2-11). The natural ventilation rate

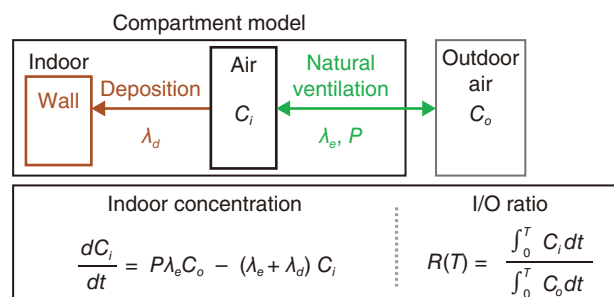


Fig.2-13 Compartment model simulating the indoor/outdoor air exchange and indoor behavior

The indoor concentration C_i and I/O ratio R are calculated with the values shown in Fig.2-12.

differed by the building year (Fig.2-12); houses built before 1980 had a greater ventilation rate than that of Western countries (0.125–1 h⁻¹). The indoor deposition rate for particles of 0.3–1 μm was approximately 0.1 h⁻¹ (Fig.2-11(a)), and the penetration factor ranged from 0.5 to 1 depending on the natural ventilation rate (Fig.2-11(b)).

The I/O ratio was then calculated by inputting the parameters shown in Fig.2-12 into the compartment model simulating the indoor/outdoor air exchange and indoor behavior (Fig.2-13). The I/O ratio was larger for older houses or higher wind speed, as the natural ventilation rate and penetration factor was greater in these cases. The I/O ratio was calculated under the assumption that all radionuclides were particulate forms and the concentration in a plume was uniform. However, in real nuclear accidents, radioiodine consists of non-reactive gaseous forms, reactive gaseous forms (I₂), and particulate forms. Additionally, the concentration in a plume cannot be uniform. Unfortunately, there is little information on the relevant parameters of I₂. Future work should thus investigate the failures of this assumption and relevant parameters of I₂, and then use this to evaluate the sheltering effectiveness under more realistic conditions.

This study was partly supported by the Secretariat of the Nuclear Regulation Authority (NRA), Japan.

Reference

Hirouchi, J. et al., Investigation of Reduction Factor of Internal Exposure for Sheltering in Japan, Proceedings of Asian Symposium on Risk Assessment and Management 2018 (ASRAM 2018), Xiamen, China, 2018, 8p., in USB Flash Drive.

2-5 Detailed Investigation of the Fracture Toughness of a Reactor Pressure Vessel

— Fracture Toughness Evaluation of Heat-Affected Zone under Overlay Cladding Using Miniature Specimen —

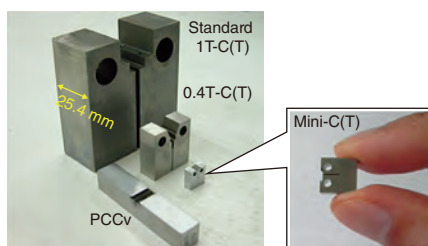


Fig.2-14 Fracture toughness test specimens

The standard specimen has a thickness of 1 inch (25.4 mm), while that of a smaller specimen such as 0.4T-C(T) and the PCCv is 10 mm; that of a Mini-C(T) is only 4 mm.

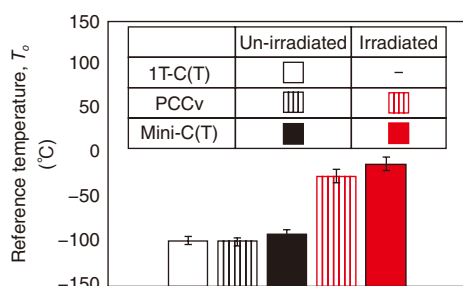
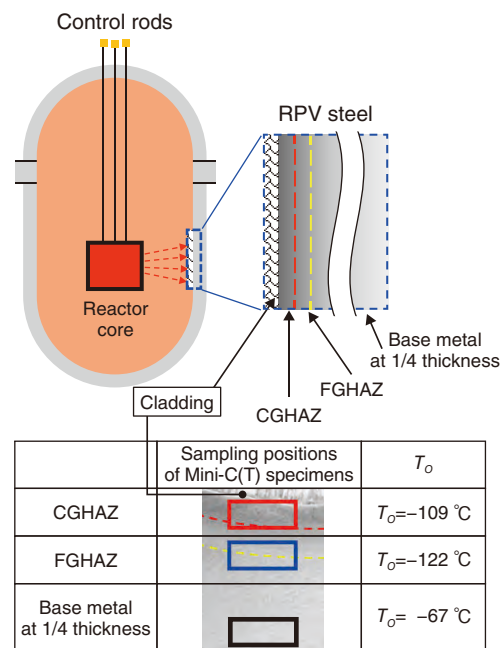


Fig.2-15 Fracture toughness test results of un-irradiated and irradiated RPV steels

The reference temperature, T_o , equivalent to 1T-C(T) and PCCv was obtained using Mini-C(T) for both un-irradiated and neutron-irradiated materials without significant specimen size dependence. Here, T_o is the parameter that characterizes the fracture toughness of ferritic steel in the ductile-brittle transition temperature region.

The reactor pressure vessel (RPV) in nuclear power plants is the most important component for safe operation. The ability of the RPV steel to resist fracture (i.e., the fracture toughness) decreases with neutron irradiation in a process, which is known as irradiation embrittlement. Since stainless steel is weld overlaid (i.e., cladding) on the inner surface of the RPV, a heat-affected zone (HAZ) with an inhomogeneous microstructure is formed under the cladding to a depth of approximately 10 mm. The irradiation embrittlement of this HAZ region, where the irradiation dose is high due to its close proximity to the reactor core, becomes critical for a structural integrity assessment of the RPV. Nevertheless, it is difficult to investigate the fracture toughness distribution of the narrow and inhomogeneous HAZ region using a standard-size specimen. Therefore, specimens with a thickness of 4 mm (i.e., miniature compact-tension specimen (Mini-C(T))), see Fig.2-14) were employed to clarify the fracture toughness distribution of the HAZ.

One of difficulties encountered by employing such small specimens is dependency of fracture toughness on specimen size. As the fracture toughness specimen becomes smaller, the plastic deformation becomes easier due to weak plastic constraint. To prevent plastic deformation and obtain correct fracture toughness, tests must be performed at very low temperatures as possible within the ductile-brittle transition temperature region. However, the valid test temperature range is specified in Japan Electric Association Code 4216 as the test standards, and the test temperature range for Mini-C(T) is considerably narrow. The test temperature for Mini-C(T) was



□ indicates the sampling positions of the Mini-C(T) specimens.

Fig.2-16 Fracture toughness distribution in the HAZ region under overlay cladding using Mini-C(T)

The fracture toughness distribution in the HAZ region was examined using Mini-C(T). Both CG and FGHAZ showed better fracture toughness than base metal at 1/4 thickness of a plate, which represents the fracture toughness of RPV steel.

thus carefully adjusted for each test by referring to previously obtained test results using 1T-C(T), allowing valid fracture toughness data required for the reference temperature (T_o) evaluation to be obtained. The obtained T_o values equivalent to 1T-C(T) and PCCv for both un-irradiated and neutron-irradiated materials are shown in Fig.2-15. These results indicate that the Mini-C(T) can be used in fracture toughness evaluation without significant specimen size dependence.

A fracture toughness evaluation of the HAZ region under the cladding of un-irradiated RPV steel was then performed using the Mini-C(T). The microstructure of HAZ was changed from coarse-grain (CG) HAZ to fine-grain (FG) HAZ with increasing distance from the cladding. The sampling positions along the Mini-C(T) and evaluated T_o values are shown in Fig.2-16. The fracture toughness of CGHAZ and FGHAZ could be evaluated individually using the Mini-C(T). Here, lower T_o corresponds to better fracture toughness. The fracture toughness of HAZ region was changed with increasing distance from the cladding. The fracture toughness of CGHAZ near the cladding was lower than that of FGHAZ, meanwhile, both fracture toughness were better than that of the base metal at 1/4 thickness of a plate, which represents the fracture toughness of RPV steel.

Future work will involve evaluating the fracture toughness of HAZ in neutron-irradiated RPV steel and clarifying the sensitivity of the HAZ region to irradiation embrittlement.

A part of this study was sponsored by the Secretariat of the Nuclear Regulation Authority (NRA), Japan.

Reference

Ha, Y. et al., Fracture Toughness Evaluation of Heat-Affected Zone under Weld Overlay Cladding in Reactor Pressure Vessel Steel, Proceedings of the ASME 2018 Pressure Vessels and Piping Conference (PVP 2018), Prague, Czech Republic, 2018, PVP2018-84535, 6p.

2-6 More Rational Inspection of the Piping System

— Evaluating the Ratio of Welds to be Inspected Based on a Risk Informed In-Service Inspection —

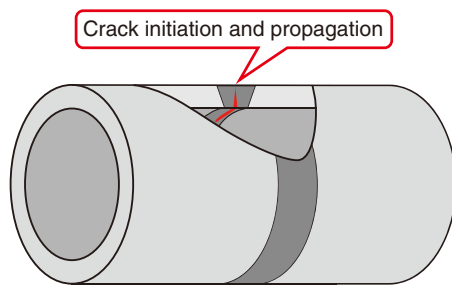


Fig.2-17 Image of a crack in a pipe

Cracks can initiate in the welds of pipes in nuclear power plants during long-term operation. To ensure the structural integrity of pipes, they must be inspected through ISIs. Cracked pipes can then be repaired or replaced as necessary.

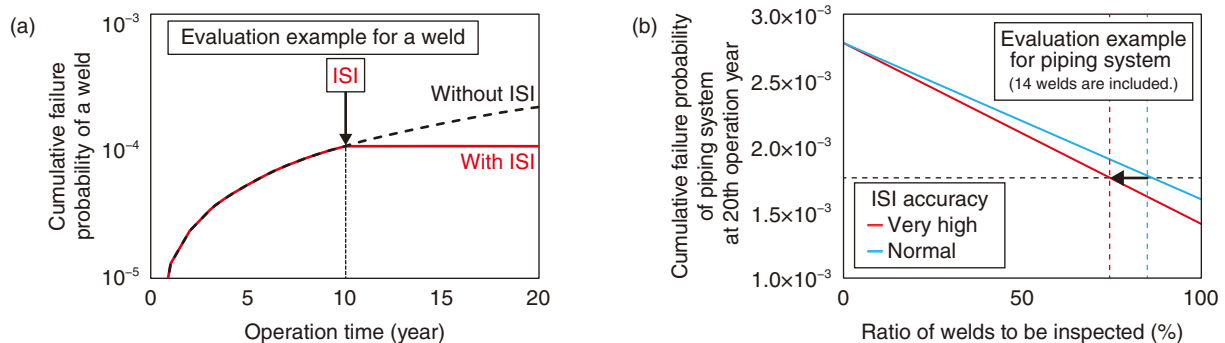


Fig.2-18 Evaluation examples of influence of ISI on failure probability

(a) The relationship between failure probability of a weld and operation time. The failure probability decreases by ISI because cracks are detected and eliminated by repair or replacement. (b) The relationship between failure probability and ratio of welds to be inspected. When ISI with “Very high” accuracy was implemented, even with 10% low ratio of welds to be inspected, it can have the almost same failure probability in the case of ISI with lower accuracy of “Normal”.

Cracks can initiate and propagate in the welds of pipes due to aging degradation during long-term operation of nuclear power plants (Fig.2-17). These cracks may cause pipe failure. To ensure the structural integrity of pipes, non-destructive examinations are performed for welds as a part of in-service inspection (ISI). In case of a crack detection, structural integrity assessment, including crack growth and pipe failure evaluations, is performed. If the structural integrity of the cracked pipe cannot be ensured, the pipe is repaired or replaced. Therefore, ISI has an important role in ensuring the structural integrity of pipes.

In some countries, such as the United States, a risk informed ISI (RI-ISI) is applied to focus inspection resources on important pipes for plant safety, in which the failure probability of the piping system including multiple welds is calculated as a numerical index. The ratio of welds to be inspected in piping system is then determined based on the calculated failure probability. Probabilistic fracture mechanics (PFM) is considered as an evaluation method applicable to RI-ISI. In this method, crack existence or initiation in a weld is considered and crack growth and pipe failure evaluation are performed considering the uncertainties of influential factors. A huge number of pipe evaluations are computed based on the Monte Carlo method for evaluating failure probability, which is the ratio of the number of failed pipes to the total number of evaluated pipes. In addition, PFM can simulate crack detection through the probability of crack detection (POD) model as well as repair or replacement of pipes in ISI. Thus, failure probability can be calculated

reasonably and quantitatively by using PFM.

We have been developing a PFM analysis code PASCAL-SP, for piping system. This work has aimed to evaluate the influence of the ratio of welds to be inspected on failure probability of a piping system using PASCAL-SP.

The failure probability of a weld in typical carbon steel piping system was first evaluated; results are shown in Fig.2-18(a). The cumulative failure probability was shown to increase with operation time due to fatigue crack propagation; the increasing failure probability was mitigated by ISI. Then, a failure probability calculation method was developed for the piping system including multiple welds and used to evaluate the influence of the ratio of welds to be inspected. Here, two POD models of “Very high” and “Normal” which express different accuracy of ISI proposed in the United States were used. The evaluation results are shown in Fig.2-18(b). The failure probability decreased with the increase of the ratio of welds to be inspected. In addition, when ISI with “Very high” accuracy was implemented, even with 10% low ratio of welds to be inspected, it can have the same failure probability in the case of “Normal” accuracy in ISI.

Overall, the application of the PFM evaluation method allows for more reasonable determination of the ratio of welds to be inspected. Future work will continue the research for practical use of PFM including RI-ISI.

This study was partly supported by the Secretariat of the Nuclear Regulation Authority (NRA), Japan.

Reference

Mano, A. et al., An Application of the Probabilistic Fracture Mechanics Code PASCAL-SP to Risk Informed In-Service Inspection for Piping, Proceedings of Asian Symposium on Risk Assessment and Management (ASRAM 2017), Yokohama, Japan, 2017, paper 1023, 12p., in USB Flash Drive.

Advanced Science Pioneers the Future

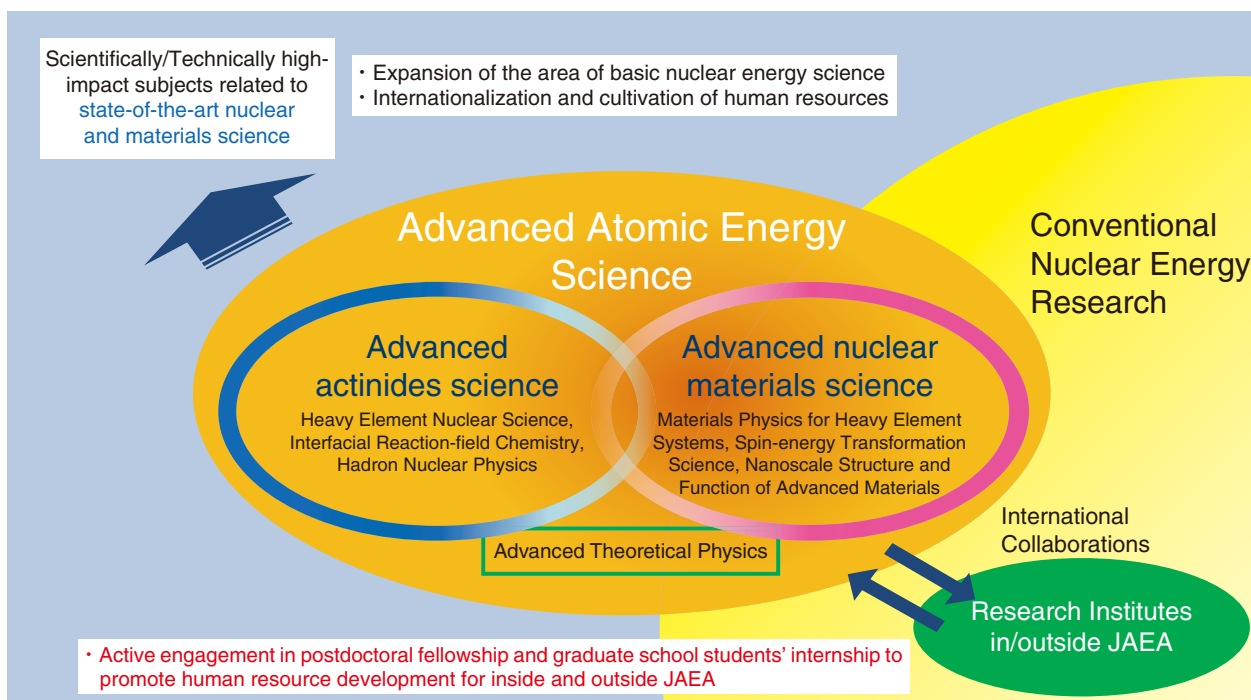


Fig.3-1 The role of advanced nuclear scientific research

In this study, we aim to perform high-impact scientific and technical studies related to state-of-the-art nuclear and material science.

A large part of nuclear-energy-related technology is grounded in basic science. Besides seeking solutions to today's energy problems, future research must respond to the new stage of nuclear energy development that expected in the next few decades.

The Advanced Science Research Center (ASRC) has explored nuclear energy through the lens of basic sciences in an effort to establish new research fields and further develop the existing science and technology.

The mid-term plan, which began in FY2015, focuses on the advancement of two main areas: actinides and nuclear materials science. Respectively, these aim to conceptualize nuclear and heavy-element-based actinide science, and investigate and develop new materials for nuclear-energy purposes. Through interactions between these two areas and collaboration with research institutes within and outside of the Japan Atomic Energy Agency (JAEA), new fields of nuclear-energy science have been cultivated (Fig.3-1).

Numerous achievements have been made during FY2018. Through advanced actinides science, the origin of mass-asymmetry was clarified in fission fragments of actinides using a stochastic differential equation called the Langevin equation.

(Topic 3-1). This will allow for a better understanding of the limit of existence of chemical elements. Through biochemical research, an effective method of removing strontium from seawater by coprecipitation with barite was developed. (Topic 3-2). Additionally, a new double-lambda hypernucleus, the second in the world, was observed. (Topic 3-3). This decaying event was named “MINO” after an ancient name of Gifu Prefecture, where enormous amounts of data were analyzed, and is expected to contribute significantly to future theoretical studies on hadrons. Substantial results have also been achieved in the field of advanced nuclear materials science. It was found that superconductivity can be derived from ferromagnetic fluctuations at high pressure using a uranium compound, UGe_2 (Topic 3-4). Generally, superconductivity and ferromagnetism are seen as two opposing phenomena, and superconductivity is destroyed by the presence of magnetic field. Studying the mechanism of ferromagnetic superconductivity could lead to the development of new superconducting materials, such as superconducting wires that work stably in highly magnetic fields.

The ASRC considers that developing human nuclear resources with expertise and demonstrating their total abilities via basic nuclear research are vital.

3-1 Unveiling the Unique Fission Process of Fermium Nuclides

— Clues towards Understanding the Existing Limit of Super-Heavy Elements —

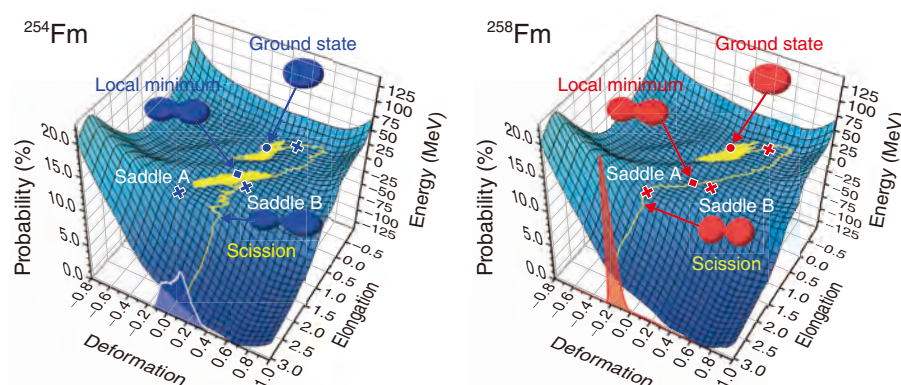


Fig.3-2 Shape evolution and fission for two fermium isotopes, ^{254}Fm and ^{258}Fm

Fission proceeds by passing through the local energy minima on the potential energy surface as shown by the yellow curve. Probability distribution on the deformation parameter at the scission point is shown.

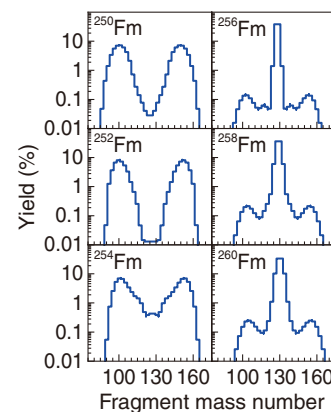


Fig.3-3 Calculated fission fragment mass distributions

Fission of $^{250,252,254}\text{Fm}$ dominantly produce light and heavy fragments, whereas that of $^{256,258,260}\text{Fm}$ shows a sharp mass-symmetric distribution.

In the approximately 80 years since the discovery of nuclear fission, the phenomenon has been applied to atomic power reactors. Neutrons from research reactors are used for cancer therapy and fundamental science research. The fission of uranium produces two fragments with large and small mass numbers, called as mass-asymmetric fission. Due to its complexity, the fission mechanism has yet not been fully understood, remaining as a challenging subject in nuclear physics. Nuclear fission also has a large impact on other fields of science, such as super-heavy element research, noticed by the discovery of element 113, led by RIKEN team. The existing limit of the heaviest element is determined by its stability against fission, which can be predicted by understanding the nuclear-shape evolution in fission over the wide range of nuclides toward heavy elements.

Approximately 40 years ago, surprising results regarding the fission of fermium isotopes (Fm, atomic number 100) was reported. Whereas the lighter Fm isotope shows a mass-asymmetric fission, the heavier nuclide ^{258}Fm exhibits a mass-symmetric fission with a prominent peak structure. This unique fission is expected to dominate in the super-heavy element region, thus influencing stability against fission. Understanding the fission of fermium region makes an important step in this field; however, a quantitative description of this phenomenon has not yet been achieved.

The model presented here successfully explained the mechanism of this phenomenon. The potential energy of nuclides ^{254}Fm and ^{258}Fm is shown in Fig.3-2, in which the nuclear shape is shown to evolve with time by following the local minima. For ^{254}Fm , the nucleus was trapped in the intermediate local minimum after overcoming the first saddle point before fissioning by passing over the saddle point B. On the contrary, ^{258}Fm fissions by surmounting the saddle point A, without staying in the local minimum. A significant change was thus demonstrated: asymmetric fission to sharp symmetric fission, as shown in Fig.3-3. The nucleus has two saddle points, A and B, at a similar height. By reaching to the heavier isotope ^{258}Fm , the system can eventually undergo fission by passing through saddle point A. The mechanism is similar to that of a seesaw, where the slope can turn over quickly by a subtle balance or imbalance of the weights: a small change in the mass of a fissioning nucleus can guide the fission in a different direction. The fission mode inherent in ^{258}Fm would be a common feature for super-heavy nuclei. Thus, this theoretical approach can be considered as a first step for deeper understanding of the heaviest nuclei.

The results were obtained from a student involved with the summer student program of JAEA. For the improvement of the theoretical model, the experimental data taken at the JAEA tandem facility in Tokai were used.

Reference

Miyamoto, Y., Nishio, K. et al., Origin of the Dramatic Change of Fission Mode in Fermium Isotopes Investigated Using Langevin Equations, Physical Review C, vol.99, issue 5, 2019, p.051601-1–051601-7 (R).

3-2 How Removal of Strontium from Seawater ?

— Use of Coprecipitation Method by Barite Controlled Chemical Composition —

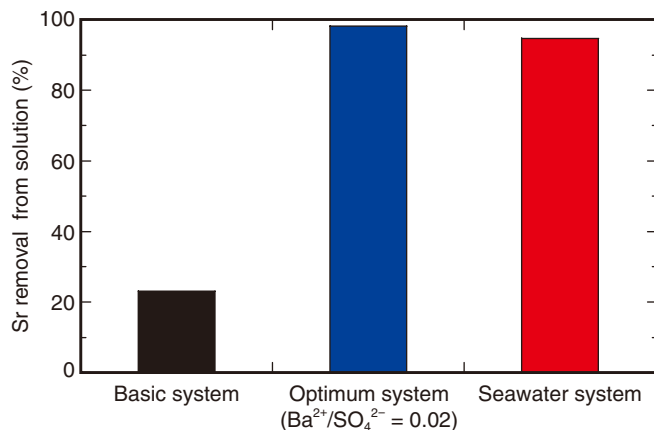


Fig.3-4 Strontium (Sr) removal by coprecipitation with barite
This figure depicts an optimal system (blue) for Sr removal from an aqueous solution by controlling a basic system (black: Sr^{2+} 0.01 mM, pH 2.0, IS 0.08 M, no coexistent ions, $\text{Ba}^{2+}/\text{SO}_4^{2-} = 1$). A seawater system (red) was also examined in the optimum condition and showed a high removal capacity.

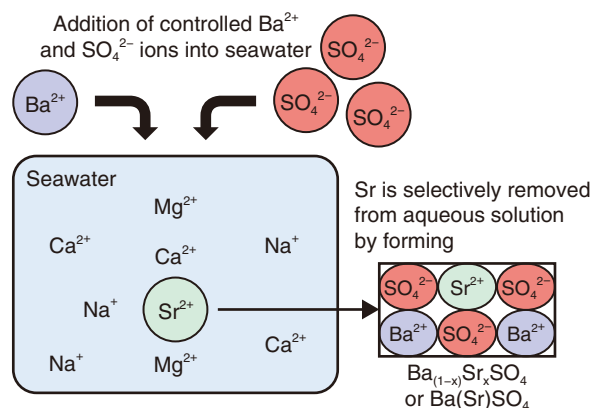


Fig.3-5 Experimental design for removing Sr from seawater by coprecipitation with barite
Sr was effectively removed from seawater by controlling the $\text{Ba}^{2+}/\text{SO}_4^{2-}$ ratio in the initial solution.

Strontium-90, which is a fission product of uranium and can be released to the environment during nuclear plant accidents, has a low adsorption capacity on clays and a high mobility in environments. There are few effective techniques for removing Sr from seawater because of the strong inhibition of Sr uptake by the high concentration of sodium and other competitive ions in seawater. In this work, barite (BaSO_4) was used under various experimental conditions to develop techniques for the direct removal of Sr from seawater.

Barite is a common compound in many geological environments and easily precipitated from an aqueous mixture of Na_2SO_4 and BaCl_2 . Several trace elements, including Sr, can be incorporated into the crystal lattice of barite during a coprecipitation process. The effects of pH, ionic strength (IS), coexistent Ca^{2+} and Mg^{2+} ion, and $[\text{Ba}^{2+}]/[\text{SO}_4^{2-}]$ ratio in the initial solution were investigated for determining the optimum condition

for Sr removal by using barite. The resulting removal efficiency for three of the studied systems is shown in Fig.3-4. The main parameter found to affect the removal efficiency was the $[\text{Ba}^{2+}]/[\text{SO}_4^{2-}]$ ratio in the initial aqueous solution; Sr was completely removed from the aqueous solution when the $[\text{Ba}^{2+}]/[\text{SO}_4^{2-}]$ ratio is low. A high removal efficiency of 90% was also achieved in seawater (≈ 1 mg/L), despite its high saline concentration, due to the negligible effect of IS and competitive ions (Na^+ , Ca^{2+} , and Mg^{2+}). Thus, compared to previous techniques, barite was shown to present a reliable material for the removal of Sr from aqueous solutions, including seawater, after optimization of the $[\text{Ba}^{2+}]/[\text{SO}_4^{2-}]$ ratio and other parameters (Fig.3-5).

This method can be applied to other radioactive anions present in high-level waste at Fukushima, such as selenium-79 and iodine-129, for safety assessments of long-term geological disposal.

Reference

Tokunaga, K. et al., A New Technique for Removing Strontium from Seawater by Coprecipitation with Barite, Journal of Hazardous Materials, vol.359, 2018, p.307–315.

3-3 Observation of a New Double Lambda Hypernucleus during a J-PARC Experiment — As a Microscopic Image, the Second Case Where the Nuclide is Identified —

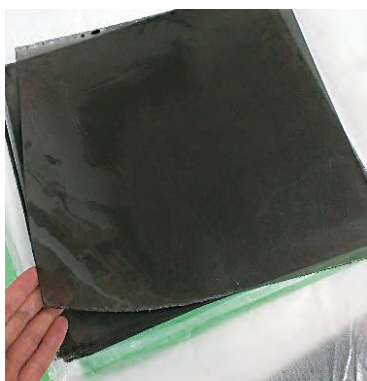


Fig.3-6 A photographic emulsion sheet for nuclear experiments (after photographic processing)

This sheet is square with a side length of 35 cm and is approximately 0.6 mm thick. Double Lambda hypernuclei were recorded somewhere in the sheets as microscopic photographic images.

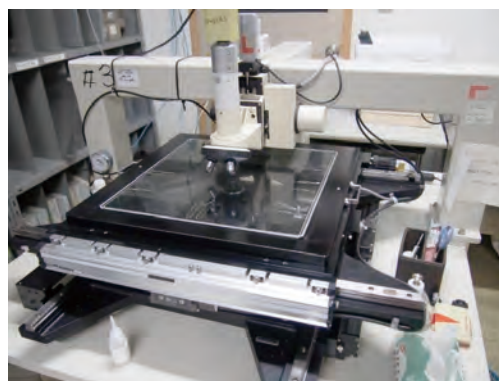


Fig.3-7 A dedicated microscope for scanning the large emulsion sheet

An in-house control software with dedicated image processing was used.

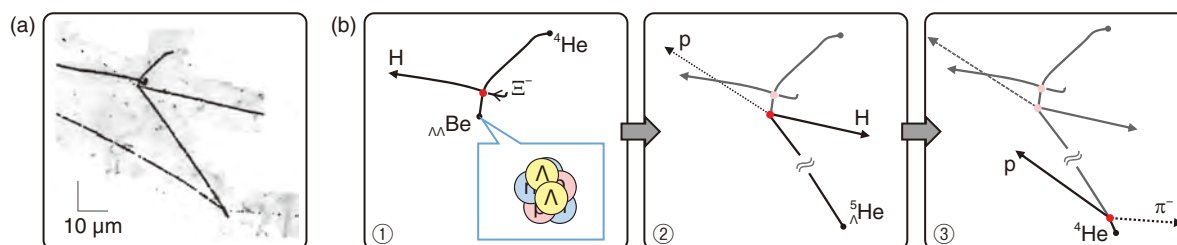


Fig.3-8 MINO event: a typical double Lambda hypernucleus event found in 2018

(a) A micrograph of the MINO event. (b) Schematic of the event, where (1) is a fission process induced by a Xi-minus particle, and one of the 3 fission fragments is the double Lambda hypernucleus. This fragment caused the sequential decay shown in (2) and (3), where “p” and “H” indicate a proton and hydrogen isotope, respectively.

A double Lambda hypernucleus (DLH) event was observed during a J-PARC experiment. DLH is a rare nucleus containing 2 Lambda particles. Whereas normal nuclei are made of protons and neutrons, which are composed of up- and down-quarks, Lambda particles resemble nucleons consisting of three quarks but have a “strange-quark”, i.e., a 3rd quark.

The study of DLH is an important issue in modern hadron-nuclear physics because DLH is a valuable information source of Lambda–Lambda interaction. This interaction is theoretically unique; experimental data is necessary to test theories that describe the dynamics and interactions between quarks, hadrons, and nuclei.

The largest experiment with DLH thus far at J-PARC was therefore designed and performed at a scale 10 times larger than the previous study. As of the 2000s, only 9 DLH events have been observed. Among these, only one event, in 2001, has been identified as ${}_{\Lambda\Lambda}^6\text{He}$. Various DLH data are necessary to systematically study Lambda–Lambda interaction.

Fifteen hundred photographic emulsion sheets were used as the main detectors, one of which is shown in Fig.3-6. Only this detector can detect rare DLH events in a large background as

tiny photographic images. After the accelerator experiment, the sheets were analyzed under dedicated optical microscopes, as shown as Fig.3-7. This microscope is used for the event search and detail event-by-event analysis.

Eleven DLH events have been detected thus far. Their geometrical features were reconstructed using a three-dimensional image processing with an accuracy of 0.1 μm to reconstruct the detailed physics process.

One of these events, identified as a beryllium DLH and observed for the first time in 17 years, is shown in Fig.3-8. The Q-value of the fission process was reconstructed and the mass of the DLH was calculated. The identified Lambda–Lambda interaction was determined to be a weak attractive force; however, a slightly different strength was calculated than in the 1st identified DLH due to the difference of nuclides. Theoretical analysis of this event, names “MINO” after the southern part of the Gifu Prefecture where it was found, is ongoing.

The search for more events such as these is also ongoing. Further impressive events are expected in the near future. This experiment was conducted by the J-PARC E07 collaboration, which consists of 24 institutes in 6 countries.

Reference

Ekawa, H., Yoshida, J. et al., Observation of a Be Double-Lambda Hypernucleus in the J-PARC E07 Experiment, Progress of Theoretical and Experimental Physics, vol.2019, issue 2, 2019, p.021D02-1–021D02-11.

3-4 Superconductivity Driven by Ferromagnetic Fluctuations in the Uranium Compound UGe_2

— Correlation between Superconductivity and Ferromagnetic Fluctuations Studied by Magnetic Measurements at High Pressure —

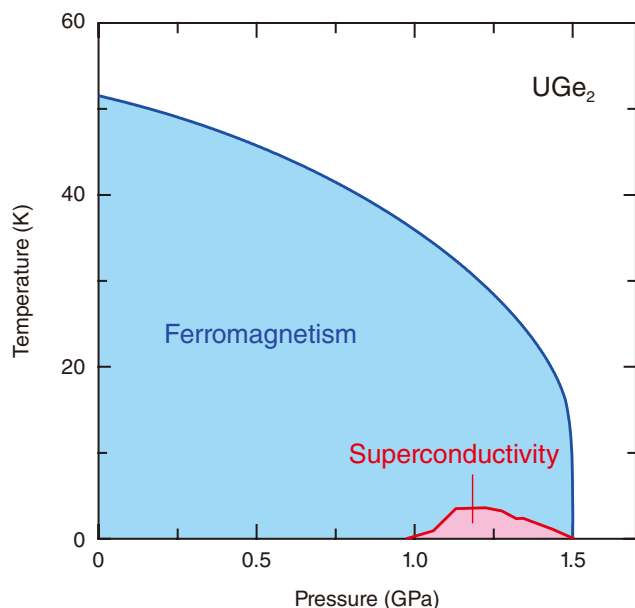


Fig.3-9 Temperature–pressure phase diagram of UGe_2
 UGe_2 shows a ferromagnetic transition at $T_C = 54$ K and ambient pressure. T_C decreases with increasing pressure. The superconductivity appears from 1.0 to 1.5 GPa and coexists with the ferromagnetism.

The electrical resistivity of a superconducting material drops to zero below the superconducting transition temperature T_{sc} . Applications of superconductivity, such as superconducting magnets used in various aspects of industry or medical services, have been developed. Generally, the superconductivity and ferromagnetism have been seen as competitive phenomena. The superconductivity is destroyed by the application of a magnetic field, thus representing a drawback in technological applications. A case study regarding this competitive nature on the uranium compound UGe_2 is thus introduced.

UGe_2 is a simple ferromagnet with a Curie temperature of 54 K at ambient pressure. Surprisingly, the superconductivity appears above 1 GPa, where the compound is still in the ferromagnetic state, as shown in Fig.3-9. Here, the superconductivity and the ferromagnetism coexist under high pressure. Although many experimental and theoretical studies have been done for UGe_2 , it is not clear why the superconductivity emerges in the ferromagnetic state.

To study the mechanism of the superconductivity in UGe_2 , a high-pressure apparatus was developed for magnetic measurements at high pressures up to 10 GPa. A high-quality single crystal sample of UGe_2 was prepared by the Czochralski pulling method. The magnetization of UGe_2 was measured at high pressure and the data was analyzed with spin fluctuation theory.

In uranium compounds, the 5f electrons are responsible for the magnetism and the superconductivity. In the ferromagnetic state, the magnetic moment of the 5f electrons are aligned in one direction. Meanwhile, the direction and size of the magnetic

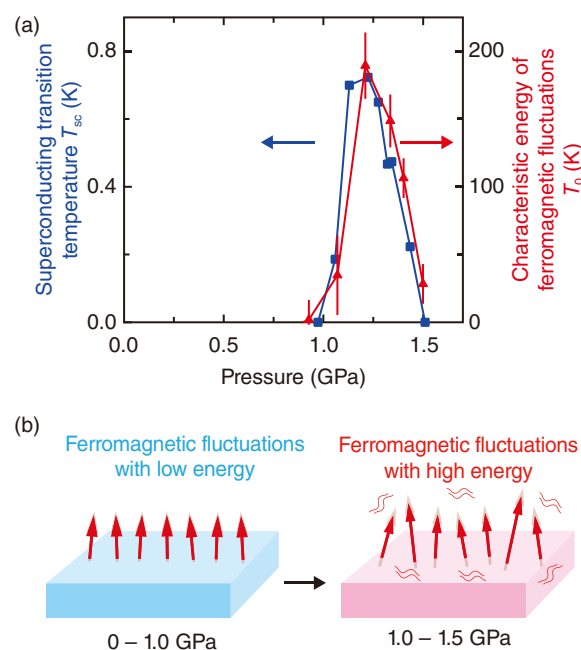


Fig.3-10 Ferromagnetic fluctuations and superconductivity in UGe_2

(a) Characteristic energy of the ferromagnetic fluctuations T_0 and the superconducting transition temperature T_{sc} peaked at approximately 1.2 GPa. (b) Schematic of the pressure-enhanced ferromagnetic fluctuations that play an important role for the appearance of the superconductivity.

moments fluctuate due to the thermal energy. This is called “ferromagnetic fluctuations”. The characteristic energy of the ferromagnetic fluctuations T_0 was examined. The effect of pressure on T_0 was determined from the theoretical analysis of magnetic data. Above 1 GPa, the superconducting transition temperature T_{sc} increases until reaching a maximum at approximately 1.2 GPa, before decreasing again, as shown in Fig.3-10(a). A similar pressure dependence of T_0 was also seen. This suggests a clear correlation between the superconductivity and the ferromagnetic fluctuations.

In conventional superconductors like lead (Pb) or tin (Sn), the superconducting pairs called “Cooper pairs” are formed through interactions between the electrons and the vibration of a crystal lattice named “phonons”. Instead, the ferromagnetic fluctuations may take an important role in the formation of the Cooper pairs in UGe_2 . Therefore, the superconductivity in UGe_2 may belong to a new type.

These results may contribute to the understanding of the coexistence of the ferromagnetism and the superconductivity. The uranium ferromagnetic superconductivity is relatively stable in the high magnetic field when compared with conventional superconducting materials. An understanding of the mechanism of the ferromagnetic superconductivity could lead to the development of new superconducting materials, such as superconducting wires, that work stably in high magnetic fields.

This work was supported by the Japan Society for the Promotion of Science (JSPS) KAKENHI Grant-in-Aid for Scientific Research (C) (No.16K05463).

Reference

Tateiwa, N. et al., Strong Correlation between Ferromagnetic Superconductivity and Pressure-Enhanced Ferromagnetic Fluctuations in UGe_2 , Physical Review Letters, vol.121, issue 23, 2018, p.237001-1–237001-6.

Fundamental Technologies for Nuclear Energy Innovation

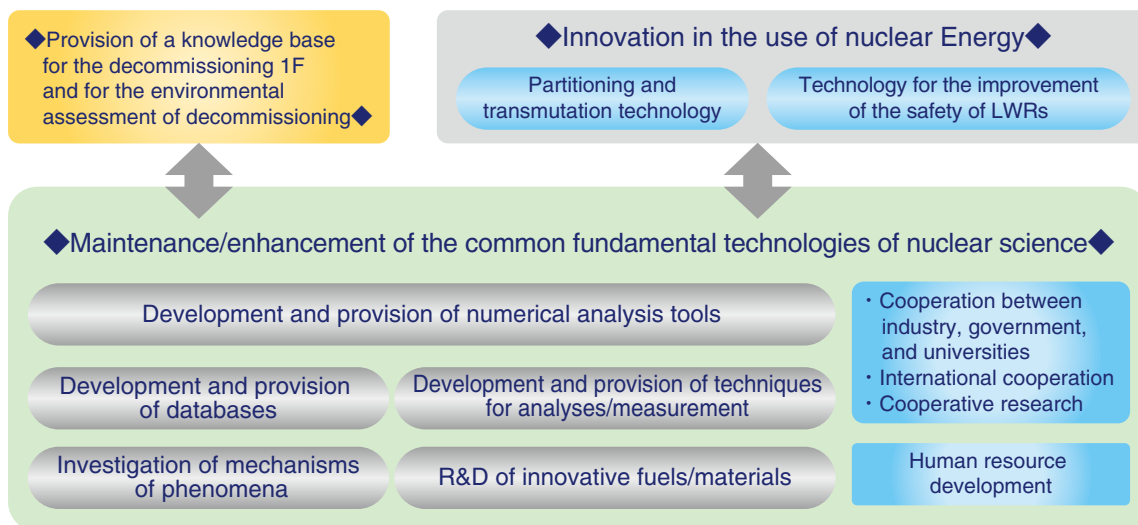


Fig.4-1 Overview of nuclear science and engineering research

The Nuclear Science and Engineering Center maintains and enhances fundamental technologies for the use of nuclear energy and radiation. The Center also aims to provide a knowledge base for the decommissioning of the TEPCO's Fukushima Daiichi NPS (1F), and contribute to the safety improvements of light water reactors (LWRs) and the development of partitioning and transmutation technology for reducing the impact of radioactive wastes.

Common fundamental technologies and knowledge platforms, such as databases, numerical analysis tools, analytical technologies, and knowledge of phenomena mechanisms, are necessary to support the use of nuclear energy and radiation. The Nuclear Science and Engineering Center (NSEC) tries to keep these fundamental technologies and knowledge of nuclear science state-of-the-art and provides the technologies and knowledge for industry, universities, and governmental agencies. NSEC has also contributed to safety improvements of LWRs and the development of partitioning and transmutation technology for reducing the impact of radioactive wastes (Fig.4-1).

Recent results of the ongoing research and development (R&D) activities at NSEC are introduced in this chapter.

Previous researches have suggested that the efficiency of transmutation via deuteron is higher. A theoretical model that can explicitly consider the breakup of deuterons to more accurately predict deuteron-induced reactions was therefore developed and experimentally verified (Topic 4-1).

The risk of stress corrosion cracking (SCC) becomes higher in older nuclear reactors. The initiation and propagation mechanism of the SCC is difficult to investigate experimentally, because SCC is related to the internal environment of microscopic crevices under high-temperature and high-pressure water. A sensor system capable of estimating the internal environment of crevices was therefore developed. Using the developed system indicated that dissolved impurities cause the internal environment of a crevice to become corrosive and that intergranular corrosion occurs inside the crevice (Topic 4-2).

A "SELECT process" to separate nuclear fuel elements and minor actinides from spent-fuel solution was developed, experimentally verified, and then used to theoretically explain the mechanism by which developed solvents separate using a quantum chemistry simulation. Selectivity in the separation mechanism was indicated to be caused by the differences of bond distances and overlaps of electron orbitals between Am-N

and Cm-N, i.e., between minor actinides and nitrogen atoms of the separation solvent (Topic 4-3).

As scintillators are widely used to detect radiation, a mathematical model calculating scintillation light yield was developed. We showed that calculated scintillation light yields of various types of radiation using the new model are well equal to the experimental values. The developed mathematical model is expected to contribute to the development of new scintillators (Topic 4-4).

The validity of applying the International Commission on Radiological Protection (ICRP) reference exposure dose, which is based on an average Caucasian physique, to Japanese people needs to be confirmed. Using models covering a variety of Japanese people's physiques, the average Japanese person's external exposure dose was shown to be applicable with $\pm 10\%$ uncertainty using the ICRP reference dose (Topic 4-5).

The release of fission products (FP) such as cesium from LWRs under severe accident conditions leads to public exposure. To evaluate the amount of released FP from LWRs more accurately, the chemical behavior of FP during transportation in a reactor, from the core through the vessel and building to the environment, was examined through the development of a FP chemistry database ECUME based on the chemical reaction kinetics of a cesium and boron system. The development of ECUME contributed to improve the accuracy of estimated public exposure (Topic 4-6).

Spallation reaction phenomena play a key role in the neutronic and shielding analyses of accelerator facilities such as J-PARC and accelerator-driven systems (ADSs). Because conventional models are complex and predicting a fission event originating from the spallation reactions is difficult, a simplified model for fission probability was developed. It was demonstrated with experimental results that the developed model is able to calculate fission events with higher accuracy (Topic 4-7).

4-1 Contribution by Nuclear Physics to Transmutation Study

— Accurate Prediction of Deuteron Transmutation —

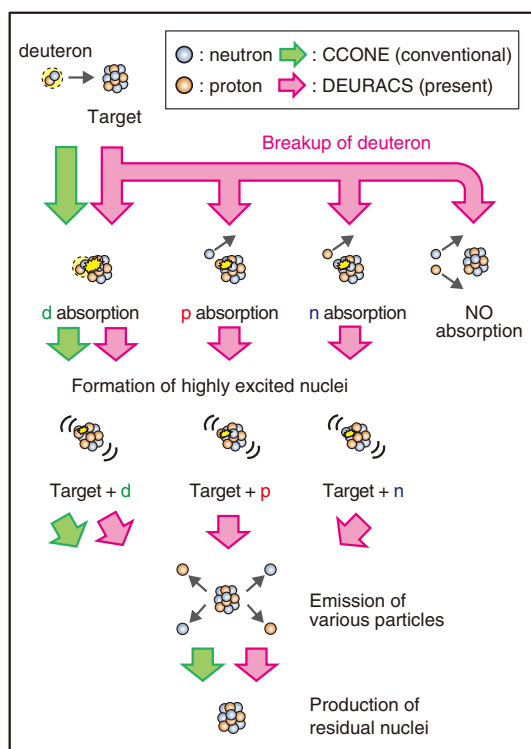


Fig.4-2 Schematic of the calculation in DEURACS

Whereas only one calculation pathway is available when using the conventional CCONE model, three pathways are taken into account in DEURACS.

As produced radionuclides with long half-lives require long-term management, it is strongly desired to transmute them into stable or short-lived ones. Spallation has been recommended for the transmutation of long-lived fission products (LLFPs). Furthermore, using deuteron as an incident particle, rather than a proton, has been suggested to improve the efficiency of transmutation.

Investigating the feasibility of using a deuteron primary beam for transmutation requires accurate cross section data of deuteron-induced reactions over a wide range of target mass numbers and incident deuteron energies. However, the amount and scope of available experimental data of deuteron-induced reactions have been limited. Reliable theoretical models thus are required to provide the necessary data.

We have thus been developing a computational system for deuteron-induced reactions, called DEURACS. In the present study, DEURACS has been improved and used to calculate deuteron-induced spallation reactions on typical LLFPs. As illustrated in Fig.4-2, three composite nuclei types can be formed by the absorption of a neutron or proton produced by the breakup of the incident deuteron or by the absorption of the incident deuteron itself. Whereas prior nucleon-induced reaction models such as CCONE have only considered deuteron absorption, DEURACS considers all three absorption types.

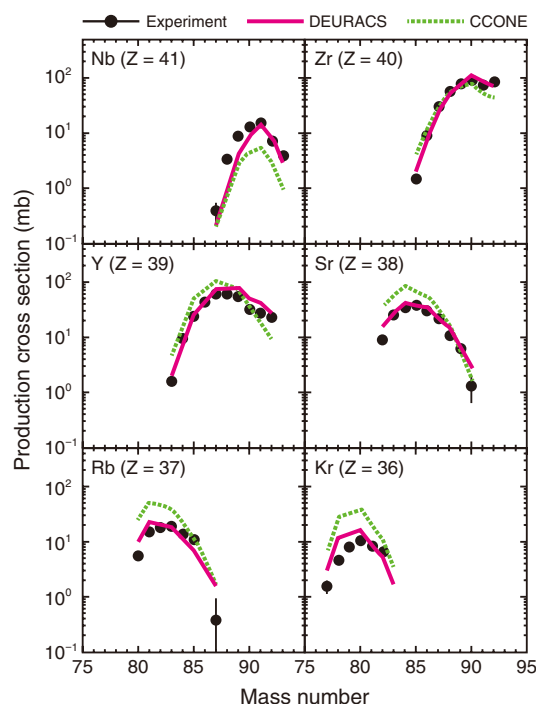


Fig.4-3 Isotopic production cross sections for the $^{93}\text{Zr}+d$ reaction at 210 MeV

The closed circles represent experimental data points, and the solid and dashed curves represent the results calculated via DEURACS and CCONE, respectively.

The calculated and experimental isotopic production cross sections for the $^{93}\text{Zr}+d$ reaction are shown in Fig.4-3 for an incident deuteron energy of 210 MeV. For comparison, the results calculated with the CCONE code, in which the deuteron breakup processes are not taken into account, are also shown. DEURACS more accurately reproduced the experimental data across the wide mass number range studied. The DEURACS-calculated values for $^{107}\text{Pd}+d$ reactions at incident deuteron energies of 236 and 392 MeV were also in good agreement.

The framework of the improved DEURACS was thus deemed applicable to deuteron-induced spallation reactions on LLFPs. Furthermore, it was demonstrated that considering the breakup processes is essential in the accurate prediction of deuteron-induced spallation reactions.

Research and development on a transmutation system using a deuteron primary beam would make great progress by the present work. The developed model and results presented here are expected contribute to further work involving deuteron-induced reactions, such as the production of medical radioisotopes and evaluating radioactivity in deuteron accelerator facilities.

This work was partly supported by the ImPACT Program of Council for Science, Technology and Innovation (CSTI), Cabinet Office, Government of Japan.

Reference

Nakayama, S. et al., Role of Breakup Processes in Deuteron-Induced Spallation Reactions at 100–200 MeV/nucleon, *Physical Review C*, vol.98, issue 4, 2018, p.044606-1–044606-8.

4-2 Microscopic Corrosion Behavior in High-Temperature, High-Pressure Environments

— In-Situ Measurement of Electrical Conductivity of Solution in Stainless Steel Crevices —

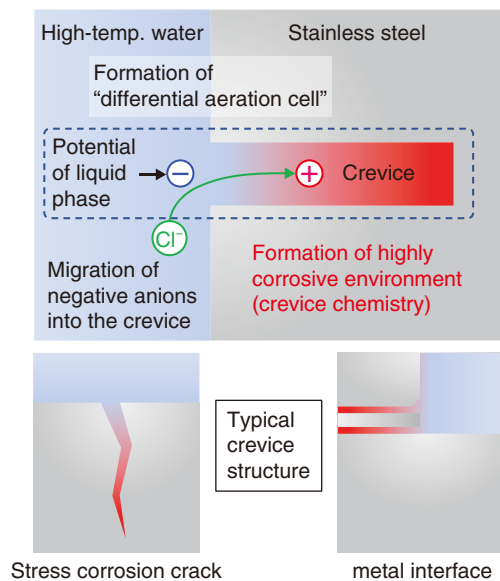


Fig.4-4 Schematic representation of chemical condition within a crevice

A differential aeration cell was formed between the crevice-free surface and the crevice with a limited oxygen supply. This cell acted as driving force to concentrate impurities into the crevice, thus forming a corrosive chemical condition within the crevice (crevice chemistry). Crevice chemistry can be found at the interface of metal (e.g. bolts, nuts, and washers) and inside the stress corrosion crack.

Stainless steels are susceptible to stress corrosion cracking (SCC) in high-temperature and high-pressure water represented by boiling water reactor (BWR). SCC of stainless steels have been recognized as a major corrosion related problems of ensuring safety of nuclear power plants. The chemical conditions within a crevice including stress corrosion crack may become more corrosive than those of the bulk coolant (Fig.4-4), and this plays an important role with regard to crack propagation. The chemical conditions within a crevice often referred to as crevice chemistry have been widely studied, however, analysis of the crevice chemistry is still challenging because crevice with micro-meter gap under high temperature and high pressure is experimentally difficult to access.

A sensor system was thus developed to conduct measurement of the crevice chemistry (Fig.4-5). The system is characterized by high durability in the harsh environment, uses small electrodes to allow for measurement in very tight crevices, and in-situ analysis of the chemistry by electrochemical method. The

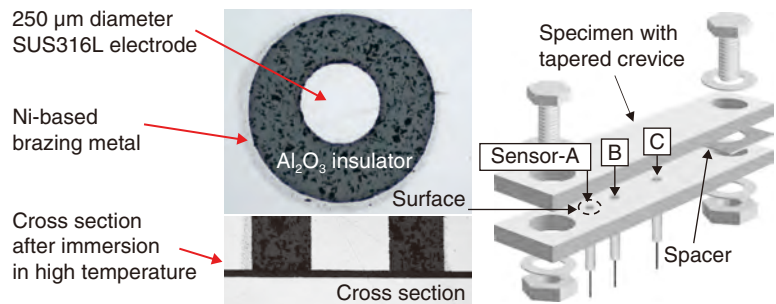


Fig.4-5 Developed sensor systems to measure the crevice chemistry
Small sensors were installed in the crevice to measure the electrical conductivity of the crevice solution. The crevice was tapered to simulate a crack tip of SCC.

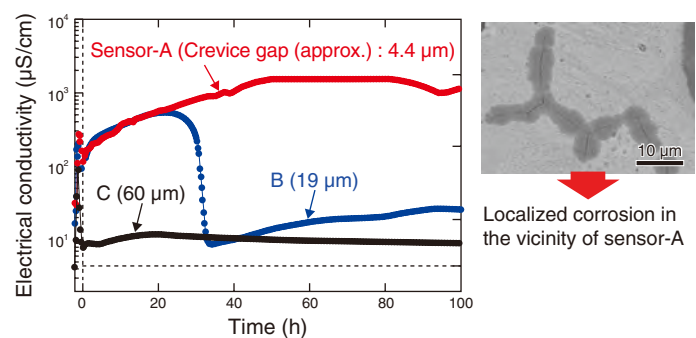


Fig.4-6 Electrical conductivity of the solution within the crevice in 288 °C pure water with dissolved oxygen concentration of 32 ppm
The sensor at the smallest crevice gap detected high electrical conductivity of the crevice solution. Localized corrosion occurred in the vicinity of this position.

sensors were installed at different positions within a tapering crevice of Type-316L stainless steel and measurement of the local electrical conductivity of the crevice solution beneath the sensor was carried out.

Fig.4-6 shows the time variation of electrical conductivity of the crevice solution at different position in 288 °C and 8 MPa high purity water. The results indicated that smaller crevices led to higher conductivity; sensor-A, with a gap of 4.4 µm had conductivity values over 100 times greater than those at sensor-C, with a gap of 59.3 µm, and sensor-B with an intermediate gap detected high conductivity comparable to sensor-A up to 20 h, but thereafter, it dropped rapidly. Localized corrosion occurred in the vicinity of the sensor-A. Thermodynamic consideration indicated that the high conductivity values corresponds to the acidification of the solution. Thus, corrosive environments were formed in crevice with small gaps and caused the localized corrosion.

Reference

Soma, Y. et al., In-Situ Measurement of Electrical Conductivity of Solution within Crevice of Stainless Steel in High Temperature and High Purity Water, Zairyo-to-Kankyo, vol.67, no.9, 2018, p.381–385 (in Japanese).

4-3 Origin of Am/Cm Selectivity Elucidated by Chemical Bonding

— Focusing on the Covalent Interaction between Metal Ions and Separation Ligands —

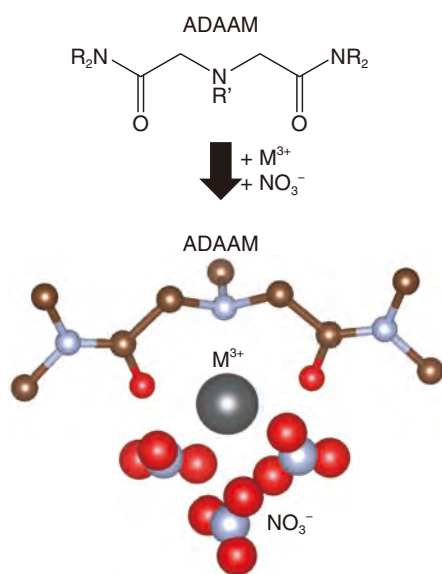


Fig.4-7 Structure of complex Am/Cm ion and an ADAAM separation ligand

Am and Cm ions (shown as metal ions) form a complex with one alkyldiamideamine (ADAAM) molecule and three nitrate ions. The lower picture shows the model complex including a metal ion, ADAAM, and nitrate ions.

To reduce the toxicity of high-level radioactive liquid waste (HLLW), the partitioning of minor actinides (MAs), which have extremely long half-lives, and the transmutation of short-life nuclides, partitioning and transmutation, has been developed. Although americium (Am) and curium (Cm) should be separated during partitioning due to the heat generating property of Cm, their similar chemical properties have made separation difficult. Therefore, We developed a process to selectively separate Am from Cm using alkyldiamideamine (ADAAM) as a separation ligand. Furthermore, the mechanism by which ADAAM shows higher selectivity of Am over Cm was clarified using a quantum chemical calculation.

Am and Cm exist as trivalent ions, Am^{3+} and Cm^{3+} , respectively, and form complexes with separation materials. The complex consisting of the metal ion (M^{3+}), nitrate ion (NO_3^-), and ADAAM was modeled as $[\text{M}(\text{ADAAM})(\text{NO}_3)_3]$ (Fig.4-7), by referring to the result of the previous separation experiment (*1, *2). The Gibbs energy difference on the formation of each complex was then calculated to indicate that the Am complex is more stable than the Cm complex. The calculated value of the separation factor of Am from Cm was 6.2 and reproduced the experimental value, 5.5.

The coordination bonds between the metal ion and ADAAM were then examined with the aim of understanding the higher observed Am selectivity. ADAAM forms bonds with the metal

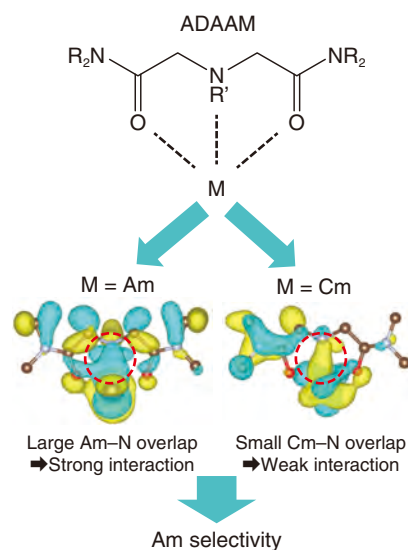


Fig.4-8 Interaction between Am/Cm ions and a molecular of ADAAM ligand

When analyzing the overlap of electron orbitals between the nitrogen atom of ADAAM and a metal ion (the red circle), the overlap between the Am ion and nitrogen atom is larger than that of the Cm ion and nitrogen atom, indicating a stronger interaction. This suggests that the difference in the interaction originates in the Am ion selectivity with ADAAM. The yellow and blue regions indicate the difference in the sign of phase in electrons as wave property.

ion using one amine nitrogen atom and two carbonyl oxygen atoms. Calculated result of coordination geometry revealed that the bond lengths between the metal ion and nitrogen atom of the ADAAM were 2.91 and 2.94 Å for the Am and Cm complexes, respectively. Furthermore, the covalent interactions of the coordination bonds were then analyzed by calculating the overlap of electron orbitals between the metal ion and nitrogen atom. The strength of the covalent interaction between atoms represents the degree of the overlap between electron orbitals. The overlap of the Am-N bond was larger than that of the Cm-N bond (Fig.4-8), thus indicating that the difference in the bonding strength between the metal ion and the ADAAM is a key to understand the Am/Cm selectivity. This work and future work on the selectivity in the separation of MAs is expected to contribute to the development of materials used for separating metal ions.

This work was supported by the Japan Society for the Promotion of Science (JSPS) KAKENHI Grant-in-Aid for Young Scientists (B) (No.17K14915).

*1 Sasaki, Y. et al., Extraction of Various Metal Ions from Nitric Acid to *n*-dodecane by Diglycolamide (DGA) Compounds, *Journal of Nuclear Science and Technology*, vol.44, no.3, 2007, p.405-409.

*2 Suzuki, H. et al., High-Performance Alkyl Diamide Amine and Water-soluble Diamide Ligand for Separating of Am (III) from Cm (III), *Analytical Sciences*, vol.33, issue 2, 2017, p.239-242.

Reference

Kaneko, M. et al., Theoretical Elucidation of Am(III)/Cm(III) Separation Mechanism with Diamide-Type Ligands Using Relativistic Density Functional Theory Calculation, *Inorganic Chemistry*, vol.57, issue 23, 2018, p.14513-14523.

4-4 Accurate Detection of Particles in Accelerators, Space, and Medicine

— Understanding the Mechanism that Determines the Scintillation Light Yields —

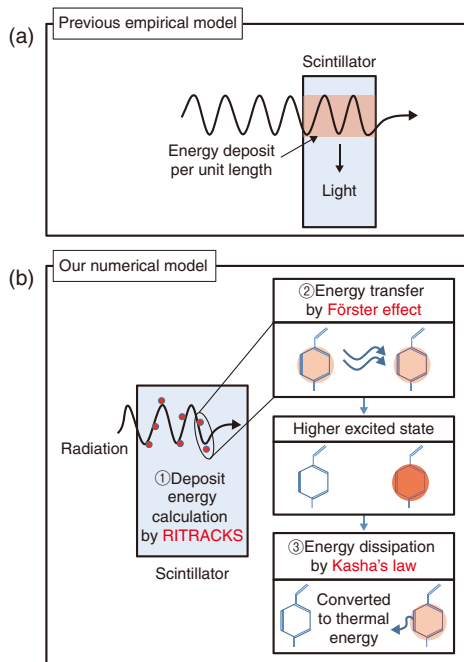


Fig.4-9 Schematic of the developed scintillation light yield prediction model

Unlike previous empirical models (a), the developed numerical model (b) considers the dissipation of energy deposition by the incident particle.

Scintillation detectors, which convert radiation to photons, are widely used to measure photons, neutrons, and their dose owing to their efficiency and low cost. Moreover, scintillation detectors can be used to measure the energy of radiation because the scintillation light yield is approximately proportional to the deposited energy. However, as the light yield from protons and ions, which are important for accelerators, space development, and medical applications, depends not only on the energy deposition but also on the particle species, the dose cannot be evaluated from the light yields alone. It is therefore necessary to clarify the relationship between the energy deposition and resulted light yields based on the scintillation light production mechanism.

Based on the assumption that the light yield suppression depends on the energy deposition and its topological arrangement, a numerical model composed of three procedures was developed, as shown in Fig.4-9(b): ① incoming radiation deposits its energy to the scintillator, ② deposited energy is transferred between the molecules, and ③ the transferred energy is dissipated as heat by the transition between excited states. In step ①, the spatial arrangement of the energy deposited by incoming radiation was

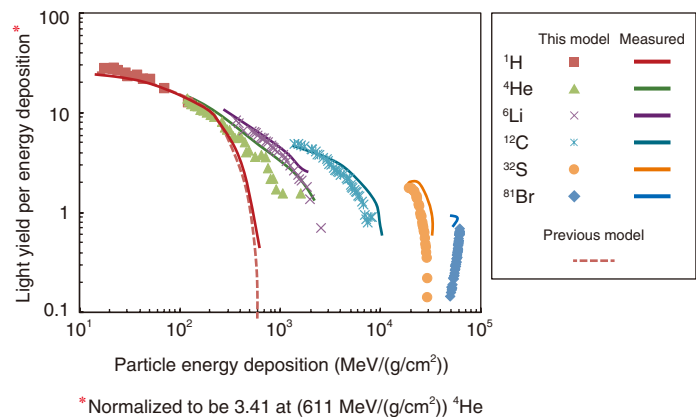


Fig.4-10 Light yield and energy deposited by ions

The developed model can more accurately reproduce the light yielded by heavy ions, in particular ${}^4\text{He}$ – ${}^{81}\text{Br}$ in this figure.

simulated using a track-structure calculation code RITRACKS, originally developed for radiation biology studies, taking into account the particle dependence of the energy deposition distribution. The energy transfer between the molecules in step ② was calculated based on the Förster resonance energy transfer. In step ③, the excitation energy given to a molecule more than once, which is often the case for heavy projectiles depositing energy in high density, was dissipated as heat, rather than light, in accordance with Kasha's law.

The developed numerical model was then applied to general-purpose scintillators to calculate the light yield by α -rays, β -rays, γ -rays, protons, and heavy ions. The calculated results, shown in Fig.4-10, agreed well with experimental data. Moreover, the mechanism that suppresses the light yield, particularly strong for protons and heavy ions, was explained by this model.

The developed model may be useful for scintillator-based detection of protons and heavy ions in accelerators, space development, and medical treatments, as well as for the development of new scintillation detectors, for example, which can specify the particle species and the energy based on the output of detector complex.

Reference

Ogawa, T. et al., Analysis of Scintillation Light Intensity by Microscopic Radiation Transport Calculation and Förster Quenching Model, PLOS ONE, vol.13, issue 8, 2018, p.e0202011-1–e0202011-19.

4-5 Evaluation of Exposure Doses Considering Variations in Physiques of Japanese — Completion of Adult Japanese Human Model Series —

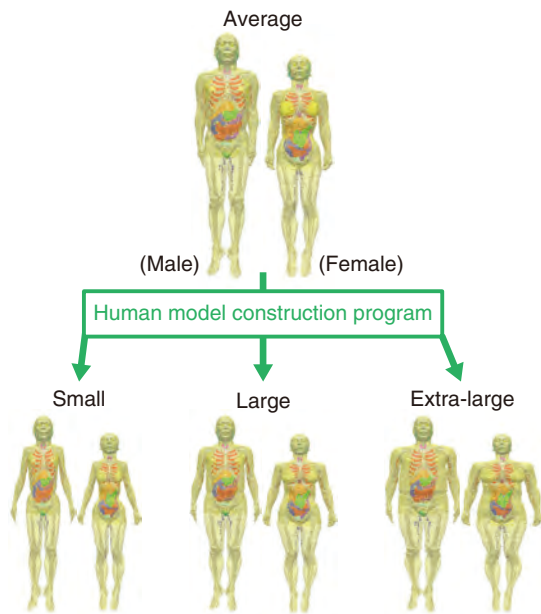


Fig.4-11 Construction of Japanese male (left) and female (right) models by using the developed human model construction program

The perimeters (e.g., chest), height and weight were used as input information to the developed program for constructing the human model series covering physique of most adult Japanese.

Exposure dose, which is an index indicating the effects of radiation on a human, is evaluated by the computer simulation. In computer simulation, the human model (model), which represent physiques and organ shapes of human on computer, are utilized. In dose assessment for medical exposures and epidemiological studies, the detailed exposure conditions have to be taken into account. Therefore, this study developed a practical construct technique for models capable of assessing exposure doses against Japanese with various physiques. The developed technique was then used to validate the applicability of the exposure dose to organs (organ dose) recommended by the International Commission on Radiological Protection (ICRP) to dose assessments for the purposes of radiation protection in Japan (e.g., operation plan preparation for radiation facilities).

In recent years, anatomical correct models were constructed by processing medical images of actual persons. Here, we devised a new technique for model construction. The devised technique enables us to numerically represent a human's body surface shape and to properly decide organ arrangement by using information about perimeters in body (e.g., chest), which is closely related to the body mass index (BMI). An automatic model construction program was thus developed by applying the devised technique. Thus, models with various physiques

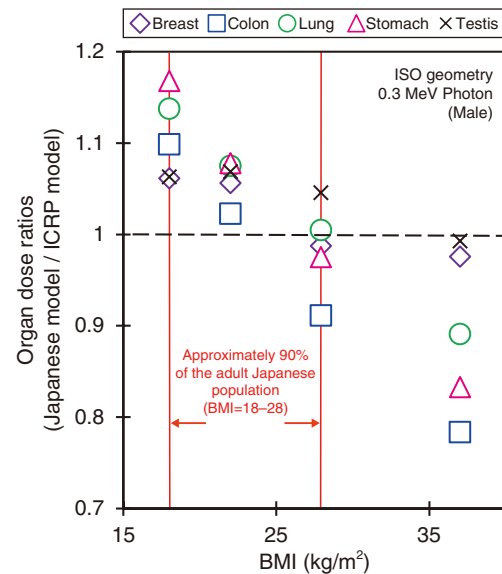


Fig.4-12 Comparison of organ doses due to external photon irradiation between Japanese models with various physiques (JM) and the average CM recommended by ICRP

Doses to the breast, colon, lung, stomach and testis, which are important for dose assessment, were analyzed.

can be easily constructed on the basis of average adult male and female Japanese models previously developed at JAEA in an extremely shorter period of time compared to conventional methods (Fig.4-11), without acquiring new medical images. A model series covering the physiques of most adult Japanese (JM) were constructed using the developed program.

We validated the applicability of the organ doses based on the average Caucasian model (CM) recommended by ICRP to Japanese for the radiation protection purposes. The organ doses to external photons using CM and JM under various irradiation geometries and energies were calculated and compared. The resulting organ doses for CM and JM at varying BMIs with an isotropic (ISO) geometry at an energy of 0.3 MeV are compared in Fig.4-12. ISO geometry approximates irradiation from a large cloud of radioactive gas to human. The resulting doses to the lung, stomach and colon varied depending on physiques due to the shielding effect of subcutaneous adipose and muscle tissues. However, the doses to most organs for the JM with physiques (BMI: 18–28) including about 90% of the adult Japanese population agreed with those for CM within 10%. Thus, the impact of physique variations of adult Japanese on dose assessment are limited, indicating that the organ doses provided by ICRP are applicable for external dose assessment for radiation protection purposes in Japan.

Reference

Sato, K. et al., Construction of Adult Japanese Voxel Phantoms with Various Body Sizes and Their Applications to Evaluation of Organ Doses Due to External Photon Irradiation, Japanese Journal of Health Physics, vol.52, no.4, 2017, p.247–258 (in Japanese).

4-6 Estimation of Fission Product in a Light Water Reactor under a Severe Accident — Development of Fission Product Chemistry Database ECUME —

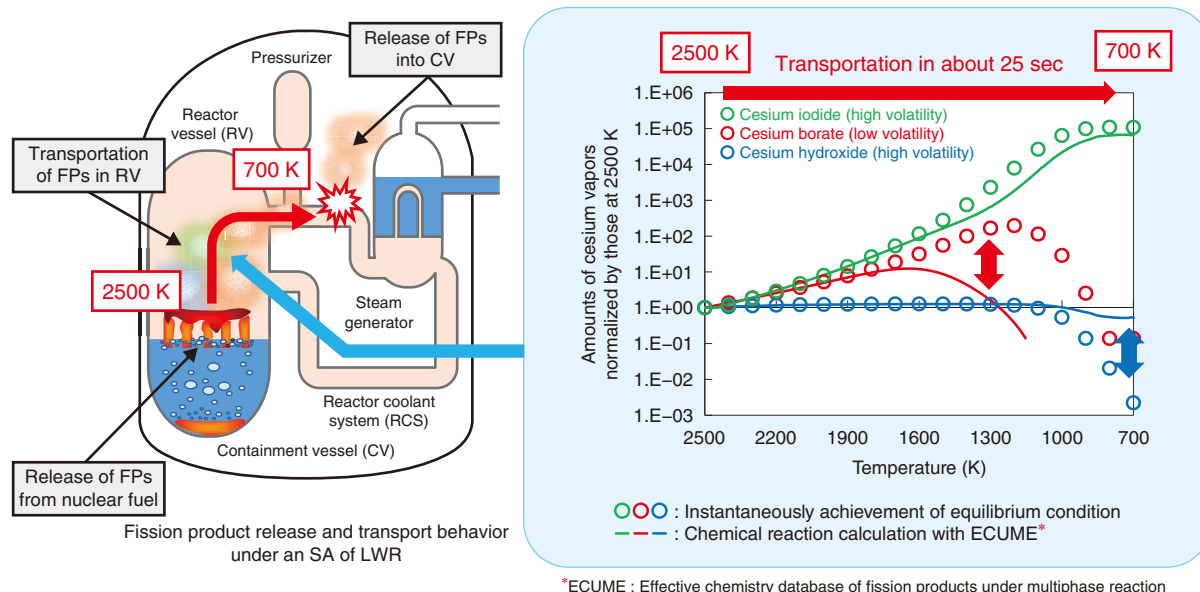


Fig.4-13 Amounts of cesium vapors transported to the lower temperature regions in a reactor under an SA calculated considering chemical reaction kinetics

A FP chemistry database named ECUME including cesium and iodine was developed to accurately estimate the chemistry of FPs under an SA based on chemical reaction kinetics. The amount of cesium vapors during transportation in a reactor under an SA were estimated by applying ECUME to chemical reaction calculation. Large discrepancies were seen between the amounts of cesium vapors obtained using ECUME and using chemical equilibrium calculations applied to the existing SA analysis codes. Thus, the release amount of cesium may be over- or under-estimated using the existing SA analysis codes; chemical reaction kinetics should rather be used to more accurately evaluate public exposure to FPs.

Fission products (FPs) are released from nuclear fuel and transported into the containment vessel and environment through the high-temperature regions of the reactor vessel (hereafter, FP release and transport behavior) under a severe accident (SA) in a light water reactor (LWR). To enhance LWR safety, public exposure should be evaluated more accurately through a detailed estimation of FP release and transport behavior under an SA. The FP release and transport behavior is significantly influenced by FP chemistry, namely the kinds of reactions that take place and the chemical forms of the FPs. However, some of the existing SA analysis codes assume that equilibrium is instantaneously achieved, meaning that chemical reactions are assumed to process at infinite rates. Thus, there is large uncertainties on FP chemistry in the lower temperature regions, where the chemical reaction kinetics becomes slower.

A database of chemical reaction rate constants was therefore developed to estimate the FP chemistry during an SA considering chemical reaction kinetics. The developed FP chemistry database, ECUME, includes elemental models and thermodynamic data in addition to the chemical reaction rate constants for more accurate estimation of the FP chemistry. The chemical system of cesium

and iodine was treated in ECUME due to their importance on public exposure to FPs under an SA. ECUME was the first documented database to include the data on boiling water reactor (BWR) control rod material boron which significantly affects the chemistry of cesium and iodine.

The amounts of cesium vapors during transportation from 2500 K to 700 K in a reactor under an SA were estimated using ECUME (Fig.4-13). The results were compared with those estimated using chemical equilibrium calculation applied to the existing SA analysis codes. Some vapors like cesium borate vapor showed large discrepancies between the data obtained by ECUME and those obtained by chemical equilibrium calculation. This indicates the possible over-estimation of low-volatile cesium borate deposits using the existing SA analysis codes, which can lead to the under-estimation of the amount of cesium released into the environment. Chemical reaction kinetics should thus be applied for more accurate evaluation of public exposure to FPs under an SA.

Future work will consist of experimentally validating ECUME, and expanding the ECUME to include other FPs like ruthenium to enhance the safety of reprocessing plants.

Reference

Miyahara, N., Miwa, S. et al., Chemical Reaction Kinetics Dataset of Cs-I-B-Mo-O-H System for Evaluation of Fission Product Chemistry under LWR Severe Accident Conditions, Journal of Nuclear Science and Technology, vol.56, issue 2, 2019, p.228–240.

4-7 Improving the Prediction Accuracy of Spallation Product Yields

— Improving a Stochastic Model of Nuclear Fission Induced by a High-Energy Particle —

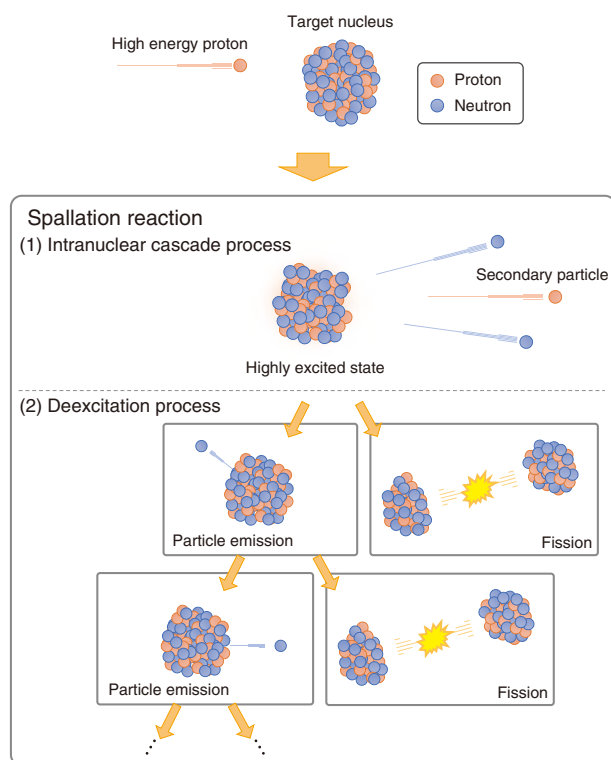


Fig.4-14 Competition between nuclear fission and particle emission in the spallation reaction

In the de-excitation process, a highly excited nucleus produced from the intranuclear cascade process releases its excitation energy by emitting particles or by undergoing fission.

When a target nucleus is bombarded with a high-energy particle, a spallation reaction occurs. From the perspective of a dynamic or temporal process, this reaction is divided into two processes: the intranuclear cascade and de-excitation processes (Fig.4-14). In the first process, i.e., the intranuclear process, neutrons and protons consisting of the target nucleus continuously interact and some are emitted from the nucleus. The remaining nucleus, which is in a highly excited and unstable state, then releases its excitation energy in the de-excitation process by emitting additional particles or by undergoing fission for heavy nuclei like lead and mercury. The nuclei or particles produced from these processes are referred to as spallation products.

Various spallation reaction models have been developed for the use of neutronic and shielding design of high-energy accelerator facilities such as J-PARC and ADS. However, their complicated theory for the de-excitation process has made

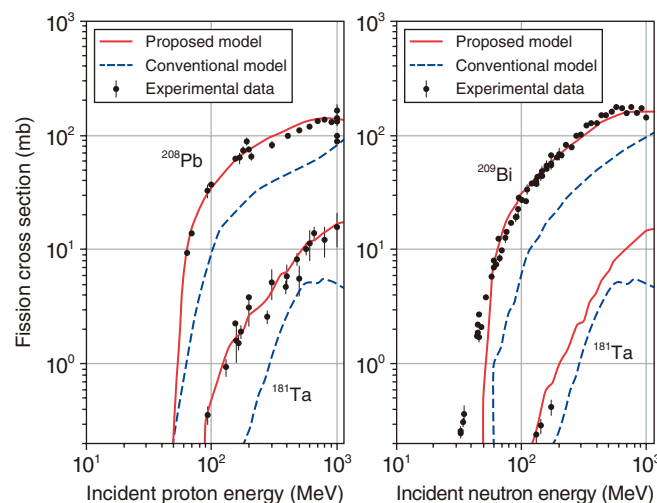


Fig.4-15 Comparison of fission cross sections

The fission probability is expressed as the fission cross section. The conventional model underestimates the experimental fission cross sections. The developed model predicts the fission cross sections for various incident energies and target nuclei with improved accuracy.

improving their prediction accuracy difficult. In particular, it has been pointed out that the conventional models underestimate the yield of the spallation products produced from the fission reaction.

This work has thus aimed to model the probability of fission induced by the spallation reaction. The fission probability was described using a simpler, systematic expression, and then confirmed to predict fission cross sections for various incident energies and target nuclei with about quintuple accuracy, as demonstrated in Fig.4-15.

Future work will aim to further improve spallation reaction modeling, focusing on the spallation products produced from other mechanisms such as neutron evaporation.

This work was supported by the Japan Society for the Promotion of Science (JSPS) KAKENHI Grant-in-Aid for Young Scientists (B) (No.17K14916).

Reference

Iwamoto, H. et al., Unified Description of the Fission Probability for Highly Excited Nuclei, Journal of Nuclear Science and Technology, vol.56, issue 2, 2019, p.160–171.

Contributions to Developments in Science, Technology, and Academic Research Using Neutron and Synchrotron Radiation

In accordance with the Science and Technology Basic Plan formulated by the Government of Japan, we have aimed to contribute to the advancement of science and technology and the promotion of industry in Japan through researching using neutron and synchrotron radiation. This has included using the high-intensity proton accelerator at the Japan Proton Accelerator Research Complex (J-PARC) and the JAEA synchrotron-radiation beamlines at the Super Photon ring-8 GeV (SPRING-8), as well as upgrading neutron facilities and devices and pursuing world-leading research in the fields of nuclear energy and materials sciences using neutron and synchrotron radiation.

(1) Research and development at J-PARC

J-PARC, shown in Fig.5-1, is comprised of three proton accelerators, including a linear accelerator (LINAC), 3-GeV rapid cycling synchrotron (RCS), and 50-GeV synchrotron, and three experimental facilities. These facilities include the Materials and Life Science Experimental Facility (MLF), where research is performed over a wide range of fields using neutron and/or muon beams, the Hadron Experimental Facility, where nuclear and particle physics experiments using K-mesons and other particles are conducted, and the Neutrino Experimental Facility, where experimental work on T2K particle physics using neutrinos are performed. Each of these experimental facilities is open to users from across the globe.



Fig.5-1 Japan Proton Accelerator Research Complex

Successive tests and component improvements have been conducted to realize stable operation of the accelerators with a beam of 1 MW. In Linac, a radio frequency (RF)-driven negative hydrogen ion (H^-) source was developed. To increase the intensity of the beam current and operation time of the ion source, an H^- beam with a peak current of 72 mA was injected into the Linac. The antenna damage rate was reduced to less than one-third by extending the life of radio frequency antennas (Topic 5-1).

The mechanism of beam loss in the RCS was determined via experimental and modeling work, a solution was then introduced. In FY2018 at the MLF, a user program for eight scheduled run cycles (176 days) was successfully implemented with an availability of over 90%, and a continuous 1-MW beam operation was achieved. Also at the MLF, 20 neutron spectrometers and 2 muon instruments were operated, and a wide range of experiments related to materials and life science were conducted. With the BL01 Four Seasons, the effect of electron correlation on spin fluctuation in the magnetic excitation structure of an iron-based superconductor has been investigated.

As a result, observations and a theoretical interpretation of the spin fluctuation in the very high energy range of approximately 200 meV was successfully conducted (Topic 5-2). Additionally, a bump cathode for a 2d neutron detector with high detection efficiency and high resolution has been developed to utilize a high intensity pulsed neutron beam effectively (Topic 5-3). Furthermore, the design of a spallation neutron source was evaluated. The neutron flux was also measured and the ortho-para conversion characteristics of molecular hydrogen was evaluated for future improvements (Topic 5-4).

This research will help further the efforts to continue improving J-PARC and the research and development of this next-generation experimental facility.

(2) Research and development at the Materials Sciences Research Center (MSRC)

MSRC aims to create innovative results and seed research in a wide range of scientific, technological, and academic fields by developing and improving neutron and synchrotron-radiation instruments for advanced structural and functional analysis in Tokai (JRR-3 and J-PARC) and in Harima (SPRING-8).

In FY2018, EuPtSi was observed to form a special particle-like topologically non-trivial spin texture called “magnetic skyrmion” under the US – Japan Cooperative Program on Neutron Scattering. This represented the first observation of the magnetic skyrmion lattice in a 4f electron compound (Topic 5-5). This discovery provided new directions to explore other compounds and unveiled other characteristics of skyrmions.

Additionally, the microstructural formation mechanism of a pearlitic steel was elucidated using an electron scanning microscope (SEM), electron backscatter diffraction (EBSD), and neutron diffraction techniques (Topic 5-6). This information is expected to accelerate the development of high-performance steels. This research was supported by the Japan Science and Technology Agency (JST) under Collaborative Research based on Industrial Demand “Heterogeneous Structure Control: Towards Innovative Development of Metallic Structural Materials”, and done in collaboration with the Tokyo Institute of Technology, NIPPON STEEL & SUMITOMO METAL CORPORATION, and JAEA.

The laser coating of a metal on a dissimilar metal substrate was observed by synchrotron radiation imaging using a time resolution of 1 ms at the SPRING-8 (Topic 5-7). Optimal conditions for laser coating were then determined by in-situ observations of the melting and solidification phenomena. As Japan lacks extensive natural resources, developing recycling technologies of useful minor metals, i.e., urban mining, is essential. A new compound capable of forming complexes with lanthanides, individual elements which are difficult to separate, was developed and contributes to the establishment of separation and recycling techniques of lanthanides on the basis of structure analysis by X-rays (Topic 5-8).

5-1 Long-Term, Stable Production of a High-Intensity and High-Quality Beam — Development of an RF-Driven Negative Hydrogen Ion Source —

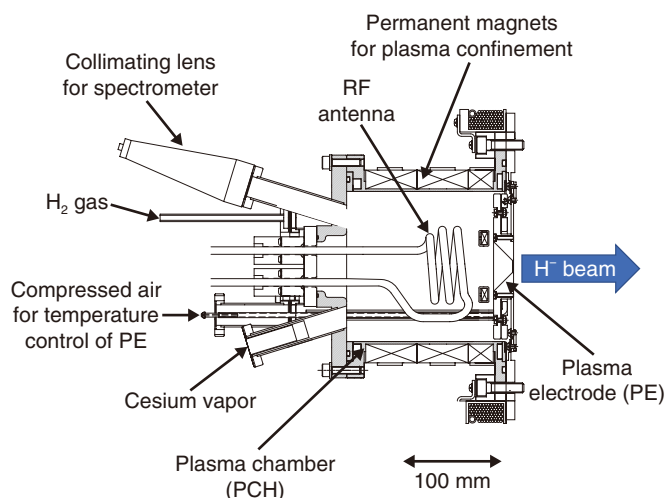


Fig.5-2 A cross-sectional view of the cesiated radio frequency (RF)-driven H^- ion source

Hydrogen plasma is produced by RF power using an RF antenna installed in the plasma chamber. The H^- ions produced on the plasma electrode surface are enhanced by introducing cesium vapor into the chamber.

A stable negative hydrogen ion (H^-) beam with a beam current, pulse length, and repetition of 60 mA, 0.5 ms, and 25 Hz, respectively, was required to deliver a world-class beam with a beam power of 1 MW to the Materials and Life Science Experimental Facility (MLF).

Until 2014, H^- beams were produced using a hot-cathode-type H^- ion source, in which a hydrogen plasma is generated by energetic electrons emitted from a hot cathode. However, this ion source produced an H^- beam with a maximum beam current of 17 mA and a maximum continuous operation time of approximately 1200 h. It was thus aimed to develop a radio-frequency-driven H^- ion source (RF-IS) to obtain a higher current and longer operational time. A schematic of the J-PARC RF-IS is shown in Fig.5-2.

In the RF-IS, cesium vapor is introduced into the plasma chamber (PCH) to enhance the H^- ions produced on the surface of the plasma electrode (PE), which is applied to -50 kV to extract the H^- beam. The PE had a 45° tapered structure to produce the H^- ions effectively and the PE temperature was

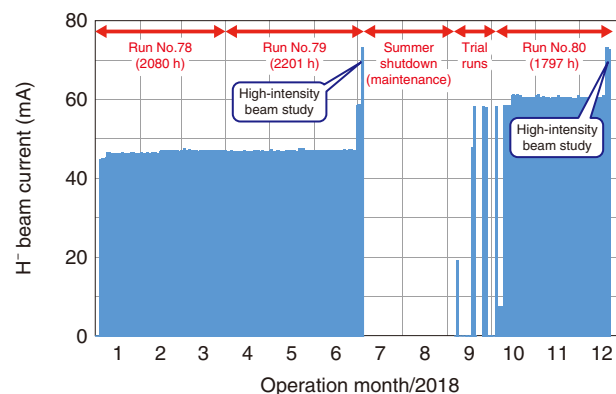


Fig.5-3 Operational history of the cesiated RF-driven H^- ion source

The H^- beam current extracted from the RF-driven H^- ion source was adjusted according to the requirements of the J-PARC users. A continuous operation time of approximately 2200 h was achieved from April to July. The H^- ion source produced an H^- beam with a beam current of 72 mA in the high-intensity beam study.

controlled to optimize the cesium evaporation on the surface. As a result, the H^- beam with a maximum beam current of 72 mA was injected into the linac.

The RF-IS had a problem of lifetime due to the damage of the RF antenna. We considered that the antenna failure is caused by the antenna surface breaking due to the collision of heavy ions in the PCH. As a result of removing impurities adhering to the inner wall of the PCH by repeating short time plasma generation and evacuation several times before beam operation (pre-conditioning), the antenna failure rate was succeeded in reducing less than one-third. Establishing this pre-conditioning method extended the lifetime of the antenna, and made great progress in the practical application of the RF-IS.

Operational history of the H^- beam current extracted from the RF-IS is shown in Fig.5-3. Continuous operation for 2201 h was achieved from April to July. In July, the RF-IS was succeeded in supplying the beam for one hour at a 1-MW demonstration test of the MLF. Since autumn, the RF-IS has been supplying the H^- beam to the linac with a beam current of 60 mA.

Reference

Shinto, K. et al., Progress of the J-PARC Cesium RF-Driven Negative Hydrogen Ion Source, AIP Conference Proceedings, vol.2052, 2018, p.050002-1–050002-7.

5-2 Linking Spin-Fluctuations to Electron Correlations

— A Combined Neutron and ARPES Study —

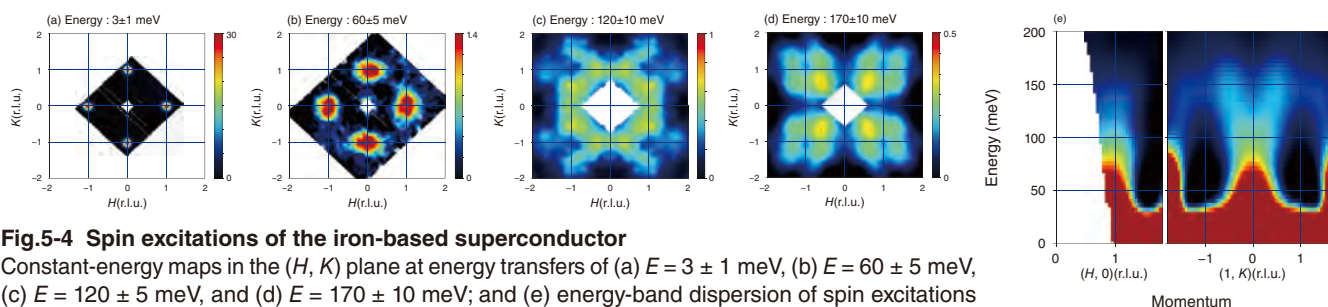


Fig.5-4 Spin excitations of the iron-based superconductor

Constant-energy maps in the (H, K) plane at energy transfers of (a) $E = 3 \pm 1$ meV, (b) $E = 60 \pm 5$ meV, (c) $E = 120 \pm 5$ meV, and (d) $E = 170 \pm 10$ meV; and (e) energy-band dispersion of spin excitations along the $(1, K)$ high-symmetry direction.

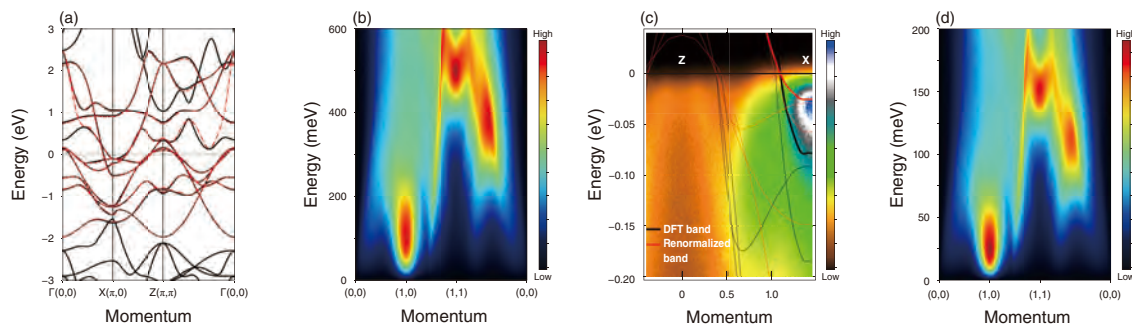


Fig.5-5 First-principles analysis of the spin excitation spectrum

(a) Electronic band structure of the iron-based superconductor obtained by first-principle calculations. (b) Spin excitation spectrum calculated using the model in Fig.5-5(a). (c) Comparison between ARPES and first-principles calculations. The black and red lines denote the original and renormalized bands, respectively. (d) Spin excitation spectrum calculated using the renormalized band structure.

The surprising discovery of high- T_c superconductivity in iron-based superconductors (FeSCs) has marked the beginning of a new era in superconductivity research. Earlier studies have suggested that FeSCs are weakly correlated materials, unlike cuprate superconductors, in which Mott physics is more fundamentally tied to superconductivity. However, increasing evidence suggests that electron correlations in FeSCs are much stronger than previously thought. The role of electron correlations is therefore the most interesting, yet not well understood, aspect of the physics in FeSCs.

Inelastic neutron scattering (INS) was used to study the effect of electron correlations on spin dynamics in FeSCs. INS measurements were performed using the BL01 4SEASONS installed at J-PARC. As seen in Fig.5-4, well-defined spin excitations were observed up to high-energy transfers of at least 200 meV.

To understand the obtained INS data, a first-principles analysis of the spin excitation spectrum was performed (Figs.5-5(a) and (b)). This analysis reproduced the spin-wave-like dispersive feature along the high-symmetry directions, but overestimated the energy scale of the excitations by a factor of three.

This overestimation of the spin excitation energy has important implications for the electronic state of FeSCs. In general, the electronic band structure determines the momentum- and energy-dependent structure of the spin excitation spectrum. The discrepancy between the experimental and theoretical spin excitations, therefore, suggests that the actual electronic structure of FeSCs deviates from that predicted from first-

principles calculations.

To gain more insight into the electronic structure, angle-resolved photoemission spectroscopy (ARPES) was then performed on crystals from the same batch as was used for the INS measurements. From the ARPES data shown in Fig.5-5(c), one can notice that the experimental band structure displays a narrowing of the Fe-3d bands by a factor of three. This narrowing corresponds to an enhancement of the effective mass due to electron correlation effects.

Considering the strong sensitivity of the spin excitations to the underlying electronic structure, one can expect that the Fe-3d bandwidth narrowing due to electron correlations is directly reflected in the spin excitation energy scale. To confirm this, we re-evaluated the spin excitation spectrum by incorporating the effect of mass enhancement. As shown in Fig.5-5(d), the spin excitation bandwidth was reduced to approximately one third of its original width, yielding a broadly consistent description of the observed INS data.

The consistency between the results of the two momentum-resolved spectroscopic methods, INS and ARPES, demonstrates a quantitative link between the magnetic response and the underlying electronic structure of FeSCs, thus indicating that INS may be used as a momentum-resolved spectroscopy for determining the correlated electronic structure. The availability of more intense neutron sources in the next few years would further improve the potential of INS as a versatile and practical spectroscopic technique to investigate the electronic and magnetic structures on an equal footing.

Reference

Murai, N. et al., Effect of Electron Correlations on Spin Excitation Bandwidth in $\text{Ba}_{0.75}\text{K}_{0.25}\text{Fe}_2\text{As}_2$ as Seen via Time-of-Flight Inelastic Neutron Scattering, *Physical Review B*, vol.97, issue 24, 2018, p.241112-1–241112-6.

5-3 Two-Dimensional Neutron Measurement with High Sensitivity and High Precision — Development of a Bump Cathode Neutron Detection Element —

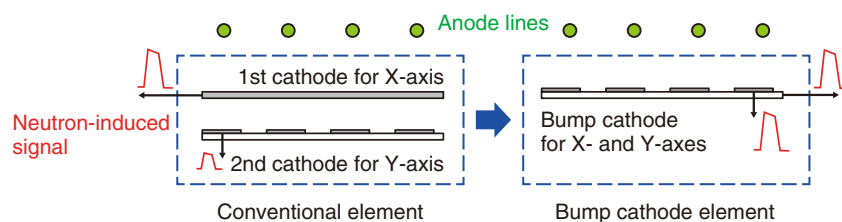


Fig.5-6 Schematic sectional view of conventional and bump cathode elements

A neutron-induced signal measured at the second cathode was reduced in a conventional element. In the bump cathode element, the neutron-induced signals of both axes are approximately equal because of the simple structure; the cathodes for the x- and y-axes are arranged on a single-layer substrate.

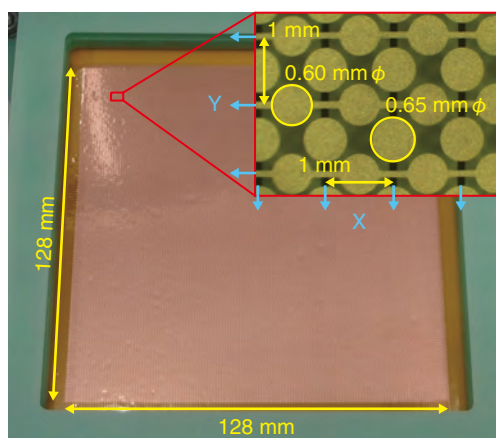


Fig.5-7 Whole and partially magnified photograph of the developed bump cathode element

The neutron sensitive area is 128 × 128 mm. The element has two types of circular bumps arranged in a triangular shape that are linked together in the x- and y-directions for the detection of incident neutrons.

A bump cathode element was developed for a two-dimensional detector system. A schematic sectional view of a conventional and proposed element is shown in Fig.5-6. The former consists of two-layer cathodes for both the x- and y-axes. The neutron-induced signals of the developed element differ based on the distance from the anode lines. The cathodes of the developed element are arranged on a single-layer substrate using printed circuit board technology. The intensity of the neutron-induced signals of both axes were approximately equal in the developed element because of its single-layer structure.

In the gaseous neutron detector used in the neutron scattering experiment, the gas pressure should be increased to obtain a high detection efficiency. However, increasing the gas pressure causes the neutron-induced signal to decrease. The developed neutron detection system employs an individual readout method for a short response and high spatial resolution; this method divides the neutron signal into several cathode lines. To measure the decreased amount of neutron-induced signals with high precision and long-term stability, the collection efficiency of neutron signals must be increased. Therefore, a bump cathode element with a single-layer cathode structure was developed to enable a more efficient collection of neutron signals than found in a conventional two-layer element.

A complete and partially magnified photograph of the

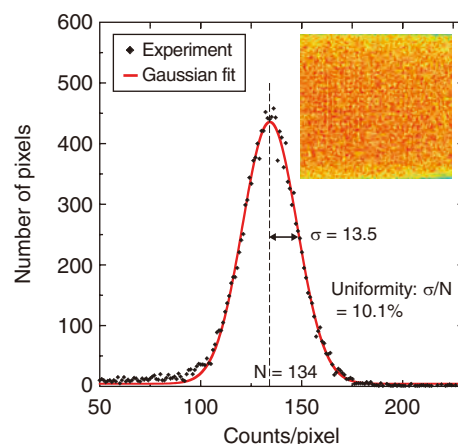


Fig.5-8 Spatial homogeneity of the detector element measured using neutrons

A neutron-induced flat-field image was obtained to confirm spatial uniformity. The warm color in the flat-field image exhibits high counts. A histogram of the pixel content was evaluated by a Gaussian fit and showed an excellent homogeneity with an average count spread of 10.1%.

developed element is shown in Fig.5-7, where the neutron sensitive area of the developed element is 128 × 128 mm with a pitch of 1 mm in both directions. The developed element consists of a polyimide substrate and two types of circular bumps with diameters of 0.6 and 0.65 mm that are arranged in a triangular shape on the surface of the substrate and are linked together in the x- and y- directions for the individual signal line readout. Neutron irradiation experiments were then performed using the developed bump cathode element. The developed element exhibited an excellent uniformity of 10.1% throughout all of the pixels, as seen in Fig.5-8, exhibiting a full width at half maximum intrinsic spatial error of 1.89 mm and a thermal neutron detection efficiency of 82%. The neutron-induced signal is generally measured by applying voltage to the detector element, though a higher voltage causes discharge degradation to the element. The voltage applied to the developed element could be lower than that applied to a conventional element because of the efficient collection of neutron signals.

The developed element will enable the improvement of high-performance neutron detectors with high precision and long-term stability that make effective use of high intensity pulsed neutrons at J-PARC. The developed element is available as a fundamental technology of various gas-based neutron detectors.

Reference

Toh, K. et al., Development of a Bump Cathode Element for Two-Dimensional Neutron Detection, Journal of Instrumentation, vol.12, 2017, p.C12011-1–C12011-8.

5-4 Measuring the Neutron Brightness Distribution from Liquid Hydrogen Moderators

— Measuring and Validating the Neutron Brightness Distribution from Liquid Hydrogen Moderators at a High-Intensity Spallation Neutron Source —

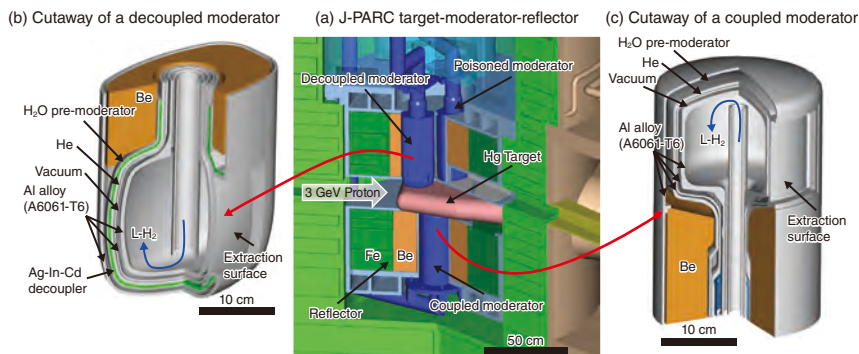


Fig.5-9 Core of high-intensity spallation neutron source
(a) Target-moderator-reflector assembly, (b) decoupled moderator, and (c) coupled moderator.

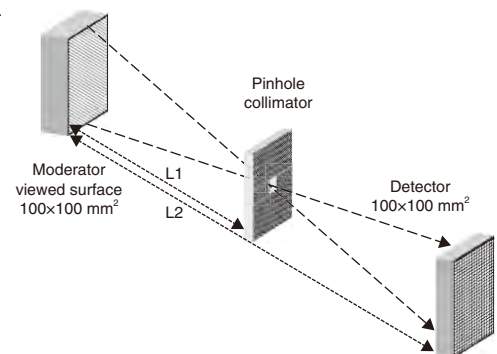


Fig.5-10 Method to measure neutron brightness on a moderator surface with pinhole collimator
i.e., inverse brightness mapping.

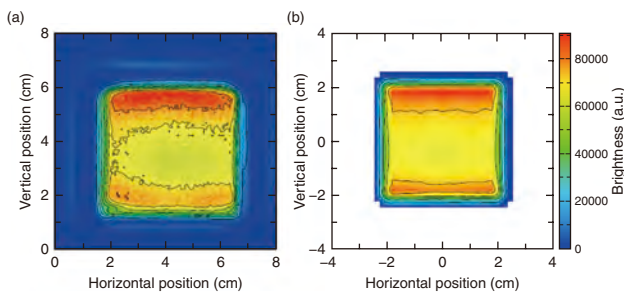


Fig.5-11 Brightness distribution on a coupled moderator surface (5–10 meV)
(a) Measured and (b) calculated

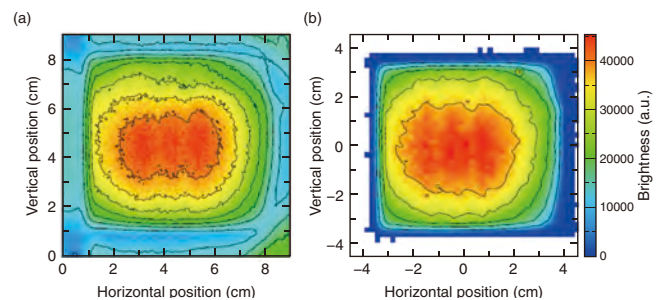


Fig.5-12 Brightness distribution on a decoupled moderator surface (5–10 meV)
(a) Measured and (b) calculated

At the spallation neutron source in the J-PARC, a high-intensity pulsed proton beam induces a mercury target to provide pulsed neutron beams to neutron experiment instruments. To enhance cold neutron beams, the neutron source has beryllium-iron reflectors and liquid hydrogen moderators (Fig.5-9). The liquid moderators, operated at 20 K, are composed of a coupled moderator to provide an intense neutron beam and two decoupled moderators to provide sharp neutron beams. The decoupled moderators are surrounded by neutron absorbing materials to sharpen the pulse shapes with a sacrifice of intensity. The neutron source was designed by a particle transport simulation code to optimize the neutron pulse characteristics while retaining heat removal, structural design integrity, and radiation damage control, to pay attention to para-hydrogen characteristics as the moderator material. The pulse characteristics used by the para-hydrogen successfully demonstrated neutron brightness distribution on a moderator surface. Therefore, a measurement

of the brightness on the moderators was done for a validation to the simulation. The brightness on a moderator surface was measured with a pinhole collimator, which provides an inversed image, as shown in Fig.5-10.

The measured (a) and calculated (b) neutron brightness in the energy region from 5 meV to 10 meV are shown in Figs.5-11 and 5-12 on a coupled and decoupled moderator surface, respectively. The measured and calculated results were in good agreement, and a higher intensity was seen on the coupled surface at the edge than at the center. In the decoupled surface, a higher intensity was observed at the center than that at the edge, also in good agreement with the experimental results.

Overall, the developed particle transport model and the accuracy of the designs was shown to accurately predict neutron brightness. By utilization of these knowledges, future works will aim to upgrade of the neutron source and development of a new neutron source.

Reference

Harada, M. et al., Experimental Validation of the Brightness Distribution on the Surfaces of Coupled and Decoupled Moderators Composed of 99.8% Parahydrogen at the J-PARC Pulsed Spallation Neutron Source, Nuclear Instruments and Methods in Physics Research Section A, vol.903, 2018, p.38–45.

5-5 Capturing of a Unique Spin Texture of a 4f Electron

—Discovery of a Magnetic Skyrmion Lattice in the 4f Electron Magnet EuPtSi—

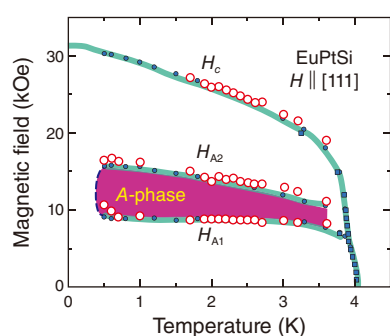


Fig.5-13 Magnetic phase diagram of EuPtSi

A field-induced A-phase only exists at a finite temperature and magnetic field.

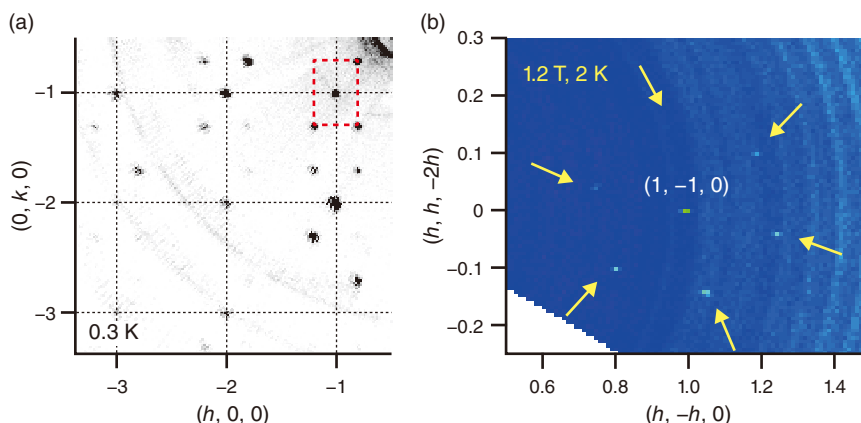


Fig.5-14 Neutron scattering intensity map of EuPtSi (a) at zero field, (b) 1.2 T

The rectangular magnetic scattering pattern found at zero field changes into a characteristic hexagon in the plane normal to the applied field when the system enters the A phase.

Magnetic skyrmions are particle-like, topologically non-trivial spin textures that have attracted interest in fundamental aspects as well as applications due to their potential as a low-power-consumption device. A magnetic skyrmion formation was first identified in a chiral magnet MnSi. This discovery has triggered an intensive search for compounds with similar crystal structures, leading to the discovery of their existence in MnGe, FeGe, and insulator Cu₂OSeO₃. A variety of characteristic properties have been unveiled as the number of skyrmion compounds has increased. Unlike this diversity, magnetic ions have been mostly limited to 3d transition metal elements.

Recently, high-quality single crystals of the 4f electron compound EuPtSi have been grown to have a similar crystal structure. In EuPtSi, seven 4f electrons carry magnetism. This compound exhibits an antiferromagnetic transition at 4 K at a zero magnetic field. Characteristic features emerged under magnetic fields, including a field-induced phase, i.e., the A phase, which appeared only at a finite temperature and magnetic field, as shown in Fig.5-13. This feature, common to the skyrmion phase of MnSi, implies the existence of a magnetic skyrmion in EuPtSi. To clarify the nature of the A phase, single-crystal neutron diffraction experiments were carried out under a magnetic field.

Neutron diffraction is a powerful probe to determine the spin arrangement under an extreme environment, such as low temperature and a magnetic field. Experiments were performed using the Wide-Angle Neutron Diffractometer (WAND²) installed at the High Flux Isotope Reactor (HFIR) in Oak Ridge National Laboratory (ORNL), U.S.A. and SENJU located at BL18 in the Materials Life Science Facility (MLF), J-PARC.

The formation of a magnetic skyrmion lattice in MnSi was evidenced by small-angle neutron scattering via an observation of six-fold magnetic diffraction patterns in the plane normal to the applied field. In EuPtSi, the magnetic structure at a zero field was helical, characterized by a rectangular form as displayed in Fig.5-14. By applying a magnetic field, the diffraction pattern exhibited substantial change when the system enters the A phase; the rectangular pattern at the zero field changed into a six-fold pattern in the plane normal to the field. Thus, the pattern common to the skyrmion phase was demonstrated.

This work revealed that magnetic diffraction pattern of EuPtSi has similar characteristics to the archetypical skyrmion lattice magnet MnSi, suggesting a formation of skyrmion lattice in EuPtSi. However, marked differences were seen. The periodicity in MnSi is quite long, requiring small-angle neutron scattering to separate magnetic and nuclear peaks, whereas the standard diffraction is sufficient to reveal magnetic patterns in EuPtSi owing to its shorter periodic length: 18 versus 1.8 nm in MnSi and EuPtSi, respectively. In addition, the A phase in EuPtSi was stabilized over a relatively wide temperature range, whereas that of MnSi exists over only a narrow region in close proximity to the transition temperature. Overall, the discovery of a magnetic skyrmion phase in 4f electron systems has provided a new direction to explore another compounds and has unveiled more characteristics of skyrmions.

This work was performed under the US–Japan Cooperative Program on Neutron Scattering, and supported by the Japan Society for the Promotion of Science (JSPS) KAKENHI Grant-in-Aid for Scientific Research (C) (No.16K05031).

Reference

Kaneko, K. et al., Unique Helical Magnetic Order and Field-Induced Phase in Trillium Lattice Antiferromagnet EuPtSi, Journal of the Physical Society of Japan, vol.88, issue 1, 2019, p.013702-1–013702-5.

5-6 Towards Higher-Performance Steels

— Elucidating the Microstructural Formation Mechanism via Electron and Neutron Beams —

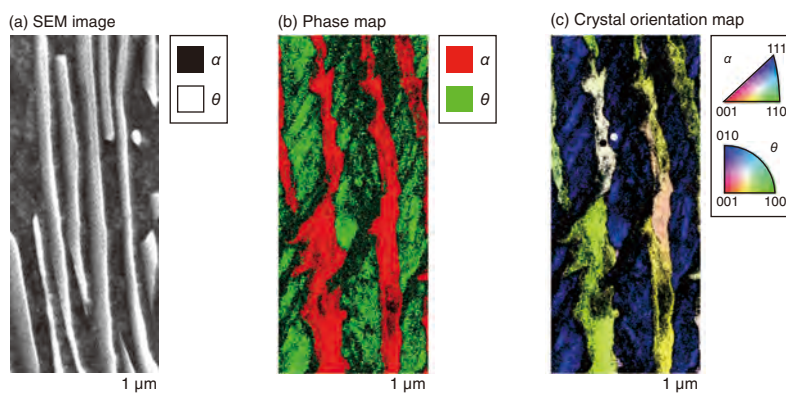


Fig.5-15 Microstructural characteristics of pearlitic steel

(a) SEM imaging of pearlitic steel, where the lamellar structure consists of α (black) and θ phases (white). (b) Phase map of the pearlitic steel obtained by the EBSD method, where the α (red) and θ (green) crystal phases are identified in the pearlite structure. (c) Crystallographic orientation distribution map of the α and θ phases in the pearlitic steel obtained by the EBSD method.

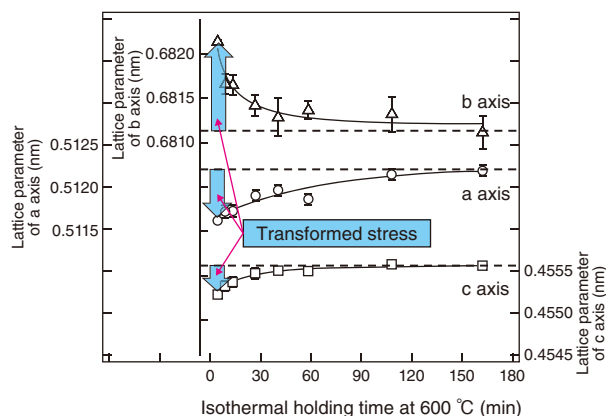


Fig.5-16 Evolution of the lattice parameter of pearlitic steel during isothermal holding

In-situ neutron diffraction confirmed the continuous evolution for the crystal cell structure of the α phase during isothermal holding. The curved and dashed lines correspond to the real-time changing structure parameters and the final structure parameters after holding for 180 min, respectively. The weakening deviations from the final structure parameters marked with dashed lines showed the transformed stress in the pearlite structure was gradually relieved.

Steel is a kind of important structural material which is indispensable for our daily lives and presents in a variety of places, from ordinary office items to social infrastructure including long-span bridges and ultrahigh-rise buildings. The strength and ductility of steels can be controlled by optimizing the microstructural parameters including the grain size and crystal morphology. It is therefore valuable to elucidate the microstructure formation mechanism to develop higher-performance steels with high fracture resistance and good manufacturing capacity, which are highly expected for the continuous development of large social infrastructure, such as ultrahigh-rise buildings. Here, the microstructural formation mechanism of a pearlitic steel was investigated using an electron scanning microscope (SEM), electron backscatter diffraction (EBSD), and neutron diffraction.

Pearlitic steel has a lamellar microstructure, consisting of a body-centered cubic crystal structure (α phase) and a simple rectangular crystal structure (θ phase), as shown in Fig.5-15(a). The phase identification and crystal orientation maps of this steel were evaluated using EBSD. The obtained constituent phase and crystal orientation maps of the pearlitic steel are shown in Figs.5-15(b) and (c), respectively. In general, a crystal grain only shows a crystal orientation (mono color) like a single crystal. However, with a lamellar structure, the color label

corresponds to a gradient change in the crystal orientation. Here, a large shift in the crystal orientation was confirmed in the α phase.

A neutron diffraction experiment was then performed using the TAKUMI (Beamline No.19), a high-resolution, high-intensity time-of-flight (TOF) neutron diffractometer at the Materials and Life Science Experimental Facility (MLF) of J-PARC. The evolution of the triaxial crystal cell parameters of the θ phase after the pearlite transformation is shown in Fig.5-16 as a function of the isothermal holding time at 600 °C. The cell structure parameters along crystal axes a, b, and c of the rectangular crystal structure of θ phase changes with increasing isothermal holding time. This indicates that the stress that occurred during the pearlite formation (Fig.5-15(c)) was gradually released over a long isothermal holding treatment.

Hence, this stress is suggested to have an important influence on the microstructural formation of pearlitic steels. Such information is valuable in developing higher-performance steels.

This research was supported by the Japan Science and Technology Agency (JST) under collaborative research based on Industrial Demand “Heterogeneous Structure Control: Towards Innovative Development of Metallic Structural Materials”, and collaborated on with the Tokyo Institute of Technology, NIPPON STEEL & SUMITOMO METAL CORPORATION, and JAEA.

Reference

Amemiya, Y., Morooka, S. et al., Dynamic Accommodation of Internal Stress and Selection of Crystallographic Orientation Relationship in Pearlite, *Tetsu-to-Hagane*, vol.105, no.2, 2019, p.314–323 (in Japanese).

5-7 Successful Observation of the Melting and Solidification Phenomena of Metal with a Time Resolution of One Millisecond — Contributing to the Advancement of Laser Welding Technology —

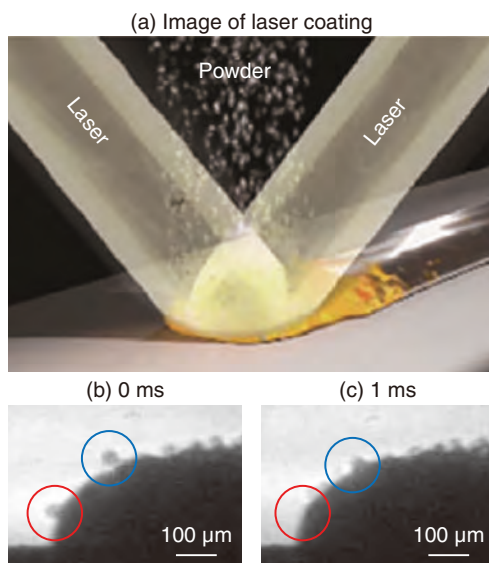


Fig.5-17 (a) Laser coating schematic; state near the tip at (b) 0 and (c) 1 ms as measured by a synchrotron radiation transmitted imaging method

In (c), the metal powder in the red circled area has been absorbed, and the metal powder in the blue circled area is being absorbed.

Laser coating is a welding technology that uses a laser to coat dissimilar metals on a metal substrate, making it possible to add characteristics to the metal substrate (e.g., hardness, heat conduction, or electricity conduction). It thus can be expected to contribute to the development of higher-strength, longer-life, lighter-weight, lower-cost, and more energy-efficient next-generation industrial parts and products.

During laser coating, as shown in Fig.5-17(a), the metal powder to be coated is sprayed towards the substrate and changes from a solid to a liquid state when passing through a laser that is obliquely irradiated near the substrate. When this liquid metal powder collides with the substrate or the molten pool formed by liquid metal powder, a metal film is formed on the substrate.

The practical application of laser coating must overcome difficulties such as controlling the coating thickness, reducing defects such as voids, minimizing distortion. To solve these problems, it is necessary to observe in high-time resolution imaging.

In this study, metal spheres were observed to form a film coating during laser coating using synchrotron radiation imaging at BL22XU in SPring-8. A metal powder that was scattered from the sky and received laser irradiation adhered to the vicinity of the coating tip (Fig.5-17(b)). After 1 millisecond, the metal

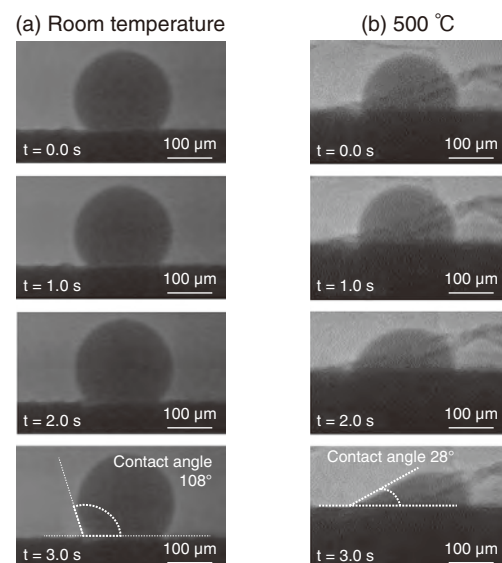


Fig.5-18 State of the titanium powder during laser irradiation

(a) The titanium powder remained nearly spherical regardless of the laser irradiation when the stainless steel substrate was held room temperature; however, (b) at a substrate temperature of 500 °C, the titanium powder spread over the substrate.

powder was absorbed by the coating film; some metal powder sprayed further from the tip was partially absorbed by the coating film (Fig.5-17(c)). This dependency on position may have been caused by a higher film temperature at the tip, causing more wetting effect.

Fig.5-18 shows the result of in-situ X-ray imaging of a 0.2 mm titanium sphere under laser irradiation. The substrate temperature differed between (a) and (b), although all measurements were performed in a vacuum. The titanium powder placed on the substrate at room temperature showed little change even after laser irradiation for 3 seconds. However, when the temperature of the substrate was 500 °C, the powder melted and spread over the substrate with time. Thus, a higher substrate temperature leads to the spreading of the metal sphere. Furthermore, the metal powder spray should be located as closely to the tip of the weld for high-quality coating.

This results were obtained using an X-ray visible light conversion unit and a high-speed camera that emphasizes time resolution. Future work will aim to apply these technologies to understand the coating phenomena of various materials and the derivation of optimum conditions, leading to the advancement and practical application of coating technology.

Reference

Sato, Y., Shobu, T. et al., Preheat Effect on Titanium Plate Fabricated by Sputter-Free Selective Laser Melting in Vacuum, Applied Physics A, vol.124, issue 4, 2018, p.288-1–288-6.

5-8 Compound Developed to Recognize Slight Size Differences of Rare-Earth Elements — Towards Efficient Recycling of Lanthanides —

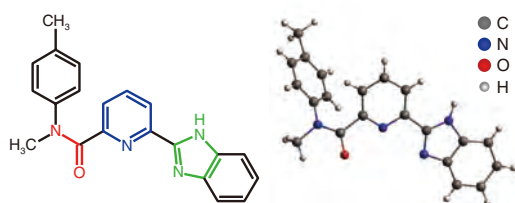


Fig.5-19 Chemical formula (left) and structure (right) of the developed BIZA

The oxygen atom on amide group (red part of left figure), the nitrogen atom on pyridyl group (blue part of left figure) and the nitrogen atom on imidazole group (green part of left figure) coordinate with lanthanide ion.

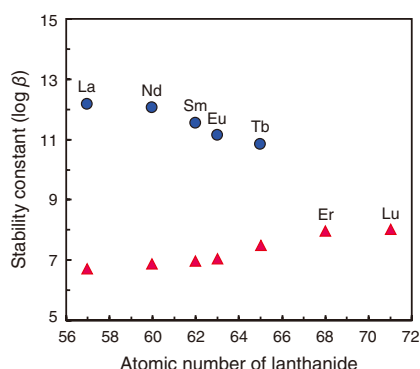


Fig.5-20 Complexation ability of BIZA with lanthanide

The horizontal axis represents the atomic number of lanthanide and the vertical axis represents the stability constant between BIZA and lanthanide in solution, where ● and ▲ represent the stability constant of the 1:2 and 1:1 complex, respectively.

Lanthanides (Lns) are essential for high-technology products, such as the voice coil motor of an electric vehicle or a hard disk drive. As Japan's manufacturing industry is currently highly dependent on Ln imports, the establishment of an efficient separation and recovery technique from waste products would help stabilize the supply. However, separating Lns is very difficult due to their similarities in chemical properties. During ongoing efforts to develop techniques to efficiently separate specific Lns, the compound BIZA, shown in Fig.5-19, was found to recognize slight differences in the ionic size of Lns.

BIZA demonstrated a characteristic complexation with Ln, as shown in Fig.5-20, investigated by spectroscopic titration. BIZA formed two complex types: one Ln ion with one BIZA molecule (1:1 complex) and one Ln ion with two BIZA molecules (1:2 complex). The 1:1 complex became easier to form with an increased atomic number of the Ln. This behavior has often been shown in compounds that form complexes with Ln. However, forming the 1:2 complex became more difficult with an increasing atomic number; this complex did form after dysprosium (Dy), which has an atomic number of 66.

The detailed structures of these complexes were thus investigated by X-ray crystallography to further understand the mechanisms behind this behavior. The crystal structures of a Neodymium (Nd) complex (atomic number 60) and a Holmium

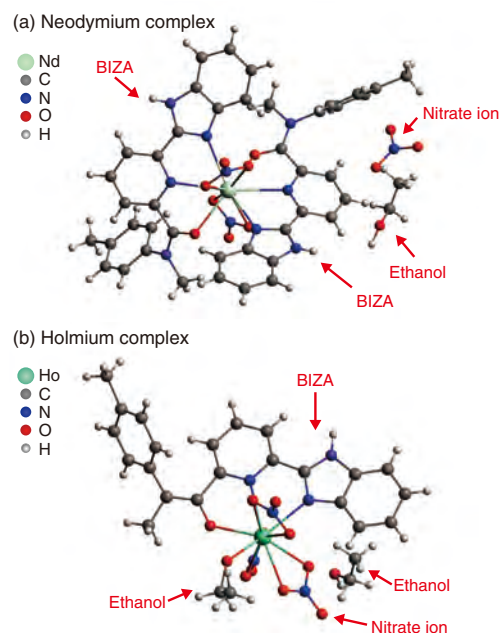


Fig.5-21 Crystal structure of lanthanide complex of BIZA

Here, (a) is the structure of the Neodymium complex of BIZA and (b) is the Holmium complex. BIZA is shown in (a) the upper left and lower right spaces of the Neodymium ion and (b) in the upper space of Holmium. Ethanol molecules and nitrate ions also fill the residual space.

(Ho) complex (atomic number 67) are shown as examples in Fig.5-21. Of the several crystal samples examined, all Nd formed a 1:2 complex and all Ho formed a 1:1 complex. In both the Nd and Ho complexes, BIZA coordinates with Ln as tridentate ligand through the oxygen atom in the amide group and nitrogen atom in the pyridyl and imidazole groups. The coordination bond distance was longer in the 1:2 complex than in the 1:1 complex and, among the 1:2 complexes, increased with increasing atomic number of Ln. As the atomic number increased, the ionic size of Ln slightly and gradually decreased, causing the coordinated molecules to become closer. However, for bulky molecules such as BIZA, repulsion between molecules occurs when they are too close together. As a result, in the 1:2 complex, the coordination bond became weaker with increasing the atomic number; past an atomic number of 65, two BIZA molecules could not coordinate with one Ln ion. Thus, the relationship between the bulkiness of ligand molecule and the ionic size of Ln determines the limit element which can form stable 1:2 complexes.

The ionic size suitable for the 1:2 complexation is expected to be controlled by control of the bulkiness of ligand molecule. Future work will aim to use the unique properties discussed here to develop a Ln separation method.

This study was supported by the New Energy and Industrial Technology Development Organization (NEDO).

Reference

Kobayashi, T. et al., Complexation Properties and Structural Character of Lanthanides Complexes of *O,N*-hetero Donor Ligand BIZA, Separation Science and Technology, vol.54, issue 13, 2019, p.2077–2083.

Research and Development on HTGR, Hydrogen Production, and Heat Application Technologies

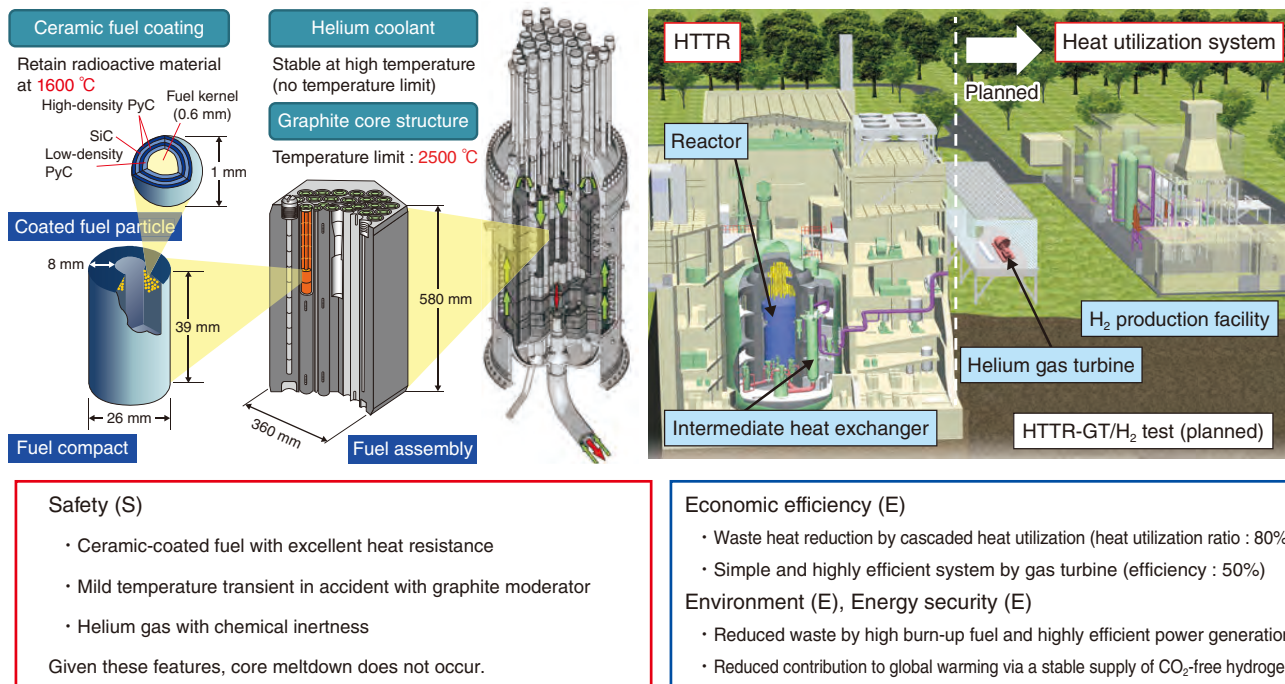


Fig.6-1 Features of HTGR and plan of HTTR-GT/H₂ test

The HTGR is a helium gas-cooled and graphite-moderated thermal-neutron reactor with excellent inherent safety features. The HTGR meets various heat application requirements such as hydrogen production and power generation. The HTGR also meets the 3E+S policy targets in Japan's Strategic Energy Plan. Our final target is demonstration of coupling of a nuclear reactor and heat application systems by connecting gas turbine and hydrogen production facilities to the Japan's first HTGR, HTTR.

Japan's energy supply-demand structure is fragile because of its excessive dependence on imported fossil resources. To remedy this situation while reducing greenhouse gas emissions that cause global warming, Japan is advancing the use of safe nuclear energy. A High Temperature Gas-cooled Reactor (HTGR) is a nuclear reactor with various industrial uses, such as high-efficiency power generation using a helium gas turbine, hydrogen production, and seawater desalination (Fig.6-1). According to Chapter 3, section 2 of the 5th Strategic Energy Plan decided by the Cabinet in July 2018, "Promotion of technology development: Technical challenges to be addressed", under international cooperation while looking at overseas market trends, GOJ also facilitates R&D of nuclear technologies that serves the safety improvement of nuclear use, such as HTGRs which are expected to be utilized in various industries including hydrogen production and which has an inherent safety.

The industrial, academic, and governmental council established by the Ministry of Education, Culture, Sports, Science and Technology (MEXT), Japan has been developing strategies for commercializing HTGRs and deploying Japanese HTGR technologies overseas. Cooperation policies and domestic organizational structures have been established for an experimental and commercial reactor in Poland. We aim to maintain the most advanced HTGR technology in the world, cultivated through the design, safety review, construction, operation, maintenance, and safety evaluation of Japan's first HTGR, the High Temperature Engineering Test Reactor (HTTR), at Oarai, Ibaraki-ken. The plant will be constructed by overseas projects and then returned to Japan.

The HTTR, constructed using domestic technology, is the

only HTGR worldwide that can extract heat at 950°C from the reactor. The HTTR attained a reactor outlet temperature of 950°C in 2004 and continuously operated at that reactor outlet temperature for 50 days in 2010. The inherent safety features of the HTGR were confirmed in a loss-of-forced-cooling test in 2010, without inserting the control rods. In these tests, the reactor intrinsically shut down and maintained a stable state.

Current research and development projects of HTGR technology includes the recycling of transuranic elements to reduce the environmental loads, conceptual design of an experimental reactor to introduce the HTGR for steam supply utilizing HTTR's knowledge, development of manufacturing technology for oxidation-resistant fuel elements to further improve the safety of the HTGR, and investigation of thermal load fluctuation absorption of HTGR based on HTTR test results (Topics 6-1–6-4). Furthermore, in research on the thermochemical IS process, which is an innovative hydrogen production technology that uses the heat of the HTGR, the design study aiming to improve the efficiency of the IS process, the development of quality control methods of glass lining materials to improve the reliability of corrosion-resistant equipment, and the development of cation exchange membranes to improve hydrogen production efficiency have been conducted (Topics 6-5–6-7).

Owing to the inherent safety features of HTGR, the HTTR is expected to restart operation confirming compliance with the new regulation standards and without large-scale modification or reinforcement. Final preparations before restarting HTTR operation are currently underway.

6-1 Proposal of Innovative Nuclear Fuel Cycle Based on High Temperature Gas-Cooled Reactor — Reduction of Cooling Time of Potential Toxicity of Radioactive Waste —

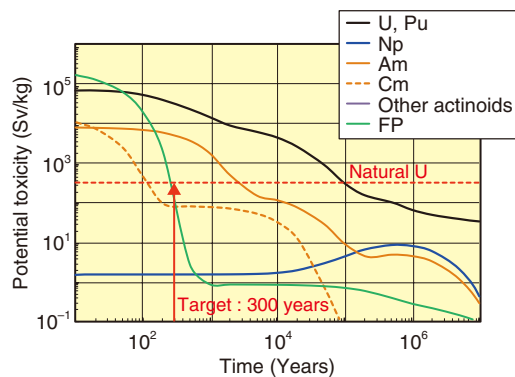


Fig.6-2 Potential toxicity in spent fuel of a Light Water Reactor (LWR)

MA (Np, Am, Cm) and FP contained in the spent fuel are vitrified as high-level radioactive waste. There is a need for transmutation of MA from the viewpoint of shortening the cooling time to reduce the potential toxicity. In addition, the toxicity of natural U depends on the required amount relating the enrichment, and are different for each fuel.

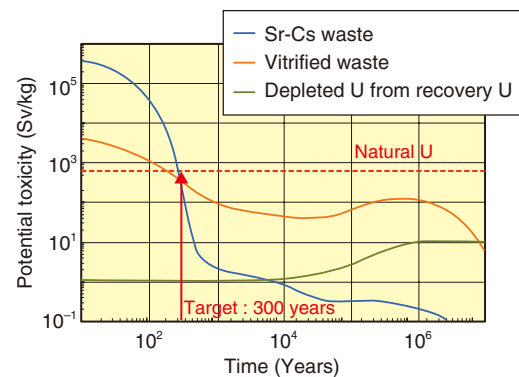


Fig.6-4 Potential toxicity of waste generated from proposed nuclear fuel cycle

MA is recovered, and Sr-Cs has been separated and disposed to reduce the number of vitrified wastes by a group-partitioning technique. The toxicity of this wastes has been shown to reduce below natural U levels within 300 years.

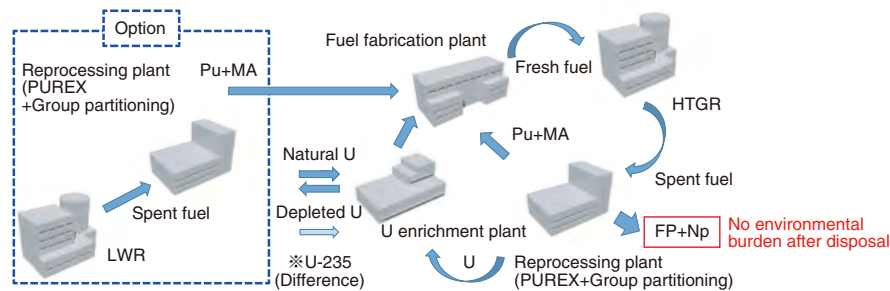


Fig.6-3 Overview of proposed nuclear fuel cycle

Environmentally burdensome TRU nuclides, namely Pu and Am, are confined in the nuclear fuel cycle. In addition, Pu and MA separated from the spent fuel of the LWR during reprocessing can be burned, thus solving the problem of LWR waste.

The safety of waste disposal during nuclear power generation must be ensured by limiting public dose. Furthermore, the potential toxicity must be reduced for public acceptance. The potential toxicity has been defined as the dose when all radionuclides present in waste are ingested orally; the target value is less than the dose of natural uranium (U) required to fabricate nuclear fuel; i.e., the aim is to ensure that the radioactive toxicity of waste is below that present in nature.

The radioactive toxicity of nuclear fuel increases when used for power generation and then decreases due to the decay of nuclides. However, approximately one hundred thousand and three thousand years are required for plutonium (Pu) and americium of Minor Actinides (MA: Np, Am, Cm), respectively, to reduce naturally and become less than the dose of natural U (Fig.6-2). Thus, this timeline must be reduced.

A fast reactor and Accelerator-Driven transmutation System (ADS) have been developed to realize a cooling time of 300 years. This work aims to shorten the cooling time using an High Temperature Gas-cooled Reactor (HTGR), which is a thermal neutron reactor. Generally, it has been thought that the shortening of the cooling time by transmutation of MA was only possible using the fast reactor system including ADS. By finding the characteristics that TRU is less likely to accumulate in thermal

neutron reactors, it is confirmed that the possibility to realize multiple recycling of TRU elements (TRU: Pu and MA) similar to fast reactor systems by core designing and fuel cycle mass balance evaluation. This represents the first documented study involving a thermal neutron reactor to establish the concept of confining a long-lasting reduction of TRU nuclides in a fuel cycle consisting of use for power generation and reprocessing (Fig.6-3). In addition, the thermal neutron reactor system's negative reactivity coefficient, large delayed neutron fraction, and high heat removal performance due to graphite structural materials in the loss of coolant accident can be utilized to take advantage of the HTGR's inherent safety features.

The potential toxicity of wastes, including Sr-Cs, vitrified, and degraded U wastes, were reduced within 300 years by evaluation of radioactive nuclear dose, as shown in Fig.6-4. In the evaluation of the footprint of disposal repository, that is compared with the that of the representative reprocessing scenario based on LWR waste disposal in order to confirm the effect of waste volume reduction. That is reduced to 1/300 compared with the representative one. Thus, it has been shown that an HTGR can be used to achieve the same cooling time as fast reactors and ADSs. Future work will focus on evaluating the economics of the proposed nuclear fuel cycle.

Reference

Fukaya, Y. et al., Uranium-Based TRU Multi-Recycling with Thermal Neutron HTGR to Reduce Environmental Burden and Threat of Nuclear Proliferation, Journal of Nuclear Science and Technology, vol.55, issue 11, 2018, p.1275–1290.

6-2 Towards Implementation of Improved HTGRs

— Conceptual Design of an Experimental HTGR for Steam Supply Based on an HTTR —

Table 6-1 Comparison of design specifications of the experimental HTGR and HTTR for steam supply compared

The HTGR for steam supply was designed by incorporating a SG into the HTTR base design instead of an IHX. To reduce costs by avoiding the installation of a containment vessel, the design adopted confinement. A natural air cooling system was adopted over a forced water cooling system, for passivation of safety.

	HTTR	HTGR for steam supply
Thermal power	30 MWt	10–30 MWt
Outlet temperature	850/950 °C	750 °C
Inlet temperature	395 °C	325 °C
Heat exchanger	IHX, Pressurized water cooler	SG
Steam supply Temperature/Pressure	—	540 °C/13.8 MPa
Reactor containment facility	Containment vessel	Confinement
Heat removal from scrammed reactor	ACS	SCS
Cooling way of VCS	Forced water cooling	Natural air cooling

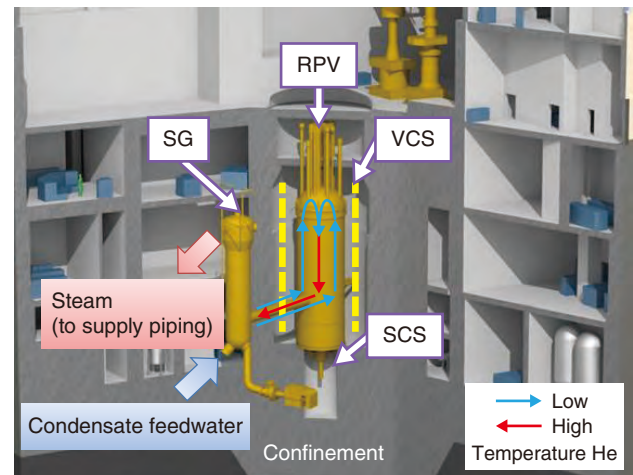


Fig.6-5 A schematic view of the HTGR for steam supply
High-temperature steam is produced by high-temperature He circulation between the reactor and steam generator. A natural air VCS is used to remove heat from the reactor vessel indirectly when the reactor emergency stop occurs.

Coal and natural gas boilers are widely installed to supply steam to chemical plants. This work aims to reduce CO₂ emissions by replacing these boilers with High Temperature Gas-cooled Reactors (HTGRs). The HTGR for steam supply design was considered based on High Temperature Engineering Test Reactor (HTTR) design in order to save design time and to take HTTR operation experience to design work. A 30 MWt of helium-cooled high-temperature gas-cooled test reactor using coated particle fuel and a graphite core block achieved continuous 950 °C for 50 days of operation in March 2010. The design specifications and a schematic view of the HTGR used for steam supply are shown in Table 6-1 and Fig.6-5, respectively. The HTGR effectively produced steam at 540 °C and 13.8 MPa to meet the demand from the chemical industry. Aiming to reduce the construction cost, the reactor core design was optimized and the component design was improved. Furthermore, plant safety was ensured with safety passivation of vessel cooling system (VCS).

➤ Optimization of reactor core design

The number of control rods within the HTGR was reduced to 40% of HTTR since reactor shutdown merging of HTTR is too conservative. Optimization of the power distribution

made the core more compact and increased the power density by 25% over that of the HTTR. In addition, the number of types of fuel enrichment was reduced for cost reduction of fuel manufacturing.

➤ Component design improvement

A helical-coil counter-current type steam generator (SG) was installed in the HTGR, as in the intermediate heat exchanger (IHX) of the HTTR. A concrete “confinement” was designed and integrated to shorten plant construction time and reduce costs. The shutdown cooling system (SCS), instead of air cooling system (ACS), directly removes heat from the reactor core after reactor emergency stop was designed and it’s placed below reactor pressure vessel (RPV). It doesn’t have piping unlike ACS of HTTR.

➤ Safety passivation of VCS

Unlike the conventional VCS design that uses forced water cooling, a passive air cooling VCS was designed that can still remove heat from outside of the reactor vessel without electricity.

Future work focuses to ensure continued plant safety and improve economic competitiveness of the implementation of the HTGR for steam supply.

References

- Ohashi, H., Sasaki, K. et al., Conceptual Plant System Design Study of an Experimental HTGR Upgraded from HTTR, Proceedings of 9th International Topical Meeting on High Temperature Reactor Technology (HTR 2018), Warsaw, Poland, 2018, HTR2018-104, 6p., in USB Flash Drive.
Goto, M. et al., Conceptual Study of an Experimental HTGR Upgraded from HTTR, Proceedings of 9th International Topical Meeting on High Temperature Reactor Technology (HTR 2018), Warsaw, Poland, 2018, HTR2018-132, 6p., in USB Flash Drive.

6-3 Improving the Fuel Safety of High Temperature Gas-Cooled Reactors during Severe Oxidation Accident — Fabrication of Oxidation-Resistant Fuel Elements for Oxygen Ingress Accidents —

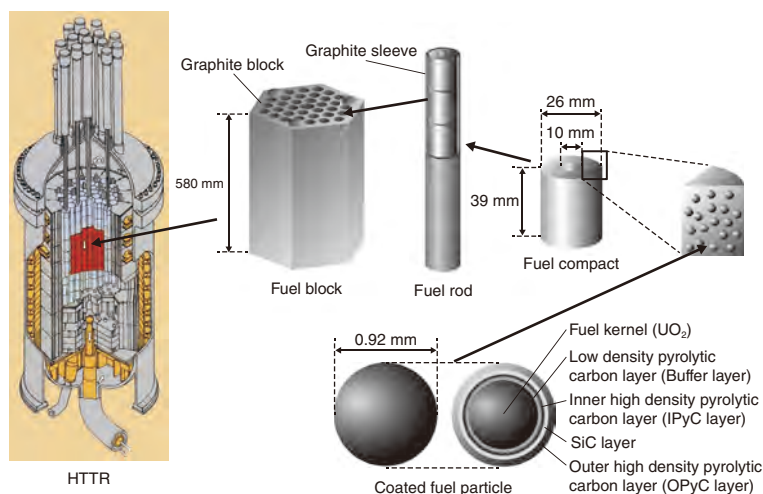


Fig.6-6 Fuel used in HTTR *1

A UO_2 fuel kernel is coated with ceramics layers to form a coated fuel particle (CFP) approximately 1 mm in diameter. A mixture of CFPs, graphite powder, and resin is sintered to form a fuel compact. Fuel compacts are put into a graphite sleeve to form a fuel rod. Fuel rods are put into holes of graphite block to form fuel block.

High Temperature Gas-cooled Reactors (HTGRs) are safe next-generation reactors with cores that will not melt. Further safety improvements of the HGTR relies on improve the oxidation resistance of the fuel for the severe oxygen ingress into the core, because almost volume of the cores of the HTGRs consist of graphite (solid C, but not diamond). The graphite is oxidized into CO or CO_2 in the oxidation atmosphere at high temperatures.

A small sphere containing fissile materials is coated with layers of ceramics to form a coated fuel particle (CFP) approximately 1 mm in diameter, as shown in Fig.6-6, which are then used in HTGRs. A mixture of CFPs and starting materials of binding material is sintered to form a fuel element. The fuel elements for the High Temperature Engineering Test Reactor (HTTR) of the Japan Atomic Energy Agency (JAEA) are called fuel compacts, of which the binding material is graphite. The binding material is then oxidized into CO or CO_2 gas in an oxidation atmosphere at high temperatures. Then the binding material can finally vanish completely in oxidation atmosphere at high temperatures.

An oxidation-resistant fuel element using a binding material of SiC and graphite was developed via collaboration between JAEA and Nuclear Fuel Industries, Ltd. (NFI). SiC is oxidized into a solid oxide, not a gaseous oxide, and does not vanish under high temperature and high oxygen partial pressure. In this study, a simulated fuel element (a simulated fuel compact) with binding material of SiC and graphite was fabricated and an oxidation test was carried out using the simulated fuel compact to investigate whether the oxidation resistance of the fabricated

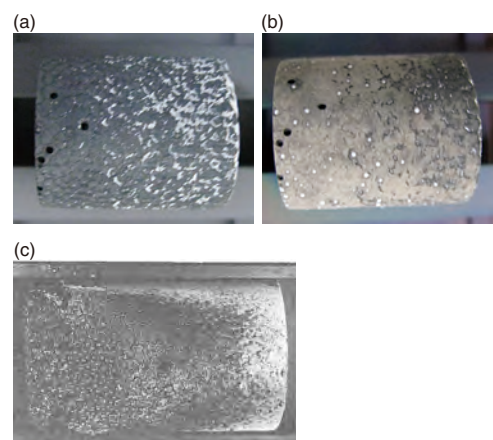


Fig.6-7 Simulated and actual fuel compact

(a) Simulated fuel compact before oxidation.
(b) Simulated fuel compact after oxidation in He including 20% O_2 at 1673 K for 10 h.
(c) Fuel compact after oxidation in air at 1673 K for 2 h. *2

simulated fuel compact is better than that of the fuel compact with graphite binding material or not.

Simulated CFPs (alumina particles) and binding material (Si powder, graphite powder and resin) were molded and sintered into a simulated fuel compact (Fig.6-7(a)), which was then oxidized in He including 20% of O_2 at 1673 K for 10 h. The fraction of O_2 was set to be similar to air. After oxidation (Fig.6-7(b)), all simulated CFPs were kept in the simulated fuel compact. On the other hand, in a past study, a part of CFPs were loosened from a fuel compact with the graphite binding material by the partially vanishment of the binding material after oxidation in air at 1673 K for 2 h (Fig.6-7(c)). Thus, it was shown that the oxidation resistance of the fabricated simulated fuel compact is better than that of the fuel compact with graphite binding material.

This study was part of the result conducted “Research on advanced fuel element for upgrading safety of high temperature gas-cooled reactors”, and carried out under the project “Center of world intelligence project for nuclear science/technology and human resource development”, sponsored by the Ministry of Education, Culture, Sports, Science and Technology (MEXT), Japan.

*1 Goto, M. et al., Conceptual Design of Small-Sized HTGR System (II) - Nuclear Design -, JAEA-Technology 2012-017, 2012, 29p. (in Japanese).

*2 Kikuchi, H. et al., Air Oxidation Behavior of Fuel for the High Temperature Engineering Test Reactor (HTTR), JAERI-M 92-114, 1992, 20p. (in Japanese).

Reference

Aihara, J. et al., Development of Fabrication Technology for Oxidation-Resistant Fuel Elements for High-Temperature Gas-Cooled Reactors, Transactions of the Atomic Energy Society of Japan, vol.18, no.1, 2019, p.29–36 (in Japanese).

6-4 Toward Load-Following, Demand-Dependent Operation of an HTGR

— Confirming the Thermal Load Fluctuation Absorption Characteristics of an HTTR —

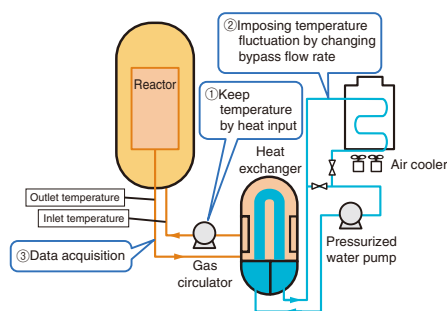


Fig.6-8 Non-nuclear heating (NNH) test on CTLFA using an HTTR during shutdown

An AE assuming thermal load fluctuation in the HUS was simulated by keeping the reactor core temperature at 120 °C (①), fluctuating the heat removal via the air cooler and by changing the flow rate of pressurized water (②), as results around max. 30 °C lowered in RITC (③).

High Temperature Gas-cooled Reactors (HTGRs) have been used as heat source for heat utilization systems (HUSs) such as gas turbine power generation and hydrogen production systems. The HUS is requested to be constructed using non-nuclear grade standards (NNGS). This involves maintaining a stable operation regardless of the operational status of the HUS and to use a load-following operation (LFO), during which the delivered power can vary within a certain range to meet varying demands.

A LFO design of an HTGR was thus proposed by JAEA in which the coolant mass flow rate and inventory were controlled by changing the coolant pressure while keeping the reactor outlet temperature of coolant (ROTC) constant to supply helium gas to the HUS.

To make a construction of HUS using NNGS feasible, stable reactor operation must be ensured. This involves the ROTC remaining below the scram alarm level (SAL), even when the fluctuation of coolant temperature is transferred to the reactor associated with an abnormal event (AE) occurring in the HUS, especially in the low-pressure condition (LPC) where the heat transfer rate from coolant to components is lowered during partial load operation by inventory control (IC).

The restriction effect of fluctuation in ROTC was then investigated in case that the reactor inlet temperature of coolant (RITC) is fluctuated after the numerical code RELAP5/MOD3 was improved to reproduce the effect using the test data acquired by the High Temperature Engineering Test Reactor (HTTR). Subsequently, it was confirmed that the reactor would remain operational when the RITC fluctuates, assuming a connection between the reactor and the HUS.

In the test using HTTR, the test data necessary to verify the code on the RITC and ROTC were acquired (Fig.6-8). The helium gas was heated by the compression of the helium gas circulator instead of nuclear heating because the HTTR was shut down. By considering the operational limitations, two coolant

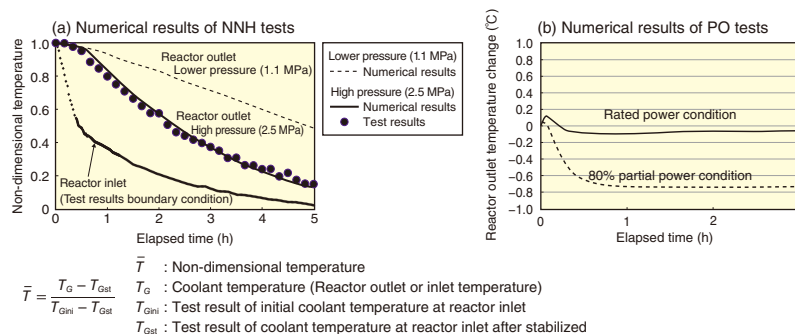


Fig.6-9 Numerical results of NNH and powered operation (PO) tests for a HTTR

The numerical results of non-dimensional ROT normalized by change of RITC showed superior CTLFA in the LPC based on NNH tests (a). The numerical results assuming 80% of the rated power in LPC showed that the CTLFA were superior to those of rated power to restrict the increase of ROT 7 °C smaller than the SAL in case that a stepwise temperature fluctuation of 10 °C was imposed on the RITC (b), which was referred from the design of commercial HTGR.

pressures (1.1 and 2.5 MPa) were selected to investigate the pressure dependency of characteristics of thermal load fluctuation absorption (CTLFA) by reactor. The AE occurrence in the HUS was simulated by changing heat release from the air cooler, in which the RITC was changed up to 30 °C in 6 hours. The results confirmed that the test results of the ROTC were well-reproduced; an example involving changing the RITC 10 °C under a high-pressure condition (HPC) is shown in Fig.6-9(a).

The pressure dependency of CTLFA was then investigated using the verified model, as shown in Fig.6-9(a). The ROTC varied more slowly under an LPC; the non-dimensional ROTC remained at approximately 0.5 for 5 hours, whereas it dipped to approximately 0.1 under an HTC. The heat capacity of the reactor side metallic components works as buffer material to absorb temperature fluctuation. This is because that the temperature change of components became still slower due to the heat transfer rate that is heat release lowered in LPC. Thus, the CTLFA by the reactor did not deteriorate, even in the LPC important in the LFO.

The transient characteristics of the ROTC were then numerically investigated using the heat transfer effect of reactor side metallic components; the results, shown in Fig.6-9(b), confirm that the reactor can be stably operated without scram even in case that the RITC is fluctuated after an AE occurred in the HUS assumed connected to HTTR. The change of the ROTC remained below the SAL associated with the slower temperature transient lowering coolant pressure from 4.0 to 3.2 MPa by the IC.

Thus, the reactor was shown to have sufficient CTLFA, meeting the requirements for constructing HUS using NNGS, in which the ROTC does not exceed the SAL even when a fluctuating RITC is transferred to the reactor after an AE occurs in HUS, during the LFO of HTGRs.

Reference

Takada, S. et al., Numerical Evaluation on Fluctuation Absorption Characteristics Based on Nuclear Heat Supply Fluctuation Test Using HTTR, Proceedings of 9th International Topical Meeting on High Temperature Reactor Technology (HTR 2018), Warsaw, Poland, 2018, HTR2018-127, 7p., in USB Flash Drive.

6-5 Improving Hydrogen Production Efficiency Using Innovative Technologies — High-Efficiency Process Design of the Thermochemical IS Process —

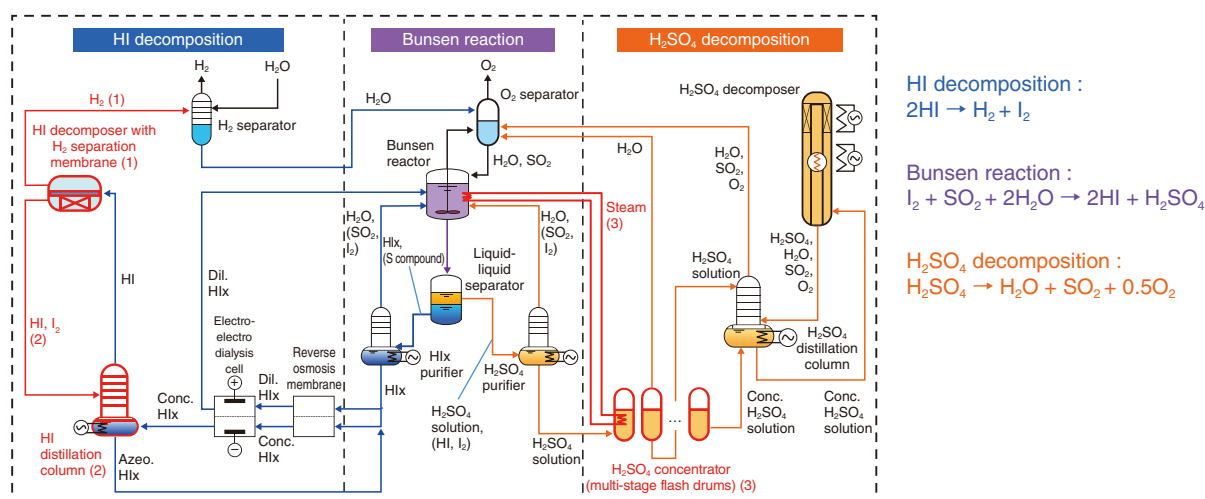


Fig.6-10 Flow diagram of the iodine-sulfur (IS) process

Innovative technologies are shown in red: (1) HI decomposer with membrane for H_2 separation, (2) direct feed of gas phase HI and I_2 into the HI distillation column, and (3) heat recovery from the Bunsen reaction by depressurized flash H_2SO_4 concentration, where Hlx denotes a mixture of HI, I_2 , and H_2O , minor compounds are within parentheses, Conc. represents concentrated, Dil. represents dilute, and Azeo. represents pseudo-azeotropic.

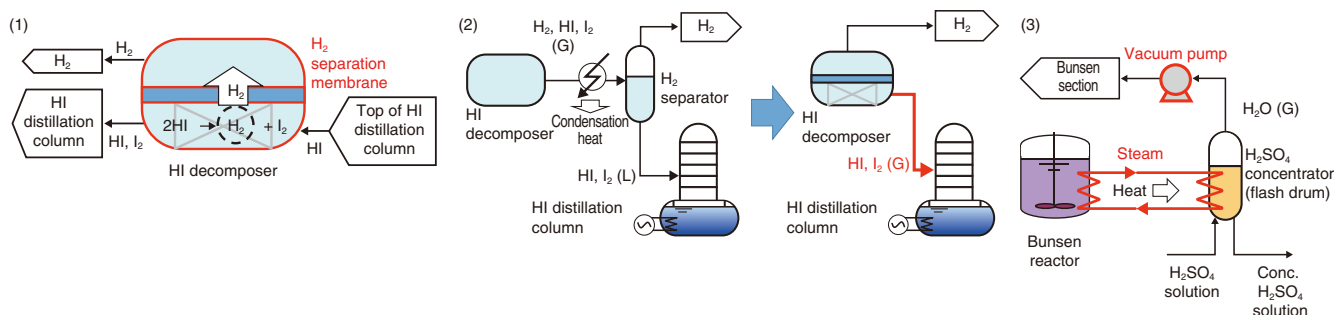


Fig.6-11 Innovative technologies for the IS process

(1) Promotion of HI decomposition by membrane separation of H_2 in an HI decomposer, (2) change from abandonment of HI and I_2 condensation heat to separate H_2 (left figure) to condensation heat recovery to the HI distillation column by feeding gas-phase HI and I_2 (right figure) and (3) heat recovery from the Bunsen reaction to the depressurized flash H_2SO_4 concentration. The excess amount is reduced by (1) and waste heat is recovered by (2) and (3).

The iodine-sulfur (IS) thermochemical hydrogen (H_2) production process was investigated as to utilize heat from the High Temperature Gas-cooled Reactors. The IS process, depicted in Fig.6-10, consists of the Bunsen reaction to produce hydrogen iodide (HI) and sulfuric acid (H_2SO_4) ($\text{I}_2 + \text{SO}_2 + 2\text{H}_2\text{O} \rightarrow \text{H}_2\text{SO}_4 + 2\text{HI}$), HI decomposition to produce H_2 ($2\text{HI} \rightarrow \text{H}_2 + \text{I}_2$), and H_2SO_4 decomposition to produce oxygen (O_2) ($\text{H}_2\text{SO}_4 \rightarrow \text{H}_2\text{O} + \text{SO}_2 + 0.5\text{O}_2$). Overall, water is decomposed to produce H_2 and O_2 .

Practical, competitive implementation of H_2 production using the IS process requires improving the efficiency of the process for cost reduction. However, excess material flow is required due to the low reaction ratio, and the exothermic Bunsen reaction and material condensation generate large amounts of excess heat. As such, a high efficiency is difficult to achieve.

As such, technologies to improve the IS process efficiency have been investigated. A HI decomposition ratio higher than reaction equilibrium (44% vs 21%, respectively) was achieved

by promoting the reaction using a membrane for H_2 separation in the HI decomposer, thus reducing the material flow in the decomposer by 52% (Fig.6-11(1)). To recover waste heat from the condensation of HI and iodine (I_2), they were directly fed into the HI distillation column, as vapor-liquid H_2 separation is not needed by H_2 membrane separation in the HI decomposer (Fig.6-11(2)). To recover the heat of the Bunsen reaction, previously ignored due to its low temperature (378 K), it was used in the multi-stage H_2SO_4 concentration flash drums by lowering boiling temperature (368 K) by depressurization with a vacuum pump (Fig.6-11(3)).

A chemical process including these technologies was designed and simulated to estimate the heat demand. Overall, the H_2 production efficiency increased from 40% to 50%. Further work on the IS process components is to reduce H_2 production cost based on the improved process design.

Reference

Kasahara, S. et al., Conceptual Design of the Iodine-Sulfur Process Flowsheet with more than 50% Thermal Efficiency for Hydrogen Production, Nuclear Engineering and Design, vol.329, 2018, p.213–222.

6-6 Reliability Improvements of Corrosion-Resistant Equipment for Hydrogen Production by the IS Process — Refined Quality Management of Glass-Lined Steel Material —

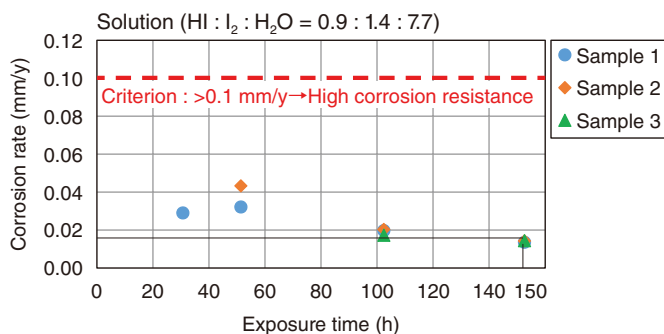


Fig.6-12 Corrosion rate of glass-lined steel in a hydroiodic acid and iodine solution

The corrosion rate was determined by weighing the specimen before and after testing. The corrosion rate after 150 h of exposure was 0.02 mm/y, lower than the criterion of excellent corrosion resistance (0.1 mm/y).

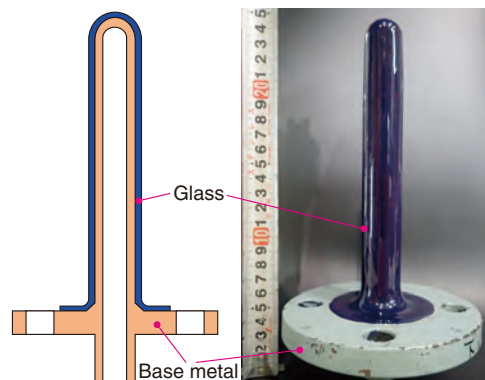


Fig.6-13 Prototype of the glass-lined thermocouple protective sheath

Based on the refined quality management, the glass-lined thermocouple protective sheath was prototyped; the prototype was thick enough and contained no inner bubbles, contamination, or pinholes.

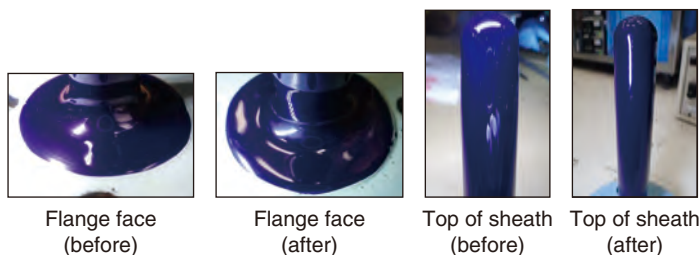


Fig.6-14 External appearance of the prototype after the heat cycle test

No breakage was seen on the lined glass after cycling from room temperature to 180 °C 10 times.

Structural materials with high corrosion resistance are required in the iodine-sulfur (IS) thermochemical water-splitting hydrogen production process, which occurs in a corrosive liquid or gaseous environment over a wide temperature range. As glass is well known as a corrosion resistant material, glass-lined steel was employed, which has both corrosion resistance and structural strength. Although glass-lined steel has adequate use results for sulfuric acid, it has not been thoroughly investigated in a hydroiodic acid environment. In addition, it may be broken by a microscopic defect because the lined glass that contacts the corrosive solution is a brittle material. A hydroiodic acid corrosion test was thus performed, and breakage factors were analyzed by fault tree analysis and quality management in manufacturing was refined.

Corrosion rates were determined by weighing the test specimens before and after exposure to the hydroiodic acid and iodine solution. The solution was heated to approximately 115 °C under atmospheric pressure. The corrosion rate was approximately 0.02 mm/y after 150 h exposure, significantly

lower than the criterion of excellent corrosion resistance (0.1 mm/y), as shown in Fig.6-12.

Additionally, defects causing breakage of the lined glass in manufacturing process were revealed, including cracks, inner bubbles, foreign substance contamination, insufficient glass thickness, and generation of pinholes. To eliminate these defects, quality management was refined by performing detailed visual observations at each manufacturing step, measuring the glass thickness after glass lining, and performing high-voltage inspection to find pinholes. From this basis, glass-lined thermocouple protective sheaths were made and subjected to heat cycle and bending load testing (Fig.6-13). No breakage occurred on the lined glass after performing 10 heat cycles from room temperature to 180 °C, nor after excessive bending load up to 150 kgf on the top of the sheath (Fig.6-14).

Future work will focus on long term testing involving the Hydrogen Production Test Facility to confirm the reliability of glass-lined thermocouple protective sheaths.

Reference

Kamiji, Y. et al., Current R&D Status of Thermochemical Water Splitting Hydrogen Production Iodine-Sulfur Process in Japan Atomic Energy Agency (II) – Reliability Improvements of Corrosion-Resistant Equipment –, Proceedings of 9th International Topical Meeting on High Temperature Reactor Technology (HTR 2018), Warsaw, Poland, 2018, HTR2018-2144, 7p., in USB Flash Drive.

6-7 Membrane Makes IS Process Chemical Reaction Efficiently

— Use of an Ion-Exchange Membrane to Reduce Water Permeation by Cross-Linking —

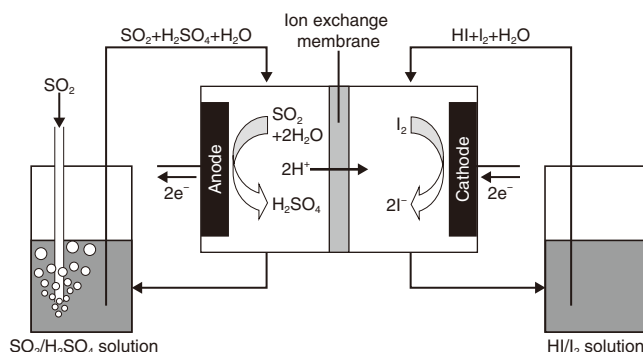


Fig.6-15 Schematic of Bunsen reaction using ion-exchange membrane

Hydriodic and sulfuric acid were produced on the cathode and anode, respectively, in an electrochemical cell equipped with an ion-exchange membrane.

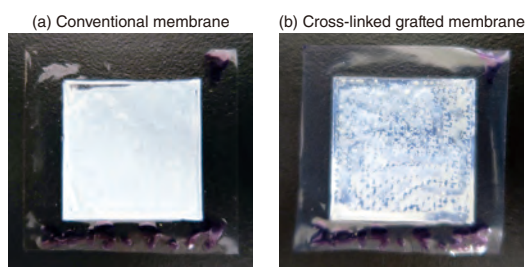


Fig.6-17 Outlook of (a) conventional and (b) cross-linked grafted membrane after membrane Bunsen reaction tests

The cross-linked grafted membrane showed a whitish color, which is evidence of sulfur formation reaction; the conventional membrane did not, indicating a lower water permeation.

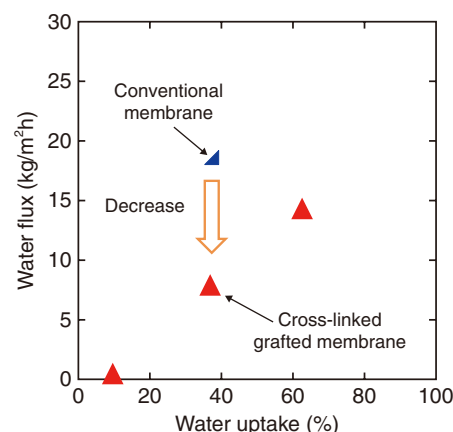


Fig.6-16 Relationship between water permeate flux and water content

The water permeate flux through the cross-linked grafted membrane decreased in relation to that of a conventional membrane having same water content.

In an effort to valorize the heat of high-temperature gas-cooled reactors, the thermochemical iodine-sulfur (IS) water-splitting hydrogen (H_2) production process has been investigated. The IS process is a promising H_2 production method using nuclear and renewable energy sources and is composed of sulfur and iodine chemical reactions. The Bunsen reaction, a key reaction of the IS process, produces sulfuric and hydriodic acids by mixing iodine (I_2) and sulfur dioxide (SO_2) with water. Liquid-liquid (LL) separation occurs by adding excess I_2 to the two acids. However, this excess I_2 decreases process efficiency and increases cost.

One alternative Bunsen reaction method investigated involves using an electrochemical cell equipped with a proton-selective ion-exchange membrane (Fig.6-15). No LL separation is needed, as the two acids can be separately produced in a cell partitioned into two channels by the ion-exchange membrane.

An ion-exchange membrane suitable for this purpose should have a high conductivity and low water permeability. Enhancing conductivity requires higher water content in the membrane however, this causes higher water permeation. A cross-linked ion-exchange membrane was therefore prepared by a radiation grafting technique developed by National Institutes for Quantum

and Radiological Science and Technology (QST). The cross-link, in which grafted chains connect, enables the membrane to retain water among the chains.

The relationships between water permeate flux and water content of the trial membranes were then measured (Fig.6-16); a lower flux was found of the ion-exchange membrane than of a conventional membrane having the same water content. Membrane Bunsen reaction tests were carried out using an electrochemical cell introducing the tested membranes, revealing a lesser degree of white turbidness of the cross-linked grafted membrane (Fig.6-17(b)) than that of a conventional membrane (Fig.6-17(a)). Thus, a cross-linked grafted membrane can reduce water permeation and the white turbidness due to sulfur formation associated with SO_2 transportation accompanied with water, indicating that a cross-linked grafted membrane can be adapted to the membrane Bunsen reaction. Future work will involve the development of an ion-exchange membrane to improve performance by using this membrane preparation technology.

This study was partly supported by Council for Science, Technology and Innovation (CSTI), Cross-ministerial Strategic Innovation Promotion Program (SIP).

Reference

Nomura, M., Tanaka, N. et al., Development of Ion-Exchange Membranes for the Membrane Bunsen Reaction in Thermochemical Hydrogen Production by Iodine-Sulfur Process, *Journal of Chemical Engineering of Japan*, vol.51, no.9, 2018, p.726-731.

Endeavors in Research and Development of Fast Reactor Cycle for Nuclear Innovation

Fast reactors using fuel cycle technology offer a sustainable energy supply in conjunction with other renewable sources, such as solar and wind power, to reduce CO₂ emissions and mitigate global warming while meeting growing energy demands. Using fast reactor cycle technology with known uranium resources will be able to meet energy demand for over a thousand years. Furthermore, it enables geological disposal of vitrified high-level radioactive waste through nuclear transmutation that greatly reduces the radiotoxicity and heat of minor actinide elements with long half-lives.

In the “strategic roadmap” published in December 2018 by Japan’s Inter-Ministerial Council for Nuclear Power, it was predicted that fast reactor technology will greatly contribute to the efficient use of resources and to energy self-sufficiency, given the uncertain global energy future and the scarcity of energy resources in Japan. To accomplish this, the volume and toxicity of radioactive waste must be reduced to address long-term nuclear waste issues. It is therefore critical to promote new and unconventional approaches in addressing these problems. In the first five years, Japan promotes technology competition among manufacturers to seek diverse, innovative, and probable technological options. Then, the government, JAEA, and electric power suppliers will scrutinize the candidates and select the options, with the aid of the manufacturers. It is expected that fast reactors will commence operation at the right time in the mid-21st century, on the basis of how much the technology has developed and how much more needs to be done. JAEA will prepare its technology infrastructure to accommodate various requests from private sectors and to promote Japan’s fast

reactor technology and standards, including safety criteria, to be adopted globally. JAEA promotes developments of advanced design evaluation and support system including state-of-the-art technologies domestically and overseas, safety enhancement technologies, radioactive waste reduction technologies, economic improvement technologies of fast reactors, fuel cycle technologies such as fuel fabrication and reprocessing.

As the advanced design evaluation and support system, JAEA will integrate the knowledge database containing various research and development outcomes and advanced analysis systems into an evaluation system to create the advanced evaluation platform called ARKADIA (Fig.7-1). ARKADIA enables developers to quickly identify optimum options that meet their targets. Towards safety enhancements, JAEA has developed models of the complex vibrations of fuel assemblies during an earthquake. Furthermore, experimental results have indicated that the coolant will react with molten fuel and turn it into fine debris to make it coolable effectively in a core melt accident (Topics 7-1 and 7-2). To reduce radioactive waste, the precision of neutron capture cross-section of minor actinides has been improved (Topic 7-3). To improve economic efficiency of fast reactors, the durability of long-life control rods has been investigated (Topic 7-4). Finally, JAEA has improved the techniques for fabricating fuel to obtain uniform uranium-plutonium mixed oxide powder while controlling the grain size (Topic 7-5).

Overall, these improvements contribute to the safety enhancement and commercialization of fast reactor cycle technology.

ARKADIA

—Advanced Reactor Knowledge- and AI-aided Design Integration Approach through the whole plant lifecycle—

- Proposes competitive plants that meet energy security, economical efficiency, environmental, and safety goals (3E+S)
- Reduces development cost and duration
- Builds and transfers knowledge, develops technology, and cultivates human resources

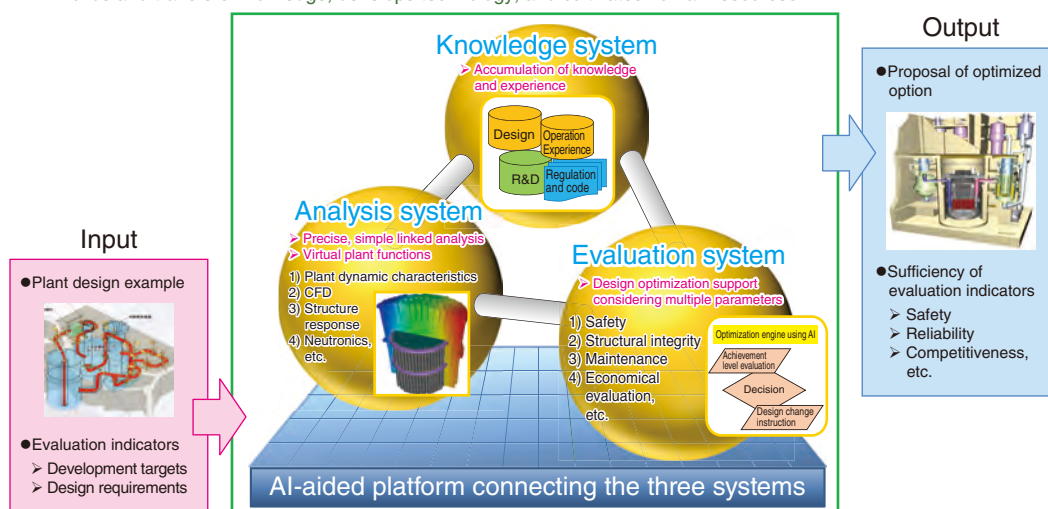


Fig.7-1 Advanced design evaluation and supporting system

The developed system is used to optimize the design of plants over their lifetimes by integrating sophisticated analysis methods using AI and knowledge data.

7-1 Examining the Behavior of Core Elements during a Strong Earthquake

— Development of 3-Dimensional Reactor Core Group Vibration Analytical Model —

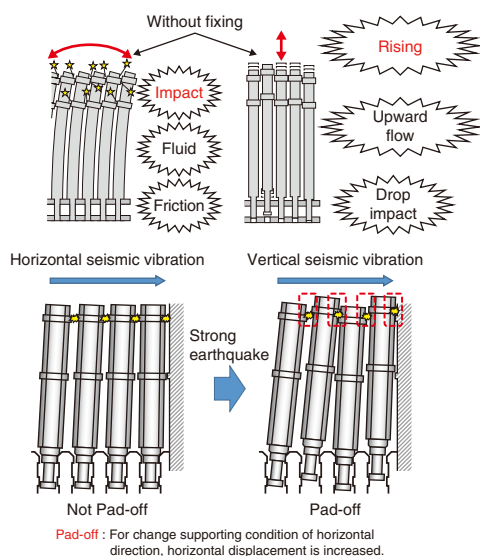


Fig.7-2 Behavior of core elements during an earthquake
The external force and displacement considered to affect the behavior of core elements during an earthquake are included.

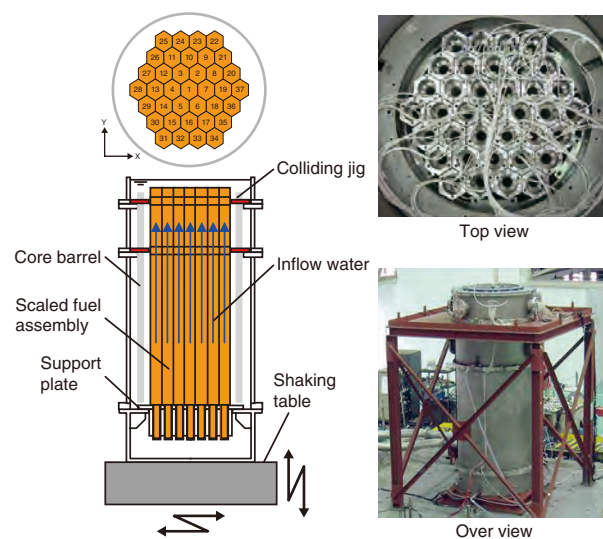
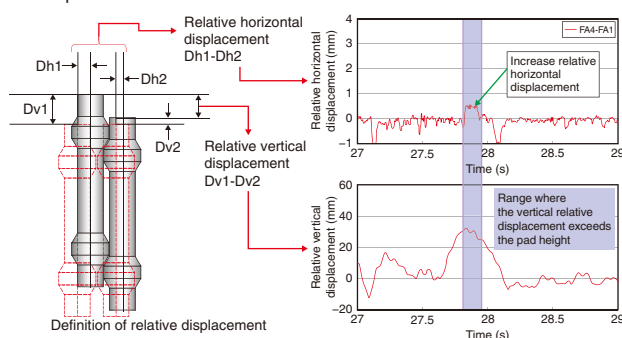


Fig.7-3 Schematic view of vibration test

A shaking table that vibrates in the horizontal and vertical directions and scaled core elements specimen was conducted to grasp the behavior of the core elements during an earthquake.

(a) Relation between horizontal displacement and vertical displacement on pad-off condition



(b) Comparison between test and analysis

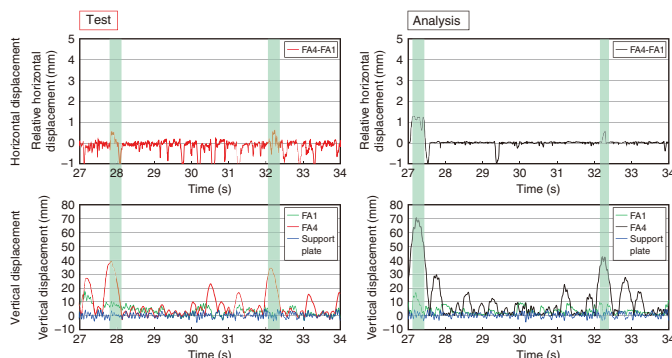


Fig.7-4 Comparison between vibration test and verification analysis results (Flowing water condition)

During time zone while relative vertical displacements between adjacent core elements are larger than the height of contact pads, contact conditions change and horizontal displacements increase. Moreover, as the result of the verification of this test using new analytical code, it is demonstrated that the test results are enough.

The core elements of a sodium-cooled fast reactor (SFR) are self-standing on the core support structure. Thus, during an earthquake condition, both the horizontal displacement, in which the core fuel assemblies collide with each other, and the vertical displacement in the rising direction must be considered. Large earthquakes must also be considered during seismic evaluations, including the large rising of the core elements. During strong earthquakes, the rising of the core elements higher than the fitting parts such as contact pads, may cause the pad will come off, thus changing the behavior of the core elements (Fig.7-2).

Therefore, a core vibration analytical code was developed to further understand the 3-dimensional behavior during an earthquake. For this development, group vibration tests using a scaled core elements specimen were carried out to allow the 3-dimensional behavior of core elements to be examined, as shown in Fig.7-3. This test equipment has a system that can test not only in air but also in water (static water and flowing water). In particular, vertical and horizontal coupling behaviors

focusing on pad off, a phenomenon in which support conditions in the horizontal direction change due to vertical displacement under strong vibration, were obtained. The vibration tests indicated that the contact conditions changed and the horizontal displacements increased when the relative vertical displacements between adjacent core elements were greater than the height of the contact pads. Moreover, as the result of the verification of this test using new 3-dimensional reactor core group vibration analytical code, it reproduces the test results well about pad-off condition (Fig.7-4).

Overall, the developed model allows for the analysis of the behavior of core elements, even considering the pad-off condition during a strong earthquake.

This study was part of the result conducted “Technology development program of fast breeder reactor international cooperation, etc”, and supported by the Agency of Natural Resources and Energy (ANRE), the Ministry of Economy, Trade and Industry (METI), Japan.

Reference

Yamamoto, T. et al., Fast Reactor Core Seismic Experiment and Analysis under Strong Excitation, Proceedings of the ASME 2018 Pressure Vessels and Piping Conference (PVP 2018), Prague, Czech Republic, 2018, PVP2018-84466, 8p.

7-2 Clarifying the Discharge Behavior of Molten Core Materials

— Simulated Experiments Using a Shallow Water Pool for Molten Core Discharge —

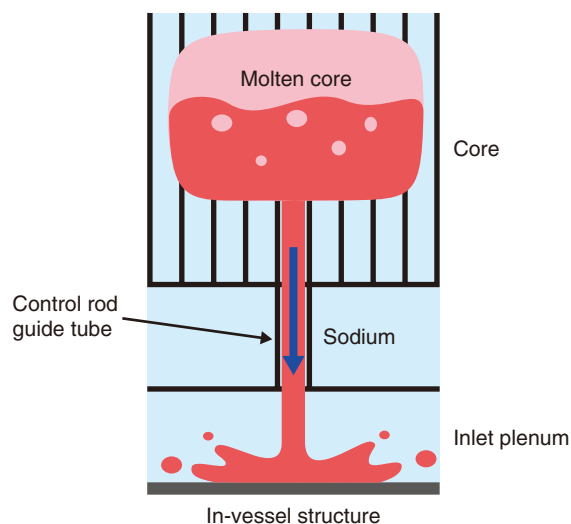


Fig.7-5 Discharge of molten cores below reactor cores

Molten cores can discharge into inlet plenums through control rod guide tubes. If the height of inlet plenums is limited, a jet of molten cores can impinge on in-vessel structures. Coolant boiling can occur simultaneously, which can affect discharge behavior.

During a core-disruptive accident, the molten core of a sodium-cooled fast reactor (SFR) can discharge into the inlet plenums and impinge on in-vessel structures (Fig.7-5). Due to the high temperature of molten cores, the coolant may boil, affecting the sedimentation states of the molten cores on in-vessel structures. Since sedimentation states affect the coolability of molten cores on inlet plenums, a coolability evaluation is crucial to show that molten cores can be retained within reactor vessels. As such, the effects of coolant boiling on the behavior of molten cores that impinge on in-vessel structures must be clarified.

Therefore, a molten core discharge was experimentally simulated using water and alloy with a low melting point (78 °C). Molten alloy (melt) was discharged through a nozzle (inner diameter: 28 mm) into a shallow water pool, and the melt jet impinged on the plate in the pool. The initial temperatures of the melt and water were 350 °C and 30 °C, respectively, to simulate an SFR accident in which stable vapor film is not formed at the interfaces between molten cores and coolant due to the high heat

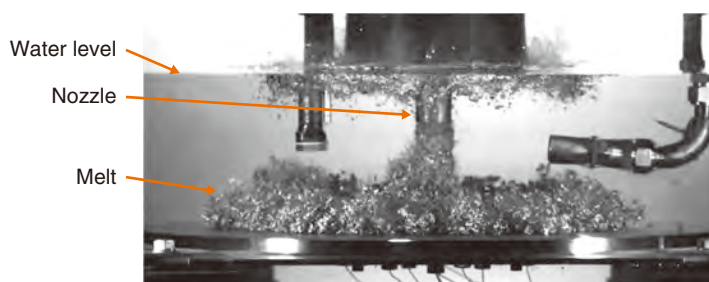


Fig.7-6 Melt dispersion in the simulated experiment

Simulated experiments using water and a molten alloy with a low melting point were conducted. This picture was taken by a high-speed camera 0.1 seconds after the jet impingement on the plate.

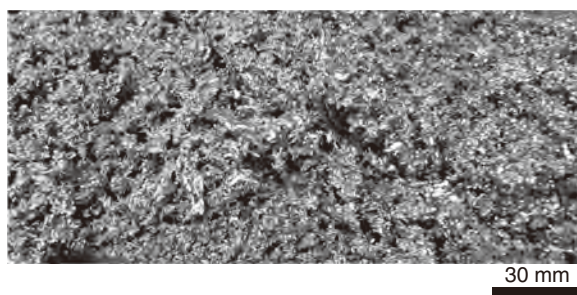


Fig.7-7 State of sediment after the experiment

The sediment was much more fragmented after the experiment than in similar experiments when coolant boiling did not occur.

transfer ability of sodium.

The melt was dispersed along the plate after the impingement on the plate (Fig.7-6), and then solidified with rapid fragmentation and cooling, i.e., the melt changed to form a rough, complex surface, or break into tiny pieces (Fig.7-7). Since this phenomenon was not seen in comparative experiments without coolant boiling, the coolant boiling caused the fragmentation. When the melt was enlarged along the plate by impingement, the contact surface area between the melt and water was also enlarged. Thus, the fragmentation and cooling by the generation of numerous tiny vapor bubbles would be greatly enhanced by the melt expansion.

This work on the molten core discharge in SFRs clarified the impingement of the melt jet on the plate with rapid fragmentation and cooling. As a result, molten cores were revealed to deposit in inlet plenums with rapid fragmentation and cooling. This suggests capability of effective cooling of molten cores in the inlet plenums.

Reference

Imaizumi, Y. et al., Fundamental Experiments of Jet Impingement and Fragmentation Simulating the Fuel Relocation in the Core Disruptive Accident of Sodium-Cooled Fast Reactors, Proceedings of 2017 International Congress on Advances in Nuclear Power Plants (ICAPP 2017), Fukui and Kyoto, Japan, 2017, 17144, 5p., in CD-ROM.

7-3 Uncertainty Analyses of MA Sample Irradiation Test Data — For Better Utilization of the Rare Data —

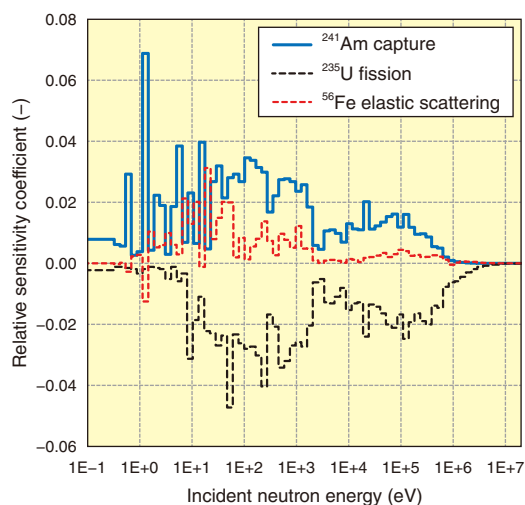


Fig.7-8 Major burnup sensitivity coefficients of the atomic number ratio of ^{242m}Am to ^{241}Am in the irradiated ^{241}Am sample at the reflector position

This figure presents the burnup sensitivity coefficients of MA, dosimeter, and irradiation field with respect to the representative nuclides and reactions.

Aiming to reduce the amount and toxicity of radioactive waste, irradiation tests of minor actinide (MA) samples, including americium and curium, were conducted using the MK-II core of the fast experimental reactor “Joyo” from 1994 to 1999. These tests intended to evaluate and improve the MA nuclear data, or incidental neutron cross-sectional data (hereafter, cross-section).

As the MA samples are minutes and their amount is a few hundred milligrams, the precise evaluation of the local neutron fluence of the MA sample is critical for the calculations of the irradiation tests. However, precisely estimating the local neutron flux via entire core calculations is difficult. The time fluctuation of the local neutron flux should be precisely estimated during long-term irradiation. Therefore, the materials having well-qualified cross-sectional data, e.g., ^{235}U , are usually loaded as a dosimeter in the same position as the MA samples to measure the neutron fluence.

When utilizing these measured data in irradiation tests, it is essential to quantify the uncertainty to judge the applicability for the validation and improvement of the MA cross-section data. The burnup sensitivity coefficients must be calculated with respect to the cross-sections (hereafter, sensitivity). Therefore, a formula, applicable when the dosimeter is considered, was derived.

The resulting major sensitivities of the atomic number ratio of ^{242m}Am to ^{241}Am are presented as “Index ^{242m}Am to ^{241}Am ” in Fig.7-8 in the reflector position. A positive large sensitivity with respect to the ^{241}Am capture cross-section was seen. In addition, negative sensitivity with respect to the ^{235}U fission cross-section, which is due to the dosimeter utilization, was observed, as the increase of the ^{235}U fission cross-section causes a decrease of calculation value by means of the neutron fluence.

Table 7-1 Uncertainty analysis of the atomic number ratios in the irradiated MA samples

This table presents the uncertainties induced by those of the measured atomic number ratios before and after irradiation, and those related to the calculations or used cross-sectional data of the MA samples, dosimeter, and irradiation field.

Index	MA loading position	Difference ^{*3} (%)	Uncertainty (%)			
			Measurement	Cross-section		
				MA	²³⁵ U	Field
^{242m} Am to ²⁴¹ Am ^{*1}	Core	-1	4	7	1	1
	Reflector	-2	8	7	1	2
²⁴⁵ Cm to ²⁴⁴ Cm ^{*2}	Core	+0	4	25	1	1
	Reflector	+9	4	10	1	7

* 1: Atomic number ratio of ^{242m}Am to ^{241}Am in the irradiated ^{241}Am sample.

As ^{242m}Am is produced by the capture reaction of ^{241}Am , the ratio of ^{242m}Am to ^{241}Am increases with burnup. Therefore, the ratio of ^{242m}Am to ^{241}Am after irradiation shows a large sensitivity with respect to the ^{241}Am capture cross-section.

* 2: Atomic number ratio of ^{245}Cm to ^{244}Cm in the irradiated ^{243}Am sample.

As ^{245}Cm is produced by the capture reaction of ^{244}Cm , which is produced from ^{243}Am , the ratio of ^{245}Cm to ^{244}Cm increases with burnup. Therefore, the ratio of ^{245}Cm to ^{244}Cm after irradiation shows a large sensitivity with respect to the ^{244}Cm capture cross-section.

* 3: Calculated vs Experimental

Furthermore, a high sensitivity with respect to the cross-section of ^{56}Fe was observed, which is a main nuclide composing the structural material.

The uncertainty analysis of two types of atomic number ratios are summarized in Table 7-1, where the cross-section-induced uncertainty was obtained by multiplying the sensitivity by the uncertainty of the cross-section. The results of Indices ^{242m}Am to ^{241}Am and ^{245}Cm to ^{244}Cm in the core position were very useful because the discrepancies between the measured and calculated values were negligible and the uncertainties of measurements and cross-section of other than MA are enough small. On the contrary, the Index ^{242m}Am to ^{241}Am in the reflector position showed high uncertainty and equals to that of MA cross-section. Furthermore, the Index ^{245}Cm to ^{244}Cm in the reflector position showed an over-estimation of the calculation value compared with the measured one. Despite low measurement uncertainty, the uncertainty of the irradiation field is quite large as well as that of the MA cross-section uncertainty. This indicates the necessity to confirm the consistency with other reactor physics data sensitive to ^{56}Fe in terms of cross-section improvements.

Subsequently, application of the cross-section adjustment technique indicated that the main cause of the discrepancy is due to the biases of the ^{244}Cm capture cross-section. Furthermore, biases of the ^{56}Fe and ^{235}U cross-sections also contribute to the discrepancy. The derived formula of sensitivity thus plays an important role on the improvement of the MA cross-section data.

This study was carried out under the contract with University of Fukui for research commissioned by the Ministry of Education, Culture, Sports, Science and Technology (MEXT), Japan to University of Fukui.

Reference

Sugino, K. et al., Cross-Section-Induced Uncertainty Evaluation of MA Sample Irradiation Test Calculations with Consideration of Dosimeter Data, *Annals of Nuclear Energy*, vol.130, 2019, p.118–123.

7-4 Development of a Long Life Fast Reactor Control Rod

—Irradiation Behavior of a Sodium-Bonded Absorber Pin—

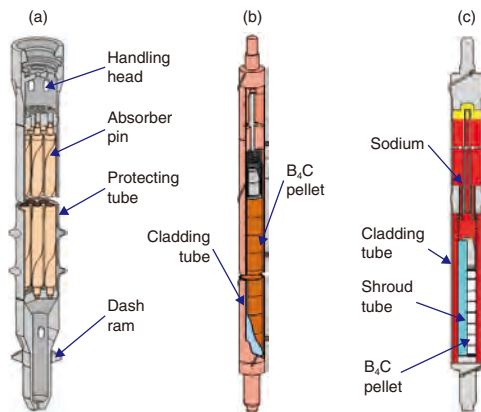
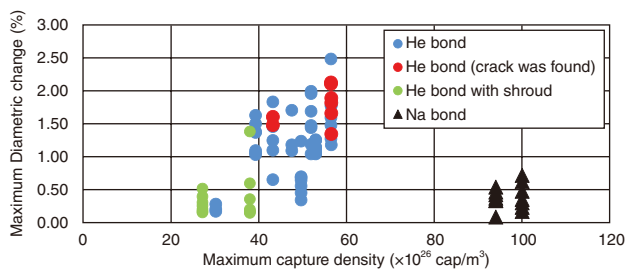


Fig.7-9 (a) Control rod, (b) He-bonded absorber pin, and (c) Na-bonded absorber pin

Seven absorber pins were installed in the control rod of the Joyo. The He-bonded absorber pin was filled with He gas in the pin. The Na-bonded absorber pin was filled with liquid Na, which has a high thermal conductivity, to lower the temperature of the pellets. In the Na-bonded absorber pin, the gap between pellets and cladding was expanded and the shroud tube was covered with pellets.



In a fast reactor, the control rod is used to control the fission reaction, adjust the produced power, and stop the nuclear chain reaction when the reactor is switched off. Boron carbide (B_4C) is used as the pellets of control rod. Boron can absorb neutrons, generating helium in a (n, α) reaction. To generate helium in the pellets and high temperature environments in the reactor, the pellets are cracked. The pellet fragments are relocated and the pellets swell. These cause absorber cladding mechanical interaction (ACMI).

Seven absorber pins were installed in the control rod of the fast breeder reactor “Joyo” (Fig.7-9(a)). A He-bonded absorber pin (Fig.7-9(b)) was filled with He gas, which provided a high thermal conductivity between the pellet and cladding. Because of ACMI, the capture density of He-bonded absorber pins are limited to $50 \times 10^{26} \text{ cap/m}^3$.

To prevent ACMI, Na-bonded absorber pins were developed (Fig.7-9(c)). Na-bonded absorber pins are filled with liquid Na to lower the temperature of the pellets, as Na has a thermal conductivity about 900 times greater than does He. The resulting Na-bonded absorber pins demonstrated an expanded gap between

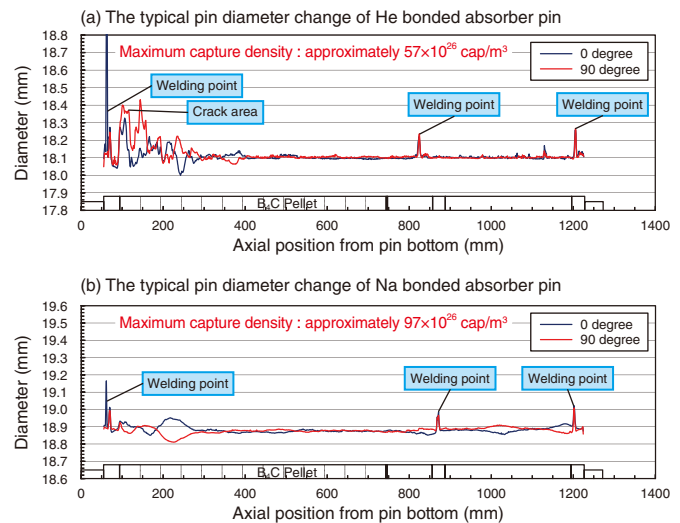


Fig.7-10 Typical pin diameter change of the (a) He- and (b) Na-bonded absorber pins

The resulting diameter change and anisotropic deformation of the Na-bonded absorber pin was lower than the He-bonded absorber pin.

Fig.7-11 Maximum diametric change as function of maximum capture density

The maximum diametric change of the Na-bonded absorber pins was lower than that of the He-bonded absorber pins with or without a shroud tube.

the pellets and cladding and a shroud tube covered with pellets.

The Na-bonded absorber pins were irradiated in Joyo to $100 \times 10^{26} \text{ cap/m}^3$ which was twice higher than upper limit of the capture density for He-bonded absorber pins, and then examined. Examples of the resulting pin diameter changes are shown in Figs.7-10 and 7-11. Because the control rods are pulled up in the operation of reactor, the lower part is the highest capture density and temperature. As a result, ACMI is caused in the lower part of the control rods. Although the Na-bonded absorber pins had a larger capture density than did the He-bonded absorber pins, the diameter change and anisotropic of Na-bonded absorber pin (Fig.7-10(b)) was lower than for the He-bonded absorber pin (Fig.7-10(a)). The maximum diametric change of the Na-bonded absorber pins was also lower than the change of the He-bonded absorber pins with or without a shroud tube. (Fig.7-11). Thus, Na-bonded absorber pins were shown to be durable for long-term use.

We will observe shroud tubes and pellets for the development of control rod.

Reference

Sasaki, S. et al., Irradiation Performance of Sodium-Bonded Control Rod for the Fast Breeder Reactor, Journal of Nuclear Science and Technology, vol.55, issue 3, 2018, p.276–282.

7-5 Advancing Microwave Heating Denitration Technology

— Development of Particle Control Technology to Improve Powder Characteristics —

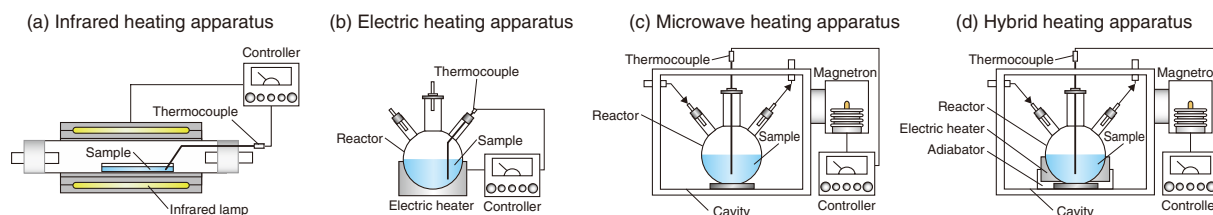


Fig.7-12 Schematics of the apparatus used for various heating methods

The hybrid heating apparatus can more uniformly heat the entire sample than the microwave heating apparatus, because it has both an electric heater installed around the reactor and microwave heating.

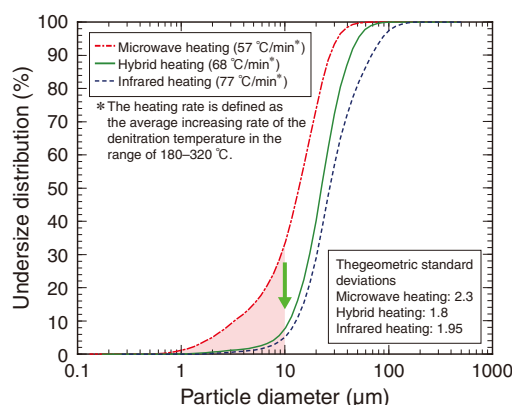


Fig.7-13 Undersize distribution of CuO powders synthesized using various heating methods

The hybrid heating method reduced the ratio of fine powders to less than 10 μm in the CuO powders and sharpened the undersize distribution because of the minimum geometric standard deviation of the undersize distribution.

During reprocessing, a mixture of plutonium nitrate and uranyl nitrate is recovered from spent fuel and converted into a mixed oxide (MOX) raw powder using a microwave heating denitration method. The raw MOX powder obtained in this method has good sinterability and can produce high-quality pellets. However, raw MOX powders contain many fine particles, making fuel fabrication difficult; therefore, particle control technology is required to improve the powder flowability, depending on particle size and shape for the powder handling such as die filling and transfer in the fuel fabrication. To investigate the effects of heating method and rate on the resulting copper oxide (CuO) powder characteristics, a copper nitrate aqueous solution was used to simulate the mixed solution of plutonium nitrate and uranyl nitrate, and was heated (Fig.7-12) using infrared heating, an electric heater, microwave heating, and hybrid heating (i.e., a combination of microwave heating and using an electric heater) under varied output power.

The resulting undersize distribution (i.e., particle size distribution) of the synthesized CuO powders is shown in Fig.7-13; at the same heating rate, the powder obtained by microwave heating was finer, with a ratio of particles less than

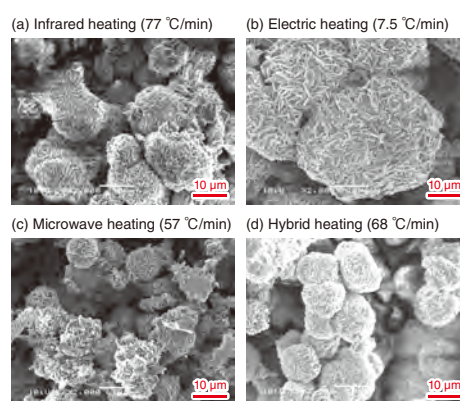


Fig.7-14 Scanning electron micrograph of CuO powders synthesized by each heating method

The CuO powder produced by the hybrid heating method present better particle characteristics, including uniform particle diameter, less irregularly shaped particles, and more spherical and smooth surface conditions.

10 μm in diameter of over 30%. The hybrid heating method provided a power with a fine powder ratio of under 10%. Furthermore, the undersize distribution became sharp because the geometric standard deviation of the undersize distribution was the smallest. Therefore, a hybrid heating method can improve the powder handling such as die filling and transfer in the fuel fabrication.

Comparing the CuO powders obtained from each heating method (Fig.7-14) showed that the particles synthesized by the hybrid heating (Fig.7-14(d)) had better particle conditions than those obtained by the other studied methods (Figs.7-14(a)–(c)). The hybrid heating method employed enabled uniform nucleation and growth of the particles, as the entire sample can be uniformly heated by a combination of internal heating (via a microwave) and external heating (via an electric heater). Thus, the hybrid heating method is an effective method for improving powder characteristics.

Future work will aim to further investigate the effectiveness of the proposed hybrid heating method, both via experiments using a nuclear fuel material and via numerically analyzing the temperature field.

References

- Segawa, T. et al., Influence of the Heating Method on the Particle Characteristics of Copper Oxide Powders Synthesized from Copper Nitrate Aqueous Solutions, *Chemical Engineering Science*, vol.153, 2016, p.108–116.
- Segawa, T., Development of Synthesis and Morphology Control Method of Metallic Oxide Particles Using Microwave Heating, Hiroshima University, Ph. D. thesis, 2018, 100p. (in Japanese).

Toward Decommissioning of Nuclear Facilities and Radioactive Waste Management

To maintain and develop its R&D capabilities by strengthening the safety of its nuclear facilities and ensure steady implementation of back-end measures, JAEA formulated the “Medium- and Long-Term Management Plan of our Facilities” (issued on April 1, 2017, amended on April 1, 2019) as a comprehensive plan which detailed the following three points:

- the selection and consolidation of facilities,
- safety measures, and
- management of back-end issue.

In the plan, 89 nuclear facilities were chosen to be decommissioned.

JAEA submitted an application for permission to proceed with the decommissioning of MONJU and the Tokai Reprocessing Plant (TRP) to the Nuclear Regulation Authority (NRA), which led to NRA granting this permission for MONJU on March 28, 2018 and for TRP on June 13, 2018.

Implementation of back-end measures requires long-term prospects and policies, including regarding the processing and disposal of radioactive waste; the decommissioning of TRP has been expected to take approximately 70 years to complete.

JAEA therefore published a long-term prospect and policy for back-end measures, i.e., the “Back-end Roadmap”, on December 26, 2018.

To ensure a safe and appropriate nuclear facility decommissioning and radioactive waste management, it is necessary to introduce new technologies and knowledge and to promote the development of technologies for advanced safety and cost reduction. We have been comprehensively developing technologies for the safe and effective dismantling of nuclear facilities, minimization and stabilization processing of radioactive wastes, and the disposal of radioactive wastes (Fig.8-1). The proposed disposal project will be able to be applied to low-level radioactive wastes from research facilities of universities and private organizations as well as our own.

Specifically, this year saw the development of an analytical method of uranyl ions in radioactive wastes (Topic 8-1), a proposed decontamination technology for radioactive wastes (Topic 8-2), a study on the stability of disposal procedures of radioactive wastes (Topic 8-3), and a study on the reclamation of Ningyo-Toge uranium mines (Topic 8-4).

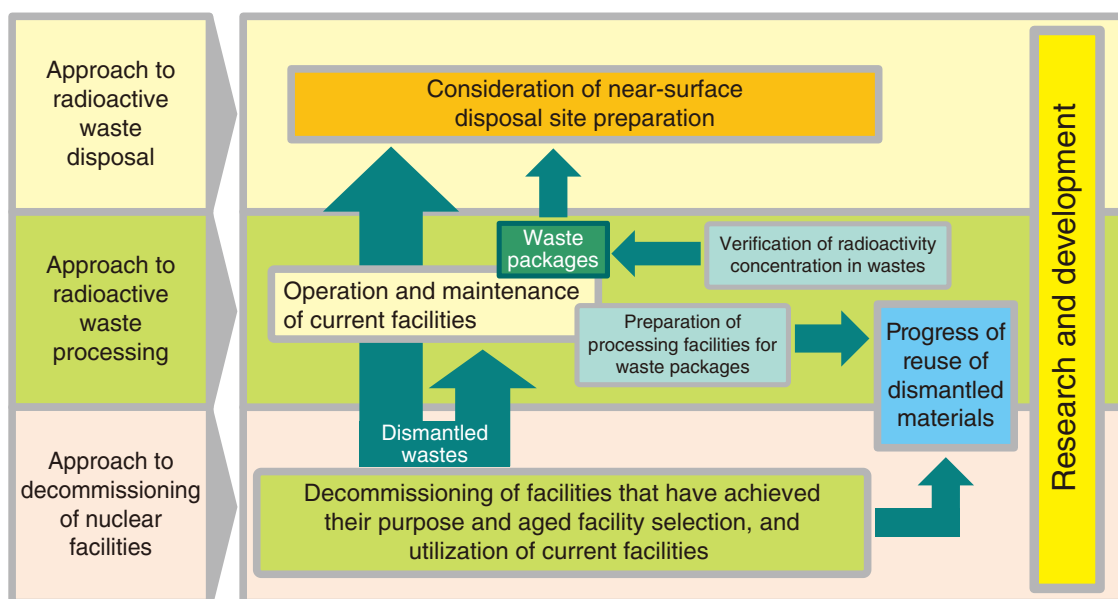


Fig.8-1 Outline of low-level radioactive waste management

The research and development of the decommissioning of nuclear facilities and the processing of radioactive wastes, including waste treatment and waste characterization, have been promoted.

R&D to Improve Technology and Reliability of Geological Disposal in Japan

Geological disposal is internationally recognized as the most appropriate method for the long-term isolation of high-level radioactive waste (HLW) produced during the generation of nuclear power from human environments. This is a critical issue which the present generation must approach sensibly and will remain as such, regardless of any revision to the national nuclear energy policy.

In Japan, fuel spent in power reactors is reprocessed to extract the reusable uranium and plutonium for power generation. The liquids separated from the spent fuel during chemical reprocessing are solidified into a stable glass form. Under the

Japanese disposal concept, vitrified waste is encapsulated in a thick steel overpack, surrounded by highly compact bentonite, and placed in a stable geological environment at a depth of more than 300 m below ground (Fig.8-2).

Implementing geological disposal methods of HLW is a long-term project that will last over 100 years. The project begins with the site selection and continues with the repository construction and operation, which is followed by backfill for repository closure. It is a national responsibility and of great importance to proceed efficiently with the project, continuously improving its sound technical basis and applying these attitudes to its

implementation, regulatory activities, and to the enhancement of public confidence. To improve the technologies used for reliable geological disposal in Japan, progress in the R&D in various fields such as geoscience, repository engineering, and safety assessment have and will continue to be of the utmost priority (Fig.8-3).

Underground Scientific Research

Research has centered around projects at two underground research laboratories (URLs), including the examination of crystalline rocks at Mizunami and of sedimentary formations at Horonobe (Topics 8-5 and 8-6, respectively).

To evaluate the long-term stability of geological environments in Japan, studies on topics such as tectonics, volcanic and faulting activities, and dating techniques are currently in progress at the Toki Geochronology Research Laboratory (TGR) (Topics 8-7 and 8-8).

R&D of Geological Disposal Technologies

Together with the above-mentioned geoscientific efforts, an extensive study to assess the performance of the disposal system, engineered barrier systems, and long-term chemistry and migration of radionuclides at Tokai (Topics 8-9 and 8-10) are being performed. These studies have exploited the data and

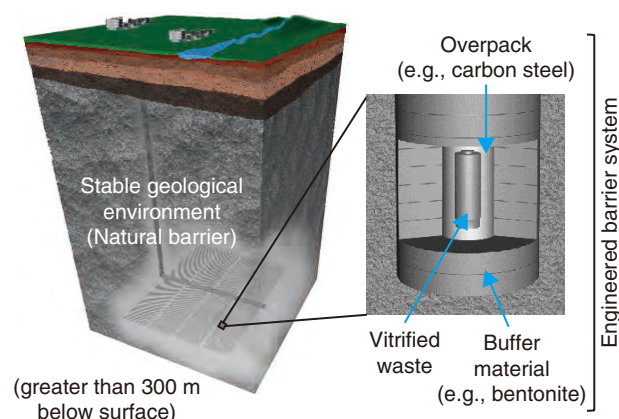


Fig.8-2 Schematic of the geological disposal concept for high-level radioactive waste in Japan

information on geological environments that were obtained through geoscientific research at the mentioned URLs.

Results of these activities have been summarized as a web-based report (CoolRep) on JAEA's public website (CoolRep: <https://kms1.jaea.go.jp/CoolRep/english.html>).

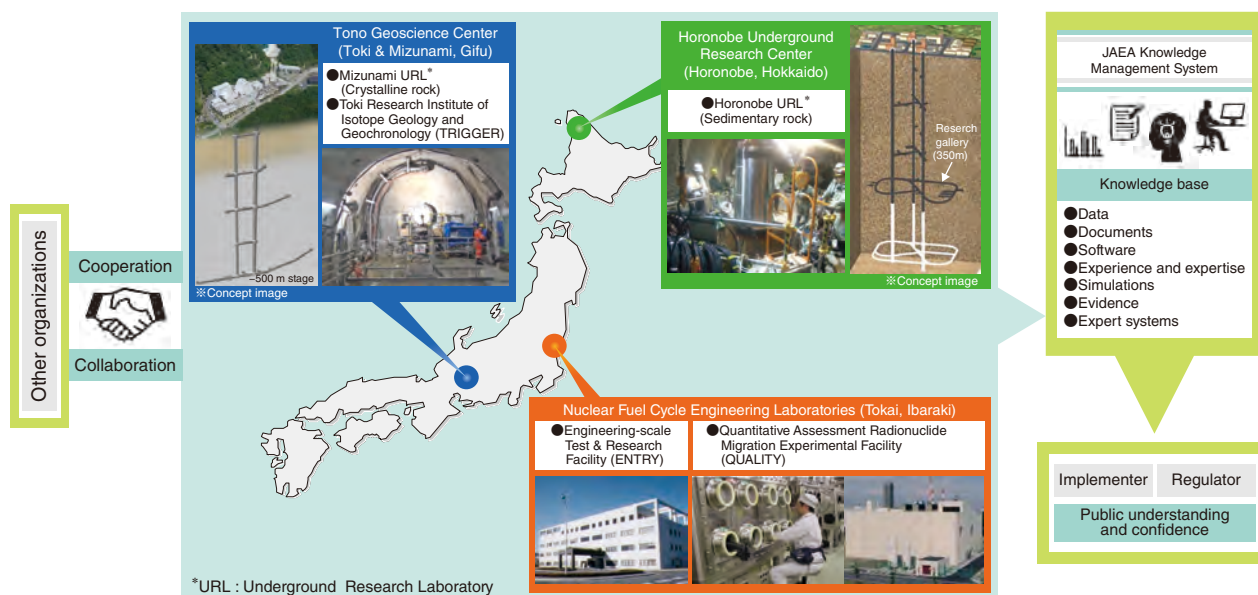


Fig.8-3 Structure of JAEA R&D activities

Improving the Safety of the TRP and Developing Decommissioning Technologies

The decommissioning plan for the Tokai Reprocessing Plant (TRP) received approval from the Nuclear Regulation Authority (NRA) in June 2018, entering the TRP into a new stage of decommissioning. The vitrification of high-level radioactive liquid waste has been conducted with primary focuses on safety and on the risk reduction of the radioactive material stored as a solution. Advanced vitrification technologies have been developed and vitrification of the high-level radioactive liquid waste is scheduled to be completed by the 2028 Japanese fiscal year.

Cementation technologies of the low-level radioactive liquid waste have been developed. However, if low-level radioactive liquid waste is solidified directly, bringing the solidified waste

into a disposal site may be restricted, since nitrates have been designated as an environmentally regulated substance for near-surface disposal. As such, installation of a new equipment that the nitrate is replaced with carbonate has been decided, and a new cement material suitable for carbonate, blast furnace slag fine powder (BFS), has been selected. Drum scale solidification tests confirmed that the solidified samples satisfied compressive strength requirements (Topic 8-11).

Additionally, the reprocessing adaptability of new fuel cladding tube material has been studied to prevent severe accidents in the nuclear reactor (Topic 8-12), and the flow in a centrifugal contactor has been studied to predict the extraction of uranium and plutonium (Topic 8-13).

8-1 Simplification of the Analysis of Uranyl Ions in Radioactive Wastes

— Development of an Analytical Method with Capillary Electrophoresis Using Novel Fluorescent Reagents —

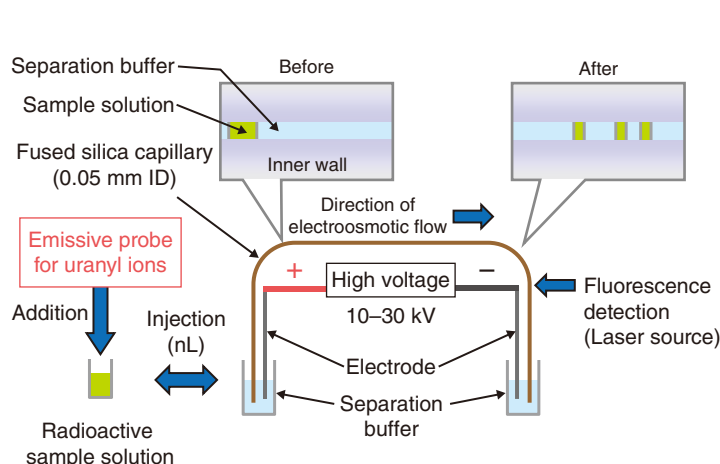


Fig.8-4 A simple analytical method with capillary electrophoresis
Capillary electrophoresis is a high-performance separation technique using the difference in electrophoretic speed due to ionic charge and size in a capillary tube with a small internal diameter.

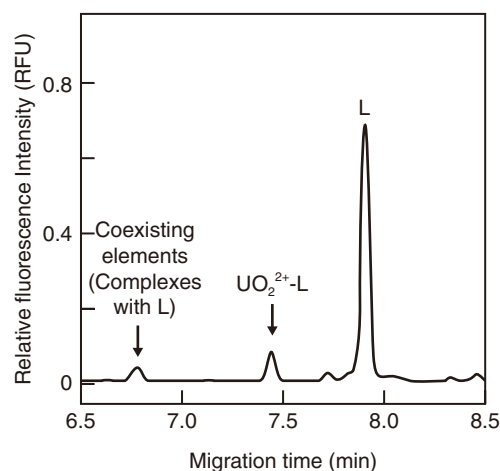


Fig.8-6 Typical electropherogram of a uranyl complex with probe L
A successful separation and detection of uranyl ions in coexisting elements using the probe L.

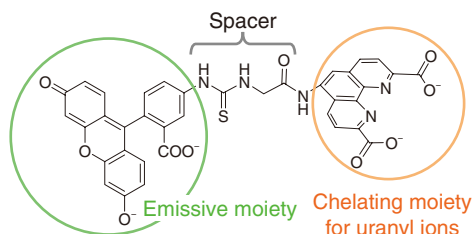


Fig.8-5 Emissive probe L for uranyl ions
The probe L is composed of an emissive moiety for improving the sensitivity and a chelating moiety for connecting to the uranyl ions.

It is necessary to evaluate the radioactivity concentrations of radionuclides in samples collected from radioactive wastes to ensure their safe disposal. To reduce exposure of operators to radiation during analytical procedure, a simple analytical method for uranyl ions was developed using capillary electrophoresis (CE) (Fig.8-4). Although CE has been employed to efficiently and easily separate ionic species due to their difference in electrophoretic speed caused by ionic charge and size differences in a small-diameter capillary tube, the sensitivity of prior methods using absorbance detection was too low for practical usage in radioactive waste samples.

This study therefore focuses on a capillary electrophoresis-laser induced fluorescent detection method (CE-LIF) to improve the sensitivity by a factor of approximately one million, from the level of ppm to that of ppt. A new emissive probe suitable for CE-LIF was designed to detect uranyl ions, UO_2^{2+} . The emissive probe was composed of an emissive moiety for improved sensitivity, a chelating moiety for connecting with uranyl ions and a spacer between them. A chelating moiety is required for stability not to dissociate from uranyl ions during migration. Emissive probes synthesized with multidentate chelating moiety

were applied to CE-LIF and to investigate the stability of the chelating moiety based on experimental studies and molecular orbital calculations. As a result, a tetradentate probe (Fig.8-5) achieved a successful separation and detection of uranyl ions (Fig.8-6). A detection limit of 0.7 ppt was obtained for uranyl ions. Therefore, the developed fluorescent detection method was one million times more sensitive conventional UV absorbance detection methods. The established CE-LIF method was then applied to radioactive liquid samples obtained from a JAEA radioactive waste treatment facility; the ability to separate and detect uranyl ions in coexisting elements was thus demonstrated. This method, requiring only a small sample volume and analytical time within ten minutes, can be used to analyze radioactive samples to reduce the radiation exposure to operators.

This research was supported by the Japan Society for the Promotion of Science (JSPS) KAKENHI Grant-in-Aid for Young Scientists (B) (No.16K17926), “Development of highly sensitive and rapid analytical method for ultratrace actinide ions in radioactive samples by capillary electrophoresis”.

Reference

Haraga, T. et al., Safe and Rapid Development of Capillary Electrophoresis for Ultratrace Uranyl Ions in Radioactive Samples by Way of Fluorescent Probe Selection for Actinide Ions from a Chemical Library, *Analytica Chimica Acta*, vol.1032, 2018, p.188–196.

8-2 Reducing the Generation of Uranium Waste

— Decontaminating Metal Using Acidic Electrolytic Water —

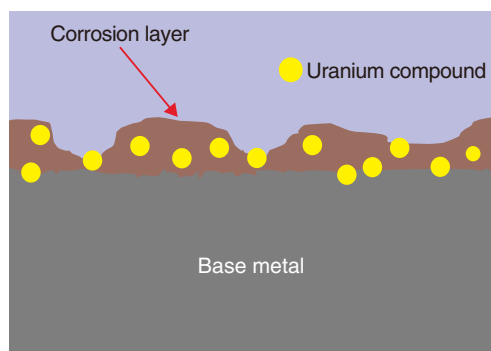


Fig.8-7 Concept of a metal surface contaminated by a uranium compound

Most uranium particles move to the corrosion layer during its formation, whereas a small amount diffuses into the base metal.

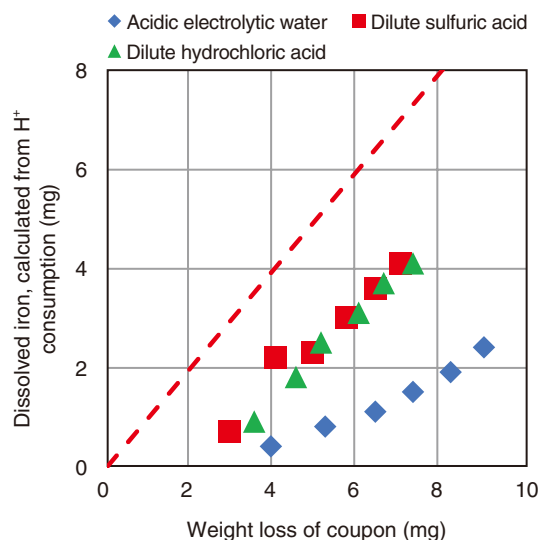


Fig.8-8 Dissolution characteristics of carbon steel coupons with a corrosion layer

Both the base metal and corrosion layer were removed, as the coupon weight loss was greater than dissolved iron, calculated from H^+ consumption. In addition, more weight was lost when using the dissolved iron in the acidic electrolytic water (pH: 2.58) than when using dilute sulfuric acid (pH: 2.53) or dilute hydrochloric acid (pH: 2.59).

To reduce costs and environmental burdens, decontamination technologies have been under development to reduce uranium waste generation. As the metal waste generated from dismantling uranium handling facilities can be contaminated with uranium, they must be decontaminated to the clearance level and then reused or disposed of as non-radioactive waste.

As metal waste encompasses a variety of materials, shapes, and surface conditions, a wet decontamination method using dilute sulfuric acid is generally applied. However, this process generates excessive secondary waste and many metals, such as carbon steel, is excessively dissolved.

A corrosion layer is easily generated on carbon steel, the main material of centrifuges used for uranium enrichment, when exposed to atmospheric water during dismantling. As the corrosion layer is formed on surface by uptake of oxygen from the atmosphere, most of the uranium on the surface has moved to the corrosion layer as shown in Fig.8-7, but a small quantity of uranium diffuses into the base metal.

Removing the corrosion layer with the conventional decontamination method is time-consuming. The added exposure time of the metal to the acid used causes secondary waste containing dissolved base metal.

The applicability of acidic electrolytic water (AEW) as a decontamination solution to dissolve uranium and minimize the dissolution of the base metal was examined. The AEW used contained approximately 100 ppm of hydrochloric and hypochlorous acid, resulting in a pH of 2.5–2.8 and an oxidation–reduction potential above 1100 mV. The following results were obtained.

- (1) Weight loss to the amount of iron dissolution for AEW was the largest in simulant coupons test. Thus, the corrosion layer was removed more effectively than when using dilute sulfuric acid (Fig.8-8).
- (2) The target surface decontamination density (0.04 Bq/cm^2) was achieved in approximately half the time when AEW combined with ultrasonic cleaning was used rather than when other acids were used.
- (3) Approximately 20% less secondary waste was generated when AEW, due to the difference of the amount of iron components in the solutions.

This study was conducted in collaboration with Japan Nuclear Fuel Limited. We will continue to work with this company on the practical use of metal decontamination technology.

Reference

Nakayama, T. et al., Study on Decontamination of Steel Surface Contaminated with Uranium Hexafluoride by Acidic Electrolytic Water, Proceedings of 2019 International Congress on Advances in Nuclear Power Plants (ICAPP 2019), Juan-les-pins, France, 2019, 8p.

8-3 Ensuring the Stability of Trench-Type Radioactive Waste Disposal Facilities

— Examination of Waste Acceptance Criteria of Sand Filling to Reduce Voids in Waste Packages —

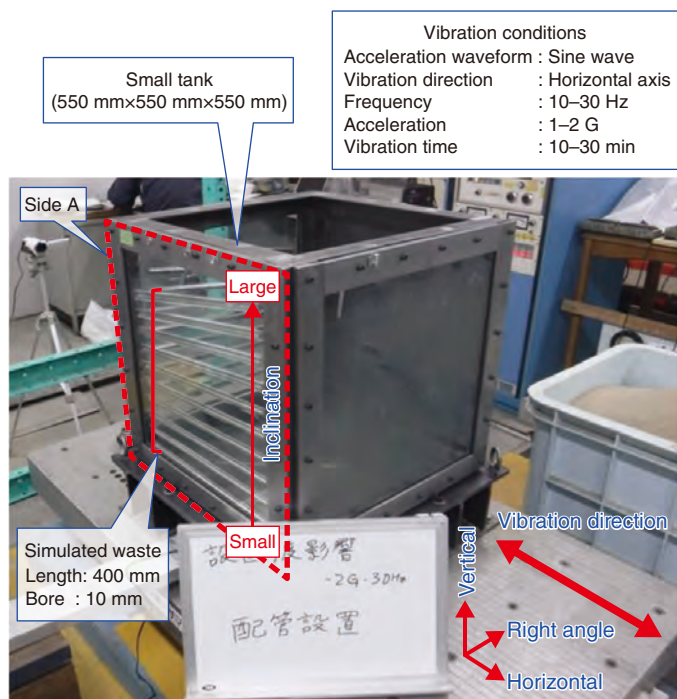


Fig.8-9 Test setup, including box and vibrator

To see the state of sandy soil filling the simulated waste container, a half-split tube was placed on the glass surface in a tempered glass box simulating a metal container. The vibration conditions were chosen as easily possible ones.

This work prototyped a trench-type disposal of very low-level radioactive wastes generated in the research and development of the nuclear energy as well as medical, industrial uses of radioisotope expect nuclear power plant in Japan. The metal waste was placed into metal containers for ease of handling and to prevent the radioactive materials from scattering.

However, voids remain in the filled containers because current regulation does not require them to be fully solidified (e.g., by filling in the voids with sand or cement). Large voids may lead to depressing the cover soil of trench-type disposal facility after long time period. It is thus necessary to fill the containers with sand to reduce the void volume to or below 20%. The void volume in a container can be evaluated on the basis on the weight and density of sand inserted into a container.

This work therefore aimed to examine the filling property of simulated wastes in a container to develop waste acceptance criteria relevant to standard filling conditions and methods to reduce the void space.

Heat transfer tubes in which a high voids are remained was used as simulated wastes. And we closed the heat transfer tubes of one side were used as a difficult filling condition of simulated

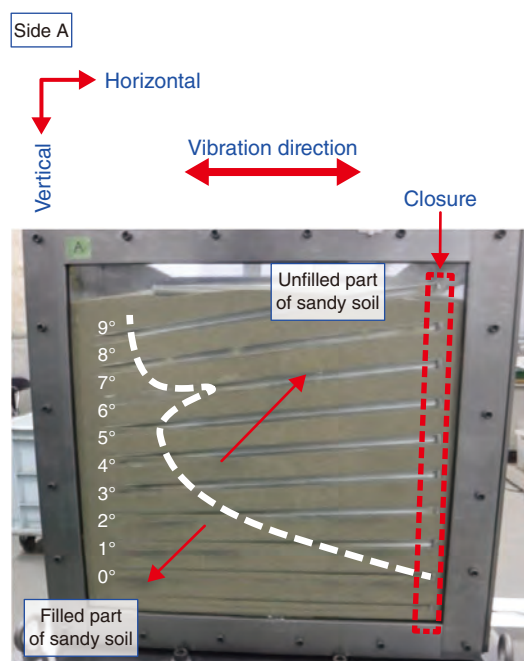


Fig.8-10 Resulting

Nine simulated wastes were installed with a 1° increment from the horizontal direction over 30 minutes of vibration using an acceleration and frequency of 2 G and 30 Hz, respectively.

wastes (Fig.8-9). As waste is normally placed into a container at random, the heart transfer tubes were placed into a test box in a way that its inclination is larger toward the upper side. The box was then filled with soil while being vibrated on a shaking table. The filling property was visually observed after a certain period of vibration.

The results indicated that box was densely and uniformly filled with soil, leaving the void volume to or below 20% when the heart transfer tubes were set horizontally to the direction of vibration. On the other, the filling rate of soil in the heart transfer tube reduced as the inclination of the heart transfer tube increased (Fig.8-10).

Overall, the void volume of the containers could be reduced to meet the standard when the waste tubes were set horizontally to the direction of vibration. Based on the result, the test conditions for the actual size (about 1 m³) of the metal container were clarified.

Future work will aim to develop filling methods and waste acceptance criteria for metal wastes disposed of in metal containers and confirm them via full-scale tests.

Reference

Nakata, H. et al., Waste Acceptance Criteria for Waste Packages Destined for near Surface Disposal Containing Radioactive Waste from Research, Industrial and Medical Facilities – Study on a Method that Fills Voidage in Waste Package with Sandy Soil –, JAEA-Technology 2017-031, 2018, 41p. (in Japanese).

8-4 Improvement of Matching Method for Seepage Flow Analysis

— Application of Inversion for Seepage Flow Analysis in Multi-Layered Earthen Cover —

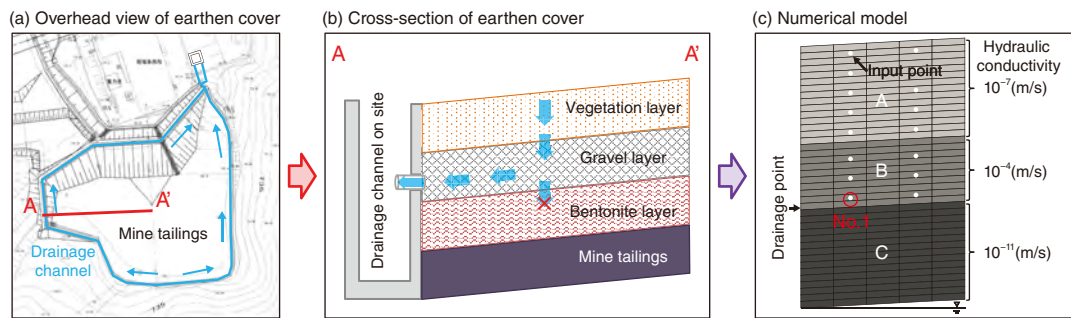


Fig.8-11 Multi-layered earthen cover

(a) Mine tailings site locations in the uranium mine surrounded by the drainage channel. (b) Earthen cover to prevent contact between infiltrated rainwater and mine tailings, including a bentonite layer with low permeability to prevent contact between infiltrated rainwater and mine tailings, a gravel layer with high permeability to drain rainwater blocked by the bentonite layer, and a vegetation layer to prevent the outflow of the gravel layer. (c) Numerical model consisting of three layers representing the earthen cover, where A, B, and C correspond to the vegetation, gravel, and bentonite layer, respectively.

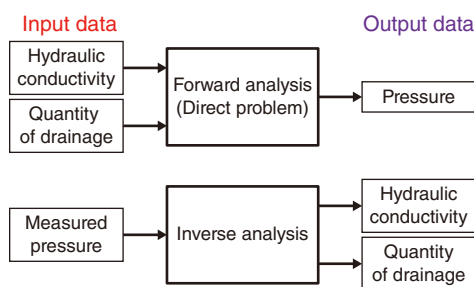


Fig.8-12 Analysis flow

Input and output data for forward (direct problem) and inverse analysis.

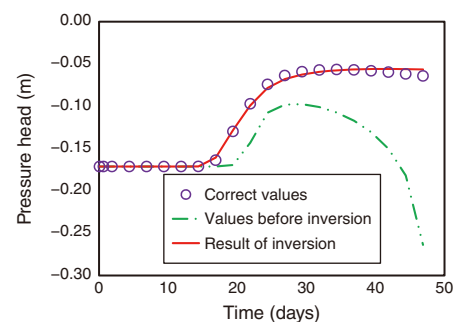


Fig.8-13 Result of inverse analysis

Pressure head match the correct value at No.1 in Fig.8-11(c).

In an effort to reduce the environmental burden of uranium mines, earthen covers have been installed on the mine tailings shown in Figs.8-11(a) and (b) to reduce the generated wastewater caused by rainwater contacting the mine tailings. Groundwater flow simulations have been used to evaluate the impact of these covers. However, the forward analysis method used in such models has often provided results that do not match the measured values at the site, likely due to the heterogeneity of soil properties caused by construction and to the measurement error of the drainage flow on the side. Model calibration is often carried out by trial and error to help remedy this problem. Unfortunately, this method increases thus subjectivity; as such, a more objective input parameter setting method is required. In another method, shown in Fig.8-12, the hydraulic conductivity and quantity of drainage flow can be simultaneously estimated by using a known water pressure distribution. This process, known as inverse analysis, leads to more efficient calibration. Furthermore, we used the adjoint state method with the quasi-Newton method to perform high-speed calculations. Therefore,

this work proposes the application of inverse analysis by the adjoint state method with the quasi-Newton method on a saturated-unsaturated flow in such a field.

A numerical analysis using inverse analysis was carried out. To evaluate the effectiveness of the inverse analysis method, the following experiment was designed. First, the water pressure distribution was calculated by forward analysis and labeled as the correct value. An inverse analysis based on the correct values was then performed to estimate the hydraulic distribution and drainage quantity; the results, shown in Fig.8-13, indicate that the correct values could be expressed appropriately with forward analysis using the estimation result by inverse analysis. Thus, uncertain parameters can be estimated by simultaneous inverse analysis. Using this method allows the necessary input parameters for forward analysis to be obtained, which may lead to an improved understanding of groundwater flow. Furthermore, applying this method to earthen covers will allow researchers to evaluate the effects of rainwater infiltration, thus contributing to the development of a rational and effective earthen cover.

Reference

Inoue, J. et al., Numerical Experiments by Saturated-Unsaturated Flow Inversion for Permeability and Boundary Conditions of Multi-Layers Aquifer, Journal of Japan Society of Civil Engineers, Ser. A2 (Applied Mechanics (AM)), vol.74, no.2, 2018, p.I_55-I_64 (in Japanese).

8-5 Evaluating the Uncertainty of the Redox Potential in Groundwater

— An Application Example Based on Monitoring Data of Water Quality in the Horonobe Area —

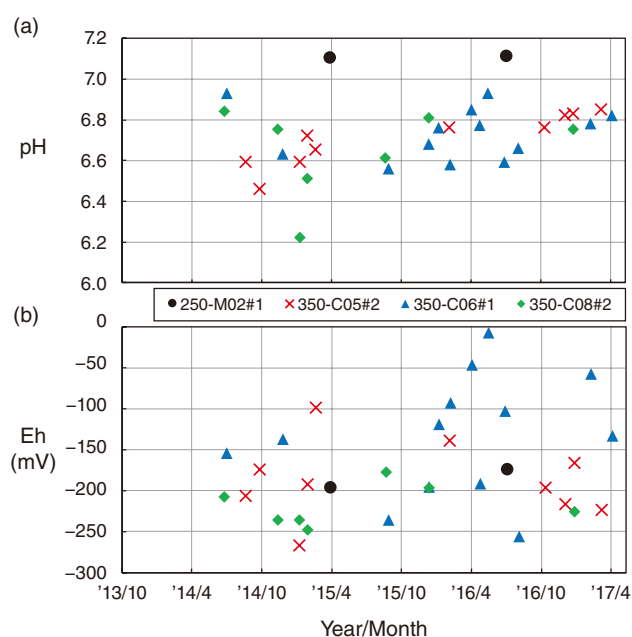


Fig.8-14 Temporal variation in pH and Eh of groundwater observed in boreholes near the URL

(a) shows temporal variation in pH, (b) shows temporal variation in Eh.

Understanding the redox condition of groundwater is important for geological disposal of high-level radioactive wastes, as it can affect the solubility of redox-sensitive radioactive nuclides and the corrosion rate of overpack. Generally, not all of the redox-sensitive species in groundwater are in equilibrium with respect to the measured redox potential (Eh). The fluctuation range or uncertainty of the Eh can be estimated by calculating the equilibrium potential and the fluctuation range of the dominant redox reactions and by comparing them with measured Eh values.

Thus, this study aimed to evaluate the uncertainty of Eh using hydrochemical monitoring data of groundwater in the Horonobe Underground Research Laboratory (URL). The measured temporal variation of the pH and Eh of the groundwater is shown in Figs.8-14(a) and (b), respectively. In zone 1 of borehole 250-M02 (250-M02#1) located at 250 m gallery, the measured pH and Eh were 7.1 and approximately -200 – -170 mV, respectively. The three boreholes located at 350 m gallery (350-C05#2, 350-C06#1, 350-C08#2), the pH and Eh ranged from 6.2 to 7.0 and from -250 to 0 mV, respectively. Significant changes in the concentration of chemical species were not found

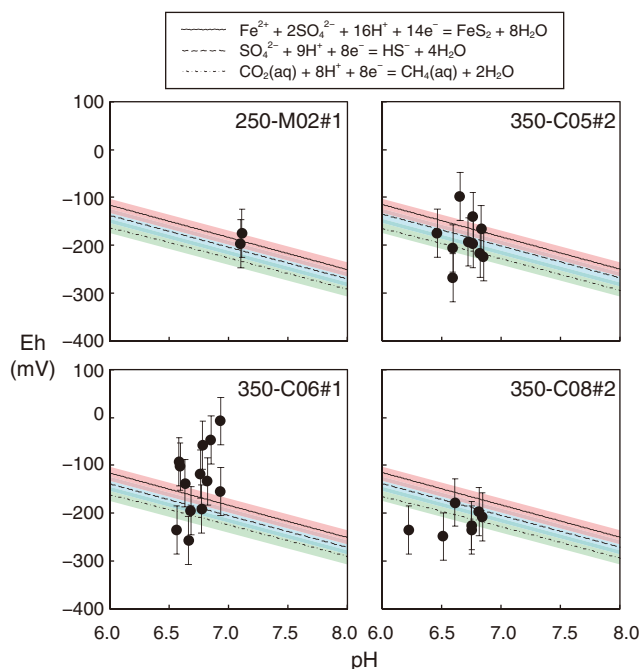


Fig.8-15 pH-Eh diagram of groundwater near the Horonobe URL

The uncertainty of equilibrium potential for reaction regarding $\text{Fe}^{2+}/\text{FeS}_2$, $\text{SO}_4^{2-}/\text{HS}^-$ and $\text{CO}_2(\text{aq})/\text{CH}_4(\text{aq})$ is shown in red, blue and green, respectively. The error bars are ± 50 mV.

after the excavation of the boreholes or niches adjacent.

A pH-Eh diagram of the estimated redox reactions is shown in Fig.8-15, where the black dots and three lines represent the measured values and equilibrium potential of the reactions, respectively. The colored area represents the possible fluctuation range of the potential of each reaction as calculated by the variation in the concentration of chemical components and groundwater temperature. The error bars in the Fig.8-15 indicate that the difference between the measured values and equilibrium potentials was approximately ± 50 mV. This is reasonable when considering the uncertainty of the measured value of Eh based on previous studies. This uncertainty is likely caused by the measurement error of the sensor, deterioration of the electrode, and sticking of bubbles degassed from the groundwater on the electrode. The data for 350-C06 was probably not in equilibrium with respect to the redox reactions because the Eh fluctuation was larger than observed in other boreholes (Fig.8-14(b)).

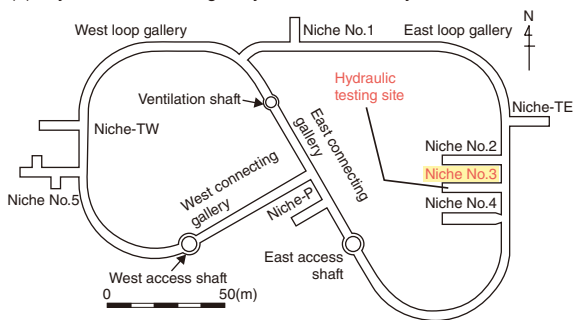
Future work will aim to continue hydrochemical monitoring work towards the development of methods to reduce the measurement error.

Reference

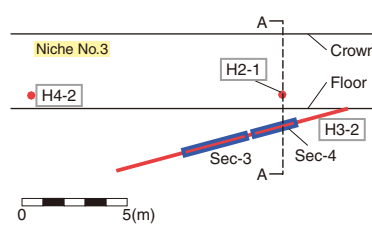
Mochizuki, A. et al., Evaluation of Uncertainty of Redox Potential in Deep Groundwater: A Case Study in the Horonobe Area, Hokkaido, Journal of Groundwater Hydrology, vol.61, no.1, 2019, p.3–20 (in Japanese).

8-6 Estimating the Hydraulic Conductivity around a Gallery before Excavation — An Estimation Method Applying the Mean Stress Index —

(a) Layout of the 350 m gallery and site for the hydraulic test



(b) Vertical section perpendicular to the tunnel axis



(c) Cross-sectional view

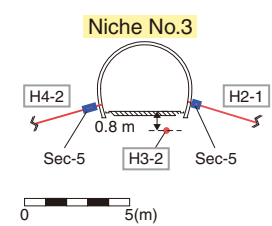


Fig.8-16 The studied site and layout of hydraulic testing

Three boreholes (H2-1, H3-2, and H4-2) were drilled for the test. Each test section was isolated by packers. The hydraulic conductivity of the EDZ around the side wall was measured in section 5 of H2-1 and section 5 of H4-2. In addition, the hydraulic conductivity of the EDZ below the floor was measured in sections 3 and 4 of H3-2.

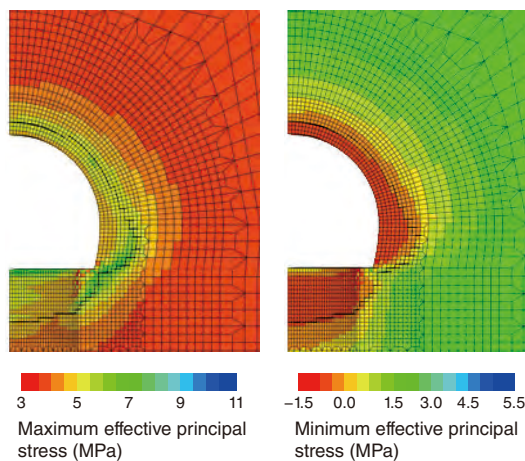


Fig.8-17 Contour map of effective stress around Niche No.3

The resulting distribution of the maximum and minimum effective stress, where compressive stress was taken to be positive.

The hydraulic conductivity around a repository of geologically disposed high-level radioactive waste is thought to be increased due to the stress redistribution during facility excavation. This stress-redistributed zone is called the excavation damaged zone (EDZ), and can provide a pathway for the migration of radionuclides around the repository. Thus, it is important to develop a method to predict the hydraulic conductivity in the EDZ applying the result of surveys performed prior to the excavation (surface-based investigation) for the efficient safety assessment.

Although researchers have estimated the hydraulic conductivity in the EDZ, the developed models cannot do so based on the result of the surface-based investigation. The highest potential hydraulic conductivity in a fault or natural fracture can be estimated using the mean stress index (MSI), which is the ratio of the effective mean stress to the tensile strength of rock. Therefore, this work aimed to estimate the highest potential hydraulic conductivity in the 350 m gallery of the Horonobe underground research laboratory using the MSI (Fig.8-16(a)).

Hydraulic tests were performed to measure the hydraulic

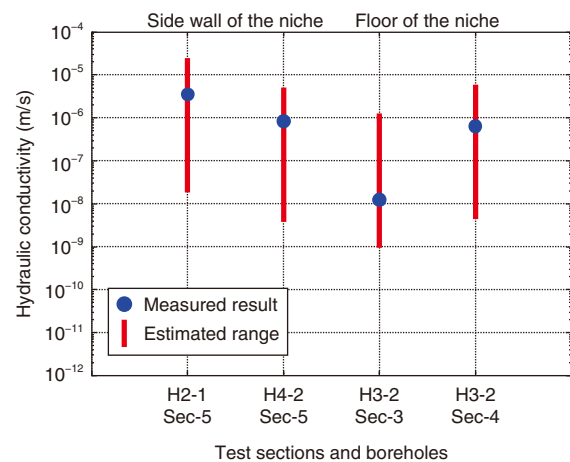


Fig.8-18 The estimated and measured highest potential hydraulic conductivities in the EDZ

The estimated ranges of the highest potential hydraulic conductivities (—) overlap with the measured results (●) on both the sidewall and below the floor of the niche.

conductivity in the EDZ in Niche No.3 (Figs.8-16(b) and (c)), and a hydro-mechanical coupling analysis was performed to simulate the maximum and minimum effective principal stress during niche excavation. The resulting distribution of effective stress is shown in Fig.8-17. From the analyzed effective stress distribution and tensile stress of rock, the highest potential hydraulic conductivity corresponding to the hydraulic test sections were estimated using the MSI model.

The estimated ranges of the highest potential hydraulic conductivity corresponding to the hydraulic test sections in the EDZ (—) are shown along with the hydraulic test results (●) in Fig.8-18. The estimated range has 2.5 orders of magnitude, as the MSI model considered the heterogeneity of hydraulic conductivity among fractures. The estimated ranges of highest potential hydraulic conductivity overlapped with the measured results on both the sidewall and below the floor of the niche. Thus, the highest potential hydraulic conductivity should be estimated based on the result of a surface-based investigation when applying the MSI model.

Reference

Aoyagi, K. et al., A Method for Estimating the Highest Potential Hydraulic Conductivity in the Excavation Damaged Zone in Mudstone, Rock Mechanics and Rock Engineering, vol.52, issue 2, 2019, p.385–401.

8-7 Dating Calcium Carbonate Using a Micro-Scale Analytical Method — A Method for Tracing Prior Underground Water Environments —

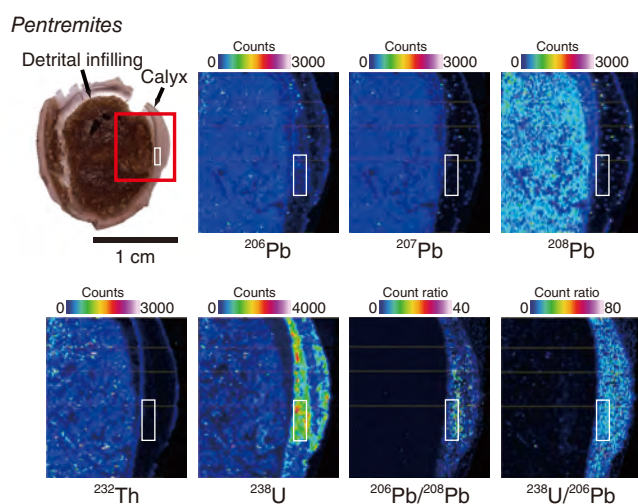


Fig.8-19 Elemental imaging map of the *Pentremites* sample
Here, the red square indicates the area of elemental imaging, and the white box indicates the area suitable for the dating method because of the higher ^{238}U concentration and higher radiogenic ^{206}Pb concentration ($^{206}\text{Pb}/^{208}\text{Pb}$ ratio).

Because calcium carbonate (hereinafter, carbonate) is as common filling mineral in rocks, the internal zoning of precipitation age, the chemical composition, and the carbonate's crystallographic structure offers a wide-use indicator to reconstruct past environmental variations. Chronological studies of fracture-filling carbonate in rocks can provide precious geological information about groundwater flow and fault movement in geological history.

As carbonate minerals often form a microscopic chemical zoning structure during growth, high spatial resolution is necessary to analyze and date these solid samples. Therefore, a uranium (U)–lead (Pb) carbonate dating method was developed using laser ablation-inductively coupled plasma-mass spectrometry (LA-ICP-MS). Difficulties applying LA-ICP-MS U–Pb dating to carbonate samples have been shown to include a lack of an international standard for *in-situ* dating and of a methodology for selecting suitable areas for dating because of the low U (parent nuclide of U–Pb systematics) concentrations.

Quantitative two-dimensional imaging maps of U, thorium (Th), and Pb isotope abundances of the carbonate samples were obtained using a LA-ICP-MS imaging technique to select suitable areas for dating (Fig.8-19). A carbonate reference material, named WC-1 and collected from marine calcite cement from the western side of the Delaware Basin in New Mexico, USA, was used for LA-ICP-MS U–Pb dating based on previous research (*). To check the validity of the proposed

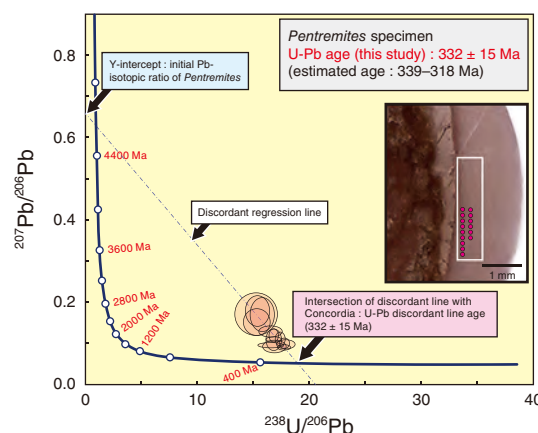


Fig.8-20 The dating result of *Pentremites* sample (Concordia plot)

As a result of the U–Pb isotopic analysis of the *Pentremites* sample, the sample was dated 332 ± 15 Ma, corresponding to almost the middle of the age range of this specimen (~ 339 to ~ 318 Ma). The 15 pink solid circles in the right photograph show the laser-irradiated points selected using the prior elemental imaging map (Fig.8-19).

dating technique, a well-preserved calcareous Carboniferous fossil specimen, *Pentremites*, (collected from the strata of the Chesterian age, from mid-Mississippian to earliest Pennsylvanian, in northeastern Oklahoma, USA, corresponding to an estimated age of ~ 339 to ~ 318 Ma), was dated.

The U–Pb age of the *Pentremites* sample was dated 332 ± 15 Ma (1σ), corresponding well to the age range of this specimen (~ 339 to ~ 318 Ma) (Fig.8-20). Thus, the proposed LA-ICP-MS dating method was successfully used to date the carbonate sample. Additionally, an examination of robust ICP condition was performed. It may be suggested that we do not need to prepare a carbonate reference material such as WC-1 under the condition to introduce nitrogen (N_2) gas into ICP.

Future work will aim to improve the analytical precision and validate the applicable age range to apply the proposed dating technique to research the long-term stability of the geological environment.

This study was part of the result conducted “R&D program supporting the development of technology for geological disposal of high-level radioactive waste”, and supported by the Agency of Natural Resources and Energy (ANRE), the Ministry of Economy, Trade and Industry (METI), Japan.

* Roberts, N. M. W. et al., A Calcite Reference Material for LA-ICP-MS U–Pb Geochronology, *Geochemistry, Geophysics, Geosystems*, vol.18, issue 7, 2017, p.2807–2814.

Reference

Yokoyama, T. et al., U–Pb Dating of Calcite Using LA-ICP-MS: Instrumental Setup for Non-Matrix-Matched Age Dating and Determination of Analytical Areas Using Elemental Imaging, *Geochemical Journal*, vol.52, issue 6, 2018, p.531–540.

8-8 Chemical Analysis and Identification of Many Mineral Grains — New Technique to Elucidate the Mountain Uplifting Process —

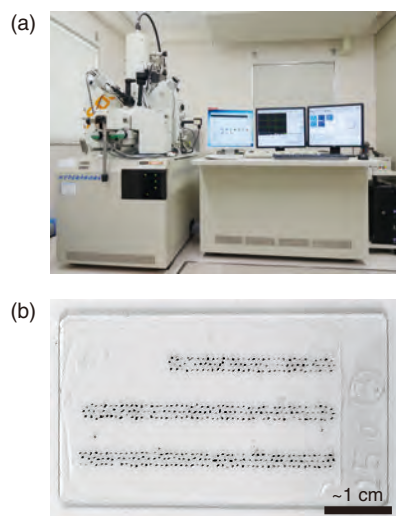


Fig.8-21 Electron probe microanalyzer (EPMA) and a prepared sample

(a) The EPMA was used for the chemical analysis of mineral grains extracted from sediment samples. (b) Hundreds of mineral grains, approximately 0.25 mm, were mounted on glass slides for continuous analysis by EPMA.

Safe geological disposal of high-level radioactive waste requires an understanding of mountain uplift, as this affects the long-term stability of the groundwater flow system.

Provenance analysis is an effective approach for understanding the mountain uplifting process. Discrimination of a category of minerals based on chemical features can be useful as a tool for provenance analysis because several kinds of minerals are resistant to weathering. Moreover, those minerals could be concentrated, but their chemical compositions have the potential to serve as indexes for provenance analysis. However, mineral identification using optical microscopy for large amounts of fine sands is time-consuming and poses a non-negligible risk of misidentification.

Therefore, an electron probe microanalyzer (EPMA) was used to perform rapid chemical analyses of a multitude of minerals extracted from the sediment and candidate provenance rocks in the studied area (Fig.8-21(a)). Provenance analysis requires the analysis of a large amount of mineral grains to grasp the overall trend of the sample. Optimizing the operating conditions to allow for the shortest possible measurement time allowed each grain to be analyzed in approximately three and a half minutes. The mineral grains were analyzed continuously, as this method does not require grain-by-grain analysis under a microscope (Fig.8-21(b)). The chemical composition data was then used to automatically identify mineral species using a spreadsheet

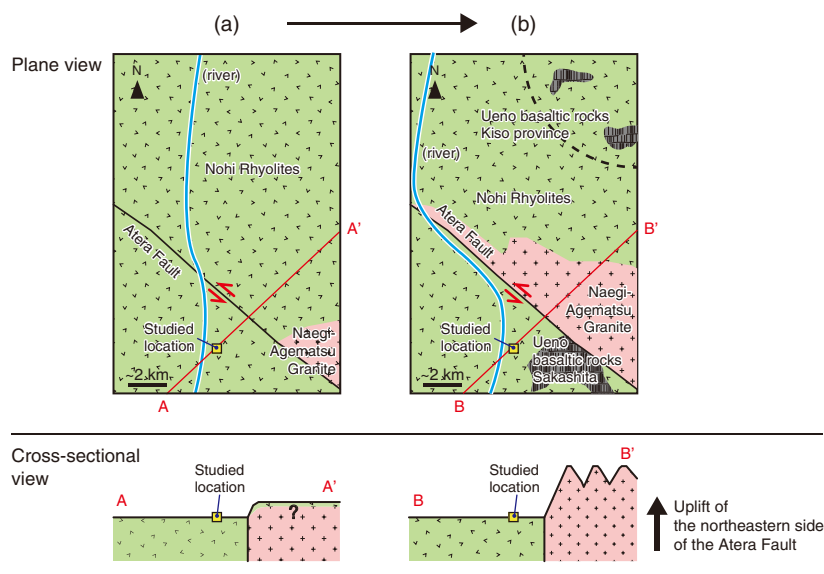


Fig.8-22 Geological outline showing the sampling point of the Toki Sand and Gravel Formation and surrounding geology

Provenance analysis of the Toki Sand and Gravel Formation revealed that the source rock of the sediment supplied to the sampling point changed from the Nohi-Rhyolite and the Naegi-Agematsu Granite, indicating that the distribution of source rocks changed.

software based on the criteria from existing data.

This method was applied to sediment samples taken from the Toki Sand and Gravel Formation in central Japan. Because the Nohi Rhyolite and Naegi-Agematsu Granite of the candidate provenance rocks in the studied area have similar formation ages, distinguishing them using grain-by-grain radiometric dating is difficult. Thus, their mineral and chemical compositions were the focus.

The result of the provenance analysis indicated that the Naegi-Agematsu Granite was exposed to the land surface in the provenance of the sampling location after deposition of the lower member, which is consistent with its gravel composition (Fig.8-22). This change could be explained by the uplift and denudation of the Atera Mountains associated with reactivation of the nearby Atera Fault, which has been estimated in previous studies.

The developed methodology for the quick quantification and mineral identification using EPMA therefore can contribute to provenance analysis focused on abundance ratio and chemical composition of minerals. This achievement will contribute to achieving efficient provenance analysis and to the development of research in the field of earth sciences.

This study was partly supported by the Agency of Natural Resources and Energy (ANRE), the Ministry of Economy, Trade and Industry (METI), Japan.

Reference

Shimizu, M. et al., Provenance Identification Based on EPMA Analyses of Heavy Minerals: Case Study of the Toki Sand and Gravel Formation, Central Japan, *Island Arc*, vol.28, issue 2, 2019, p.e12295_1–e12295_13.

8–9 Unified Management of Repository Design Information

— Development of a Design Support System for Geological Disposal Projects —

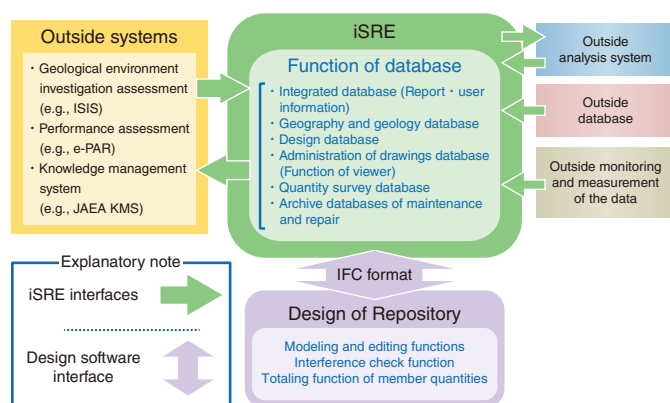


Fig.8-23 Communication between design support and external systems

The design support system centrally manages design-related information, including the information of external systems (ISIS, e-PAR, etc.) coordinated via an interface. Repository design information can also be presented on a 3D drawing.

Table 8-1 List of browsing and registration information for function confirmation

To confirm the functions of the design support system (prototype), an information list handled in the design change scenario shown in Fig.8-24 is presented.

Design of the repository	Information to be browsed	Information to be registered
1) Based on literature survey	Literature survey report (geography, geology, groundwater data, etc.)	Design document of the repository at the time of literature survey (Design conditions, analysis results, design drawings, minutes, etc.)
2) Based on preliminary investigation	Preliminary investigation report (geography, geology, groundwater data, etc.) Design document of the repository at the time of literature survey (Design conditions, analysis results, design drawings, minutes, etc.)	Design document of the repository at the time of preliminary investigation (Design conditions, analysis results, design drawings, minutes, etc.)

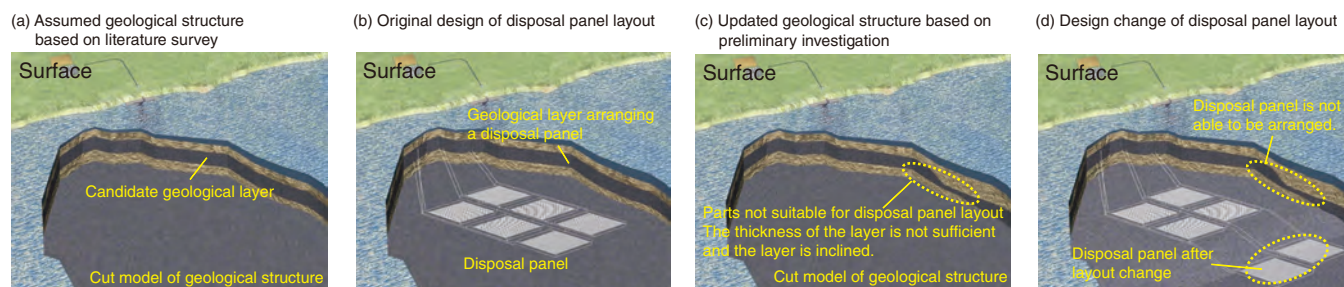


Fig.8-24 Example of design change scenario for function confirmation of design support system

The disposal panel layout was changed (d) to correspond to the geological layer (c) that was updated as a result of preliminary investigation on the repository design plan (b) for the assumed geological structure (a) based on literature survey.

The repository for the geological disposal project for high-level radioactive waste will be designed from a literature survey, then appropriately updated as research into the status of the geological formation progresses from the preliminary investigation stage to the detailed investigation stage. This design review will be performed during the construction phase of the repository.

Since the geological disposal project period is assumed to take about 100 years and engineers will be involved for more than one generation, the smooth transition of all information related to the design of the repository (i.e., the preconditions of repository design such as geological environmental conditions, design analysis, and design results), and reliable inheritance of the construction information during the construction stage of the repository is necessary.

Therefore, a design support system (Fig.8-23) that enables the unified management of these various types of information and the display of such information on a 3D drawing of the repository was examined. The main factors of this support system include a database (DB) of the data categorized into six data types related to the design and construction of the repository and an image viewer. The international standard IFC data format was selected in consideration of the long project period.

The analysis tool used in the design of the repository and the data set of the geological environment, i.e., the preconditions, are exchanged via an interface (IF). As a result, the analysis tool and DB can be updated and optimized flexibly and independently

of this system.

The effectiveness of the prototype that embodies the concept and functions shown in Fig.8-23 was confirmed through trials. One such trial involved changing the design of the repository, as shown in Fig.8-24. During design, the topography and geological information based on the literature survey shown in Table 8-1 is browsed from the topography and geological DB. The updated topography and geological information based on the preliminary investigation results (e.g., from ISIS: Information Synthesis and Interpretation System) was then registered in the DB. Then, the design of the repository based on the literature survey results browsed from the design DB was updated according to the updated topographic and geological information, and was registered in the DB as the design of the repository based on the preliminary investigation results.

The development and trial of the design support prototype system will be the basis for a practical system used in the disposal project. In addition, the visualization of information in the geological disposal project enabled by this system is expected to contribute to the promotion of social understanding and acceptance of the geological disposal project.

This study was part of the result conducted “R&D program supporting the development of technology for geological disposal of high-level radioactive waste”, and supported by the Agency of Natural Resources and Energy (ANRE), the Ministry of Economy, Trade and Industry (METI), Japan.

Reference

Sugita, Y. et al., Development of a Design Support System for Geological Disposal of Radioactive Waste Using a CIM Concept, Proceedings of 17th International Conference on Computing in Civil and Building Engineering (ICCCBE 2018), Tampere, Finland, 2018, 8p.

8-10 Realistic Modeling of Tracer Migration in Rock Fracture

— Effects of Fine-Scale Surface Alterations on the Tracer Retention in Fractured Crystalline Rock —

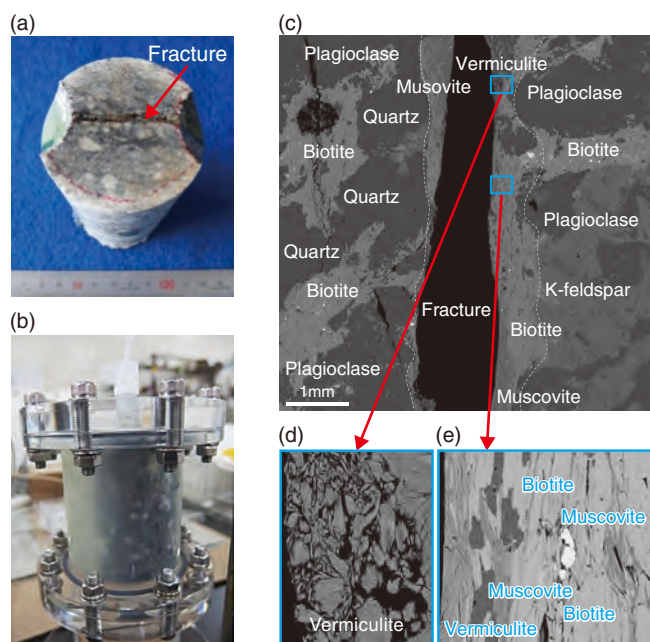


Fig.8-25 Experimental setup and EPMA observations

(a) Single-fracture sample from the GTS, (b) flow-through experimental setup, (c) heterogeneous mineral distribution around the fracture surface including the (d) weathered vermiculite and (e) foliated mica layer.

Crystalline rocks such as granites have been investigated as potential host rocks for the geological disposal of radioactive waste in many countries. Radionuclide (RN) transport in fractured crystalline rocks can be conceptualized by a dual-porosity model where RNs are transported by advective water flow through a fracture and diffusion into the surrounding rock matrix. Fine-scale alterations found around fracture surfaces are key uncertainties that need to be considered when developing transport models for fractured crystalline rocks. This work therefore focused on developing a comprehensive approach coupling laboratory tests, microscopic observations, and modeling to understand and quantify tracer transport processes occurring in natural fracture surfaces, using a single-fractured granodiorite sample from the Grimsel Test Site (GTS) in Switzerland.

Laboratory tests coupling flow-through, through-diffusion, and batch sorption were conducted using synthetic groundwater including five tracers with different retention properties: HDO (deuterated water), Se, Cs, Ni and Eu. A flow-through tracer test was carried out at a constant flow rate using a granodiorite sample containing a single natural fracture (Figs.8-25(a) and (b)). Through-diffusion and batch sorption tests were also conducted using the same tracer solution for two different samples taken from a natural fracture surface and from a matrix part. These test results indicated that tracer retention was consistently in the sequence of $\text{HDO} \approx \text{Se} < \text{Cs} < \text{Ni} < \text{Eu}$. Heterogeneities in the

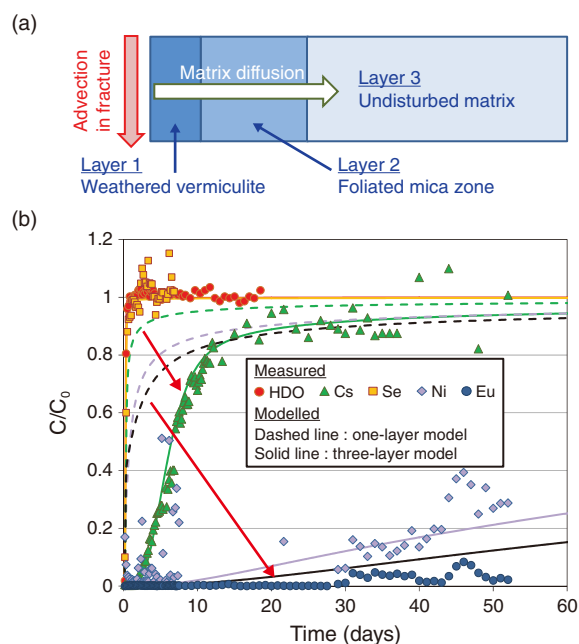


Fig.8-26 Measured and modeled breakthrough curves

(a) Conceptual transport model considering three layers at the fracture surface, (b) measured breakthrough curves and simulated results for one- and three-layer model.

mineral and pore distribution around the fracture were clarified by coupling X-ray computed tomography (X-ray CT) and electron-probe microanalysis (EPMA). Heterogeneous mapping of the fracture apertures was visualized and evaluated using X-ray CT images. By comparing the elemental maps from EPMA and the chemical composition of primary minerals, heterogeneous mineral distributions were identified, indicating a foliated mica-rich zone near the fracture surface and a weathered vermiculite zone at the outermost surface (Figs.8-25(c)–(e)).

Based on these microscopic observations, a three-layer model including weathered vermiculite, foliated mica, and undisturbed matrix layers (Fig.8-26(a)) and their properties such as thickness, porosity, sorption, and diffusion parameters, obtained from laboratory tests, provided a better interpretation of the breakthrough curves of all tracers, measured in flow-through tests, than either a one-layer model assuming only an undisturbed matrix corresponding to a traditional dual-porosity model (Fig.8-26(b)). Mechanistic understanding and detailed modeling considering the effects of fine-scale surface alteration around a natural fracture will improve the safety assessment of fractured crystalline rocks.

This study was partly supported by the Agency of Natural Resources and Energy (ANRE), the Ministry of Economy, Trade and Industry (METI), Japan.

Reference

Tachi, Y. et al., Effects of Fine-Scale Surface Alterations on Tracer Retention in a Fractured Crystalline Rock from the Grimsel Test Site, *Water Resources Research*, vol.54, issue 11, 2018, p.9287–9305.

8-11 Stabilization of Low-Level Radioactive Waste Solutions

— Cement Solidification of Low-Level Radioactive Waste Solutions Containing Carbonates —

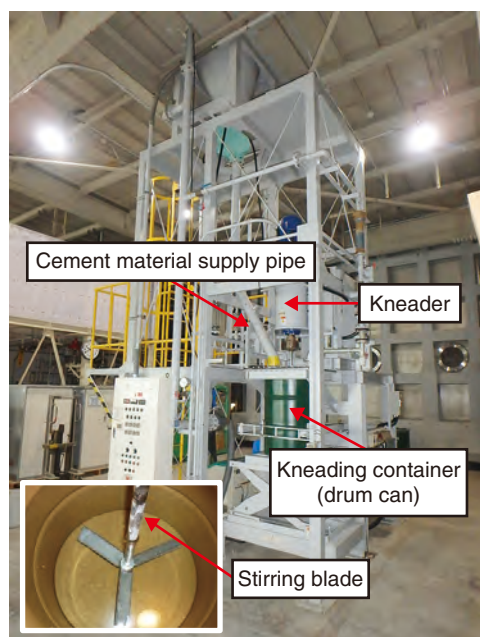


Fig.8-27 Real-scale kneading machine

As the drum-can-sized solidified cement product is kneaded, physical property data is acquired.

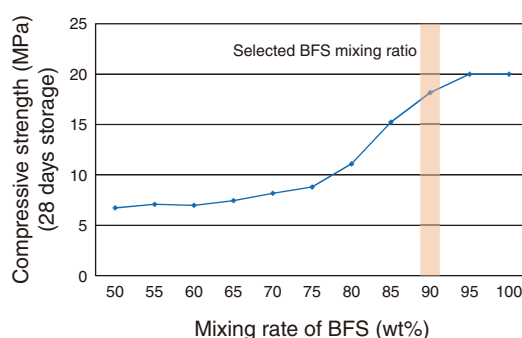


Fig.8-28 Changes in BFS mixing ratio and compressive strength for OPC

An increase in compressive strength was confirmed as the BFS mixing ratio increased. Solidification days are required when the BFS concentration is $\geq 95\%$, so mixed cement (BFS:OPC = 9:1) will be adopted at the LWTF to provide solidification days and fluidity suitable for operation.

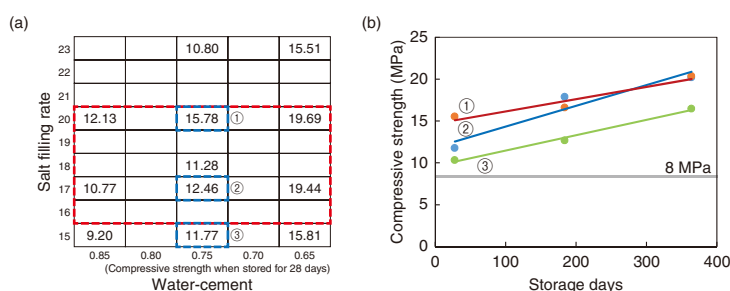


Fig.8-29 (a) Core compressive strength in mixed cement and (b) rate of change in compressive strength during long-term storage

(a) Compressive strength of 8 MPa or greater was obtained even over a wide range of water-cement mass ratios (0.65 to 0.85) and salt filling rate (15wt% to 23wt%). (b) A long-term increase in compressive strength was confirmed for the samples within the blue dotted line (① to ③).

At the Low-Level Radioactive Waste Treatment Technology Development Facility (LWTF), the low-level radioactive concentrated liquid waste and phosphoric acid liquid waste generated at the reprocessing facility is to be solidified. Of these, low-level radioactive concentrated liquid waste is subjected to nuclide separation (coprecipitation/ultrafiltration, Cs/Sr adsorption) and separated into slurry waste liquid and nitrate waste liquid. Nitrate waste liquid is converted to carbonate waste liquid by nitrate decomposition and it is planned to be cemented by using an in-drum mixing method. Carbonate waste liquid generated by nitrate decomposition treatment accelerates cement solidification, causing ordinary Portland cement (OPC), generally used for cement solidification, to cure too quickly. A new cement material must thus be selected and examined. Thus, the solidification range under various conditions such as water: cement ratio and salt filling rate (ratio of salt contained in solidified body when solidified), and the compressive strength during long-term storage was investigated using a real-scale kneading machine (Fig.8-27). The cement studied was a mixture of blast-furnace slag fine powder (BFS), which hardens slowly by reacting with alkali, and OPC. Increasing the ratio of BFS caused an increase of compressive strength and fluidity (Fig.8-28). Based on these results, real-scale kneading

was performed using mixed cement with a BFS:OPC ratio of 9:1. As the ratio of water and carbonate is expected to at the LWTF, the range of possible solidification was also investigated using the water: cement ratio and salt filling rate, which greatly affect the solidification properties, as parameters (Fig.8-29(a)). As a result, a the water-cement ratio of between 0.65 and 0.85 and salt filling rate between 15wt% and 23wt% satisfied the target compressive strength (≥ 8 MPa). From the red dotted line centered on ② (in the error range of LWTF operation), it was confirmed that solidification was possible even in consideration of fluctuations in the ratio of water and carbonate. Furthermore, the long-term change in compressive strength of the solidified material was found to increase over a long term (Fig.8-29(b)), likely because the BFS contained in the cement reacts slowly, slowly increasing the compressive strength. In addition, since no abnormalities such as cracks were observed after long-term storage, the solidified body was confirmed to be stable and did not expand or contract.

These results can be used to design a cement solidification facility for installation in the LWTF. In future work on cement solidification tests, a wider range of solidification condition will be studied to optimize LWTF operation.

Reference

Matsumura, R. et al., Development of Cement Based Encapsulation for Low Radioactive Liquid Waste in Tokai Reprocessing Plant, Proceedings of 3rd International Symposium on Cement-Based Materials for Nuclear Wastes (NUWCEM 2018), Avignon, France, 2018, 4p., in USB Flash Drive.

8-12 Investigation of Fuel-Cladding Materials for the Reprocessing of Spent Nuclear Fuel

— Evaluation of the Nitric Acid Resistance of New Materials Preventing Severe-Accident Progression —

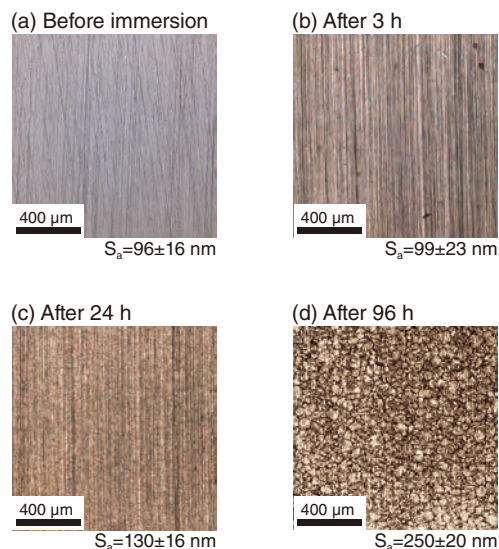


Fig.8-30 Specimen surface before and after immersion in a boiling nitric acid solution

The surface of the specimen was observed by laser microscope. Corrosion marks were observed on the surface after 96 h of immersion. The surface roughness, evaluated by the arithmetical mean height of the surface (S_a), increased with the immersion time, indicating the progress of corrosion.

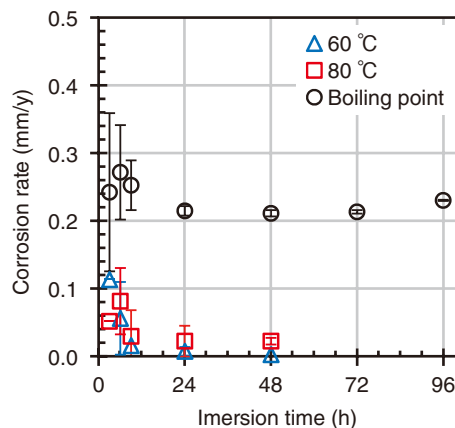


Fig.8-31 Corrosion rates of the FeCrAl-ODS steel in 3 mol/dm³ nitric acid solution at different temperatures

The corrosion rate (mm/y), which was calculated by mass loss (g), at the boiling point was higher than that at 60 °C and 80 °C, where it decreased to approximately 0.22 mm/y with increased immersion time.

Hydrogen generated from the oxidation of zirconium (Zr) -alloys used in various components on light-water reactors is believed to have caused the explosion at the TEPCO's Fukushima Daiichi NPS. FeCrAl-oxide dispersion strengthened (ODS) steels have been developed for accident-tolerant fuel cladding of light water reactors and are expected to enhance accident tolerance more than did Zr-alloys.

The reprocessing of spent nuclear fuel having Zr-alloy cladding has been established, as has the behavior of Zr-alloys in the reprocessing process. However, the behavior of FeCrAl-ODS steels in the reprocessing process remains uncertain. Therefore, the corrosion behavior of FeCrAl-ODS steel during the dissolution process, which is the first chemical process in the reprocessing process, was evaluated.

As in the fuel dissolution process, simulated fuel cladding specimens were immersed into a high-temperature solution with a high concentration of nitric acid (3 mol/dm³, as is the operational concentration in the dissolver). After several hours of immersion, the specimen was weighed and its surface was observed. The resulting variation of the specimen surface in the immersion experiment is shown in Figs.8-30(a)–(d). After 3 h of immersion, no clear sign of corrosion was observed, indicating a favorable corrosion resistance of FeCrAl-ODS steel. The resulting corrosion rate is shown in Fig.8-31, indicating that

FeCrAl-ODS steel has a better corrosion resistance than does stainless steels utilized for component of reprocessing process.

The behavior of elements on the top surface of the FeCrAl-ODS steel specimen shown in Fig.8-30(d) was investigated via X-ray photoelectron spectroscopy (XPS). The results indicated that an oxide film was generated on the top surface and iron (Fe) was selectively dissolved from the oxide film. Chromium (Cr) and aluminum (Al) remained as oxides on the top surface.

The strong oxide film generated on the top surface provided the good corrosion resistance of FeCrAl-ODS steel. It is necessary to evaluate the effects of various elements and radiation in spent nuclear fuel, because these are important factors for corrosion under actual dissolution conditions. Future work will involve evaluating the corrosion behavior of FeCrAl-ODS steels similar conditions, and the effect of corrosion products on reprocessing process will be investigated.

This study was part of the result conducted “Development of a Technical Basis for Introducing Advanced Fuels Contributing to Safety Improvement of Current Light Water Reactors”, carried out under the project “Development of a Technical Basis for Safety Improvement at Nuclear Power Plants”, and sponsored by the Agency for Natural Resources and Energy (ANRE), the Ministry of Economy, Trade and Industry (METI), Japan.

Reference

Takahatake, Y. et al., Corrosion Behaviour of FeCrAl-ODS Steels in Nitric Acid Solutions with Several Temperatures, Proceedings of Annual Topical Meeting on Reactor Fuel Performance (TopFuel 2018), Prague, Czech Republic, 2018, 9p.

8-13 Predicting the Flow and Mixing Behavior in an Extractor

— Simulating Fluidity, Dispersion, and Mass Transfer in a Centrifugal Contactor —

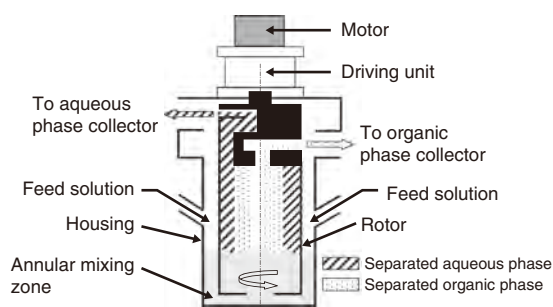


Fig.8-32 Schematic of a typical centrifugal contactor

The aqueous and organic phases supplied from each inlet are mixed and dispersed in the annular mixing zone by the rotation of the rotor, which causes mass transfer between both phases. The dispersion entering the rotor is forcibly separated by a high centrifugal force and the separated phases are discharged from the upper part of the rotor.

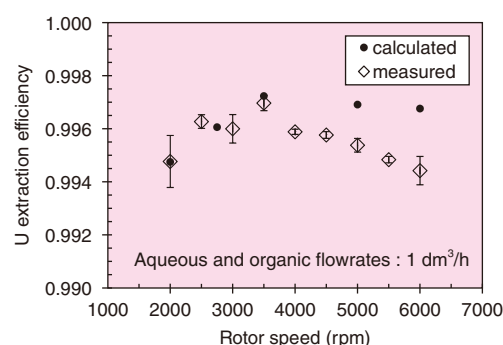


Fig.8-34 Variation of uranium extraction efficiency with rotor speed

Both simulation and experimental results indicated that a maximum U extraction efficiency was obtained at a rotor speed of approximately 3500 rpm.

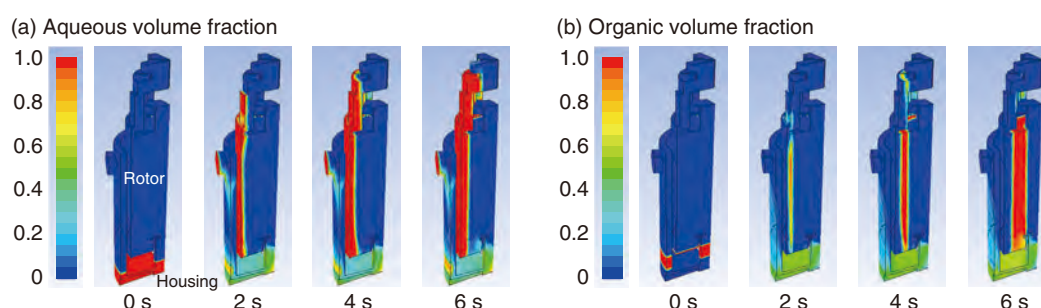


Fig.8-33 Time dependency of (a) aqueous and (b) organic volume fractions in a centrifugal contactor with a rotor diameter of 28 mm

Simulation results under aqueous and organic flowrates of 100 cm³/min and a rotor speed of 3500 rpm

During the reprocessing of spent nuclear fuel, several extractors are used to extract uranium (U) and plutonium (Pu) from the nitric acid dissolver solution into the organic solvent. Among various extractors, centrifugal contactors (Fig.8-32), which mix and separate the aqueous and organic phases by high-speed rotor rotation, have some attractive advantages, such as a high throughput and superior phase separation performance. The flow and dispersion behaviors of the aqueous and organic phases in this contactor are closely related to its extraction performance. As such, a numerical analysis was developed to predict the effect of operating conditions on these behaviors and U extraction. This developed model can calculate the time dependency of aqueous and organic flow and dispersion in a centrifugal contactor, as well as the change of U concentration in each phase.

The resulting time dependencies of the aqueous (a) and organic (b) volume fractions in a centrifugal contactor are shown in Fig.8-33. Each phase flowed down from the inlet and was mixed in the annular mixing zone by the rotating rotor. The dispersion entering the rotor was quickly separated by centrifugal force into the outer, heavier, aqueous phase and the inner, lighter, organic phase.

Varying the operating conditions indicated that higher rotor speed and lower flowrate divided the zone with a high liquid volume fraction in the annular mixing zone into two regions, which decreased the mixing time. The liquid flow moving toward the center of the housing bottom was obtained in any conditions. Additionally, the droplet size of the dispersed phase in the annular mixing zone decreased with increasing rotor speed and decreasing flowrate. Overall, these results were in good agreement with experimental results, thus confirming the effectiveness of the designed model.

Prior U-extraction experiments using a centrifugal contactor obtained a maximum extraction performance at an appropriate rotor speed. As shown in Fig.8-34, the simulation results also showed the same tendency.

Future work will aim to apply the designed simulation to investigate the effect of the contactor structure and improve the performance of the centrifugal contactor.

This study was conducted in collaboration with YOKOHAMA National University, “Study on flow and dispersion characteristics in extractors” (2013–2017).

Reference

Sano, Y. et al., Simulation of Fluidity, Dispersion and Mass Transfer in an Annular Centrifugal Contactor, KAGAKU KOGAKU RONBUNSHU, vol.44, issue 6, 2018, p.335–340 (in Japanese).

Computational Science for Nuclear Research and Development

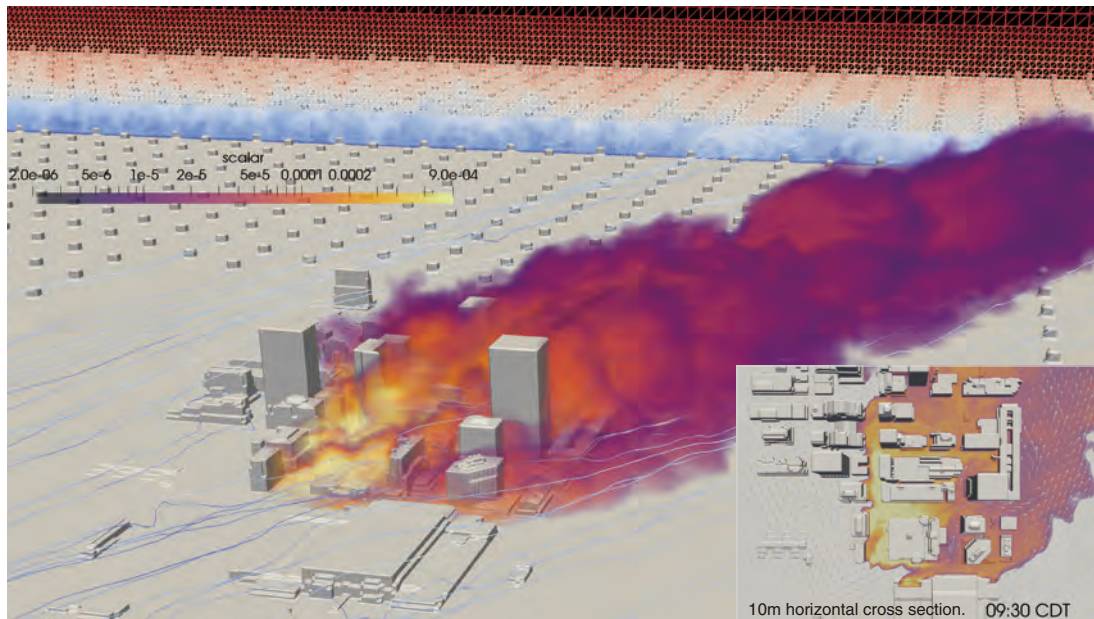


Fig.9-1 GPU-accelerated simulation of the wind-induced dispersion of radioactive material

The utilization of specialized hardware “GPU”, which is suitable for the fast calculation of a large number of simple arithmetic, enables nearly perfect computational efficiency and makes it possible to carry out large-scale simulations beyond the capacity of current supercomputers. The simulation result of the wind-induced dispersion of radioactive material, accounting for the effects of surrounding buildings and using an accelerated algorithm optimized for GPU, is shown here.

Nuclear research and development often necessitates the treatment of radioactive materials, which requires high costs and efforts. For effective and efficient research, combining traditional experiments with computational modeling is becoming more and more important. For example, in the analysis of severe accidents in nuclear reactors, melting and mixing behavior of nuclear fuel, various structural components, and the spread of radioactive material released into the environment must be modelled. In the design process of next-generation reactors, the safety and integrity of structural materials and nuclear fuels in unconventional environments must be assessed. Simulations prior to experimentation can help predict necessary experimental settings to yield safer and more effective results for the problems under consideration.

Computational analysis using supercomputers plays a crucial role in employing this strategy. Owing to the limitations of computational capacity, analytical models have often been simplified to carry out simulations in a reasonable amount of time. Using state-of-the-art technologies such as GPU and AI-based calculations will allow realistic simulations of complex models to be carried out with few or no simplifications. These simulations will provide detailed information not yet accessible by experiments and shed new light on the problem under consideration.

As such, Center for Computational Science & e-Systems (CCSE) is developing simulation frameworks to analyze complex phenomena comprised of various interacting model components to investigate severe accidents and material design for new reactors. These developing fundamental technologies of accelerated large-scale computations will be necessary for the next-generation exa-scale supercomputers (Fig.9-1). These simulation frameworks for complex phenomena will serve as

a common fundamental technology for nuclear R&D and for scientific research on the whole.

Research activities in computational science in FY2018 are summarized as follows. For the reconstruction and revitalization of the Fukushima Prefecture, experimental measurements of hardness of various model fuel debris were reproduced and analyzed from the viewpoint of atomistic structures. These results contributed to the planned decommission of the TEPCO’s Fukushima Daiichi NPS (Chapter 1, Topic 1-2). Software for the precise estimation of radiation exposure in residential area was also developed that can take the details of terrain and trees in the area into account and calculate a detailed distribution of air dose rate (Chapter 1, Topic 1-17). Specific computational technologies that have been under development for future exa-scale calculations include a GPU-accelerated algorithm for simulating the wind-induced dispersion of radioactive material (Topic 9-1) and parallel calculation techniques for fast and large-scale fluid dynamics simulations to analyze severe accidents (Topic 9-2). Specific advanced techniques of multi-physics, multi-scale simulation frameworks for the analysis of complicated phenomena discussed here include an analysis of laser-beam machining by sector of fast reactor and advanced reactor research and development (Topic 9-3), the effect of ambient hydrogen on the mechanical properties of materials (Topic 9-4), and the application of AI-related technologies to the simulation of the quantum many-body effect in strongly-correlated electron systems such as heavy-element compounds (Topic 9-5).

Furthermore, research on simulation and computational techniques have been promoted to form a common foundation for nuclear research and development and are being provided to the nuclear R&D and scientific research communities.

9-1 Acceleration of Plume Dispersion Model

— Reduced-Communication Algorithm for GPU-Based Supercomputers —

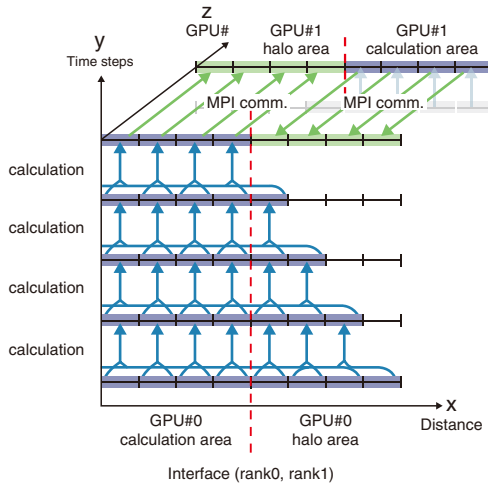


Fig.9-2 Timeline of the reduced-communication algorithm

Each grid performs time evolution (y-axis) using neighbor grid points (x-axis). The proposed algorithm reduces the required communication by replacing redundant sequential communication with one communication in halo area.

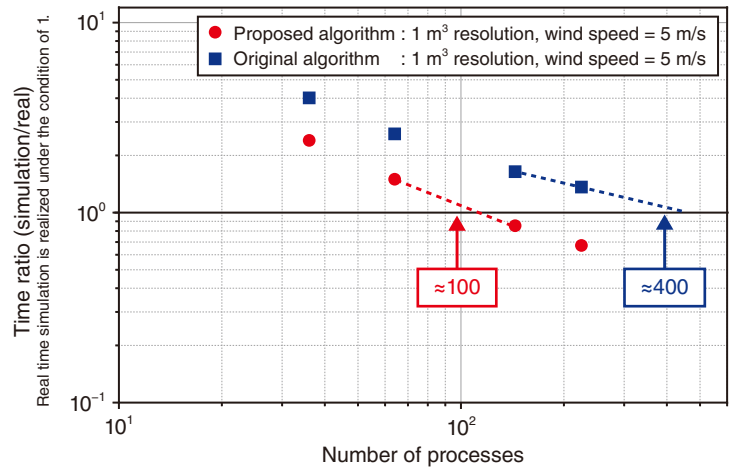


Fig.9-3 Performance of the reduced-communication algorithm on the supercomputer TSUBAME 3.0

The reduced-communication algorithm (●) operated significantly faster than the conventional algorithm (■), and real-time simulation was realized using 100 GPUs.

Nuclear security depends on the accurate prediction of environmental dynamics of radioactive substances based on detailed airflow models of plume dispersion. Such wind simulations can be applied to a wide range of industrial needs, including smart city design and nuclear security. Since turbulent airflows in large cities can reach Reynolds numbers of several million, multi-scale computational fluid dynamics (CFD) simulations are needed. Predicting the diffusion of pollutants requires several times faster calculations than real time. Existing wind analysis codes cannot realize real-time simulation with high resolution; new models suitable for next-generation supercomputers must be developed.

As such, an adaptive mesh refinement method was employed that changes the grid resolution according to the flow scale and general-purpose GPU (GPGPU) programing was implemented that enables the use of thousands of GPU cores. Although GPU achieves about 10 times higher computational performance than CPU, the communication performance between processors is comparable; communication time is a severe bottleneck on GPU platforms. Furthermore, GPU computing requires complicated pre- and post-processing steps related to halo data

communications and synchronous processing of data between parallel computers. A reduced-communication algorithm based on a temporal blocking method was thus developed that optimizes data structures to reduce the number of communications (Fig.9-2). In the conventional algorithm, each GPU performs a time evolution only on the calculation area and updates the halo area by communicating with the neighbor GPUs at every step. The proposed algorithm replaces sequential communication processes in the halo area with redundant time evolution calculation (Fig.9-2, →) and MPI communications are executed after the computational procedures (Fig.9-2, →).

The wind airflow model was then evaluated on TSUBAME at the Tokyo Institute of Technology. By implementing the proposed algorithm, the communication cost was reduced by 64% and strong scaling was improved by 200 GPUs (Fig.9-3). The results indicate that real-time airflow simulations for a two square kilometer area with a wind speed of 5 m/s is feasible using 1 m resolution.

This study was partly supported by the Joint Usage/Research Center for Interdisciplinary Large-scale Information Infrastructures (JHPCN) (jh180041-NAH) in Japan.

Reference

Onodera, N. et al., Communication Reduced Multi-Time-Step Algorithm for Real-Time Wind Simulation on GPU-Based Supercomputers, Proceedings of 9th Workshop on Latest Advances in Scalable Algorithms for Large-Scale Systems (Scala 2018), Dallas, USA., 2018, p.9–16.

9-2 Matrix Solvers for Multiphase CFD Simulations with One Hundred Billion Grids — Communication Avoiding Multigrid Methods —

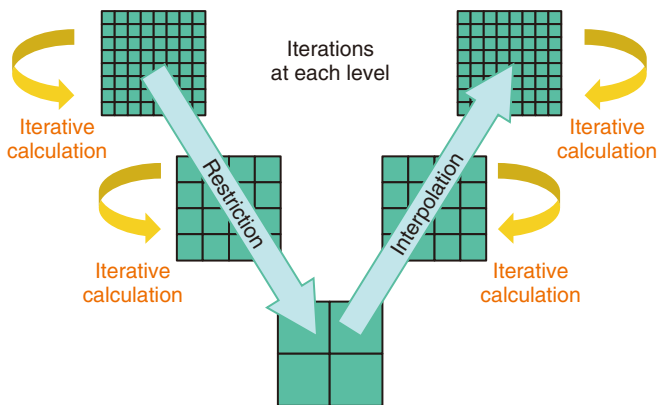


Fig.9-4 Multigrid method

Multigrid methods interpolate solutions on multi-scale grid systems with different resolutions and reduce errors at different scales independently by iterative calculations, leading to improved convergence properties in multi-scale problems.

JAEA promotes the development of multiphase computational fluid dynamics (CFD) to analyze complex thermal hydraulic phenomena in reactor core including structure materials and molten debris in severe accidents. Future exascale supercomputers are expected to enable whole reactor simulations that require one hundred billion grids. However, such large-scale simulations are characterized by multi-scale phenomena, and pressure Poisson solvers, which are main components in the multiphase CFD codes, show significant convergence degradation. A matrix solver was therefore proposed to compute multi-scale problems efficiently. As a result, an order of magnitude speedup was achieved in multi-phase CFD simulations with one hundred billion grids.

Solutions of multi-scale problems involve errors in the long and short wavelength regimes. Although matrix solvers are converged by reducing errors through iterative calculations, the information propagation of long-wavelength errors takes more time with a larger number of grids, leading to slower convergence. A multigrid method was thus introduced for use in multi-scale problems. In this method, slow convergence is avoided by reducing errors at different scales on multi-scale

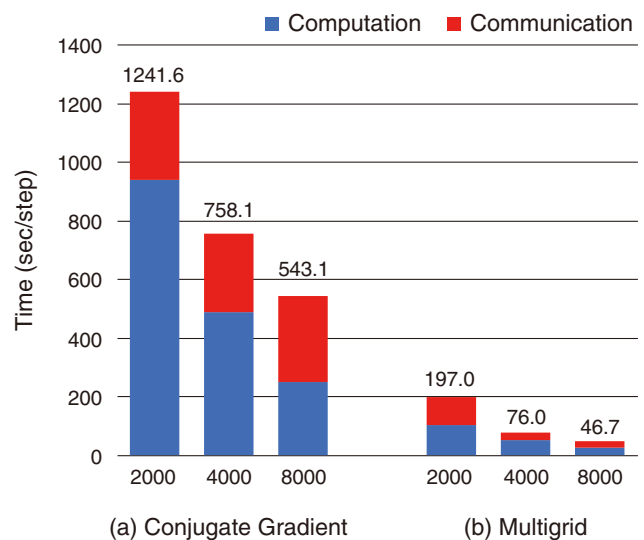


Fig.9-5 Scaling of computational performance up to the full system of the Oakforest-PACS supercomputer

The computational performances of the conventional matrix solver: (a) (i.e., the preconditioned conjugate gradient method) and the proposed matrix solver: (b) (the multigrid preconditioned conjugate gradient method) are shown using the Oakforest-PACS supercomputer in JCAHPC with 8000 computing nodes.

grid systems independently (Fig.9-4).

Research aimed at reducing the computational and communication costs for iterative calculations at each level was also required. The precision requirement on the multigrid method was first relaxed by using it as a preconditioner for the conventional conjugate gradient (CG) method, and single (32 bit) and double (64 bit) precision computations were then applied to the multigrid and CG methods, respectively. This mixed precision approach enabled a 50% reduction of computation and communication in the multigrid method while maintaining the precision of final solutions. The developed solver was tested in multiphase CFD simulations with one hundred billion grids on the Oakforest-PACS, which is the largest CPU-based supercomputer in Japan; a speedup of 11.6x speedup compared with the conventional matrix solver was achieved (Fig.9-5).

This study was supported by the Ministry of Education, Culture, Sports, Science and Technology (MEXT), Japan (Grant for Post-K priority issue No.6), “Development of Innovative Clean Energy”, and carried out under the project “Large-scale HPC Challenge”, the Joint Center for Advanced High Performance Computing (JCAHPC).

Reference

Idomura, Y. et al., Communication Avoiding Multigrid Preconditioned Conjugate Gradient Method for Extreme Scale Multiphase CFD Simulations, Proceedings of 9th Workshop on Latest Advances in Scalable Algorithms for Large-Scale Systems (ScalA 2018), Dallas, USA., 2018, p.17–24.

9-3 Prediction of Laser Irradiation Condition in Laser Processing

— Provision of Laser Irradiation Condition for Melting and Solidification Processing Using Computational Science Code SPLICE —

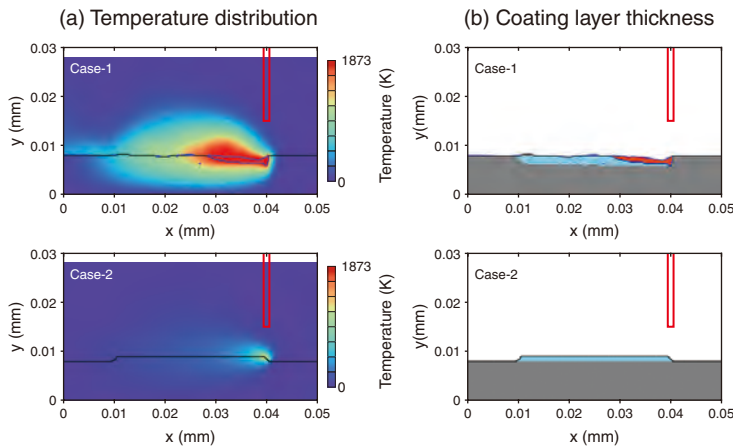


Fig.9-6 Simulation results using SPLICE: (a) temperature distribution and (b) coating layer thickness

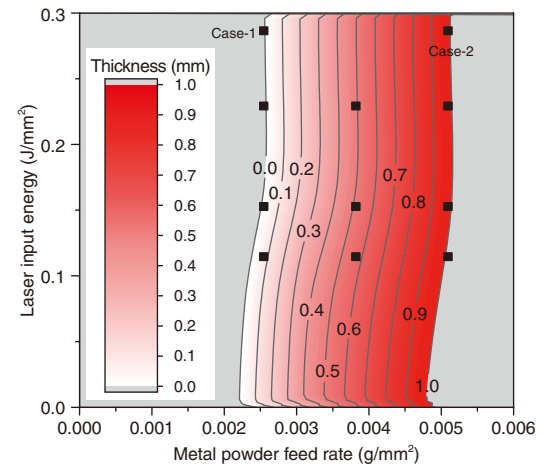


Fig.9-7 Design space for coating layer thickness, which is formed on a substrate by laser coating, derived with SPLICE

Lasers have been used in manufacturing processes for their high efficiency, high speed, low energy usage, low environmental impact, and low costs. The accurate representation of laser processing parameters within a database requires extensive experimentation, as performance is reliant on many parameters, including wavelength, output power, pulse width, sweep speed, and atmospheric conditions. Historically, the experience and intuition of experts have been relied upon to find and update processing parameters. If this system of judgments, observations, and actions can be realized in a cyberspace, a process equivalent to experts processing can be realized. Thus, a general-purpose thermohydraulics computational science numerical simulation code SPLICE was constructed.

This model was designed for gas-liquid-solid consolidated incompressible viscous flows including phase changes in various laser applications such as welding, cutting, and additive manufacturing. Here, SPLICE was applied for laser coating in order to make design spaces, and due to derive the optimum condition. As an additive manufacturing technology, laser coating is attractive due to its ability to freely form shapes. Additionally, it is an effective metal surface cladding technique, capable of increasing component lifetimes by melting and depositing an additive material such as a powder onto the substrate. To form a

high quality coating layer, optimum conditions, such as the laser output power and metal powder feed rate, must be determined. SPLICE allowed for finding optimum conditions to satisfy the design demands in a shorter amount of time.

The SPLICE-modeled results are shown in Fig.9-6, where (a) and (b) show the temperature distribution and coating layer thickness, respectively. In Case-1, excess laser energy caused the penetration of the coating layer into the substrate. Better control of the laser input energy and metal powder feed rate in Case-2 then allowed for the coating layer to be formed on the substrate without penetration. The coating layer thickness under varying powder feed rate and laser input energy are shown in Fig.9-7, where the black plot (■) indicates the simulation results for 11 cases including Case-1 and Case-2, which have been spline interpolated to represent the contour lines with a coating thickness of 0.1 mm as solid lines. These results were then confirmed with laser coating experimental results.

Visualizing the design space using SPLICE will greatly expand the scope and convenience of laser processing.

This study was partly supported by Council for Science, Technology and Innovation (CSTI), Cross-ministerial Strategic Innovation Promotion Program (SIP).

Reference

Muramatsu, T., Provision of Laser Irradiation Conditions for Melting and Solidification Processes using Computational Science Simulation Code SPLICE, Journal of Smart Processing, vol.8, no.1, 2019, p.4-8 (in Japanese).

9-4 Modeling the Effects of Hydrogen on Metallic Materials

— Spontaneous Separation of Aluminum Grain Boundaries by Hydrogen —

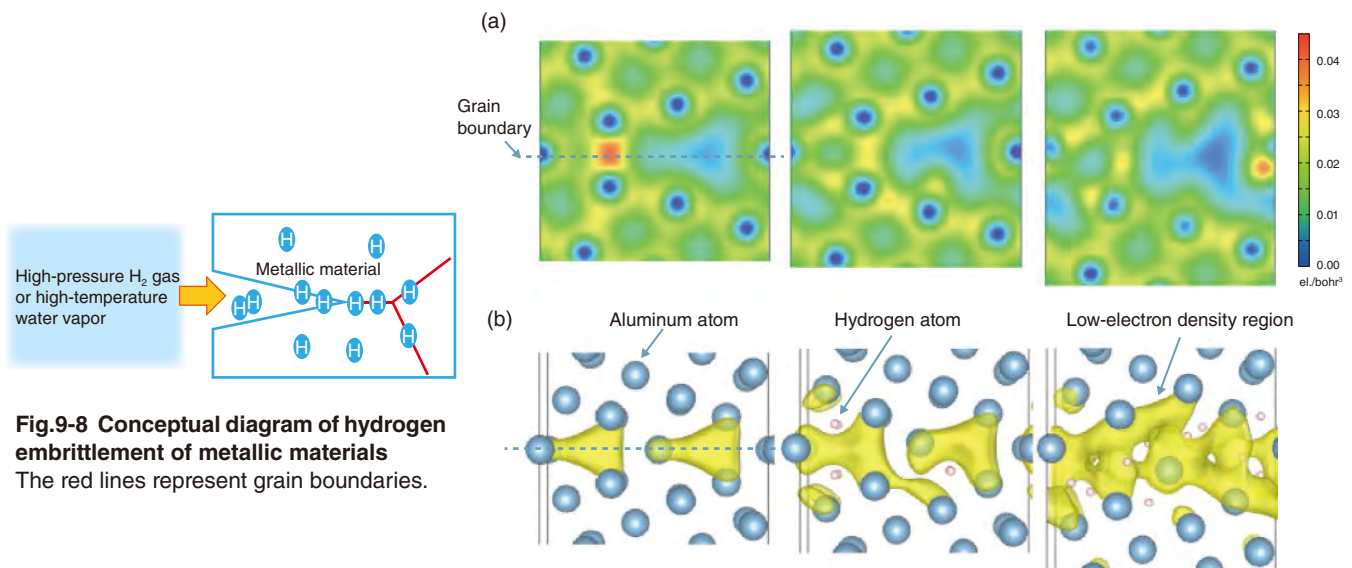


Fig.9-8 Conceptual diagram of hydrogen embrittlement of metallic materials
The red lines represent grain boundaries.

Fig.9-9 Separation of aluminum grain boundaries by penetration of hydrogen atoms
(a) Cross-sectional view of the electron density (electron/bohr³) connecting the atoms together; (b) three-dimensional region with a low atomic structure and electron density in the same region as the electron density above. The number of hydrogen atoms in the grain boundary increases from left to right. First-principle calculations capture a large expansion of the aluminum grain boundaries in the vertical direction perpendicular to the grain boundaries due to the penetration of hydrogen atoms.

As the materials inside a light water reactor are exposed to strong radiation and high-temperature water vapor, they must be resilient against deterioration over a long period. In some next-generation nuclear reactors, liquid metal is used as a refrigerant instead of water; either way, material deterioration due to liquid metal or hydrogen and oxygen must be addressed and prevented. The Center for Computational Science and e-Systems has aimed to clarify the mechanism of material degradation caused by the invasion of substances in the environment using simulations (Fig.9-8). As an application development, the degradation mechanism of aluminum by hydrogen was investigated. Hydrogen has been considered a promising energy source in the fight against global warming, but usage requires materials that can safely store hydrogen. However, hydrogen weakens many metals in a phenomenon known as hydrogen embrittlement. The aluminum alloy currently used for hydrogen storage is known to be less susceptible to hydrogen embrittlement under normal conditions, but it is known to be susceptible to embrittlement under more severe conditions, and its mechanism has not been clarified. The mechanism of hydrogen embrittlement must be clarified to allow for the design of better materials.

The effect of hydrogen atoms on aluminum was therefore

investigated using a first-principle calculation method to solve the Schrodinger equation and thus better understand the behavior of the electrons responsible for the properties of matter. In particular, calculations on the grain boundaries where hydrogen atoms to penetrate revealed interesting phenomena. In the case of iron and other materials, when hydrogen atoms enter a grain boundary, they expand up to a certain extent. However, when a hydrogen atom enters the crystal grain boundary in aluminum, the aluminum tends to expand endlessly and separate spontaneously to allow the hydrogen atom to enter, as shown in Fig.9-9.

Aluminum has a lower bonding energy between atoms than iron. A mechanism was discovered in which hydrogen atoms enter the gap and bond with aluminum atoms while breaking the bonds between aluminum atoms, thus stabilizing the structure. Furthermore, hydrogen atoms were shown to penetrate and split the material by pulling slowly even with a weak force. Such phenomena only occurred in environments with higher pressures and corrosion. In this way, the research methods developed in the research of nuclear materials are also effective in the research of metal materials for industrial use, producing ripple effects.

This work was partly supported by the Japan Science and Technology Agency (JST) (No.JPMJSK1412).

Reference

Yamaguchi, M. et al., First-Principles Calculation of Multiple Hydrogen Segregation along Aluminum Grain Boundaries, Computational Materials Science, vol.156, 2019, p.368–375.

9-5 AI-Assisted Acceleration of Quantum Simulations

— Analysis of Strongly Correlated Electron Systems with Sparse Modeling —

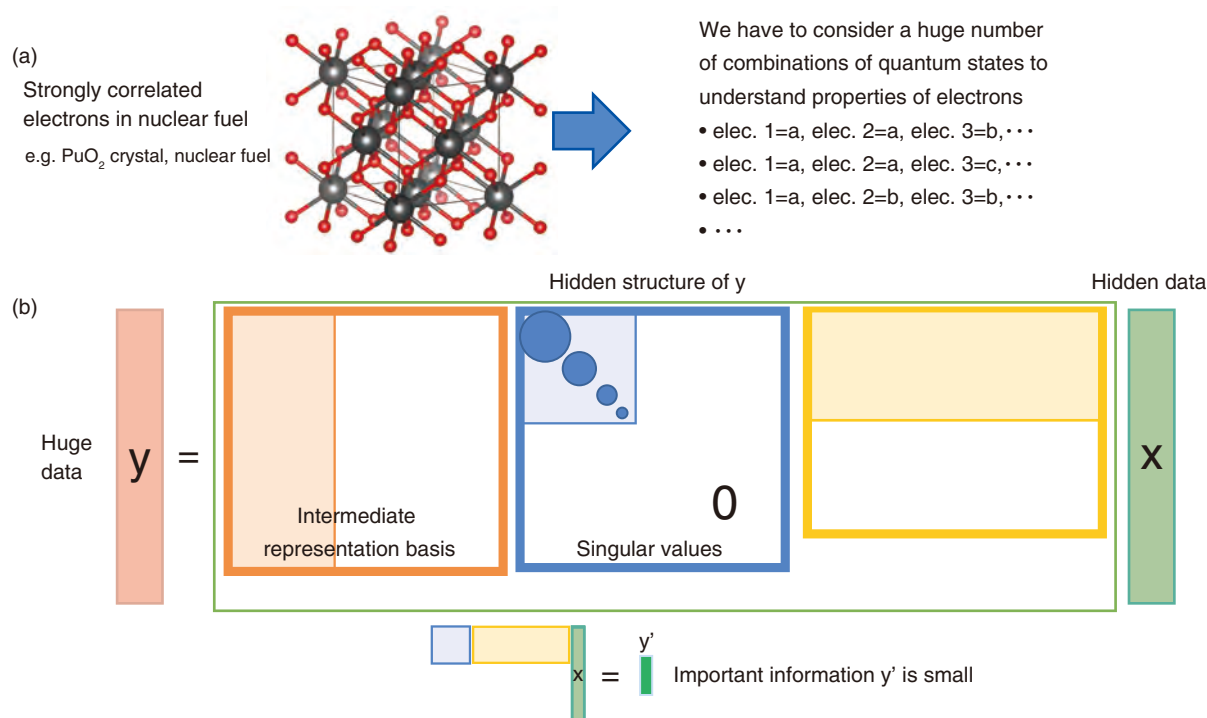


Fig.9-10 Schematic of sparse modeling approach

(a) Strong electron–electron interactions increase the calculation cost in materials with heavy elements. (b) Singular value decomposition and an intermediate representation basis allows for the simplification of large datasets.

Many properties of a material are a result of differences in the behavior of its electrons. In particular, materials such as high-temperature copper-oxide superconductors and heavy element compounds including uranium are called strongly correlated electron systems, in which electrons interact strongly. Understanding the behavior of a large number of interacting electrons is one of the most important issues in modern physics, but modeling the quantum mechanics of many electrons (quantum simulation) is extremely computationally intensive due to the large number of electronic states. Even with the latest supercomputers, the accurately reproduction of properties in strongly correlated electron systems is difficult (Fig.9-10(a)). Furthermore, the large dataset obtained makes it difficult to extract meaningful physical quantities that could be compared with experimental data.

Therefore, artificial intelligence (AI) technology that has been rapidly developing in the field of computational science was used. As AI technology generally handles large amounts of data for a small amount of important information, a method to extract only that important information, sparse modeling, was developed. Here, the important information was extracted from a large dataset using an AI technology for quantum simulation known as dynamical mean field theory with the exact diagonalization

(DMFT-ED).

In DMFT-ED, if a system size becomes large, the amount of calculation data increases. Large systems used for investigating physical phenomena can incur exceedingly high calculation costs. A new data expression method, intermediate expression, was therefore introduced to represent a large matrix as a product of matrices whose elements are almost zero in a process known as singular value decomposition. Then, only important information can be extracted. Application of this method indicated that the important information of any size model can be represented by at most a dozen numerical values (Fig.9-10(b)). From this result, even with models that have been considered impossible to calculate using conventional methods, the calculation cost can be greatly reduced.

By reducing the computational cost, complex models reflecting the electronic structure of heavy element compounds such as uranium compounds can be handled, thus allowing various physical properties of these materials to be clarified.

This study was supported by the Japan Society for the Promotion of Science (JSPS) KAKENHI Grants-in-Aid for Scientific Research (C) (No.18K03552), (No.18K11345), and Grant-in-Aid for Scientific Research on Innovative Areas (Research in a proposed research area) (No.18H04228).

Reference

Nagai, Y. et al., Smooth Self-Energy in the Exact-Diagonalization-Based Dynamical Mean-Field Theory: Intermediate-Representation Filtering Approach, Journal of the Physical Society of Japan, vol.88, issue 6, 2019, p.064004-1–064004-5.

Development of Technology and Human-Capacity Building in the Nuclear-Nonproliferation and Nuclear-Security Fields to Support the Peaceful Use of Nuclear Energy

The Integrated Support Center for Nuclear Nonproliferation and Nuclear Security (ISCN) has been conducting the following activities on technology and human-resources development related to nuclear nonproliferation and security in cooperation with affiliated domestic and overseas institutions toward a world without threats of nuclear weapons or nuclear terrorism (Fig.10-1).

Technology Development for Japanese and International Applications

A variety of technologies are under development to strengthen nuclear nonproliferation and security in accordance with domestic and international trends. Current projects on nuclear material detection and measurement technology development include the technology for detection of nuclear materials in heavily shielded containers using nuclear-resonance fluorescence (NRF) analysis, and non-destructive assay technology to measure nuclear material retaining high radiation levels by irradiating neutrons from an external pulsed neutron source. The development of software capable of calculating the photoelastic scattering probability affecting NRF measurement is outlined in Topic 10-1. The developed code was integrated into the Geant4 toolkit released in December 2018 and contributes to a wide range of research areas by improving the computation accuracy of photoelastic scattering. The accuracy and speed of nuclear forensics analysis technologies to identify the origin and processing history of nuclear materials used in criminal acts has been improved. A detector for first-responders following a nuclear terrorism events and artificial intelligence (AI) for analyzing nuclear forensic signature are also under development. Furthermore, evaluation metrics for the attractiveness of nuclear or radioactive material for nuclear security are being developed in collaboration with the U.S.

Policy Research Based on Technical Expertise

The factors affecting denuclearization have been studied based on requests from related administrative agencies through case studies of denuclearization in countries such as South Africa, Libya, Iran, and Iraq. This study has taken many factors into account, including the incentive for the development of nuclear weapons, situations at home and abroad, progress in development, and effectiveness of sanctions, as well as the technical procedures related to the disarmament, disabling, dismantlement, and verification in a view of peaceful use of nuclear energy.

Support for Human-Capacity Development

Following Japan's national statement at the April 2010 Nuclear Security Summit, ISCN has conducted capacity-building support activities targeting Asian countries since 2011. As of March 2019, about 4200 participants from Asian countries including Japan have joined in ISCN training activities on nuclear nonproliferation (safeguards) and nuclear security. ISCN's capacity-building support activities have contributed to human-resource development in Asia and have drawn high praise from the U.S. and Japanese governments.

Contributions to the International Verification Regime for CTBT

To establish a global verification regime for nuclear testing, the international monitoring system of the Comprehensive Nuclear-Test-Ban Treaty (CTBT) and a related national data center have been under provisional operation. The joint radioactive noble gas measurement project began with the CTBT Organization (CTBTO) to strengthen CTBTO's capability of detecting nuclear tests based on a voluntary contribution made to the CTBTO by the Government of Japan in February 2017. The project has been carried out by installing dedicated monitoring systems at Horonobe-Cho of Hokkaido and at Mutsu City of Aomori in January and March of 2018, respectively, and has contributed to the implementation of national policies for strengthening of nuclear test monitoring capability.

Support for JAEA's Nuclear-Fuel Transportation and Procurement of Research Reactor Fuels

Efforts towards nuclear transportation performed by our research and development centers are also supported, including by procuring fresh fuels and properly disposing of spent fuels for our research reactors. These activities have allowed for the contribution to the Global Threat Reduction Initiative (GTRI), which has been strengthening global nuclear security by promoting the systematic return of highly enriched uranium to the U.S.

Efforts to Promote Understanding

ISCN aims to help promote understanding of this field at home and abroad by investigating and analyzing international trends related to nuclear nonproliferation and security, by delivering the ISCN News Letter, and by holding the International Forum on Peaceful Use of Nuclear Energy, among other activities.

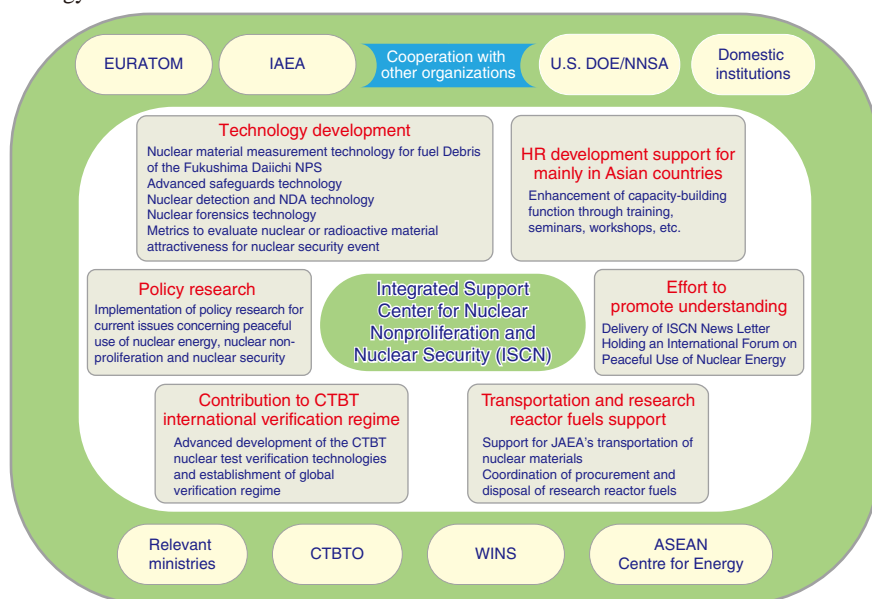


Fig.10-1 ISCN Activities and Affiliated Institutions

ISCN has played an active role in strengthening nuclear nonproliferation and nuclear security in cooperation with affiliated domestic and overseas institutions.

10-1 Nondestructive Assay of Nuclear Materials Using γ -rays

—Development of Simulation Code for γ -ray Elastic Scattering—

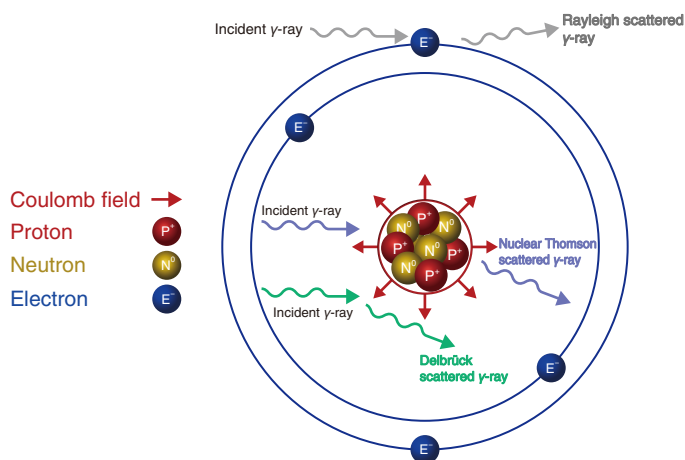


Fig.10-2 Schematic of γ -ray interactions in competition with the NRF

Three scattering processes acting as an on-beam background to photons emitted by the NRF process, including Rayleigh, nuclear Thomson, and Delbrück scattering.

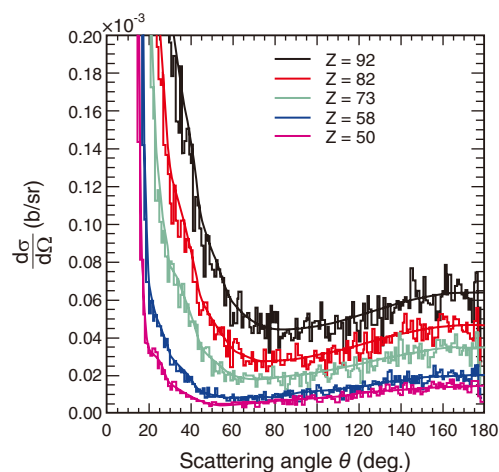


Fig.10-3 Differential cross section of 2.7 MeV γ -rays elastically scattered by different elements
The overlaid curves represent elastic scattering cross-sections calculated by the developed simulation. Experimental data are shown by histograms. Z denotes atomic numbers.

ISCN is developing technologies using a nuclear resonance fluorescence (NRF) method relevant to the nondestructive detection and assay of nuclear materials for nuclear safeguard and safety purposes. In this method, isotope-characteristic γ -rays emitted in NRF are measured using high-energy γ -rays that can penetrate a considerably thick and heavy shielding.

Only NRF γ -rays are taken into account when measuring highly enriched material. However, several materials are included in one sample, the effects from each material must be considered. For example, a typical nuclear fuel pellet contains about 90% of the host material ^{238}U and less than 1% of ^{239}Pu , an isotope of interest. When measuring the NRF of ^{239}Pu , a considerable background would be detected due to the elastic scattering by ^{238}U . Therefore, an estimation of the elastic scattering caused by the host material is essential for precise determination of an isotope of interest.

The interfering interactions include the elastic scattering of γ -rays from Rayleigh, nuclear Thomson, and Delbrück scattering as shown in Fig.10-2. Whereas Rayleigh scattering and nuclear Thomson scattering involve interactions between electrons and nuclei, Delbrück scattering represents a scattering of photons in a virtual Coulomb field produced by the nucleus and occurs more often in high-Z nuclei such as Pb and U which cause strong electric fields outside the nuclei.

Current methods of estimating elastic scattering are insufficient, as they do not include Delbrück scattering. Therefore, a model was developed to account for scattering events caused by interactions other than NRF interactions. This allows the on-beam background to easily be estimated by the simulation. The developed simulation considers three different scattering process as shown in Fig.10-2. The differential cross sections of these three processes were superimposed to account for the integrated effect of the on-beam background. The simulation code was implemented in the Geant4 framework. An example of the simulation is shown in Fig.10-3. The simulation can satisfactorily account for the on-beam background encountered in NRF measurements for several materials with different Z-values.

Based on these developments, elastic scattering γ -ray backgrounds can be accurately determined. Furthermore, the developed simulation code can be used for the evaluation of detector geometry to reduce the backgrounds. Future work will involve the investigation of the effect of photon polarization on the elastic scattering cross section.

This may help decrease the effect of the on-beam background by selecting appropriate scattering geometries.

This study was sponsored by the Ministry of Education, Culture, Sports, Science and Technology (MEXT), Japan.

References

- Omer, M. et al., Including Delbrück Scattering in GEANT4, Nuclear Instruments and Methods in Physics Research B, vol.405, 2017, p.43–49.
Omer, M. et al., Geant4 Physics Process for Elastic Scattering of γ -Rays, JAEA-Data/Code 2018-007, 2018, 32p.

Research Field Index

Research Field	Page	Topic	Title
Highlight	11	1-0	Research and Development on the Post-Accident Environmental Restoration and Decommissioning of Fukushima Daiichi NPS Providing Advanced Scientific Knowledge by Concentrating Expertise
	29	2-0	Nuclear Safety Research Implementing Continuous Improvements in Safety
	36	3-0	Advanced Scientific Research Advanced Science Pioneers the Future
	41	4-0	Nuclear Science and Engineering Research Fundamental Technologies for Nuclear Energy Innovation
	49	5-0	Applied Neutron and Synchrotron-Radiation Research and Development Contributions to Developments in Science, Technology, and Academic Research Using Neutron and Synchrotron Radiation
	58	6-0	HTGR Hydrogen and Heat Application Research Research and Development on HTGR, Hydrogen Production, and Heat Application Technologies
	66	7-0	Research and Development of Fast Reactors Endeavors in Research and Development of Fast Reactor Cycle for Nuclear Innovation
	72	8-0	Research and Development on Fuel Reprocessing, Decommissioning, and Radioactive Waste Management
	87	9-0	Computational Science and E-Systems Research Computational Science for Nuclear Research and Development
	93	10-0	Development of Science & Technology for Nuclear Nonproliferation Development of Technology and Human-Capacity Building in the Nuclear-Nonproliferation and Nuclear-Security Fields to Support the Peaceful Use of Nuclear Energy
Radiation, Accelerator and Beam Technologies	37	3-1	Unveiling the Unique Fission Process of Fermium Nuclides – Clues towards Understanding the Existing Limit of Super-Heavy Elements –
	39	3-3	Observation of a New Double Lambda Hypernucleus during a J-PARC Experiment – As a Microscopic Image, the Second Case Where the Nuclide is Identified –
	42	4-1	Contribution by Nuclear Physics to Transmutation Study – Accurate Prediction of Deuteron Transmutation –
	45	4-4	Accurate Detection of Particles in Accelerators, Space, and Medicine – Understanding the Mechanism that Determines the Scintillation Light Yields –
	48	4-7	Improving the Prediction Accuracy of Spallation Product Yields – Improving a Stochastic Model of Nuclear Fission Induced by a High-Energy Particle –
	50	5-1	Long-Term, Stable Production of a High-Intensity and High-Quality Beam – Development of an RF-Driven Negative Hydrogen Ion Source –
	51	5-2	Linking Spin-Fluctuations to Electron Correlations – A Combined Neutron and ARPES Study –
	52	5-3	Two-Dimensional Neutron Measurement with High Sensitivity and High Precision – Development of a Bump Cathode Neutron Detection Element –
	53	5-4	Measuring the Neutron Brightness Distribution from Liquid Hydrogen Moderators – Measuring and Validating the Neutron Brightness Distribution from Liquid Hydrogen Moderators at a High-Intensity Spallation Neutron Source –
	55	5-6	Towards Higher-Performance Steels – Elucidating the Microstructural Formation Mechanism via Electron and Neutron Beams –
	56	5-7	Successful Observation of the Melting and Solidification Phenomena of Metal with a Time Resolution of One Millisecond – Contributing to the Advancement of Laser Welding Technology –

Research Field	Page	Topic	Title
Fission Energy Engineering	57	5-8	Compound Developed to Recognize Slight Size Differences of Rare-Earth Elements – Towards Efficient Recycling of Lanthanides –
	15	1-4	Uncertainty Estimation in the Criticality of Nuclear Systems Containing Fuel Debris – Development of a Criticality Calculation Method for Randomly Distributed Materials –
	30	2-1	Uncertainty Reduction in Source Term Evaluation – Dependence of Decontamination Factor on Aerosol Particle Number Concentration in Pool Scrubbing –
	59	6-1	Proposal of Innovative Nuclear Fuel Cycle Based on High Temperature Gas-Cooled Reactor – Reduction of Cooling Time of Potential Toxicity of Radioactive Waste –
	60	6-2	Towards Implementation of Improved HTGRs – Conceptual Design of an Experimental HTGR for Steam Supply Based on an HTTR –
	62	6-4	Toward Load-Following, Demand-Dependent Operation of an HTGR – Confirming the Thermal Load Fluctuation Absorption Characteristics of an HTTR –
	68	7-2	Clarifying the Discharge Behavior of Molten Core Materials – Simulated Experiments Using a Shallow Water Pool for Molten Core Discharge –
	69	7-3	Uncertainty Analyses of MA Sample Irradiation Test Data – For Better Utilization of the Rare Data –
Nuclear Plant Technologies	12	1-1	Estimate the State of the RPV and PCV after a Severe Accident – Upgrading of the Comprehensive Identification of Conditions Inside Reactor –
	32	2-3	Safety Evaluation Considering Uncertainties of Accident Progression – Development of Simulation-Based Risk Assessment Methodologies –
	35	2-6	More Rational Inspection of the Piping System – Evaluating the Ratio of Welds to be Inspected Based on a Risk Informed In-Service Inspection –
	47	4-6	Estimation of Fission Product in a Light Water Reactor under a Severe Accident – Development of Fission Product Chemistry Database ECUME –
	67	7-1	Examining the Behavior of Core Elements during a Strong Earthquake – Development of 3-Dimensional Reactor Core Group Vibration Analytical Model –
Nuclear Fuel Cycle and Nuclear Materials	13	1-2	Numerical Evaluation of Fuel Debris Hardness – First-Principle Calculation of the Mechanical Properties of Fuel Debris –
	14	1-3	Degradation Mechanism of a BWR Control Blade – Understanding the Behavior of Boron Compounds during a Severe Accident –
	17	1-6	Determination of the Optimum Shape of Hydrogen Recombination Catalysts – Hydrogen Elimination Effect Experimentally Verified for Full-Size Equipment –
	18	1-7	Estimating Radioactive Waste Inventory – Sorption Behavior of Actinides on Zeolite –
	19	1-8	Towards Routine Analysis of Difficult-to-Measure Radionuclides – Preparation of Analysis Manuals for ⁹³ Zr, ⁹³ Mo, ¹⁰⁷ Pd, and ¹²⁶ Sn Waste –
	20	1-9	Assessing the Safety of Reusing Contaminated Rubble – Restricted Reuse in the TEPCO's Fukushima Daiichi NPS Site –
	21	1-10	Development of Robot Simulator for Decommissioning Task Training – Multi-Copter Simulator and Virtual Operator Proficiency Training System –
	31	2-2	Toward a More Reliable Safety Evaluation for Loss-of-Coolant Accidents – Uncertainty Quantification of Fracture Limit of Fuel Cladding Tube –
	34	2-5	Detailed Investigation of the Fracture Toughness of a Reactor Pressure Vessel – Fracture Toughness Evaluation of Heat-Affected Zone under Overlay Cladding Using Miniature Specimen –

Research Field	Page	Topic	Title
	40	3-4	Superconductivity Driven by Ferromagnetic Fluctuations in the Uranium Compound UGe_2 – Correlation between Superconductivity and Ferromagnetic Fluctuations Studied by Magnetic Measurements at High Pressure –
	43	4-2	Microscopic Corrosion Behavior in High-Temperature, High-Pressure Environments – In-Situ Measurement of Electrical Conductivity of Solution in Stainless Steel Crevices –
	44	4-3	Origin of Am/Cm Selectivity Elucidated by Chemical Bonding – Focusing on the Covalent Interaction between Metal Ions and Separation Ligands –
	70	7-4	Development of a Long Life Fast Reactor Control Rod – Irradiation Behavior of a Sodium-Bonded Absorber Pin –
	71	7-5	Advancing Microwave Heating Denitration Technology – Development of Particle Control Technology to Improve Powder Characteristics –
	74	8-1	Simplification of the Analysis of Uranyl Ions in Radioactive Wastes – Development of an Analytical Method with Capillary Electrophoresis Using Novel Fluorescent Reagents –
	75	8-2	Reducing the Generation of Uranium Waste – Decontaminating Metal Using Acidic Electrolytic Water –
	76	8-3	Ensuring the Stability of Trench-Type Radioactive Waste Disposal Facilities – Examination of Waste Acceptance Criteria of Sand Filling to Reduce Voids in Waste Packages –
	78	8-5	Evaluating the Uncertainty of the Redox Potential in Groundwater – An Application Example Based on Monitoring Data of Water Quality in the Horonobe Area –
	79	8-6	Estimating the Hydraulic Conductivity around a Gallery before Excavation – An Estimation Method Applying the Mean Stress Index –
	80	8-7	Dating Calcium Carbonate Using a Micro-Scale Analytical Method – A Method for Tracing Prior Underground Water Environments –
	81	8-8	Chemical Analysis and Identification of Many Mineral Grains – New Technique to Elucidate the Mountain Uplifting Process –
	82	8-9	Unified Management of Repository Design Information – Development of a Design Support System for Geological Disposal Projects –
	83	8-10	Realistic Modeling of Tracer Migration in Rock Fracture – Effects of Fine-Scale Surface Alterations on the Tracer Retention in Fractured Crystalline Rock –
	84	8-11	Stabilization of Low-Level Radioactive Waste Solutions – Cement Solidification of Low-Level Radioactive Waste Solutions Containing Carbonates –
	85	8-12	Investigation of Fuel-Cladding Materials for the Reprocessing of Spent Nuclear Fuel – Evaluation of the Nitric Acid Resistance of New Materials Preventing Severe-Accident Progression –
	86	8-13	Predicting the Flow and Mixing Behavior in an Extractor – Simulating Fluidity, Dispersion, and Mass Transfer in a Centrifugal Contactor –
	90	9-3	Prediction of Laser Irradiation Condition in Laser Processing – Provision of Laser Irradiation Condition for Melting and Solidification Processing Using Computational Science Code SPLICE –
Fusion Energy Engineering	94	10-1	Nondestructive Assay of Nuclear Materials Using γ -rays – Development of Simulation Code for γ -ray Elastic Scattering –
	91	9-4	Modeling the Effects of Hydrogen on Metallic Materials – Spontaneous Separation of Aluminum Grain Boundaries by Hydrogen –

Research Field	Page	Topic	Title
Health Physics and Environmental Science	16	1-5	Measuring Alpha-Particle Emitters Flying in Nuclear Facility Buildings – A Highly Reliable Alpha Dust Monitor Using a GPS Scintillator Plate –
	22	1-11	Observed Decrease of Radiocesium in River Water – Result of Three-Year-Long Observation –
	23	1-12	Radiocesium Behavior from Forest to Stream Water and River – Understanding How Dissolved Radiocesium is Discharged from Upstream –
	24	1-13	Clarifying the Distribution of Sediment-Associated Radiocesium at the Bottom of a Pond without Sediment Sampling – Visualizing the Vertical Distribution of Sediment-Associated Radiocesium –
	25	1-14	Exploring the Migration of Radionuclides to the Deep Ocean – Elucidation of Subduction from the Vertical Distribution of Concentration –
	26	1-15	Quickly and Accurately Measuring Environmental Radiation Levels – Advanced Conversion Method for Airborne Radiation Monitoring –
	27	1-16	Evaluating the Effective Dose Based on a Detailed Radiation Map – Providing Protection from Radiation in the Specified Reconstruction and Revitalization Base –
	28	1-17	Modeling the Distribution of Air Dose Rates in Habited Areas of Fukushima Prefecture – Developing the 3D Air Dose Rate Evaluation System –
	33	2-4	Evaluating of Sheltering Effectiveness against Internal Exposure at a Nuclear Accident – Factors Affecting Sheltering Effectiveness and Influence of Environmental Factors on Indoor/Outdoor Ratio –
	38	3-2	How Removal of Strontium from Seawater ? – Use of Coprecipitation Method by Barite Controlled Chemical Composition –
	46	4-5	Evaluation of Exposure Doses Considering Variations in Physiques of Japanese – Completion of Adult Japanese Human Model Series –
	77	8-4	Improvement of Matching Method for Seepage Flow Analysis – Application of Inversion for Seepage Flow Analysis in Multi-Layered Earthen Cover –
Others	88	9-1	Acceleration of Plume Dispersion Model – Reduced-Communication Algorithm for GPU-Based Supercomputers –
	54	5-5	Capturing of a Unique Spin Texture of a 4f Electron – Discovery of a Magnetic Skyrmion Lattice in the 4f Electron Magnet EuPtSi –
	61	6-3	Improving the Fuel Safety of High Temperature Gas-Cooled Reactors during Severe Oxidation Accident – Fabrication of Oxidation-Resistant Fuel Elements for Oxygen Ingress Accidents –
	63	6-5	Improving Hydrogen Production Efficiency Using Innovative Technologies – High-Efficiency Process Design of the Thermochemical IS Process –
	64	6-6	Reliability Improvements of Corrosion-Resistant Equipment for Hydrogen Production by the IS Process – Refined Quality Management of Glass-Lined Steel Material –
	65	6-7	Membrane Makes IS Process Chemical Reaction Efficiently – Use of an Ion-Exchange Membrane to Reduce Water Permeation by Cross-Linking –
	89	9-2	Matrix Solvers for Multiphase CFD Simulations with One Hundred Billion Grids – Communication Avoiding Multigrid Methods –
	92	9-5	AI-Assisted Acceleration of Quantum Simulations – Analysis of Strongly Correlated Electron Systems with Sparse Modeling –

About the Cover Design

The cover was designed with white hexagons similar to the pattern on a tortoise shell, which represents an ancient Japanese symbol of people's wish for longer lives. Coincidentally, this shape is also that of core fuel assemblies for the prototype fast breeder reactor "MONJU" and the high-temperature engineering test reactor "HTTR".

The top left figure shows results from the core-material melting and relocation (CMMR) test, and the bottom right figure shows the shape evolution and fission for two fermium isotopes, ^{254}Fm and ^{258}Fm .

The core-material melting and relocation (CMMR) test was conducted to understand the collapse, melting, and relocation of core materials during the TEPCO's Fukushima Daiichi NPS accident. A fuel assembly simulating the core structure of a boiling water reactor (BWR) were heated by high-temperature plasma (here, ZrO_2 pellets were installed, rather than fuel pellets). More details can be found on page 12 in Chapter 1, Topic 1-1.

The fission process for two fermium isotopes, ^{254}Fm and ^{258}Fm , proceeds by tracing the local minima on the potential energy surface. More details can be found on page 37 in Chapter 3, Topic 3-1.



About the activity status of the whole agency including CSR, please see the annual report "Japan Atomic Energy Agency 2019".

JAEA R&D Review 2019-20

Published by

Japan Atomic Energy Agency in January 2020

Editorial Board

Chief editor: Hiroshi Nakashima

Editors: Kenji Tatematsu, Tomoaki Suzudo, Mitsuo Koizumi, Takaumi Kimura,
Kazuki Iijima, Asako Shimada, Hiroyuki Koura, Yasuji Morita,
Yukiharu Takeda, Kenji Sakai, Takashi Takata, Shinji Kubo,
Hirotsugu Hamada, Takashi Mizuno, Kazuhiko Sato

This publication is issued by Japan Atomic Energy Agency (JAEA) on a yearly basis.
Inquiries about availability and/or copyright of the contents in this publication should be addressed
to Institutional Repository Section, Intellectual Resources Management and R&D Collaboration
Department, Japan Atomic Energy Agency (JAEA).

Address: 2-4 Shirakata, Tokai-mura, Naka-gun, Ibaraki-ken 319-1195, Japan

Phone: +81-29-282-6387, **Facsimile:** +81-29-282-5920, **e-mail:** ird-seika_shi@jaea.go.jp

All Rights Reserved by JAEA ©2020